Corrosion Control of Magnesium

for Stent Applications

Nabila Mustafa Elmrabet

Thesis submitted to the University of Nottingham

for the degree of Doctor of Philosophy

2017

Abstract

Biomaterials used for implants may be metallic, ceramic, polymeric or composite. Currently, metals that are gradually broken down in the body have been attracting much attention, as a new generation of biodegradable implants. Magnesium (Mg) and related alloys are promising candidates for degradable biomaterials, comprising temporary mechanical properties with biological acceptance to the human body. However, the target periods set clinically, with respect to the practical uses of Mg for biodegradable stents, have yet to be achieved. Hence, improved understanding of the corrosion behaviour of Mg in the biological environment is needed.

Novel Mg narrow walled minitubes, for degradable stent applications, have been produced using radio frequency magnetron sputtering (RF-MS) physical vapour deposition (PVD). The microstructural development of the as-deposited minitubes have been investigated, as a function of annealing temperature, using the combined complementary analytical techniques of scanning electron microscopy (SEM), energy dispersive X-ray spectroscopy (EDS), X-ray diffractometry (XRD) and microhardness indentation. The as-deposited minitubes exhibited columnar grain structures with high levels of porosity, but were very brittle. Slight alteration to the crystal structure, from columnar to more isotropic grain growth, was demonstrated at elevated temperature, along with increasing material densification, hardness and corrosion resistance. It is suggested that stabilisation of the columnar grains and the formation of oxide layers during the sequential Mg-layer deposition process, acted as a barrier, preventing the development of a fully dense, equiaxed structures.

The onset and development of Mg corrosion may be addressed by the use of coatings or near surface modification processes. Accordingly, the corrosion resistance of ~ 1-2 µm thick Al coatings, deposited by RF-MS on polished Mg surfaces, within Ar and Ar/H_2 environments, were appraised. The coatings were heat-treated at 300°C and 450°C, with the aim of inducing the formation of bioinert Al_2O_3, and samples were corroded within phosphate buffered saline (PBS) solution at 37°C to mimic the biological environment. Both as-deposited and heat-treated coatings were found to delay the onset of corrosion, but showed higher initial corrosion rates, once established, as compared to the polished Mg surfaces. Slight improvement in coating

performance was achieved through the addition of H_2 to the system, which acted to inhibit Al-Mg alloying and enhance Al_2O_3 formation. However, localized accelerated corrosion associated with substrate polishing damage emphasised the need for improved process control and coating uniformity. Si-H coatings deposited on Mg surfaces within Ar/H_2 ambient using a PVD technique was also investigated. The as-deposited coatings comprised dense, crack-free amorphous a-Si-H layers with thickness of $\sim$ 1 μm. Fourier transform infrared spectroscopy (FTIR) and X-ray photoelectron spectroscopy (XPS) analyses provided evidence for the presence of SiH_2 as well as SiO_x. The corrosion resistance of a-Si-H coated Mg increased significantly in contact with PBS, in both electrical and immersion tests, due to improved coverage of the substrate.

The effect of rapid thermal processing techniques on the corrosion resistance of Mg surfaces was also investigated. Mg surfaces treated by large area electron beam (LAEB) irradiation showed refinement of the surface grain structure, with increased grain boundary delineation, although localised ablation, roughness and crater formation increased with increasing cathode voltage and number of pulses. The corrosion potential and corrosion rate of LAEB modified surfaces generally increased with increase the energy imparted to the surface. The extended corrosion performance of low energy EB processed surfaces, under immersion testing was consistent with the trend of improved corrosion resistance during the early stages of immersion in PBS. However, surfaces over-processed at high energies experienced higher corrosion rates in both potentiodynamic and immersion testing, due to the development of inclusions, craters and cracks on the modified surface.

Further, Mg surfaces, modified by laser surface melting (LSM) under conditions of low energy laser irradiation, experienced rapid melting, causing surface smoothening and grain refinement centred along the laser beam tracks, whilst coarser grains decorated the overlapping regions, due to the Gaussian shape of the laser beam profile. More uniform surface processing was achieved by increasing the laser beam spot size, which acted to improve the corrosion resistance of Mg. Under high energy LSM processing conditions, Mg surfaces showed conventional laser melting rippled patterns, along with craters and cracks, and the redeposition of MgO particles, causing an increase in surface roughness and corrosion rate. The corrosion performance under immersion testing showed the corrosion rate similar to that of the original polished Mg samples, due to non-uniform surface modification and the mixed

development of fine and coarser grains. However, observation revealed that refined grain regions along the centre of the laser tracks were able to resist corrosion for longer times.

Generally, annealed Mg-minitubes produced by PVD, and the near surface modification of Mg by EB and LSM, showed that fine grained Mg can affect the electrochemical response of Mg within the physiological environment, due to the rapid, enhanced development of the passivation layer, promoted by improvements in surface homogeneity and an increase in grain boundary density.

Publications

- Elmrabet, N. M., Roe, M., Neate, N., Grant, D. M., Brown, P. D., *Investigation of Al Coated Mg for Biomedical Applications*. Magnesium Technology 2015, Florida, USA, 2015.

- Elmrabet. N., Botterill, N., Grant, D. M., Brown, P. D., *Characterisation of Mg biodegradable stents produced by magnetron sputtering*, Journal of Physics: Conference Series, 644 (2015) 012036

Presentations

- Elmrabet, N. M., Roe, M., Neate, N., Grant, D. M., Brown, P. D., *Investigation of Al Coated Mg for Biomedical Applications,* oral presentation, The minerals, metals, and materials society, TMS 2015 Annual Meeting & Exhibition, Magnesium Technology 2015 conference, Florida, USA, May 2015.

- Elmrabet. N., Botterill, N., Grant, D. M., Brown, P. D., *Characterisation of Mg biodegradable stents produced by magnetron sputtering*, oral presentation, Electron Microscopy and Analysis Group Conference (EMAG2015), Manchester, July 2015

Table of Contents

Acknowledgements

I would like to express my deepest gratitude to my supervisors, Professor Paul D Brown and Professor David Grant for their excellent guidance, patience, enthusiasm and encouragement, regarding my education and personal development. It would not be possible to complete this thesis without their endless support and understanding. I also would like to thank my internal assessor, Professor Matthew Hall for his valuable notes and suggestions during my study.

I would like to thank the staff in the Wolfson Building for technical assistance, including Keith Dinsdale, Dr Deen Zhang, Dr Nigel Neate, Dr Xuanli Luo, Thomas Buss, Martin Roe, Jason Greaves, Stuart Banston and Mark Daine. I also would like to give special thanks to Dr Nicholas Botterill for the opportunity to work with him on Mg stent project; and to Dr Katy Voisey, Dr Adam Clare, Dr James Murray and Dr Chunling Li for their guidance and valuable discussions regarding corrosion testing and electron beam processing.

Thank you to my colleagues, especially Hesham Sakr, Jessica Butterworth, Chou Pui, Nesma Aboulkhair, Marwa Abbas and Reda Felfel *et al.* for their friendship and assistance.

Thank you my parents and siblings for encouragement and respect of my choices. I am thankful for Husein Sherif, my husband and lifetime companion, for his infinite support, understanding and taking care of our children Mohamed, Abdulhadi, Alyakin and Ithar, and thank you for their patience during my long journey, you are all the air I breathe.

I would like to take this opportunity to thank the Biotechnology Research Centre and the Ministry of Higher Education-Libya for the financial support of my PhD study at the University of Nottingham.

List of Abbreviations

ASTM	American Society for Testing and Materials
BSE	Backscattered electrons
CE	Counter electrode
CR	Corrosion rate
CVD	Chemical vapour deposition
CW	Continuous wave
DC	Direct current
EB	Electron beam
E_b	Breakdown potential
ECAP	Equal-channel angular-pressing
E_{corr}	Corrosion potential
EDS	Energy dispersive X-ray spectroscopy
E_F	Flade potential
E_{pt}	Pitting potential
EW	Equivalent weight
fcc	Faced centred cubic
FTIR	Fourier transform infrared
FWHM	Full width half maximum
gs	Grain size
HA	Hydroxyapatite
hcp	Hexagonal close packed
HCPEB	High current pulsed electron beam
HIPIB	High-intensity pulsed ion beam
HRDSR	High-ratio differential speed rolling
Hv	Vickers microhardness
i_{corr}	Corrosion current density

LAEB	Large area electron beam
LCPEB	Low current pulsed electron beam
LEHCPEB	Low energy high current pulsed electron beam
LSM	Laser surface melting
Nd:YAG	Neodymium doped yttrium aluminium Garnet
NDE	Negative difference effect
OCP	Open circuit potential
OM	Optical microscope
PBR	Pilling-Bedworth ratio
PBS	Phosphate buffered saline
PECVD	Plasma-enhanced chemical vapour deposition
PVD	Physical vapour deposition
Ra	Surface roughness
RE	Rare earth
RF-MS	Radio frequency magnetron sputtering
RSP	Rapid solidification processing
RTP	Rapid thermal processing
SBF	Simulated body fluid
SCE	Saturated calomel (Hg_2Cl_2) electrode
SE	Secondary electron
SEM	Scanning electron microscopy
SHE	Standard hydrogen electrode
WE	Working electrode
XPS	X-ray photoelectron spectroscopy
XRD	X-ray diffractometry

CHAPTER 1 Introduction

Biomaterials are natural or synthetic materials, used to make structures or implants to replace damaged or diseased biological structures, or support the body to fully repair. For materials to help improve the quality of life and longevity of people, they must be biocompatible [1]. Biocompatibility refers to the ability of a material to prompt an appropriate host response, to allow the body to repair without any deleterious changes to the material or body [2]. A few examples of biomaterial applications are intravenous, urinary or gastric catheters; heart-valves, stents and vascular grafts; orthopaedic devices such as joint replacement components, pins, screws, plates, rods, tacks, suture anchors and fixators; dental and ophthalmic implants; tissue adhesives; wound dressings; and suture materials [3]. Initially, readily available materials were used, but today biomaterials science is becoming more sophisticated and filled with endless possibilities for construct design, across a variety of biomedical applications.

Biomaterials as used for implants can be metallic, ceramic, polymeric or composite [4]. Metals such as stainless steel, cobalt-chromium alloys and titanium alloys, for example, have received much attention due to their biocompatibility combined with their excellent mechanical properties such as strength, hardness, stiffness, toughness, ductility, wear resistance and corrosion resistance [4] [5]. Such properties make these materials suitable for orthopaedic load bearing implants, fixation devices and dental and cardiovascular applications.

There is current interest in developing advanced biomaterials comprising temporary mechanical properties with biological acceptance to the human body, for coronary stent applications. The selection requirements for a metallic stent, a small tubular mesh placed and expanded inside a blocked

blood vessel, should be benchmarked against the mechanical properties of stainless steel, which is the preferred standard for clinicians. Furthermore, when considering mechanical properties as a function of degradation time, the stent properties should not be compromised by the corrosion process until physiological arterial remodelling has been completed ($\sim$ 6-12 months) [4]. Additionally, the corrosion processes that stent materials experience should not have a negative effect on patient physiology and health. For instance, the corrosion products must not generate toxic, carcinogenic or mutagenic effects; they must not block vessels somewhere in the vascular bed, nor generate particles with geometries larger than a few microns; they must be safe to be adsorbed by blood and cells, and should be eliminated by conventional physiological mechanisms.

Biodegradable metals have been investigated during the last decade, as an alternative to currently used permanent metallic implants [6] and more bulky degradable polymeric stents [4]. Polymeric stents in particular suffer from non-linear degradation, autocatalytic effects resulting in acid burst [7] and subsequent high inflammatory response, and more importantly require larger wall thicknesses due to their inferior mechanical properties compared to metals [8] [9] [10]. Recently, particular attention has been paid to biodegradable magnesium (Mg) alloys, which provide the potential for patient recovery without the need for secondary surgery to remove the implant [11]. The first use of Mg was reported in 1878, in stopping bleeding vessels [12], but it has rarely been used clinically due to its high corrosion rate. However, the ability of Mg-alloys to degrade safely within a biological environment may allow for the development of temporary intravascular stents, *e.g.* for use within growing babies [13-16]. In addition, the degradation products of Mg may be involved in various biological processes, such as enzyme co-factors, without toxic effects [5] [17].

Although there has been much promise in this area, the target periods set clinically and scientifically for Mg and Mg-alloy biodegradation have yet to be achieved, with a target corrosion rate of 0.02 mm/year [18]. Mg has a tendency to degrade quickly in the range of 2.7 mm/year within a physiological environment, before vessel remodelling and the healing process are complete [19] [20]. In practice, the corrosion of Mg / Mg-alloys is both rapid and non-homogeneous, due to localised attack [21], with galvanic corrosion taking place wherever there are impurities or secondary phases. Further, the high rate of corrosion of Mg results in the formation of hydrogen gas bubbles within ~ 1 week, which disappear after ~ 2-3 weeks [22], being associated with a local change in pH and a possible decrease in biocompatibility [21].

Mg-alloys, *e.g.* AE21 (2% Al and 1% rear earth elements Ce, Pr and Nd) and WE43 (0.4% Zr, ~ 4% Y and ~ 3% rare earth elements) have been studied, with a view towards the development of biodegradable stents [23] [24]. However, the main problems related to Mg-alloys were revealed, in the form of rapid galvanic corrosion, both *in vitro* and *in vivo*, leading to premature failure of the stents before the arterial healing process was functionally complete. The complexities of the associated degradation mechanisms for such metallic biomaterials in the physiological environment are not well understood. Hence, the purpose of this thesis, to conduct a detailed investigation and gain improved understanding of the corrosion behaviour of pure Mg within biological media, as current candidate Mg-alloys do not perform well under physiological conditions [17, 25].

Metallic stents may be produced using various micro- and nano-scale processing techniques, including minitube casting, powder metallurgy and electroforming, in order to achieve the desired stent dimensions [4]. In particular, the technique of physical vapour deposition (PVD) provides for

effective control over the diameter and wall thickness of fine-scale Mg stents. However, the grain structures produced by PVD need to be refined before being brought into contact with physiological solution. In this context, an initial feasibility study to produce a novel Mg stent, fabricated by radio frequency magnetron sputtering (RF-MS) is reported on in Chapter 4, along with an appraisal of the effects of post deposition thermal treatments. The findings of this work pointed towards a need for improved understanding of the surface processing of Mg, in order to delay the onset of corrosion and provide for improved control of the corrosion rate. This led to a comparison of surface coating and near surface modification strategies for the processing of Mg. For example, an investigation of Al-O and Si-H based coatings, developed using PVD and thermal annealing procedures on Mg, and their corrosion properties in phosphate buffered saline (PBS), is reported on in Chapter 5. An alternative strategy to refine the near surface structure of Mg using the rapid solidification techniques of electron beam and laser surface melting is reported on in Chapter 6. In particular, a detailed investigation of the enhanced passivation and corrosion performances of these processed Mg surfaces is presented.

Throughout this investigation, the examination of material microstructure was performed using the combined complementary characterisation techniques of scanning electron microscopy (SEM), energy dispersive X-ray spectroscopy (EDS), X-ray diffractometry (XRD), X-ray photoelectron spectroscopy (XPS), Fourier transform infrared (FTIR) spectroscopy and microhardness testing, with corrosion performance appraised by potentiodynamic polarisation and immersion corrosion testing.

Accordingly, this thesis is organized into eight chapters. Chapter 1 provides an introduction to the technical requirements for biodegradable Mg stent development and outlines the organisation and structured development

of the thesis. Chapter 2 presents a literature review and the research context for the development of stents, including a review of current materials used, degradable metals, Mg structure, corrosion mechanisms, types of corrosion, measurement procedures, factors affecting the corrosion of Mg and strategies for the protection of Mg. Chapter 3 describes the techniques used to manufacture Mg minitubes, the conditions for the deposition of PVD coatings and the near surface modification of Mg, as well as outlining the basis of the characterisation and corrosion testing techniques employed. Chapter 4 presents a feasibility study of the PVD fabrication of pure Mg minitubes and the effect of thermal treatments on their structured development, and their mechanical and corrosion properties. Chapter 5 describes an investigation of the development of Al-O and Si-H based coatings, as protective barrier layers on Mg surfaces, and their corrosion performance within PBS solution. Chapter 6 reports on the use of electron beam and laser surface melting procedures to refine the Mg near surface, in order to appraise the effects of microstructure and homogeneity on corrosion performance. Chapter 7 presents an overview discussion of the corrosion behaviour of Mg, as a function of the developed microstructures and processing strategies applied. Chapter 8 provides the general conclusions of this thesis and outlines some opportunities for future developments in this field of study.

CHAPTER 2 Literature review

2.1 Introduction

Degradable metallic stents have attracted research attention because they can perform their required mechanical function over a specific period of time and then dissolve gradually by corrosion, as healing progresses [26]. Magnesium (Mg) / Mg-alloys is a promising materials system for stent applications due to its biocompatibility. The main issue with Mg is its relatively low corrosion resistance when in contact with the biological environment. Hence, improved control over the corrosion rate of Mg is needed, in order to extend the time period for dissolution and to achieve optimal temporary mechanical function.

This Chapter presents a review of established literature, relevant to the main themes of this thesis. The context is the development of biodegradable stents, candidate materials and their methods of manufacture, and the potential of Mg and Mg-alloys. Emphasis is given to the corrosion of pure Mg in the biological environment, including types of corrosion, methods of measurement and the factors affecting corrosion behaviour. Various strategies for protecting Mg are examined. The surface coating of Mg with a protective oxide layer, by physical vapour deposition (PVD), is a promising technique. The near surface modification of Mg using electron beam and laser surface melting, for grain refinement and homogenisation, is an alternative strategy which can affect the corrosion properties of Mg. Alloying of Mg with various elements, as another route towards corrosion protection, is also reviewed briefly. Although the literature review will consider a range of Mg-alloys being used in biomedical application, this thesis will be focussed mainly on the performance of pure Mg in the biological environment.

2.2 Introduction to stents

2.2.1 Stents – application & environment

The implant market is increasing, with more than one million stents implanted in human arteries each year [27]; of which, 80% cardiovascular interventional surgeries are coronary stents [28]. Stents are used widely to treat severe coronary artery disease by restoring blood flow [29]. Generally, stents are permanent implants placed and expanded inside an artery to provide mechanical support and keep the lumen of arterial vessel open [16], (Figure 2-1). Stents are categorised into two major groups; *i.e.* balloon expandable and self-expandable [30]. Balloon expandable stents are fabricated, traditionally, from a mesh of narrow diameter stainless steel tubes or wires mounted on an angioplasty balloon and then deformed plastically to their final diameter, once located within the artery, by inflation of the balloon [30] (Figure 2-2(a)). Sigwart *et al.* [31] introduced a self-expanding coronary stent, made from stainless steel, for scaffolding blood vessels after balloon angioplasty. Such self-expandable stents comprise a small diameter tube or wire mesh made from stainless steel, Nitinol (Ni-Ti alloy) or Tantalum (Ta), manufactured in expanded shape and then compressed into a small diameter, delivery catheter, and then positioned and expanded at the required site (Figure 2-2(b)) [30]. Vascular stents may also be used in peripheral vascular sites, *e.g*. lower limb, renal, carotid and neurovascular, as well as in coronary vessels [30].
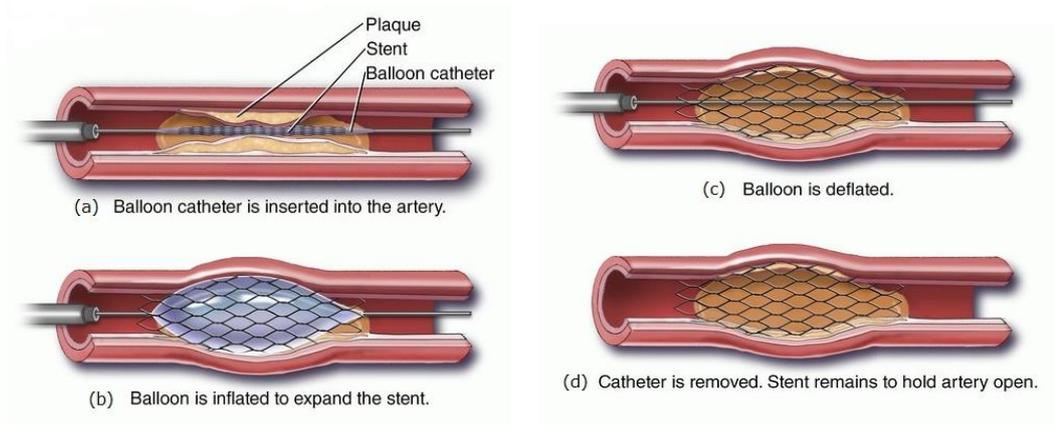
Figure 2-1 Stent procedure inside a coronary artery [32].

Such stent implants remain within the blood vessel for the rest of the patient's life [33]. However, this is largely unnecessary, since the healing process for a blocked artery takes ~ 6 - 12 months [34], and the presence of a stent for a long time period could interfere with artery remodelling and provoke in-stent restenosis, a re-occurrence of a narrowing of the blood vessel in the presence of the stent due to cell proliferation at locally injured tissue [35] and later stent thrombosis [15]. In addition, metal stents based on stainless steel and Ni-Ti alloy can release Cr and Ni ions, which are considered to be carcinogenic [36].
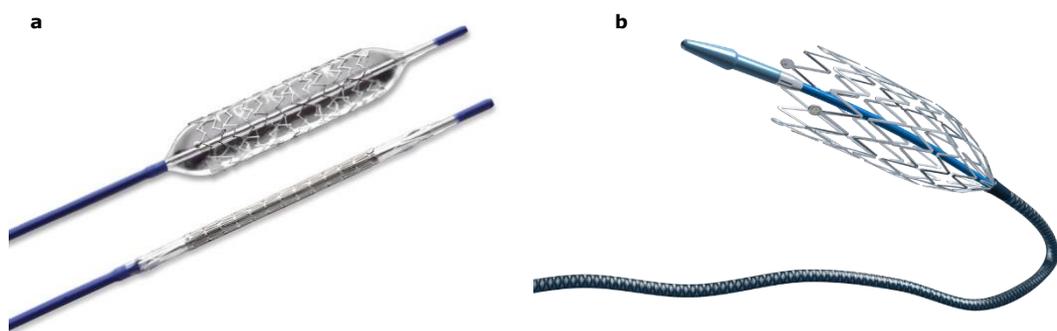
Figure 2-2 (a) Balloon expandable stainless steel stent (ParaMount Stent) [37]; (b) Self-expanding Nitinol stent (Zeus SX stent) [38].

2.2.2 Materials for stents

Current stents made from corrosion resistance metals such as stainless steel (316L SS), Nitinol and cobalt-chromium (Co–Cr) alloys [16] are typically fabricated from a narrowed walled, small diameter tube and laser cut into the desired pattern, followed by annealing, electrolytic polishing, cleaning and rinsing [39]. 316L SS is the most commonly used metal for stents providing for good mechanical properties and high corrosion resistance, and hence regarded as a standard reference material against the development of new materials for stents [9]. Nevertheless, the use of 316L SS for stents is limited due to its ferromagnetic nature, being non-compatible with magnetic resonance imaging (MRI), as well as exhibiting low biocompatibility and being associated with possible allergic reactions [9].

The shape-memory alloy Nitinol may be used as a self-expanding stent because of its shape memory effect, transforming from martensite at room temperature to austenite at body temperature which drives the expansion process inside the arteries [40]. However, the use of Ni-Ti shape memory alloys is restricted because of the considerable amount of Ni content, hence the alternative shape memory alloy Ti-Nb-Sn now under development for implants [41]. Co-Cr alloys have attracted the stent industrial sector due to their high elastic modulus and strength, making it possible to produce stents with ultra-thin struts [9]. However, Co-Cr alloys are also limited due to the risk of dissolution of toxic Cr into the blood stream [6].

2.2.2.1 Biodegradable materials for stents

Implants have been fabricated typically from bioinert metals such as stainless steel or Ni-Ti alloy. However, their clinical need is only for a maximum of six months, to allow the healing process to occur [42]. In order to remove the implant, second surgery is required, which puts the patient at risk along with additional cost. The alternative is to leave the implant for the rest of patient's

life, but this carries a risk of adverse effects such as allergic reaction to the metal [42]. The development of an effective bio-absorbable implant can overcome these problems, providing potentially a temporary opening for the artery during the first stage of healing followed by remodelling as the stent safely degrades. Degradable stents can also be replaced and another inserted in the same place if the initial treatment is un-successful [43]. Hence, degradable implants can potentially reduce healthcare costs and clinical difficulties associated with the use of permanent stents [44].

Biodegradable polymeric stents are also becoming established in clinical applications, as a solution for long-term complications. The first materials used for degradable stents utilised polymers, *e.g.* from the highly bio-compatible Poly-L-Lactic acid (PLLA) [33], glycolic and caprolactone families [45] [46] [47]. However, polymeric stents face difficulties in reproducing the mechanical properties of stainless steel, and hence metallic stents are gaining more attention [48]. Bio-degradable metals such as Mg-based and Fe-based alloys exhibit mechanical properties similar to that of 316L SS [16]. The first degradable iron stents (Fe > 99.5%; Armco iron), implanted in the descending aorta of New Zealand white rabbits, maintained their mechanical properties without failure [49]. However, pre-clinical studies showed that the Fe-stents did not corrode completely during the test time, and hence acceleration of the degradation rate of Fe-based stents is required [49]. The ferromagnetic nature of Fe would interfere with MRI observations, making it necessary to alloy with Mn to become anti-ferromagnetic [16].

Table 2-1 compares different stent materials, with regard to mechanical and technical viewpoints.

Table 2-1 Properties & trends of candidate materials for stent applications [50].

Remarks	Metallic stents		Polymers stents
	Non-degradable (SS, Co-Cr, Nitinol)	Degradable (Fe-, Mg-alloy)	Degradable
Manufacturing process	Laser cutting; wire technologies	Laser cutting	Casting; injection moulding
Main advantages	Verified biocompatibility; radiopacity; high radial force (SS, CoCr); superelasticity	Degradability; no inflammatory effects	Degradability; drug release
Main dis-advantages	Fatigue issues; no potential as drug carrier	Low radiopacity (visualisation); degradation uncontrolled	Recoil; local inflammation; poor visualisation; poor mechanical properties
Mechanical performance	high	moderate	low
Clinical experience	+++	+	+
Current market	+++	n/a	n/a
Price trend	SS↓ , Co-Cr → , Nitinol →	Mg ↑	None on the market
Expected growth rate	+	++	++
Need for further research	→	↑↑	↑↑

2.2.2.2 Magnesium alloys for degradable metallic stents

Mg is a promising candidate for biodegradable implants with significant advantages of high strength to weight ratio, and visualisation via intravascular ultrasound and MRI techniques [51]. Recently, *in vivo* and *in vitro* studies showed implants based on Mg to have good biocompatibility [52] [53]. The Mg^{2+} cation represents the fourth most abundant cation stored in the human body, being involved in many enzymatic reactions as well as the transmission of nerve signals [54] [55]. The adult body contains ~ 21-28 g of Mg, with bone accounting for more than half of this concentration, while only 1% (85-121 mg/L) is present in blood and serum [56] . Mg ion regulation occurs naturally, being eliminated from the human body by the kidneys and through urine to maintain its concentration in an acceptable range [44]. The release of Mg ions also can enhance Mg/cell surface interactions and show antibacterial properties [57].

The development of Mg and alloys as biodegradable stents addresses the current disadvantages of traditional metallic and polymeric implants, such as restenosis and late thrombosis (Figure 2-3). The first application of Mg as an implant material was reported in 1878, when Huse used Mg wire to stop vessels bleeding [12]. In more recent years, Heublein *et al.* [58] [23] investigated the use of AE21 alloy for stents in the coronary arteries of domestic pigs and found that the stents showed positive remodelling, but fast degradation rates. The results of these experiments led to a new generation of Mg-alloy stents (Biotronik-Germany) [4] and it is anticipated that these will be able to scaffold the arterial wall until the healing process has completed, then degrade normally and be expelled from the body [33].
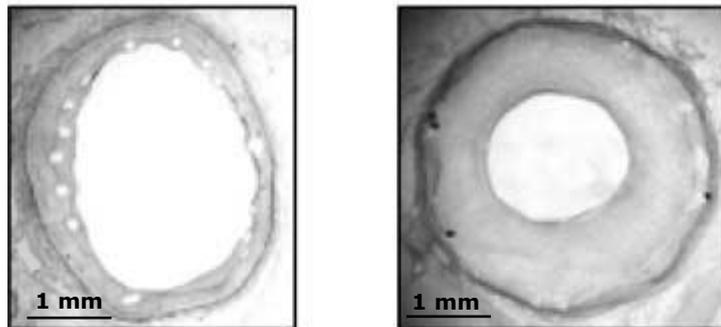
Figure 2-3 Comparison of Mg-alloy (WE43, left) and stainless steel (316L SS, right) stents in a normal porcine coronary artery showing partial restenosis in the 316L SS stent [59].

However, Mg has an inherent low corrosion resistance, especially in the presence of aggressive *e.g.* Cl^- ions, which affects its mechanical properties and limits its applicability as an implant [4]. The corrosion rate considered acceptable for a degradable implant application is 0.02 mm/year [18]. The main challenge with Mg is its rapid degradation which results in a local increase in OH^- and H_2, leading to an increase in pH which may be deleterious to cells [44], raising the possibility of inflammation around the implant and leading to a loosening between the implant and surrounding tissue [60]. Fast degradation leads to a decrease in mechanical properties, especially the

strength of Mg, risking stent failure before the tissue has fully healed or recovered. It is thought that Mg can remain in the body and maintain mechanical integrity for ~ 12-18 weeks [53].

2.2.2.3 Commercial Mg-alloy stents

In the field of cardiovascular devices, significant progress has been made with the development of degradable Mg stents, to the stage of pre-clinical and clinical trials [61]. Early pre-clinical work reported on a stent made from AE21 Mg-alloy, containing 2% Al and 1% RE, implanted in pig coronary artery [23], with the stent losing mechanical integrity due to fast degradation. Further, Waksman *et al.* [24] reported on the safety and efficiency of WE43 Mg-alloy (Lekton Magic) stents containing Zr, Y and RE metals (Figure 2-4 (a,b)), as compared with stainless steel (Lekton Motion) stents, for 3 months, finding that Mg-alloy stented vessels were positively remodelled, with no sigh of thrombosis and inflammation, as compared to stainless steels stents segments.
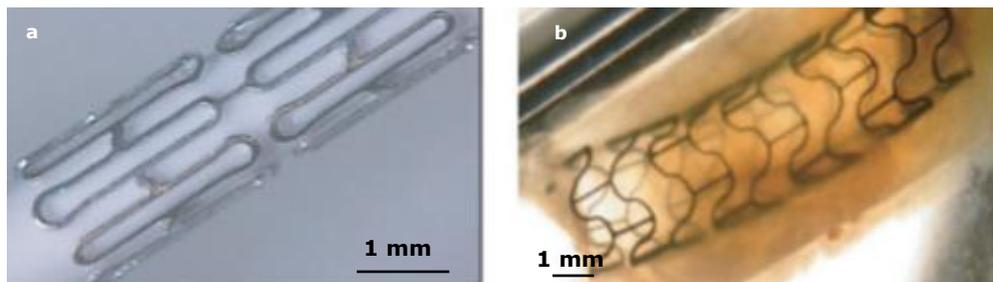
Figure 2-4 Photo-micrographs showing an Mg-alloy stent (a) unexpanded; and (b) expanded in a coronary artery [24]

Indeed, clinical studies utilizing WE43 Mg-alloy (Lekton Magic-Biotronik) stents containing 5%Y, 5%Zr and 5% RE on human peripherals [59]; AE21 alloy (Biotronik) stents in males coronary arteries [62]; and Mg-alloy (93% Mg and 7% RE; AMS; Biotronik) stents in baby arteries [63] [64], all showed

improved corrosion resistance and degradation over four months compared to the two months degradation in initial animal studies [62]. However, even though these studies showed promising developments for the safe degradation of stents in humans, the corrosion rates were still faster than the desired clinical values [61]. Table 2-2 summaries the mechanical properties, degradation rates and grain sizes of various Mg-alloy biodegradable stents, with the properties of 316 SS presented for comparison [4]. It should note that whilst Mg has limited ductility compared with SS, ductility can be improved by alloying or by employing advanced processing techniques, *e.g.* hot extrusion [16].

Table 2-2 Mechanical properties, electrochemical degradation rates and grain sizes of different Mg-alloy biodegradable stents [16] [4] [65].

Material	Yield strength / MPa	Tensile strength / MPa	Elongation / %	Degradation rate / mm/year	Average grain size /μm
316L SS annealed	190	490	40	-	12-30
Pure Mg: as-cast	20	86	13	6.02	-
WE43: extruded	195	280	2	1.35	10
AM60B–F: die cast	-	220	6–8	8.97	25
ZW21: extruded	200	270	17	-	4
WZ21: extruded	140	250	20	-	7

In order to address the issue of fast corrosion rates, coatings of degradable polymers, such as PLLA for drug eluting stents (DES), have been investigated, with drugs, such as antagonists of restenosis, being released into surrounding tissue during the degradation process to help overcome the problem of stent thrombosis [4]. However, polymer coatings can experience rupture, due to their poor mechanical properties, which can release small particles into the bloodstream.

2.2.3 Stent manufacturing methods

The general manufacturing process for a metallic cardiovascular stent is summarised in Figure 2-5. The first step of the process is the production of a metallic ingot through casting [4]. The melting process is performed under vacuum conditions to prevent oxidation and remove dissolved gas to avoid porosity [66]. The ingot is either directly cast into shape, or subsequently formed by forging, rolling or extrusion at high temperature [4], with hot working processes followed by cold working and heat treatment being used to achieve the desired shape, and physical and mechanical properties [67]. Next, the formation of a minitube can be achieved through weld-redrawing or seamless processes [4]. After achieving the final minitube shape, laser cutting is used to pattern the minitube to the final stent design. Annealing processes are then used to relieve the residual stresses generated during drawing and laser cutting, and to improve the mechanical properties [68]. The stent then undergoes acid pickling to remove burrs and debris [4]. The stent is then electro-polished, in ionic solution, to obtain a smooth surface.

There is particular demand to obtain stents with the smallest possible size, to allow access to very narrow vessels in growing children and to minimize the contact area between stent and vessel wall [69]. Hence, new processes for the fabrication of biodegradable metallic stents are being investigated, such as powder metallurgy (PM) which involves powder metal compaction and heat treatment to densify the material, *e.g.* as used to produce Nitinol stents [4]. However, high oxygen content and porosity are the main limitations of PM. Alternative manufacturing methods include electroforming, photoetching and micro-electro-discharge machining, which have been used to fabricate metal foils from which stents have then been produced [69].

Figure 2-5 Conventional fabrication process for a cardiovascular stent [4]

```
┌─────────────────────────────┐
│   Casting of metallic ingot  │
└─────────────────────────────┘
              ▼
┌─────────────────────────────┐
│       Thermomechanical       │
└─────────────────────────────┘
              ▼
┌─────────────────────────────┐
│       Minitube drawing       │
└─────────────────────────────┘
              ▼
┌─────────────────────────────┐
│         Laser cutting        │
└─────────────────────────────┘
              ▼
┌─────────────────────────────┐
│   Annealing and acid pickling │
└─────────────────────────────┘
              ▼
┌─────────────────────────────┐
│        Electropolishing      │
└─────────────────────────────┘
```
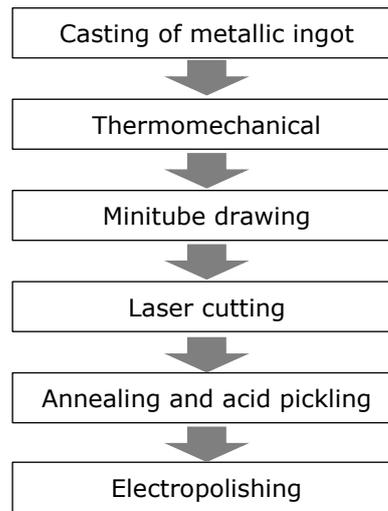
Based on the interests of Mg stent development, the structure and properties of Mg / Mg-alloys will be presented in the following section.

2.3 Introduction to Magnesium and Mg-alloys

2.3.1 Mg-structure and properties

The term "pure-Mg" refers to highly pure Mg comprising 99.99 wt.% Mg with an Fe level less < 40 ppm [13]. There are effectively unlimited supplies of Mg, discovered in 1774, being the sixth most abundant element on Earth [70]. It is widespread in the form of magnesite ($MgCO_3$) and dolomite ($MgCO_3.CaCO_3$), as well as in seawater which contains 0.13% Mg [70]. Mg has the appearance of a silvery white metal with a density range between 1.7–2.0 g/cm^3 [55]. The atomic mass and diameter of Mg are 24.30 amu and 0.32 nm, respectively, and it is able to support a wide range of solute elements having ±15% difference in atomic size [70]. Hence, Mg can form various alloys with unique properties which can be utilised as lightweight materials [70]. Table 2-3 summarises the physical and mechanical properties of pure Mg.

16

Table 2-3 Properties of pure Magnesium [70, 71]

Properties		Magnesium
Atomic	*Symbol*	Mg
	Element classification	Alkaline earth metal
	Atomic number	12
	Atomic weight	24.3050(6) amu
	Atomic volume	14.0 cm^3/mol
	Atomic radius	0.160 nm
	Ionic radius	0.072 nm
	Orbital electron states in free atoms	1s 2 , 2s 2 , 2p 6 , 3s 2
	Electrons per shell	2, 8, 2
	Most common valence (oxidation)	2^+
Physical	*Density (at 20°C)*	1.738 g/cm^3
	Melting point	650 ± 1°C
	Boiling point	1090°C
	Linear coefficient of thermal expansion at 20 – 100°C	26.1×10^{-6} $°C^{-1}$
	Thermal conductivity (at 20°C)	157.5 W/m °C
Mechanical	*Elastic Modulus*	41-45 GPa
	Fracture Toughness	15-40 MPa m $^{1/2}$
	Compressive Yield Strength	65-100 MPa
	Hardness	40-41
	Ultimate tensile strength (annealed sheet)	160-195 MPa

Mg adopts the hexagonal close packed (hcp) structure; hence, the four-index Miller indices system *(h k i ℓ)* is used to represent atomic planes and directions [70], with *i*, which is equivalent to $-(h + k)$, being a redundant index, showing variation symmetries. The Mg lattice parameters at 25°C are a=0.32094 nm, c=0.52108 nm and c/a=1.6236; with angles α: 90°, β: 90° and γ: 120° [70]. Figure 2-6 illustrates the crystal structure and the principal planes and directions in Mg. Slip in Mg occurs mainly on the basal planes and there are two independent slip systems. Due to its hcp structure and high c/a ratio, plastic deformation in Mg at ambient temperatures occurs by slipping on the basal plane (0001) and {10$\bar{1}$0} in the close-packed direction of <11$\bar{2}$0>; and by twinning on the pyramidal {10$\bar{1}$2} planes [72]. At elevated temperatures > 250°C, the pyramidal {10$\bar{1}$1} slip planes become active [72] (Figure 2-6) In particular, polycrystalline Mg shows a tendency towards brittleness [72].

Figure 2-6 Magnesium crystal structure: a) lattice positions; b,c) principle basal, pyramidal and prismatic planes; d) principal directions [73].

2.3.2 Mg-alloys and properties

A diverse range of solute elements can be added to Mg, in order to improve its mechanical and corrosion properties. However, some general observations should be made when choosing an alloying elements [74]: i) Mg can form a continuous solid solution with hexagonal metals such as Zn, Cd and Zr; ii) Mg is electropositive which promotes the formation of compounds with less electropositive metals, such as Si; iii) the formation of a solid solution is restricted by atomic size factors (±15% difference). Figure 2-7 indicates those elements whose size factors favour solid solution formation.

Currently, binary systems with chemical elements showing considerable solubility tend to be used for Mg stents, falling roughly into the following categories [74]: Peritectic systems incorporating In, Mn or Zr; eutectic systems with solid solubility exceeding ~ 1%, incorporating Ag, Gd, Sn, Al or Zn; and eutectic system with solid solubilities up to 1%, incorporating Au, Ce,

Ca, Co, Fe or Si. The main beneficial influence of such alloying elements with Mg is improved corrosion resistance, through the development of a more uniform protective layer combined with the removal or passivation of impurities [75].
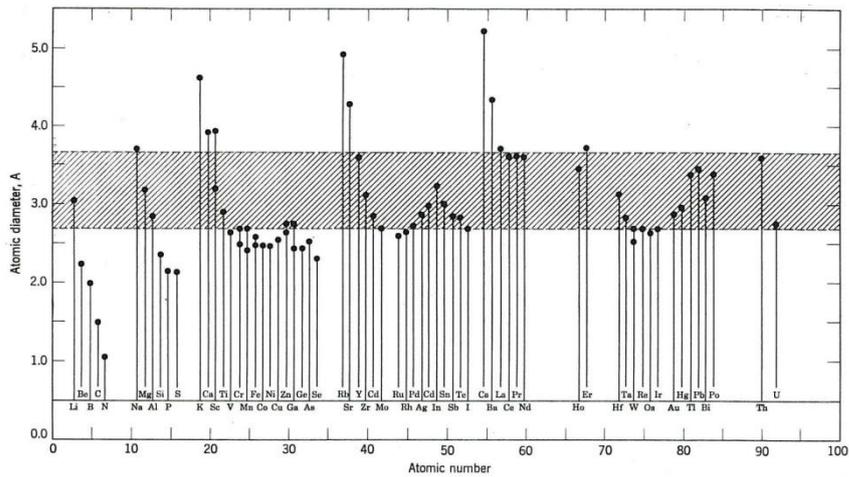
Figure 2-7 Favourable sizes of elements with respect to Mg [73].

The code system applied for the designation of Mg-alloys was adopted from the American Society for Testing and Materials (ASTM) index. In this system, the first two letters indicate the principle alloying elements, with the greatest quantity used in front. The following code shows the most common letters used in Mg-alloys: A: aluminium; B: bismuth; C: copper; E: rare element; H: thorium; K: zirconium; M: manganese; Q: silver; S: silicon; Z: zinc; and W: yttrium [76]. These letters are followed by numbers denoting the weight compositions of the alloy components [70]. Table 2-4 summaries the compositions of common Mg-alloys.

Table 2-4 Minimal composition of common Mg-alloys (wt.%)[77].

Alloy	Al	Mn	Zn	Zr	RE	Y
AM60	6	0.15				
AZ31	3	0.2	1			
AZ61	6.5	0.15	1			
AZ91	9	0.13	0.68			
WE54				0.5	3.5	5.25
ZE63			5.8	0.7	2.6	
ZK21			6	0.8		
ZM21		1.2	2.2			

The degradation of metals such as Mg in the physiological environment depends mainly on the corrosion processes occurring at the metal/solution interface, hence the principles of corrosion processes in general, and for Mg in particular, are described in the following section.

2.4 Introduction to Corrosion

2.4.1 Electrochemical corrosion

Generally, the corrosion phenomena of metals in metal-fluid media can be defined as an electrochemical process that destroys the bulk material, starting at the metal surface [11]. For example, the corrosion of metal in aqueous media is caused by an unalterable oxidation-reduction reaction [70]. In this electrochemical process there are two reactions: Firstly, anodic, in which the metal dissolves in the medium, providing ions to the electrolyte, expressed as [70]:

$$M \rightarrow M^{n+} + ne^-$$ Eq 2-1

At the same time, the released electrons from the metal will be consumed by other species in the electrolyte, giving rise to a cathodic (reduction) reaction, given by the following equation in natural or alkaline solution:

$$O_2 + 2H_2O + 4e^- \rightarrow 4OH^-$$ Eq 2-2

The corroded surface reaches equilibrium as metal ions enter and leave the solution at the same rate, in which case the flow of current is equal in

opposite directions and the net current is zero. However, the dissolution of metal ions leads the metal surface obtaining a negative charge which attracts ions from solution to the surface. This causes a non-homogenous distribution of ions at the metal surface, with the formation of an electric double layer which is the origin of the potential difference across the metal/solution interface [78], and any increase in anodic or cathodic reaction acts to disrupt the equilibrium state of this layer, affecting the open circuit potential (OCP), allowing passivation/corrosion to proceed [79].

The tendency of any metal to corrode in aqueous media is given by the standard electrode potential E^o, which is a thermodynamic equilibrium potential and the more negative the value the stronger the tendency of the metal to spontaneous corrosion. E^o is measured relative to a standard hydrogen electrode (SHE) which has a potential value of 0 V [70]. Table 2-5 summaries the standard electrode potentials for various metals.

Table 2-5 Standard electrochemical series for selected metals [80].

	Reaction			Potential / V
Noble	$Au^{3+} + 3e^-$	$\Leftrightarrow$	Au	1.42
	$Pt^{2+} + 2e^-$	$\Leftrightarrow$	Pt	1.20
	$Ag^+ + e^-$	$\Leftrightarrow$	Ag	0.80
	$O_2 + 2H_2O + 4e^-$	$\Leftrightarrow$	$4OH^-$	0.40
	$H^+ + e^-$	$\Leftrightarrow$	$1/2\ H_2$	0.00
	$2H_2O + 2e^-$	$\Leftrightarrow$	$H_2 + 2OH^-$	-0.83
	$Al^{3+} + 3e^-$	$\Leftrightarrow$	Al	-1.66
	$Mg^{2+} + 2e^-$	$\Leftrightarrow$	Mg	-2.37
Active	$Na^+ + e^-$	$\Leftrightarrow$	Na	-2.71

The OCP, also termed the corrosion potential, is a mixed potential from the anodic and cathodic reactions [70]. For example, if Mg showed values E > OCP it would mean that the Mg was not in direct contact with solution due to the development of a passivation film. Indeed, OCP values can vary as a function of the physical and chemical condition of the metal surface and solution [70]. The galvanic series, a list of corrosion potentials with respect to a reference saturated calomel (Hg_2Cl_2) electrode (SCE), allows the relative

corrosion resistance of different metals to be compared. The OCP of Mg at 25°C in sodium chloride is 1.63 V (SCE) [81].

2.4.2 Corrosion mechanisms of pure Mg

Mg-alloys in an aqueous environment degrade through an electrochemical reaction with water: with the production of dissolved Mg^{2+} ions, magnesium hydroxide ($Mg(OH)_2$) and hydrogen gas (H_2) [55]. The corrosion mechanism is insensitive to oxygen concentration [82]. The general chemical formula for Mg reaction with water is [25, 82, 83]:

$$Mg_s + \ 2H_2O_{(aq)} \rightleftharpoons Mg\,(OH)_{2\,(s)} + H_{2\,(g)} \qquad \text{Eq 2-3}$$
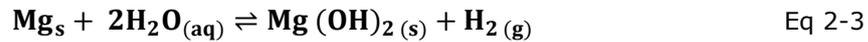
However, this overall reaction may involve the following partial anodic and cathodic reactions [25]:

$$Mg_{(s)} \rightleftharpoons \ Mg^{2+}_{(aq)} + 2e^- \qquad (anodic\ reaction) \qquad \text{Eq 2-4}$$

$$2H_2O + 2e^- \ \rightleftharpoons \ \ H_{2\,(g)} \ + 2OH^-_{(aq)} \quad (cathodic\ reaction) \ \ \text{Eq 2-5}$$
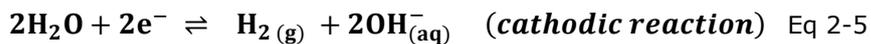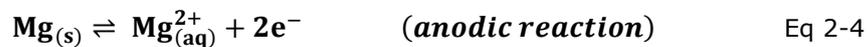
The formation of a surface passivation film occurs through the following precipitation reaction [84]:

$$Mg^{2+}_{(aq)} + 2OH^-_{(aq)} \ \rightleftharpoons \ \ Mg\,(OH)_{2\,(s)} \qquad (product\ formation) \ \ \text{Eq 2-6}$$
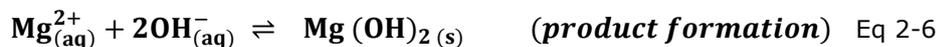
Figure 2-8 illustrates this coupled electrochemical reaction at the Mg surface in aqueous solution. The electrons lost by oxidation of Mg are consumed in the reduction of water to form hydroxide and hydrogen gas.
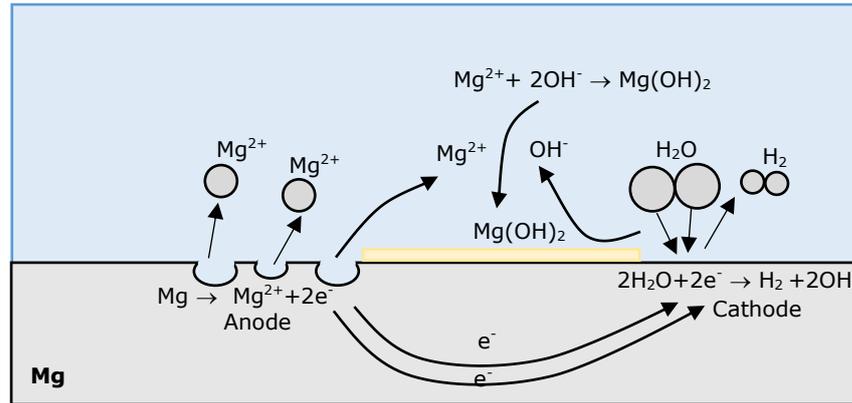
Figure 2-8 Coupled electrochemical reactions occurring at different sites on a Mg surface in aqueous solution

The formation of hydroxide from the reduction reaction of water is typical for implant metals, and the formation of magnesium hydroxide raises the pH to ~ 11 [82]. However, atomic hydrogen produced at the corroding surface combines to form hydrogen molecules which evolve to form H_2 bubbles from the surface which may account for a proportion of cracking in $Mg(OH)_2$ [85]. It is also possible for atomic hydrogen to enter the metal and dissolve in its lattice, and Mg has significantly capacity for the storage of hydrogen gas [85].

2.4.3 Negative difference effect

The negative difference effect (NDE) was observed for Mg by Petty *et al.* [86] and Song *et al.* [84] [87]. In most metals, when the applied surface potential increases above the corrosion potential ($E_{appl} > E_{corr}$), as illustrated by Figure 2-9, the anodic reaction rate increases and should follow the solid line I_a until reaching the point $I_{Mg,e}$. Consequently, the cathodic partial reaction normally follows the line I_c until the point $I_{H,e}$ indicating a reduction of the hydrogen evolution rate. The case of Mg is contrary, with the hydrogen evolution reaction rate increasing, following line I_H until the point $I_{H,m}$, as the potential of the surface increases. Hence, the anodic and cathodic reactions increase with an increase of applied potential, and the difference Δ for an applied galvanostatic current density I_{appl} ($I_{appl} = I_{Mg,m} - I_{H,m}$)[88] is given by:

$$\Delta = I_0 - I_{H,m} \qquad\qquad \text{Eq 2-7}$$

Where I_0 is the spontaneous hydrogen evolution reaction rate on Mg in the electrolyte at the corrosion potential and $I_{H,m}$ is the measured hydrogen evolution rate for corresponding applied current. $I_{H,m}$ is higher than I_s so the difference value for Mg is negative.
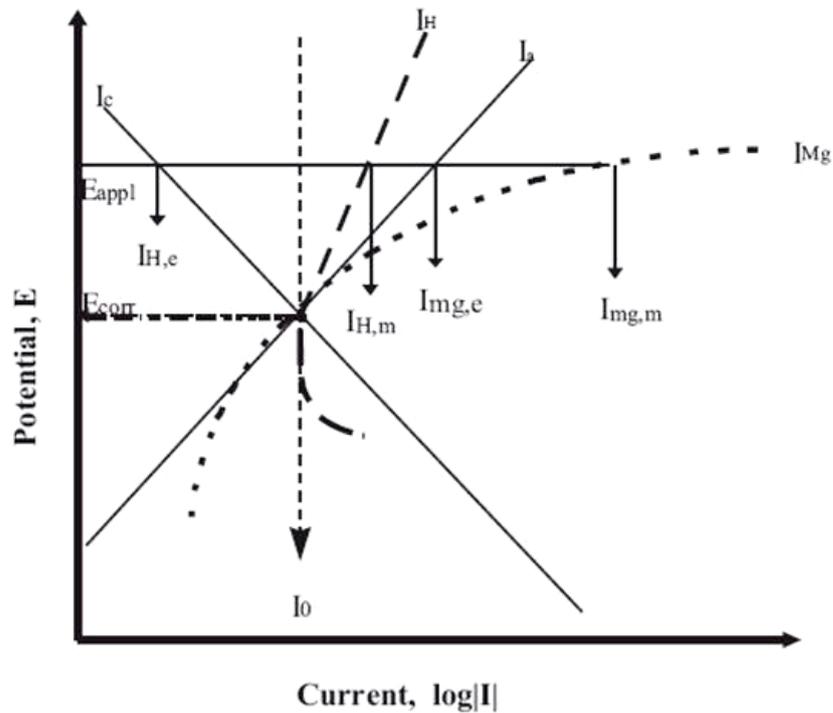
Figure 2-9 The negative difference effect (NDE) [84].

The NDE is based on experimental observations of the anodic dissolution of Mg, for which: i) the anodic dissolution of Mg, line I_{Mg}, produced by the applied anodic current is higher than that predicted electrochemically, following line I_a, and the measured weight loss, $I_{Mg,m}$ is higher than that predicted using the Faraday law at I_{appl}; and ii) an increase in the applied anodic current or potential causes an increase in the amount of hydrogen evolved, rather than a decrease [84]. Consequently, a univalent Mg^+ model is proposed for Mg dissolution in an electrolyte, noting that during cathodic polarization, a passivation film covers the Mg surface at sufficient cathodic

potential (E < pitting potential E_{pt}) [87]. During anodic dissolution, the protective film partially breaks down, as the external potential or current density increases above a critical value, termed the "pitting potential E_{pt}", and the film becomes progressively disturbed [75]. On film free areas, anodic dissolution becomes easier and involves the intermediate species of mono-valent Mg^+ ions, produced electrochemically [75]:

$$Mg \rightarrow Mg^+ + e \qquad\qquad\qquad \text{Eq 2-8}$$

$$Mg^+ \rightarrow Mg^{2+} + e \qquad\qquad\qquad \text{Eq 2-9}$$

However, it must be stated that unitary Mg^+ has not been observed in experimental work [89] [90]. Song *et al.* [84] assumed that Mg^+ is a very short lived intermediate which cannot be detected. It is considered that these mono-valent Mg^+ ions react to produce hydrogen, according to the following reaction sequence [75]:

$$2Mg^+ + 2H^+ \rightarrow 2Mg^{2+} + H_2 \qquad \text{(Chemical reaction)} \quad \text{Eq 2-10}$$

Or

$$2Mg^+ + H_2O \rightarrow 2Mg^{2+} + 2OH^- + H_2 \qquad\qquad \text{Eq 2-11}$$

$$2H_2O + 2e^- \rightleftharpoons H_2 + 2OH^- \qquad\qquad\qquad \text{Eq 2-12}$$
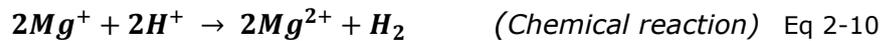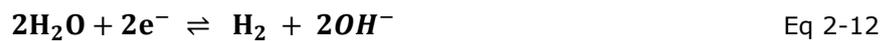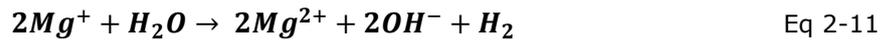
The dissolution of Mg^{2+} and the production of H_2 become difficult on a surface covered by a passivation film. The amount of H_2 produced on a free surface involves the reaction of both Mg^+ and Mg^{2+} with water to produce molecules of H_2 which accounts for the high amount of H_2 produced during anodic dissolution. A study by Bender *et al.* [91], however, assumed that during the investigation of Mg corrosion by external polarization two cathodic processes occur; one indicates electrons are consumed by the potentiostat as more Mg ions go into solution; and the other is associated with water dissociation and the formation of H_2 gas bubbles.

2.4.4 Passivity and passivation layer breakdown

Passivity, *i.e.* the formation of a protective film, happens due to the reaction of a metal with its environment, leading to a reduction of the chemical or electrochemical activity of the metal [92]. The corrosion resistance of Mg in a specific environment depends generally on the characteristics of the surface film. For example, the exposure of Mg to air results in the formation of a spontaneous amorphous film, being a mixture of inner MgO and outer $Mg(OH)_2$ a few nanometres (20-50 nm) thick [93], with the concentration of $Mg(OH)_2$ being greater than MgO [94] which provides for limited protection. In aqueous solution, the initial layer will hydrate to form a duplex layer of MgO and $Mg(OH)_2$ with an inner MgO layer next to the metal Mg and an outer porous $Mg(OH)_2$ layer at the surface, being similar to an air-formed film [94] [82]. The Pilling-Bedworth ratio (PBR), used to predict the sign and magnitude of growth stress induced by a surface oxide layer, given by the ratio of molecular volume of oxide to molecular volume of metal, returns values for MgO and $Mg(OH)_2$ of 0.81 and 1.77, respectively [95]. The combination of MgO in tension and $Mg(OH)_2$ in compression may account for the cracking and curling of hydroxide films [70].

Nordlien *et al.* [93] used transmission electron microscopy (TEM) to study the morphology of surface passivation films on pure Mg after immersion in distilled water for 48 h. They reported that the film had a three-layer structure, consisting of an inner porous MgO layer of 0.4 - 0.6 μm thickness, a middle dense region of MgO, $\sim$ 20 - 40 nm thick, and an outer $Mg(OH)_2$ layer with platelet-like morphology $\sim$ 1.8-2.2 μm thick, giving a total film thickness of $\sim$ 2.2-2.8 μm (Figure 2-10). Further, Santamaria *et al.* [96] reported that $Mg(OH)_2$ increases in thickness with increasing immersion time, whilst the inner oxide layer retains a constant thickness.
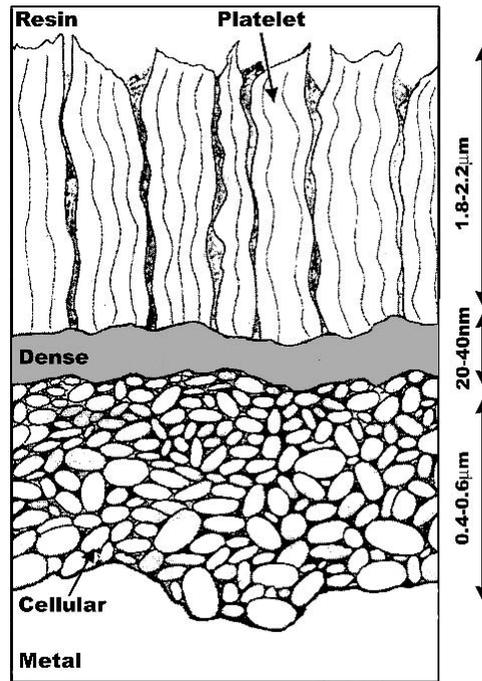
Figure 2-10 Schematic illustration of the passivation film structure formed on Mg immersed in water (after 48 h) [93].

The combined oxide and hydroxide films act as a protective layer on the Mg surface [82] [87], by inhibiting the transformation of metal ions to solution, the migration of solution anions to the metal, and the migration of electrons across the interface. However, when the surrounding environment contains chloride Cl^- ions, the $Mg(OH)_2$ tends to become extensively nanoporous, with very high surface area, which results in rapid non-protective corrosion [97]. The $Mg(OH)_2$ tends to breakdown and become highly soluble $MgCl_2$, thereby making the Mg surface more active, by decreasing the protective area, leading to an acceleration of the electrochemical reaction rate and further dissolution of Mg to magnesium univalent ions [25], in the form of pitting corrosion. This reaction is expressed as [55]:

$$Mg + 2Cl^- \rightarrow MgCl_2 + 2e \qquad \text{Eq 2-13}$$

$$Mg\,(OH)_2 + 2\,Cl^- \rightleftharpoons MgCl_2 + 2OH^- \qquad \text{Eq 2-14}$$
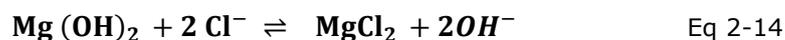
Brun *et al.* [98] studied the film formed on Mg immersed in 3% sodium chloride using infrared spectroscopy and X-ray diffractometry, and reported $Mg(OH)_2$, along with the presence of chloride containing compounds, corresponding to $MgCl_2.6H_2O$ and $Mg_3(OH)_5Cl.4H_2O$ (hydroxychloride).

The passivation layer on a metal surface is regarded as a barrier to corrosion [80]. Metal used in biomedical applications depend on the formation of this spontaneous oxide film to limit metal ions reaching the surface. Jacobs [80] commented that such oxide must be continuous, without pores or voids, and hence capable of limiting the migration of metal ions and electrons across the interface. Further, the passivation layer must be stable under mechanical loading and stress. Any defect structures, such as vacancies or impurities, within the oxide layer act to reduce the ability of the kinetic barrier to resist corrosion.

The dissolution of Mg^{2+} ions in media and hydrogen evolution during the corrosion process occur for Mg, depending on the conditions at the surface and into the bulk metal. The different types of corrosion observed on Mg surfaces are now reviewed, in advance of a description of methods used to measure corrosion rate.

2.5 Types of corrosion

The resistance of pure Mg to corrosion is weakened considerably due to the nature of its surface hydroxide layer and impurity elements [81, 82]. The following section describes the main types of corrosion observed in Mg-alloys

2.5.1 Galvanic corrosion

Galvanic corrosion occurs when two metals with different electrochemical potentials are in contact, in the presence of an electrolyte [27]. The metal having less noble potential becomes an anode which corrodes and produces

corrosion products on the contact site with the cathode [99]. Mg is a very reactive metal in the electrochemical series and hence will behave as an anode in most corrosion reactions. Further, Mg containing impurity elements, typically Ni, Fe, Cu and Co, with electrochemical potential lower than Mg, are also susceptible to galvanic corrosion [81]. These elements, once present in pure Mg or Mg-alloys, act as cathodic sites, while the Mg behaves as an anode. Galvanic corrosion can also occur in the presence of intermetallic alloys in an Mg matrix, because each secondary phase results from the interaction of Mg with a nobler metal [75] (Figure 2-11).
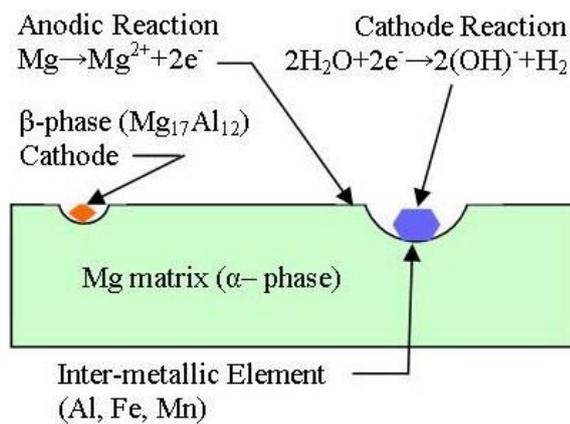
Figure 2-11 Galvanic corrosion in the presence of intermetallic elements [99]

2.5.2 Pitting Corrosion

An initial layer of MgO/Mg(OH)$_2$ is formed immediately on the surface of Mg when exposed to atmosphere. This layer is thin, amorphous, dense and relatively dehydrated [70]. In ambient air, the initial oxide layer thickness on pure Mg is ~ 2.2 ± 0.3 nm and increases linearly in thickness with exposure time [70]. This very thin layer is not stable when subjected to mechanical loads or presented to an aggressive environment. In natural solutions containing chloride ions, the passivity of the Mg surface breakdowns, leading

to the formation of an electrolytic cell between protected and non-protected surfaces [81]. The more electro-active sites on the surface start to dissolve, and a corrosion pit forms as a hemi-spherical shape (Figure 2-12) [81]. The mouth of the pits is narrow such that the environment inside the pits is very aggressive and saturated with chloride and Mg ions which enhances the growth of the pits [99].

Pitting corrosion is considered to be more serious than other forms of corrosion because the pits are small, corrosive and grow deeper, harming the metal matrix. Pitting corrosion can develop further in the presence of impurities due to the galvanic effect. The parameters usually used to indicate the resistance of Mg-alloys to pitting corrosion are: i) the passive current density i_p that measures the protective quality of the passivation layer; and ii) the breakdown potential E_b, which denotes the resistance of the passivation layer to breakdown and pitting attacks [82]. The more nobler the E_b values, the stronger the protective ability of the surface film [82]
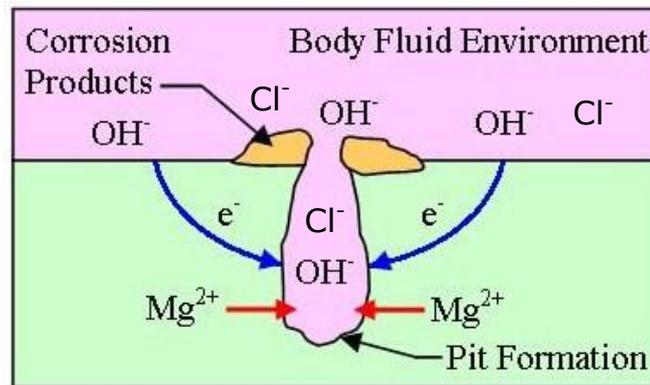
Figure 2-12 Pitting corrosion on the surface of Mg [99].

2.5.3 Crevice, filiform and intergranular corrosion

Crevice corrosion is initiated at sites where metal and metal/or non-metal components are in contact. There must be a narrow gap, with sufficient width between them, to allow for solution flow (Figure 2-13). Stagnant fluid leads to

a difference in Mg^{2+} concentration between the entrance and the bottom of the gap, and hence a corrosion cell is generated which attacks the Mg surface [99].
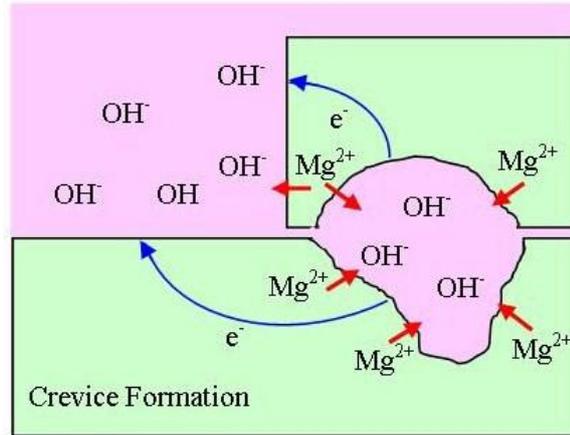
Figure 2-13 Crevice corrosion of Mg in solution [99].

Further, thread-like filiforms are initiated on the Mg surface, having a protective coating in which pitting corrosion starts and then narrow semi-cylindrical filaments develop from the pit [70]. The head of each filament is anodic and the tail is cathodic [81]. The propagation of filiform corrosion is driven by hydrogen evolution occurring on the head and outside each filament [76] [100].

Intergranular corrosion is a deep and narrow pathway and can develop at an Mg-alloy surface as a result of grain boundary corrosion [81]. Localised attack can occur at the interface between the Mg matrix and precipitates of impurity aggregates, segregated along grain boundaries during solidification [81].

However, Makar and Kruger [82] argue that true inter-granular corrosion does not occur for the case of Mg-alloys, as the grain boundaries always act as cathodic sites for the grains of the Mg matrix. Instead, granular attack leads to the undercutting and removal of grains, delineated by their boundaries with the Mg matrix.

Overall, the corrosion of Mg in contact with aqueous solution occurs through the dissolution of Mg^{2+} ions and the development of $Mg(OH)_2$ and hydrogen gas. Methods used to measure the corrosion rate of Mg in detail are presented in the following section.

2.6 Measurement of corrosion

The corrosion of Mg in a biological environment (termed bio-corrosion, *e.g.* in simulated body fluid (SBF) [13]) is a complex process which requires different approaches for complete characterisation [13]. *In vitro* tests provide an initial step to determine the suitability of an Mg model for *in vivo* study. However, strong correlation between *in vivo* and *in vitro* testing has not been established to date, due to the required use of different techniques in different environments, leading to possible mis-interpretation of data.

2.6.1 *In vitro* testing

Generally, the *in vitro* methods used to measure corrosion rates are categorised as: static-steady state and dynamic, depending on the test conditions and parameters applied [13]. Further, static corrosion tests are denoted as un-polarised and polarised, related to the force, *i.e.* electrochemical polarization, driving the material to corrode, either applied or measured during the testing process [13]. *In vitro* studies should be carried out in solution which close to the real body fluid composition, *e.g.* Hank's solution, SBF, artificial plasma (AP), phosphate buffered saline (PBS) solution or minimum essential media (MEM). Experiments should also be performed at the physiological temperature, T (37 ± 1°C) and pH 7.4 ± 0.05 [13].

2.6.1.1   Steady state testing

2.6.1.1.1   *Immersion or weight-loss testing*

The mass loss experiment is the simplest corrosion test which requires a sample, test media and microbalance. The examined sample is washed with acetone, dried, weighed and then placed in the corrosion medium for a set time [76]. The sample is then removed and the corrosion products are removed from the specimen surface using dilute chromic acid, and the final mass measured accurately using a microbalance [55]. According to the ASTM-G31-12a protocol, the corrosion rate *in vitro* can be measured under these test conditions, and calculated using:

$$\mathbf{CR} = \frac{K\Delta \mathbf{W}}{\mathbf{A.t.\rho}} \qquad \text{Eq 2-15}$$

where CR is the corrosion rate (mm/year); K is constant (8.76×10^4), ΔW refers to the weight loss (g); A is the original surface area exposed to the corrosive media (cm^2); t is the exposure time (h); and ρ is the standard density (1.74 g/cm^3) [101] .

Since the removal of the corrosion layer is minimised, without affecting the bulk material, the results obtained from this test are considered accurate. However, the immersion test does not describe the mechanisms involved in the corrosion process, even though it can observe whether specific samples corrode faster than others [13]. Other techniques may provide more appropriate information about what actually happens during the corrosion process, other than just the observation of Mg mass loss [102]. For examples, the polarization curves obtained from potentiodynamic testing present differences in corrosion potentials and reaction kinetics, which differ for different Mg treatment methods [13]. The potential changes at the implant surface, and the related anodic and cathodic reactions, are important to the components of the physiological environment [13], because the Mg

corrosion products, Mg^+, OH^- and H_2, released into the surrounding medium, cause a localised increase in pH. A passivation layer of $Mg(OH)_2$ and CaP may develop on the sample surface, leading to a steady state in the corrosion rate, and may cause a weight gain [13, 76]. In addition, the ratio of the volume of the medium to the sample surface area is affected by the change in pH value. The standard volume of the test solution (0.2-0.4 ml/mm^3) is not suitable to accommodate the change in pH, and hence the examination of Mg corrosion [13]. The best conditions require a larger volume-to-sample area ratio.

2.6.1.1.2   *Hydrogen evolution test*

The general corrosion formula for Mg indicates that the dissolution of one Mg atom in media equates to the evolution of one hydrogen molecule [75, 76, 88]. Hence, the cathodic reaction results predominantly in hydrogen evolution whilst the reduction of oxygen is negligible [76]. The measured volume of hydrogen gas is equivalent to the mass loss of Mg, from immersion tests [13].

$$Mg + 2H_2O \rightarrow Mg^{2+} + 2(OH)^- + H_2 \qquad \text{Eq 2-16}$$
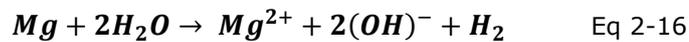
Hence, one mol., *i.e.* 24.31 g of Mg corrodes for each mol, *i.e.* 22.4 L of H_2 gas produced [88]. The H_2 evolution rate, V_H (ml/cm^2/day), is related to the Mg weight loss rate, ΔW (mg/cm^2/day):

$$\Delta W = 1.085\, V_H \qquad \text{Eq 2-17}$$

Hence, the corrosion rate (mm/y) corresponding to hydrogen evolution [88]:

$$CR_H = 2.279\, V_H \qquad \text{Eq 2-18}$$

In the hydrogen evolution experiment, the sample is immersed in the corrosion medium and a collector for the H_2 gas is placed on the sample surface (Figure 2-14). The collector contains an inverted funnel and burette which is filled by the test solution and replaced by the hydrogen gas released [103].
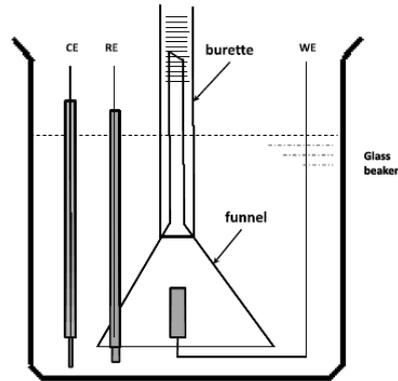
Figure 2-14 Schematic showing the experimental arrangement for H_2 gas evolution experiments [102]

The main advantage of H_2 testing is that direct measurement, at any time during the experiment, does not affect the corrosion process [75]. Hence, the data obtained from hydrogen evolution reveals the different stages of Mg-alloy corrosion. However, similar to the mass-loss test, the H_2 evolution method cannot explain the behaviour of Mg-alloys during the corrosion process [13], *i.e.* the test does not give exact reasons for changes in the H_2 evolution rate [13]. Furthermore, during the initial corrosion period, a low amount of H_2 gas is emitted, which makes it is difficult to capture and measure accurately [13]. In particular, the solubility of H_2 gas in water varies, depending on temperature and the medium volume to sample surface area. Hence, H_2 solubility is a source of error that must be taken into consideration [13]. Consequently, this test is limited for the measurement of corrosion rate, in the early stages of corrosion and for high corrosion resistance metals that emit very low volumes of H_2 gas. Capturing and measuring H_2 gas volume is difficult for such metal when the experimental set-up involves the effect of the flow of solution [13].

2.6.1.1.3 *pH monitoring*

According to the general corrosion reaction, corroding Mg results in the generation of hydroxide ions (OH⁻), which causes a local increase in pH at the surface and a subsequent rise in pH of the bulk solution [12]. This overall change in pH of the corrosion medium can be used to monitor the corrosion rate of Mg-alloys. This method has been used widely to study the activities of Mg biomaterials, by measuring pH levels close to and away from the surface [104-106]. However, by exceeding the natural biological pH ~ 7.4-7.6 level, the corrosion medium becomes an unrealistic environment for the measurement of Mg corrosion [13]. Hence, this test tends to be used to monitor the set-up of experiments in which the pH is closely controlled [13].

2.6.1.1.4 *Electrochemical, potentiodynamic polarization testing*

If the metal is not in equilibrium in contact with an electrolyte, a change of electrode potential from the steady state potential is termed polarization. When a change in potential occurs by an external source, the composition of the double layer at the surface will change, leading to the production of an electric current. By apply a potential, in the anodic direction, the material will produce a current as it corrodes, which can be measured.

Hence, potentiodynamic polarisation is an electrochemical technique widely used to measure corrosion rate. The measurement of polarisation curves is preceded by measuring the open circuit potential (OCP), which allows the material surface (working electrode (WE)) to reach a stable potential within the electrolyte [13]. A controlled voltage rate change, *e.g.* 5mV/minute, is then established between varied pre-set potentials, changing the flow current between the WE (Mg) and the counter electrode ((CE), inert metal). Firstly, a negative potential < OCP is applied, and then progressively scanned towards a more positive value [13]. The produced curve of potential verses log current density is then plotted (Figure 2-15). The point of intersection between the

anodic and cathodic Tafel region is termed the corrosion potential (E_{corr}) and corresponds to the corrosion current density (i_{corr}). The electrochemical corrosion rate can then be measured by Tafel extrapolation of the anodic and cathodic branches of the polarization curve, based on following equation [107]:

$$CR_i = K \frac{i_{corr}}{\rho} EW \qquad \text{Eq 2-19}$$

where CR_i is the corrosion rate; K is constant = 3.27×10^{-3} mm.g/µA cm year); i_{corr} is the corrosion current density (µA/cm^2); EW is the equivalent weight (atomic weight / number of electrons required to oxidise an atom of the element in the corrosion process, EW_{Mg}=12.15); and ρ is the standard density of Mg (g/cm^3). The above equation can be simplified to [88]:

$$CR_i = 22.85 i_{corr} \qquad \text{Eq 2-20}$$

The current density i_{corr} can be extracted from the polarization curve in which the linear portion of Tafel region, the straight lines shown in Figure 2-15, can be extrapolated back to corrosion potential E_{corr}.

The polarization curve can indicate the development of active regions, resulting from an increase of the dissolution rate with increasing electrode potential; the active/passive transition at the flade potential when the passive film is being formed on the metal surface; and passive regions, which form when the dissolution rate decreases slightly under the application of a nobler potential due to the formation of passive film [92]. The dissolution rate rises again at very high potential to form a trans-passive region, which indicates the evolution of oxygen by breakdown of the water in the electrolyte. Figure 2-15 summaries the key values that can be extracted from the polarisation curve.

The curve labels include:

$2H_2O \rightarrow O_2 + 4H^+ + 4e^-$

Trans-passive

$Mg^{2+} + 2OH^- \rightarrow Mg(OH)_2$

Passive

Flade potential

E_{corr}

$Mg \rightarrow Mg^{2+} + 2e^-$

Active/passive transition

$2H_2O + 2e^- \rightarrow H_2 + 2OH^-$

Active **Tafel region**

i_{corr}

Log current density

Critical current density of passivation
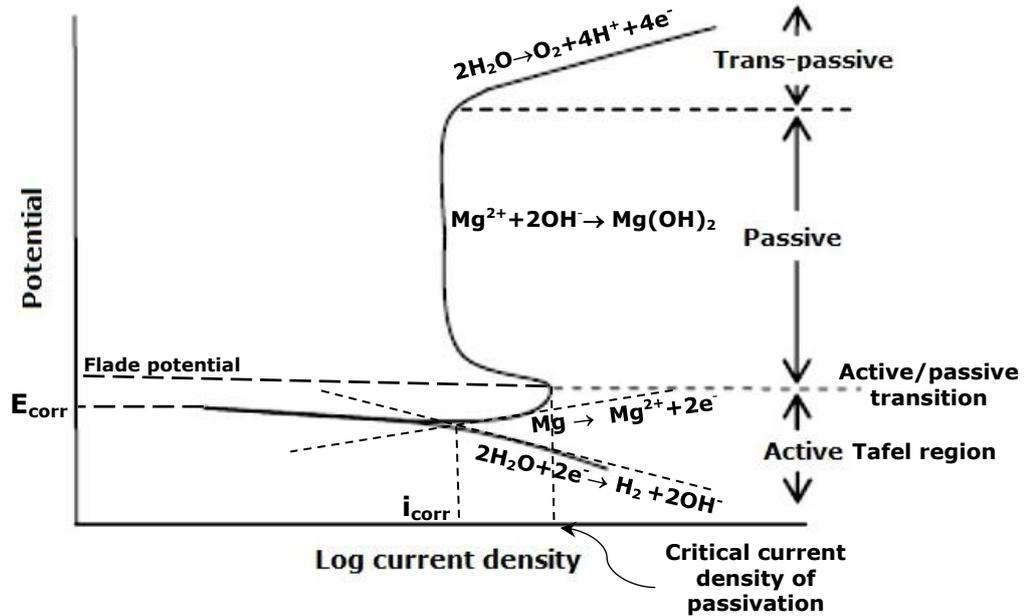
Figure 2-15 Typical polarization curve illustrating active-passive behaviour and the extraction of key parameters. The active region refers to hydrogen evolution and Mg dissolution; the passive region refers to the formation of a passivation film on the Mg surface; and the trans-passive region refers to oxygen evolution.

2.6.1.2 Dynamic testing

The conventional (static mode) methods used to assess the potential of a metal during corrosion are valuable tools [11]. However, they do not reflect truly the dynamic environments that stents will experience during implantation: In the physiological environment, body fluid is in continuous exchange in a constant circulation process [55]. Hence, it is appropriate to design *in vitro* tests that mimic physiological systems, in terms of refreshment and circulation, and improved understanding of the behaviour of degradable stents from an *in vitro* dynamic test will help to improve the development of biodegradable cardiovascular implants [108]. This could be achieved by applying a specific test bench to simulate the changing physiological conditions, and assist in studying the interrelationship between degradation rate and physiological parameters, such as temperature, pH, blood flow rate and shear stress [33].

2.6.2 *In vivo* testing

The development of Mg stents requires a stage of clinical trials, initially on animals and eventually on humans. It is known that the degradation of Mg *in vivo* is slower than *in vitro* from electrochemical studies, due to the lower Cl⁻ ion concentration in blood plasma (150 mmol/l [27]) [11]. Witte *et al.* [11] studied the corrosion behaviour of AZ91D and LAE443 *in vitro* using immersion and potentiodynamic testing, and *in vivo* on guinea pigs. They found that the *in vitro* and *in vivo* corrosion tests showed contrary corrosion rates, with both Mg-alloys showing corrosion rates *in vivo* four orders of magnitude lower than results obtained from *in vitro* testing. Li *et al.* [109] also investigated the corrosion rates of Mg–Zr–Sr alloys, using a range of *in vitro* and *in vivo* tests, and similarly obtained inconsistent results. Consequently, whilst the corrosion mechanism *in vitro* is well established, the degradation process of Mg *in vivo* is more complex and the corrosion mechanism remains uncertain [110].

Many factors impact upon the use of *in vivo* tests, such as time and cost, in addition to the harm and discomfort caused to experimental models [13]. The use of dynamic corrosion tests with suitable test solution, *i.e.* human blood could minimize the need for animal testing.

The tendency of pure Mg to corrode in aqueous solution can be effected by material microstructure and ions in the corrosive environment. Accordingly, the factors positively or negatively influencing the corrosion performance of Mg will be addressed in the following section.

2.7 Factors influencing Mg corrosion behaviour

The corrosion resistance of Mg in physiological environments is dependent on microstructure, impurity elements and the characteristics of the environment such as pH.

2.7.1 Influence of microstructure

Grain refinement is a process used to improve material mechanical properties, *e.g.* the strength of Mg and Mg-alloys. According to the Hall-Petch equation, the tensile strength of a material is inversely proportional to the square root of grain size [111]:

$$\sigma_y = \sigma_0 + k_y d^{-1/2} \qquad\qquad \text{Eq 2-21}$$

Where σ_0 is the friction stress (12 MPa for Mg); k_y refers to Hall-Petch parameter (0.22/m for Mg); and d is the average grain size, in m [112]. This effect is attributed to the increased area fraction of grain boundaries which act as barriers to the motion of dislocations [113]. From a corrosion point of view, strength can be improved without chemical alteration of the Mg structure by alloying, and without sacrificing the corrosion performance of Mg [112]. Based on this, the electrochemical response of Mg can be altered by changing the grain structure. Birbilis *et al.* [114] suggested a relationship between corrosion current density and grain size diameter, similar to the Hall–Petch type dependence. Ralston *et al.* [115], in their work on pure metals, reported that the corrosion current density i_{corr} for a metal is proportional to the reciprocal square root of grain size (*gs*), given by;

$$i_{corr} = (A) + (B)\, gs^{-0.5} \qquad\qquad \text{Eq 2-22}$$

Where A is constant, as a function of the environment, because the same material may show a varied corrosion rate depending on the electrolyte; and B is a material constant, which depends on composition and impurity level.

Argade *et al.* [116] reported a relationship between grain size and corrosion rate, given by CR = Cd$^{-0.3}$, where C is a constant and d is the grain size diameter, as observed during constant immersion testing, with lowest

corrosion rates reported for ultrafine grains of Mg–Y–RE alloy and highest corrosion rates for coarse grained samples. The grain boundaries are areas of high energy which can lead to the formation of galvanic couples between the cathodic interior grains and the anodic grain boundaries, which promotes high corrosion rates [116].

Kim *et al.* [117] noted that AZ31Mg alloy, prepared by the high-ratio differential speed rolling (HRDSR) technique, showed a decrease in anodic reaction rate through variation of grain size, while the cathodic reaction rate was not affected by grain refinement. They also found that E_{corr} became nobler and the breakdown potential decreased with grain size reduction, suggesting enhancement in passivity of the surface film.

Further, the corrosion resistance of Mg-alloys may be enhanced by reducing the size of the second phase. Kim and Kim [118] reported that nanosized β-particles on grain boundaries decreased the tendency of microgalvanic corrosion within the Mg matrix of AZ61 alloys processed by HRDSR. The corrosion rate, measured by both polarization and immersion tests, was found to have a linear relation with the reciprocal square root of the average grain size.

However, studies on pure metal show contradictory results, regarding the effect of the applied grain refinement process on corrosion rate, such as the study on grain refinement of Mg by equal channel angular pressing (ECAP), with detrimental effects on Mg corrosion resistance being attributed to an increase in dislocation content, although fine grain structures produced by extrusion acted again to improved corrosion resistance [119]. The study by Hoog *et al.* [120] [121] reported improved corrosion resistance of Mg in NaCl solution, processed by various mechanical deformation routes. Similarly, Birbilis *et al.* [114] found that ECAP processed Mg showed a linear increase in i_{corr} with the logarithm of increasing grain size, *i.e.* a smaller grain size was

associated with a lower i_{corr}. It was concluded that the ECAP process was able to reduce the anodic kinetics, with an increase in the number of ECAP passes further helping to reduce the cathodic kinetics on Mg. The improvement in corrosion resistance of fine-grained Mg was attributed to improvements in the passivation layer formed on Mg surfaces [120] [121] [122] [123].

In addition to grain size, Gollapudi [124] highlighted the importance of grain size distribution on the development of the passivation layer (Figure 2-16). It was proposed that in passive environment (pH > 10.5), a uniform passivation layer forms as a result of the distribution of fine grains and triple junctions at the surface, hence nano-crystalline structures can develop a more compact, passive film (Figure 2-16(a)), while more open passive layers may form on coarser grains due to irregular distribution of these defects (Figure 2-16(b)). Hence, the grain distribution effect can be observed from the development of uniform and compact layers in some locations, and non-uniform layers in others locations (Figure 2-16(c)). Gollapudi [124] stated that the distribution of grain sizes in nanocrystalline materials should be decreased for high corrosion resistance. Additionally, under active environments, nanostructures can enhance shallow pitting and promote more uniform corrosion, rather than the corrosion associated with large isolated pits.
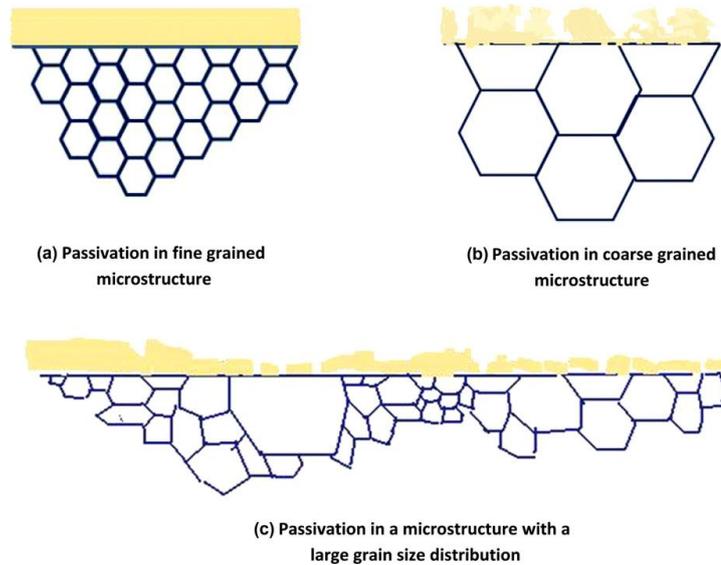
Figure 2-16 Formation of passive layers in: (a) a fine-grained microstructure; (b) a coarse-grained microstructure; and (c) a microstructure with a large grain size distribution [124].

2.7.2 Influence of impurities

The corrosion performance of pure Mg is known to be negatively affected by impurity elements such as Fe, Ni, Cu and Co [125]. The corrosion rate of Mg increases when the concentration of impurities rises above the tolerance limit, *i.e.* a critical contamination limit (Table 2-6) [125]. The mechanism of this deleterious effect can be attributed to the segregation of these elements within the Mg matrix. Due to the low solid solubility of certain impurity elements in the Mg matrix, they tend to participates and form cathodic sites, enhancing galvanic corrosion within the electrolyte. This makes the Mg surface more susceptible to localized corrosion and intergranular attack. Furthermore, when Mg corrodes, the impurity elements dissolve into the electrolyte and may interact with ions in solution, precipitating on the Mg surface and accelerating the localised corrosion process.

Table 2-6 Tolerance limits of impurities in pure Mg [99] [112] [126].

Elements	Fe	Cu	Co	Ni
Tolerance limit (ppm)	150-180 0.03-0.04 wt.%	1000-1300 0.1-0.01 wt.%	5 0.017 wt%	5 0.0005 wt.%

Hanawalt *et al.* [127] studied the effect of impurity elements on the corrosion rate of pure Mg, Mg-Zn and Mg-Mn alloys, and the results showed that corrosion rates increased dramatically when the level of common impurities exceeded the tolerance level (Figure 2-17(a)). In addition, the effect of alloying elements on the corrosion mechanisms of Mg in 3% NaCl solution was reported (Figure 2-17(b)). The tolerance level for Ni was found to increase in the presence of Zn or Mn, while increase of alloying element of Zn and Mn had no effect on tolerance level for Fe and Cu, indicating that the presence of Mn reduced the harmful effects of certain impurities and alloying elements, but did not necessarily improve the corrosion resistance [127]. Further, tolerance limits in Mg are found to be affected by the manufacturing method, and the way in which elements such as Fe are introduced to the Mg melt, *e.g.* from the steel casting moulds in the form of impurities [128]. Mn is usually added to Mg to reduce or remove Fe impurities by the formation of intermetallic phases, thus improving corrosion resistance [129].
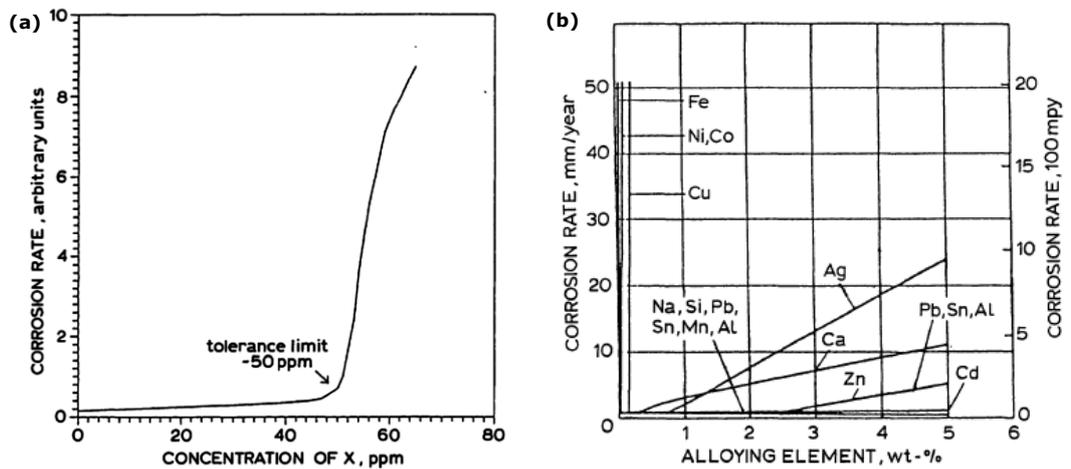
Figure 2-17 (a) General curve showing the effect of an impurity element (x) on the corrosion rate of Mg; the corrosion rate increases rapidly above the tolerance limit of ~ 50 ppm. (b) The effect of alloying additions on corrosion behaviour of binary Mg-alloys in 3% NaCl solution [127].

2.7.3 Influence of environment (electrolyte)

The interaction between metal surface and electrolyte plays a major role on the corrosion/passivation process. Mg rapidly forms a surface oxide/hydroxide layer in aqueous media. However, this layer does not provide for suitable corrosion protection, such as in Al and Ti [112]. According to the Pourbaix (potential E-pH) diagram (Figure 2-18), Mg forms dissolved Mg^{2+} over a wide range of pH, from acidic pH 2 to base pH 10.5. In the high alkaline conditions of pH $\geq$ 10.5, a stable insoluble film of $Mg(OH)_2$ forms which provides a protection layer from the solution [75], and even though Mg is thermodynamically unstable in natural media, the Mg surface still exhibits some level of passivity, with the surface showing filiform type attack instead of uniform corrosion [130].
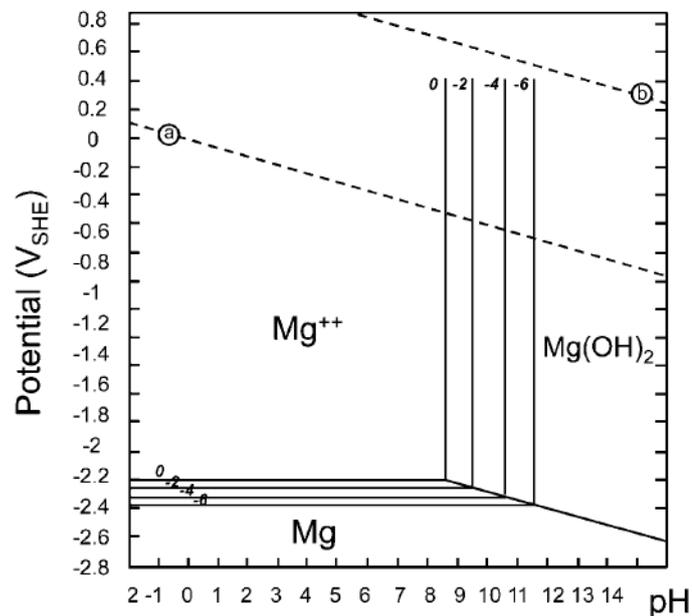
Figure 2-18 E–pH diagram for Mg in H_2O at 25°C; the water stability region lies between the (a) and (b) lines. At potentials below (a), hydrogen is evolved; whilst above (b), oxygen is evolved. (Adapted from [112] [131]).

45

The investigation of Mg corrosion in the laboratory needs a solution with composition close to physiological media. However, for solutions containing high concentrations of hydrogen carbonate (HCO_3^-) and phosphate ($H_2PO_4^{2-}$) and dissolved carbon dioxide (CO_2), such as SBF, the increase in pH during Mg corrosion increases the tendency for Mg passivation, which can occur faster due to the precipitation of insoluble hydroxyapatite (HA) and carbonate apatite (CA) at 37°C, (Figure 2-19) [18]. This can cause problems during polarisation testing, leading to the precipitation of apatite and a subsequent decrease in corrosion rate. Even though PBS does not contain a carbonate component, the possible dissolution of CO_2 in PBS ($CO_2 + H_2O \rightarrow H_2CO_3$) can lead to the slight precipitation of carbonate [55]. Xue *et al.* [132] compared the dissolution of Mg-alloys AZ31 and AZ91D in DI water, SBF and PBS, immersed for 14 days. A slow weight loss in DI water solution was identified, in which the sample surfaces became covered with passive $Mg(OH)_2$, whilst faster dissolution was observed in SBF solution, associated with the development of a complex layer of hydroxide, carbonate and phosphate. Kim *et al.* [117] reported on the corrosion products formed on AZ31 alloy surfaces after immersion testing in PBS, finding that the inner layer in contact with Mg was composed of nanocrystalline MgO, which was well-adhered with no pores at the interface, and an outer layer of crystalline $Mg(OH)_2$.

The pH for normal human blood is 7.4 ± 0.05 and this value is controlled by the lungs, with respiration affecting the rate of removal of CO_2 from blood; and through the kidneys, by extraction of acid and base from the body [18]. Hence, it is expected in such normal body conditions that passivation layers can easily dissolve in solution. Furthermore, body fluids contain aggressive ions such as Cl^- which can influence the dissolution rate and passive behaviour of Mg. Song *et al.* [87] studied the electrochemical response of pure Mg in NaCl and Na_2SO_4 across a wide range of pH, and demonstrated

that the presence of Cl$^-$ could affect the passivation behaviour of Mg, by making the surface more active or by increasing the film free area, thereby accelerating the electrochemical reaction from Mg to Mg$^+$. It was claimed that Cl$^-$ has a more harmful effect on the corrosion resistance of Mg than sulphate ions.

The flow rate of the corrosive environment is also thought to influence corrosion rates and the stability of passivation films. The Mg(OH)$_2$ layer on an Mg surface could be mechanically disrupted due to the flow of bio-liquids [25], preventing local increase in pH of solution and hence increasing the corrosion rate [75] .
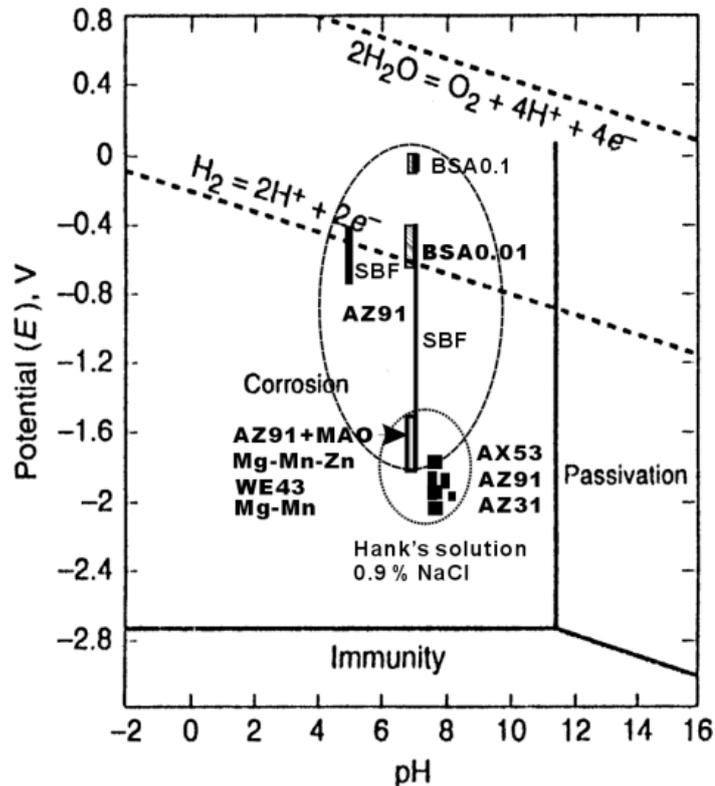
Figure 2-19 pH-potential diagram of Mg and its alloys in various SBF and bovine serum albumin (BSA) [27]

Figure 2-20 shows a schematic diagram summarising different parameters positively and negatively affecting corrosion rate, *i.e* the corrosion resistance of Mg.
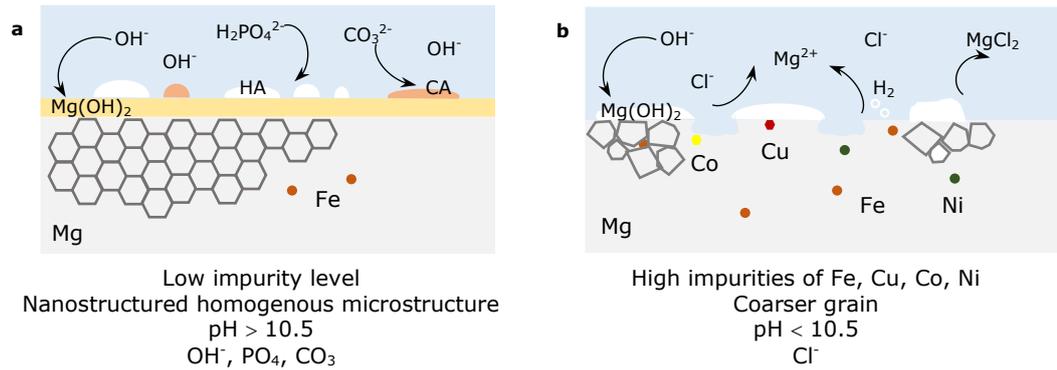
Figure 2-20 Schematic diagram summarising parameters: (a) positively and (b) negatively affecting the corrosion behaviour of Mg.

As mentioned in section 2.4.2, pure Mg has a spontaneous tendency to corrode in aqueous solution. Hence, various strategies have been adopted to control the corrosion rate of Mg, as discussed in the following section.

2.8 Strategies for the protection of Mg

The elements within degradable implants for use inside the human body should be biologically safe [133]. A balance between daily allowance and corrosion rate is necessary in order to avoid toxicological problems. Ideally, the acceptable corrosion rate should no higher than 0.02 mm/year [134]. If the corrosion rate of the bulk material exceeds this value, then anodised alloys, coatings or thermal treatment processes may be applied to the implant, to delay the onset of corrosion and slow down the initial rate of corrosion. Controlling the degradation rate of Mg may be achieved using two main strategies [21]: i) Altering the composition and microstructure of the base Mg by alloying or manufacturing methods; and ii) Near surface modification treatments, or coating formation on the Mg surface using a polymer, ceramic, metal or composite barrier layer. In this context, the focus

of the next stage of this literature review is concerned with controlling corrosion by modification of the Mg near surface.

2.8.1 Surface modification

The Mg implant should possess appropriate functional and durable bulk material properties, as well as promoting a positive biological response to the surface [20]. Initial cell-biomaterial interactions are affected by surface properties. Hence, surface characteristics may need to be modified to improve surface biocompatibility and corrosion resistance [20]. The modification of surface texture, energy and potential, for a specific clinical need, can reduce restenosis by affecting thrombosis and neointimal proliferation [9].

Surface modification may be classified into three categories (Figure 2-21):

i)   Physiochemical surface modification which includes; chemical conversion by coating [135] [136] [137] [138]; electrodeposition [139] [140]; anodization [141] [142, 143]; chemical vapour deposition (CVD) [144] [145]; physical vapour deposition (PVD) [146] [147] [148] [149]; ion implantation [150] [151] [152] [153]; thermal spraying [154] [155, 156] [157]; and laser processing [158] [159].

ii)   Functional surface modification [160] [161].

iii) Morphological processing [162] [163].
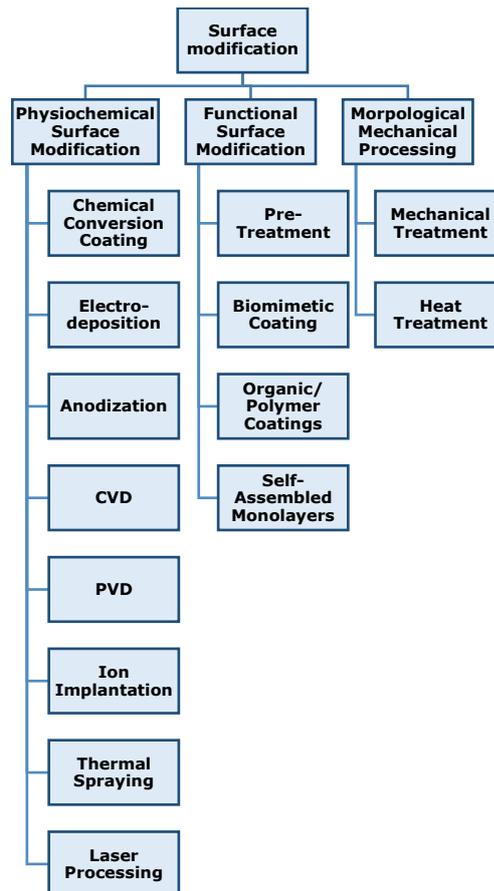
Figure 2-21 Classification of Mg surface modification techniques.

The modification of Mg surfaces is now considered, by either PVD surface coating, *i.e.* adding a barrier material layer to the surface; or by near surface modification, *i.e.* refining the near surface microstructure.

2.8.1.1   Physical vapour deposition (PVD) coating

A physical barrier such as a coating is an appropriate route to the protection of Mg surfaces from attack by aggressive species from the surrounding environment [160]. The coating must prevent the transport of ions, oxygen and water through it to reach the substrate [77]. The number of layers used could range from one to many, with coating thicknesses up to tens of micrometres, providing for adhesion to the substrate, and corrosion and wear

resistance [160]. The coating must be dense, uniform, free of porosity, and well adhered to the base material [77].

Generally, there are two approaches for forming a physical barrier to Mg; *i.e.* surface conversion and coating deposition [21]. Surface conversion is the process of forming a protective film, using chemical or electrochemical techniques [21, 82], i.e. non-reactive surface layers may be formed by the chemical reaction of the metal surface with a solution containing the coating materials [82]. Rudd *et al.* [164] reported on the formation of Ce, La and Pr coatings on the surface of pure Mg and WE43 alloy. These systems showed a significant improvement in corrosion resistance of the base material after immersion in borate buffer solution (H_3BO_3 (0.15 mol/dm) / $Na_2B_4O_7$ (0.05 mol/dm)) up to 10 h. This method is considered suitable for short term protection, *e.g.* in the case of atmospheric corrosion [82].

PVD techniques provide for the direct deposition of atoms or molecules onto a substrate surface, using highly pure target materials, under varying processing conditions [77]; including sputtering deposition, ion plating, diffusion coating [165] and laser deposition [77]. The basics of sputter deposition involves the generation of energetic ions in spark discharge plasma positioned in front of a target (cathode). The ions are attracted to the cathode and bombardment causes the removal (sputtering) of target atoms which then condense onto the substrate to form a thin layer [166].

The deposited material may be metallic, organic or inorganic [21]. Metallic coatings are usually slowly degradable or non-degradable layers, *e.g* Al, deposited on the surface of Mg-alloys. Wu *et al.* [167] successfully deposited pure Al and Ni thin films on AZ91D Mg-alloy using radio frequency magnetron sputtering (RF-MS), and showed after 48 h treatment at 350°C, that the Ni coating improved in cohesive strength, hardness and wear resistance,

compared to Al coatings which showed the development of a brittle $Al_{12}Mg_{17}$ phase.

A major challenge for the PVD coating of Mg is that the deposition should be done at temperatures < 180°C, the stability temperature related to Mg alloys where transformation starts at such processing temperature [77]. This can be achieved by applying a bias voltage to the substrate. Reiners and Griepentrog [168] deposited TiN coating on AZ91 alloy using direct current (DC) conditions, applying a 60 V bias voltage, producing very well adhered and pore free coatings. The PVD deposition of Al coatings on AZ31B alloy, under different sputtering conditions [169] [170] confirmed that Al coated surfaces showed a lower corrosion current density and a more positive corrosion potential, compared to the AZ31B substrate, when using sufficient sputtering current of 1.6 A under an Ar pressure of 0.7 Pa. Alteration of the deposition parameters, such as substrate speed, also improved coating adhesion. Taha *et al.* [171] deposited pure Al and Al-12.6%Si coatings on AZ31 alloy, using different substrate speeds and plasma activation, and reported good adhesion and corrosion resistance when Al/Mg diffusion occurred across the coating/substrate interface.

Binary Mg-alloys may also be coated using PVD, *e.g.* Mg-Zr [172] [173], Mg-V [174] [175] [176] [177] and Mg-Ti [178] coatings all exhibited columnar microstructures with high porosity, giving lower corrosion resistance compared to cast Mg.

Table 2-7 summarises some recent, relevant PVD coating literature: It can be noted that although the corrosion resistance of Mg surfaces improved slightly under test conditions, galvanic corrosion was an issue regarding the use of metallic coatings. It is recommended that the use of insulating coatings, *e.g.* oxide, can overcome the galvanic differences within the coating/Mg substrate.

Additionally, the adhesion of coatings with the Mg substrate is mainly dependent on mechanical interlocking of the coating/substrate interface, hence the deposition conditions need to ensure that sufficient adhesion occurs. It is recommended that film thickness should be in the range of a few μm because of the use of thick film can result in increased residual stress and hence introduce cracking within the coatings.

Table 2-7 Overview of PVD coating literature on Mg-alloys

Subst.	Coating	PVD	Parameter altered	Coating thickness / μm	Properties studied		Ref
					Mechanical	Corrosion resistance	
AZ31B	Al	DC	Sputtering current / Ar pressure / deposition time	-	-	Improved under 3.5%NaCl	[170]
AZ91D	Al/Ni	RF	Post thermal treatment	2	Hardness, wear, strength	-	[167]
AZ31	Al/ Al-12.6%Si		Substrate speed	1-6/ 2	Good adhesion	Under humidity	[171]
AZ31	CrN TiN (TiAl)N NbN-(TiAl)N TiN/AlN NbN/CrN	-	-	3.3 0.9 1.5 1.0+1.5 0.5+1.0 4.8 3.0	Good adhesion & hardness	CrN & (TiAl)N under 0.0001 M NaCl	[179]
AZ31	Ti-MgAlN	DC	Ar/N_2 gas		Hardness	In 5% salt spray / 0.05% NaCl EIS	[180]
AZ91	TiN	DC	Ar/N_2 gas	0.8	Hardness & adhesion	-	[168]
AZ91 hp	Cr/ CrN	RF	Ar/N_2 gas	7/ 8-9	Good adhesion & wear	Unstable in 3% NaCl	[181] [182]
AZ91	TiMgAl/ CrN/ Pox-Al_2O_3	RF	Ar/N_2 gas	17/ 18/ 3.5	Wear	Salt spray	[183]
AZ31	Mg	DC	Substrate temperature	65	Poor adhesion	Salt spray	[184]
AZ31	TiO_2 Al_2O_3	-	-	0.3 0.9	Poor adhesion	3.5%NaCl	[185]
AZ31	Ti–Al–N / Ti–Al	DC	Ar/N_2 gas	3	Satisfactory adhesion; Improved hardness	Improved under 3.5%NaCl	[186]
AZ31	Ti	DC	Ar gas	2	Densification of the oxide layer	Improved under 3.5%NaCl	[187]
AZ31	AlN/Al/DLC*	-	Ar/N_2/C_2H_2	1	Wear, hardness	Improved under 3.5%NaCl	[188]

Diamond-like carbon (DLC)

2.8.2 Near surface modification (LSM, EB)

Rapid solidification processing (RSP) techniques have attract scientific interest to modify the surface of materials due to their ability to induce high power densities of 10^9-10^{12} W/cm^2 on the sample surface, in a very short duration [189]. RSP techniques include the use of energetic ions, electrons or laser beams, leading to rapid melting and quenching of shallow depths near the surface, due to the focused conduction of heat into the bulk [190].

The important features of high energy deposition methods include rapid heating, melting, solidification, evaporation/ablation and thermal stress, and shockwave formation [191] [192]. Consequently, non-equilibrium microstructures of *e.g.* nano-sized grains, saturated solid solutions and amorphous phases can develop within the treated layers. Thermal stress and shockwaves can cause severe deformation in the sublayer. However, these mechanisms can enhance the physical, chemical and mechanical properties of the surface layers formed with respect to corrosion [189].

2.8.2.1 Pulsed electron beam techniques

Intense pulsed electron beam surface modification techniques include: Low and high current pulsed electron beam (LCPEB, HCPEB); Low energy high current pulsed electron beam (LEHCPEB); and Large area electron beam (LAEB) techniques. These irradiation methods use high density EB, without focusing the beam on the treated surface, to cover a wide area (~ 60 mm diameter) with uniform intensity to minimise the need for overlapping procedures and subsequence re-heating and re-crystallisation.

EB techniques have been applied to improve surface roughness [193] and corrosion resistance, as well as surface hardness and wear resistance. Okada

et al. [194] reported that bio-titanium alloy (Ti–6Al–4V) surfaces were greatly smoothed, with improved roughness from ~ 10 μm to ~ 1 μm, by LAEB irradiation. This finding agreed with the study of Gao [195] who reported that the surface roughness of pure Ti–(TA2) could be reduced to ~ 0.04 μm after LEHCPEB treatment with low energy density, whilst roughness increased under conditions of higher energy density and/or longer pulse duration and/or longer pulse times, due to the formation of craters. Furthermore, another study by Gao [196] reported that the value of surface roughness of TC4 titanium could be decreased to ~ 40 nm by HCPEB under the energy density range of 12–18 J/cm^2, whilst further increase in energy density caused an increase in roughness. This was attributed to a transition from melting to evaporation, when the beam energy increased beyond a certain limit.

In addition to improving surface roughness, EB processing can improve the corrosion resistance of wide range of metals [192] [197] [198] [199]. The EB modified layer usually involves three continuous layers with different depths: i) a melted and solidified layer on the surface; ii) a heat affected zone; and iii) a stress wave affected zone [200]. The melted layer may favour the formation of a homogeneous, continuous passivation layer during the corrosion process and thereby improve the corrosion resistance of the EB treated samples. Hao *et al.* [201] used HCPEB irradiation to modify surfaces of AZ91HP, with treatment parameters of energy density 2.2 J/cm^2, pulse duration 1 μs and number of pulses 5 and 10. The corrosion potential of 10 pulsed EB irradiated specimens shifted positively and the corrosion current density decreased by four orders of magnitude. This improvement in corrosion resistance was attributed to the formation of a homogenous passivation layer and the disappearance of the inhomogeneous second-phase $Mg_{17}Al_{12}$, with the surface left as a supersaturated solution after HCPEB treatment. Gao *et al.* [197] tested an irradiated AZ91HP-Mg-alloy, processed by HCPEB with beam energy

density of 3 J/cm^2 and 10 pulses, immersed under 5% NaCl. The existence of an MgO layer and the disappearance of second phase Mg$_{17}$Al$_{12}$ in the melted layer was reported, again having a positive effect on improving the corrosion behaviour [192]. Further, Uno *et al.* [193] reported that LAEB irradiated steel surfaces showed no rust after one year exposer to atmosphere, again indicating improved corrosion resistance after EB treatment. Table 2-8 summarise the key findings in literature.

Table 2-8 Summary of key findings in literature for Mg and Mg-alloys modified by EB processing

Material	EB source	Energy	No of pulses	Mechanical properties	Corrosion		ref
					Media	mechanism	
AZ91HP	HCPEB	3 J/cm^2	5,10,15	Microhardness wear	5% NaCl	Presence of Mg; disappearance of second phase in the melted layer	[197]
ZK60	HCPEB	3 J/cm^2	15	-	3.5 wt.% NaCl	Formation of ceramic layer	[202]
ZK60-1Y	HCPEB	2.5 J/cm^2	15	Wear resistance	-	-	[203]
AZ31	HCPEB	2.5 J / cm^2	5,10,15	Microhardness, wear resistance		-	[204]
Pure Mg and AZ31B	HCPEB	Voltage / 25 keV	10,15, 20	-	-	-	[205]
AZ31 and ZK60-1Y	HCPEB	3 J/ cm^2	5,10,15	wear resistance	5% NaCl	Formation of compact oxide film	[206]
Mg67Zn30Y3 quasicrystal alloy	HCPEB	2.5 J/ cm^2	10	wear resistance	-	-	[207]
AZ91HP	HCPEB	2.2 J/ cm^2	5,10	Microhardness, wear resistance	5% NaCl	Surface layer in a state of supersaturated solution	[201]
AZ31 and AZ91	LE-HCPEB	2.5 J/cm^2 and ~3 J/cm^2	5, 10 and 15	Wear resistance	5% NaCl	Al-over supersaturated *a* (Mg) solid solution, nanograined MgO layer	[208]

2.8.2.2   Laser surface melting

Secondary phases and impurities at the Mg surface can impose negative effects on corrosion resistance because they provide sites for cathodic activity, leading to galvanic corrosion [209]. Laser surface melting (LSM) has the potential to redistribute these secondary phases and impurities through the melting and rapid solidification of near surface volumes, leading to the

development of non-equilibrium (metastable) microstructures. LSM can have significant influence on the corrosion behaviour of Mg-alloys due to the refinement of secondary phase grains. Abbas *et al.* [209] used a continuous wave CO_2 laser to produce overlapping (50%) melt tracks on AZ31, AZ61 and WE43 alloys, with a laser power of 1.5 kW, traverse speed of 160 mm/s and beam diameter of 2 mm. After immersion in 5 wt.% NaCl solution for 10 days at 20°C (pH 10.5), it was found that the average corrosion rates reduced by ~ 30, 66 and 87% for the AZ31, AZ61 and WE43 alloys, respectively, because the melted layers did not dissolve fully during the corrosion test period of 10 days. The improvements in corrosion rate were attributed to microstructure refinement, with grain size being reduced by a factor of ~ 10, combined with a more uniform distribution of the secondary phase, acting as a barrier to prevent corrosion propagation. Similar results were obtained by Guan *et al.* [210] who modified the surface of AZ91D alloy using a Nd:YAG pulsed laser (power density 3.82×10^4 W/cm^2). After laser treatment, the original α-Mg and lamellar $Mg_{17}Al_{12}$ microstructures were refined to form a more cellular/dendritic structure, combined with a continuous network of fine β-$Mg_{17}Al_{12}$, providing an effective barrier against corrosion. Further, Majumdar *et al.* [211] tested MEZ alloy under continuous wave CO2 laser, with incident power of 1.5 – 3 kW and a scan speed of 100 – 300 mm/minute. LSM was found to improve pitting corrosion resistance, being attributed again to grain refinement which enhance the attachment and retention of the $Mg(OH)_2$ passivation film. Mondal *et al.* [212] noted also the absence of intermetallic phases at grain boundaries and an increase in the solid solubility of Al and Ca in Mg, which acted to minimise the tendency of ACM720-Mg alloy to pitting corrosion after Nd-YAG laser treatment.

Padmavathi *et al.* [213] used the electrochemical impedance spectroscopy (EIS) technique to study the corrosion resistance of laser melted AZ91C alloy

and found that the Mg(OH)$_2$ film formed on the surface was more stable than that formed on as-cast specimens, even with the presence of the Cl$^-$, as a result of the finer grain size of the matrix. Conversely, Dubé *et al.* [214] reported that even though near surface microstructure refinement was achieved after pulsed Nd:YAG laser modification of AZ91D and AM60B alloys, corrosion resistance in sodium solution was not affected and laser processing under conditions of high input power which acted to reduce corrosion resistance.

Guan *et al.* [215] studied the effect of overlap (25-90%) on the microstructural evolution of AZ91D alloy, treated by pulse Nd:YAG laser surface melting and found that with increasing overlap, the morphology of the solidification microstructure altered from cellular grains, to cellular–dendritic and equiaxed dendritic grains. Improved corrosion resistance of the laser treated AZ91D alloy was reported, compared to as-received surfaces, with variation in corrosion rate values being attributed to coarse microstructure and cracks formed in the melt pools of low overlap. Differences in the corrosion performance on overlapping zones and the central laser track was also observed by Gao *et al.* [216] and Guo e*t al.* [217], being attributed to the dissolution of Mg$_{12}$Nd. Table 2-9 summarises key findings in literature regarding the use of lasers to modify Mg surfaces. It is noted that grain refinement and redistribution of second phases after laser surface melting can enhance the corrosion resistance of Mg-alloys due to improvements in the self-passivation behaviour of Mg surfaces.

Table 2-9 Overview of literature for Mg-alloys, surface modified by laser processing

Material	Laser	Power / W	Scan speed	spot size / mm	Improved Properties	Corrosion media	Comments	Ref
ACM720	CW-Nd:YAG	2000	600 mm/minute	3.8	Microhardness & wear resistance	5 wt.% NaCl	Absence of 2nd phase Al_2Ca at grain boundaries, microstructural refinement and extended solid solubility of Al	[212]
AZ91C	Pulsed-Nd:YAG	100-300	5-10 mm/s	1.17-1.14	Microhardness	3.5% NaCl	Grain refinement and redistribution of $Mg_{17}Al_{12}$ intermetallic precipitates along grain boundaries	[213]
ZE41	Excimer laser	100 mJ	250-50 μm/s	rectangular 24×10	Microhardness	0.5M NaCl solution and salt-spray test	Uniform distribution of RE elements	[218]
ZE41A	CW-Nd:YAG	1818-1856	0.5-19.875 mm/min	6.5-1	-	0.001 M NaCl	Insignificant improvement in corrosion resistance	[219]
AZ91D	Pulsed-Nd:YAG	3.82×10^4 W/cm^2	10 mm/s	1 mm	-	3.5% NaCl	Different corrosion rates due to coarse structures in overlapping areas	[215] [220]
ZE41A	CW-Nd:YAG	1856- 820	19,875- 12,000 mm/min	1 mm	-	0.001 M NaCl	Surface crack-free microstructure and homogeneous distribution of alloying elements	[221]
Mg-alloy with (wt.%), 8.57Al, 0.68Zn, 0.15Mn, 0.52Ce and Mg-balance	Pulsed Nd:YAG	1.0 J	140 mm/min	300 μm	Microhardness	3.5 wt.% NaCl	Strong oxidation nature of Ce resulted in the formation of new oxide film. Increase Al concentration.	[222]

Table 2-9 continued.

Material	Laser	Power / W	Scan speed	spot size / mm	Improved Properties	Corrosion media	Comments	Ref
AZ91D	CW- high-power diode laser (HPDL)	375-600	45-90 mm/s	-	Microhardness	3.5 wt.%	Corrosion rate increased with increasing laser power and decreasing laser scanning speed	[223]
AZ91D & AM60B	Pulsed Nd:YAG	100 - 300 W	3 - 20 mm/ s	-	-	5wt% NaCl	No significant improvement in corrosion resistance	[214]
AZ31, AZ61 & WE43	CW- CO_2 laser	1.5 kW	160 mm/s	2 mm	-	5wt% NaCl	Refinement in the microstructure of the alloy and even distribution of β-phase	[209]
AZ91D	Pulsed-excimer laser	6.0 J/cm^2	-	4.0 mm	-	3.5 wt.% NaCl	Significant dissolution of intermetallic and the formation of a highly homogeneous α-Mg solid solution	[224]

2.8.3 Alloying (commercial approach)

Current Mg-alloys used for temporary implants were developed originally for the transport and aerospace industries. Alloying elements are added usually to improve the mechanical properties of the Mg. However, Mg and Mg-alloys used in biomedical applications must consider the biological effect of the ions released and their acceptable tolerance levels. The alloying material released from the implant to body fluids and tissue must not be toxic [55].

The development of alloys for controlling corrosion may be achieved through the addition of elements which alter the grain structure and precipitate phases, in addition to the effects of oxide layer composition [61]. Mg-alloys are under investigation to understand the influence of specific elements on the formation of protective layers [25]. Minimising the chemical potential difference (E^o) between Mg and the alloying elements could result in a reduced anodic tendency, and hence affect the corrosion rate in general [225]. Presently, Mg alloys used as biomaterials are divided into three major groups: i) Pure Mg with traces of other elements; ii) Al containing Mg-alloys with a trace of Zn and Mn, which suggests that Al can modify mechanical properties and improve corrosion resistance through the formation of an insoluble and stable oxide layer of Al_2O_3 [61] [25] and; Al-free Mg-alloys containing RE elements and mixtures of Zn, Ag or Zr which enhance the fine grain structure, mechanical properties and the formation of intermetallic compounds to reduce microgalvanic effects [25] [61]. Alternative alloys containing Ca are under development which reduces the dissolution of Mg due to the formation of cathodic phase at grain boundaries. A brief summary of various Mg-alloys, their phases and their effect on mechanical and corrosion properties within a biological system are presented in Table 2-10.

Table 2-10 Overview of Mg-alloys used as biomaterials [55, 133, 226]

Material family	Alloy	Alloying elements wt.%			Main phases	Effect of alloying elements		Biological effect		
						Mechanical properties	Corrosion properties	normal serum level	positive effect	high dosage
Pure Mg	Mg	99.9 Mg			Mg	-	Fast corrosion in presence of Fe, Cu, Co & Be	0.73-1.06 mmol/L	Energy metabolism	Toxicity
Mg-Al-Zn	AZ31 AZ63 AZ91	3 Al 6 Al 9 Al	1 Zn 3 Zn 1 Zn		Mg; $Mg_{17}Al_{12}$	Improved strength by solid solution strengthening, castability	Improved corrosion resistance by insoluble Al_2O_3, but high Al increase & $Mg_{17}Al_{12}$ cause pitting corrosion	Al = 2.1-4.8 μg/L	-	Dementia & Alzheimer diseases
Mg-Ca	Mg–xCa (x=1, 2,3)	xCa			Mg; Mg_2Ca	Grain boundary strengthening, grain refining	Increase corrosion rate	0.919-0.993 mg/L	Good cell attachment, stored in bone and teeth	Kidney stones
Mg-Zn-Ca	Mg–1Zn–1Ca	1 Zn	1 Ca	Mg	Mg_2Ca; $Ca_2Mg_6Zn_3$	Grain boundary strengthening	High corrosion rate	-	Good bio-compatibility no inflammatory	Neurotoxicity Kidney stones
Mg-Zn-Mn-Ca	Mg–2.0Zn–1.2Mn–1Ca	2 Zn	1.2 Mn	1 Ca	Mg;Mg_2Ca; $Ca_2Mg_6Zn_3$; $Ca_2Mg_5Zn_{13}$	Extreme grain refinement	-	-	-	Neurotoxicity Kidney stones
Mg-Si-Ca		1 Si	1 Ca		Mg; Mg_2Si; SiMgCa	Little increase in strength-	Low corrosion resistance	-	Growth bone classification	Lung diseases (SiO_2)
Mg-Zn	Mg–xZn (x=1, 3,10)	xZn			Mg; MgZn Mg_2Zn_3 Mg_7Zn_3	Improved strength and castability	-	12.4-17.4 μmol/L	Necessary in immune system	Neurotoxicity

Table 2-10 continued.

Material family	Alloy	Alloying elements wt.%			Main phases	Effect of alloying elements		Biological effect		
						Mechanical properties	Corrosion resistance	normal serum level	positive effect	high dosage
Mg-Mn	Mg–1Mn	1 Mn			Mg; Mn	High purity alloys by formation of less harmful intermetallic compounds; enhanced ductility	Increase corrosion resistance by removal of impurities such as Fe (with Al)	<0.8 μg/L	-	Neurotoxicity
Mg-RE	LAE 442	4 Li	4 Al	2 RE	Mg; Al$_{11}$RE$_3$;	Improved ductility and formability by change of lattice structure to BCC	Enhanced corrosion resistance and mechanical properties	Li=2-4 ng/g	Drug for psychiatric disorder	Lung dysfunction
	WE43	4 Y	3 RE		Mg; Mg$_{12}$YNd; Mg$_{14}$YNd$_2$	Solid solution strengthening	Enhanced corrosion resistance	-	Anti-carcinogenic	-
	ZE41	4 Zn	1 RE		Mg; MgZn(RE)	Solid solution, and precipitation strengthening	Enhanced corrosion resistance	-	-	-
	AE44	4 Al	4 RE		Mg; Mg$_{17}$Al$_{12}$; Al$_{11}$RE$_3$; Al$_{12}$RE	Solid solution, and precipitation strengthening	Enhanced corrosion resistance	-	-	-
	Mg–xGd (x=5,10,15)	xGd			Mg; Mg$_5$Cd		Decreased corrosion rate	-	-	Acute toxicity
	WZ21	2 Y	1 Zn		Mg; Mg$_y$Zn$_3$; Mg$_7$Zn$_3$; Mg$_3$YZn$_6$		Enhanced corrosion resistance	-	-	-
	Mg–8Y	8 Y			Mg; Mg$_{24}$Y$_5$ Mg$_2$Y	Improve creep resistance	Improved corrosion resistance	-	-	Adverse effect on DNA transcription factors

The degradation rate for different Mg-alloys is still undergoing extensive research. Kirkland *et al.* [227] studied the corrosion rate of a wide range of Mg-alloys potentially used in implants applications. They presented a survey of weight loss results (Figure 2-22) after 3, 7 and 14 days immersion in Minimum Essential Medium (MEM) solution and concluded that AZ91 alloy showed the slowest corrosion rate, during 14 days immersion, at 0.07 mg/cm^2/day compared to 0.8 mg/cm^2/day for highly pure Mg [227].
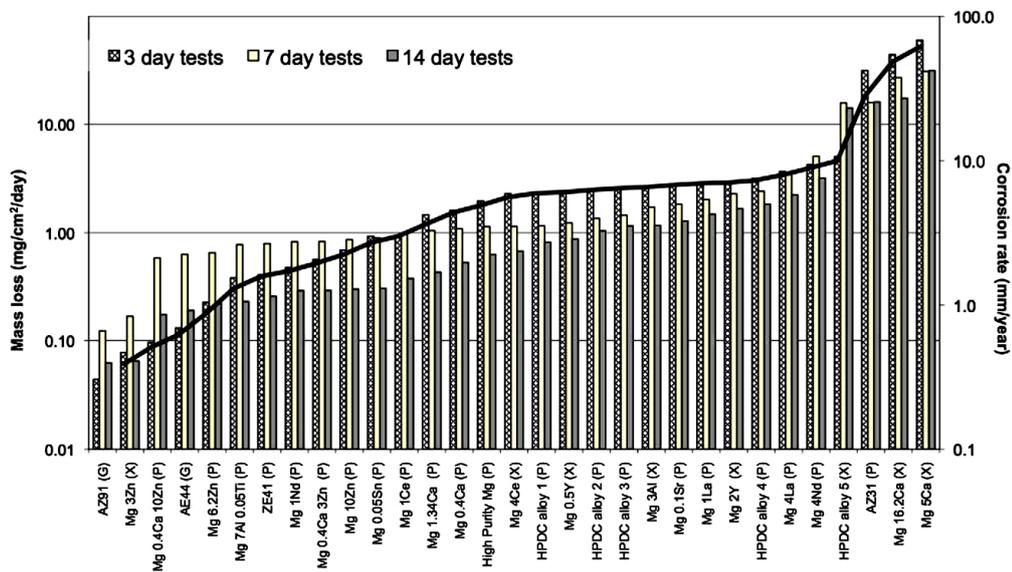
Figure 2-22 Degradation rates for various Mg-alloys in MEM, at 37°C. The symbol 'G' refers to general corrosion, 'P' pitting corrosion, and 'X' localised corrosion [227].

Gusieva *et al.* [112] interpreted the relative influence of alloying elements on anodic and cathodic kinetics and corrosion (Figure 2-23), concluding that Al and Mn alloying elements should not exceed their effective solubility limits, in order to gain improvements in corrosion activity. However, elements such as Li and Ca are more reactive than Mg, so when alloyed with Mg increase the anodic reaction rate.
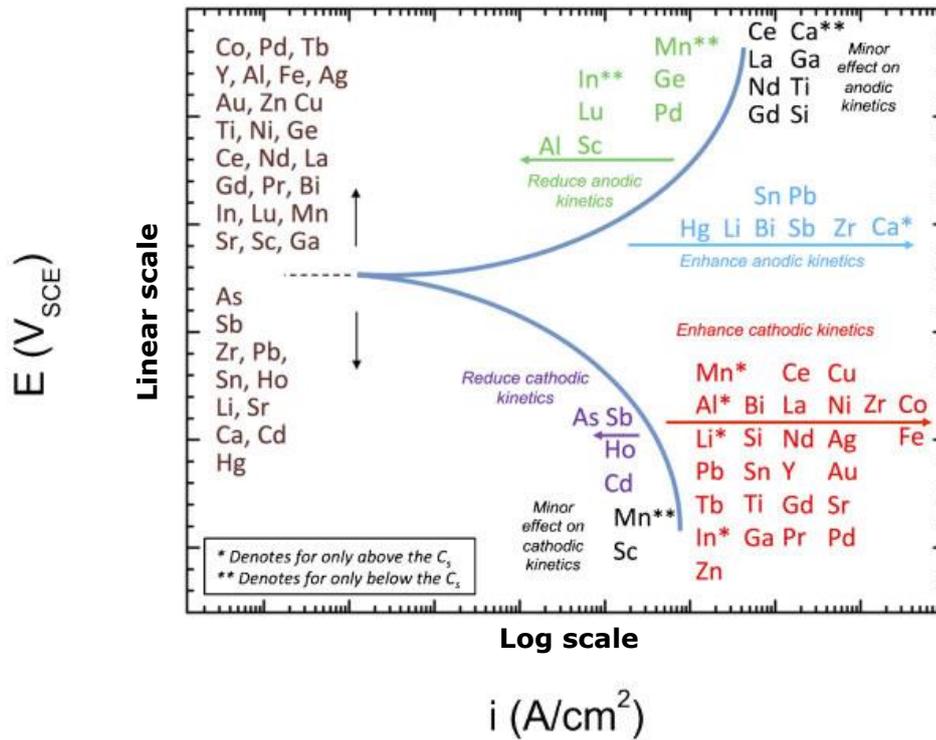
Figure 2-23 Schematic representation of electrochemical effect of alloying elements. Plot shows the ability of alloying additions to modify anodic or cathodic kinetics (or both), leading to changes in the resultant corrosion rate (i_{corr}), along with changes in corrosion potential (E_{corr}). CS represents solid solubility [112].

Regarding the control of Mg corrosion, the key factors include:

    i.   Solubility of alloying elements:

Elements added to Mg should show considerable solubility within the Mg matrix, which tends to reduce the anodic kinetics. However, when the alloying elements reached their limiting values, they tended to form intermetallic phases. Consequently, cathodic kinetics increase at these sites, leading to a high corrosion rate. Homogenous distributions of alloying elements in the Mg matrix should help reach a preferable degradation rate.

    ii.   Nature and solubility of the corrosion products:

When the surrounding environment reaches the equilibrium ion concentration, the corrosion of Mg-alloy stops [25]. However, this condition cannot be reached in practice, since the electrolyte is subjected to a dynamic process, due to varying blood flow and fluid content around the implant. Hence, equilibrium in the environment is not achievable, and complete corrosion

becomes possible. In addition, the reaction between dissolved ions and the surrounding biological environment leads to the formation of corrosion products that are varied in their nature and solubility [226] .

Depending on the alloying elements, corrosion morphologies may vary from uniform to more localised corrosion. The depth and penetration of corrosion attack should be considered carefully. Kirkland *et al.* [227] pointed out that in stent applications, the wall thickness is generally in the hundreds of microns range; hence variability and rate of corrosion must have strict levels, and no effect should be observed on mechanical integrity during the healing period. In addition, insoluble products could impose health problems and risks, such as blocking the blood stream in the artery. Their study investigated the corrosion product of Ca-rich alloys, finding that insoluble 'chalk like' Ca-rich oxides formed on sample surfaces very rapidly [227].

iii.   Effect of solution and organic content:

Various *in vitro* corrosion experiments have been performed on Mg-alloys with or without proteins in the corrosion media [25]. It is known that protein layers reduce the corrosion rate of Ti-alloys. A protective protein layer enhanced by calcium phosphate was observed and it was concluded that this layer participates in altering the corrosion rate [25]. However, in Mg-alloys, this affect has not been investigated fully, and should be addressed in future studies. The corrosive behaviour of Mg-alloys is influenced by the composition of the corrosive medium and the absence or presence of proteins [33]. In addition, the formation of new cells on stent surfaces act as local passive areas, which then cause local changes in the electrochemical conditions. These different corrosive environments could cause local anodic and cathodic sites, which could lead to locally accelerated corrosion rates resulting in pitting corrosion.

2.9 Issues for the development of biodegradable Mg stents, based on the principles of grain structure refinement

In reviewing the literature, the following areas have been identified as critical issues for the development of Mg degradable stents:

- **The relatively low corrosion resistance of Mg in the biological environment**

  Although the development of Mg-biodegradable stents can overcome some problems associated with the use of permanent implant, the actual clinical need for an implanted stent is for 6-12 months to allow full healing to occur in a blocked artery. Clinical trials on various Mg-alloys stents revealed that Mg can remain in the body and maintain mechanical integrity for ~ 12-18 weeks. The main issue with Mg-alloys is its relatively low corrosion resistance when in contact with the biological environment, especially in present of Cl^- ions. Hence, the complexity of interaction of pure Mg with various ions in the biological environment needs to be further clarified.

- **Control of the corrosion resistance of Mg**

  In order to extend the time period for dissolution and to achieve optimal temporary function of Mg stents, improved control over the corrosion rate of Mg is needed. Some surface engineering techniques such as applying coatings, and surface homogenisation by rapid solidification processes have been widely applied. However, there is an interest in investigating the effect of process parameters on the corrosion resistance of Mg when it comes in contact with physiological media.

- **Development of fabrication methods for Mg stents to achieve desired wall thicknesses**.

  In this context of the behaviour of Mg in the biological environment, there is need to develop suitable methods for the fabrication of Mg stents.

Conventional routes are usually used to fabricate stents from small diameter wires or narrow-walled tubes, laser cut into the desired pattern. However, these methods have limitation of producing stents with narrow-wall thicknesses in the range < 100 μm. There is an interest in exploring the use of nanostructured fabrication techniques to produce novel, narrow-walled Mg stents, with thickness of 10s micrometers. Hence, it becomes necessary to investigate the effect of microstructural feature within such stents on the corrosion behaviour of Mg.

Accordingly, several distinct themes related to the use of Mg in biodegradable stents will be addressed in this thesis:

- The application of magnetron sputtering techniques to obtain narrow-walled minitubes (wall thickness ∼ 100 μm) from pure Mg.

- To investigate the effect of post deposition thermal processing on the mechanical properties and corrosion resistance of pure Mg stents, as compared to commercially developed Mg-alloy stents.

- To investigate the effect of applied physical barriers, *i.e.* Al-O and Si-H based PVD coatings, on the corrosion performance of Mg.

- To investigate the enhancement of the self-passivation behaviour of Mg surfaces through rapid solidification processing.

- To investigate the effect of rapid solidification processing on surface morphology and the corrosion performance of Mg surfaces.

- To develop a detailed description of the corrosion behaviour of pure Mg, in physiological solution, in the presence of phosphate and chloride ions.

2.10 Summary

In this Chapter, general materials used in balloon expandable and self-expandable stent applications have been outlined. Degradable metals are identified as being desirable, to overcome the clinical complications of using permanent stents, such as restenosis and thrombosis. Mg and Mg-alloys are considered biocompatible and safely degrading materials, with the expectation of applications in peripheral and coronary artery angioplasty. The interactions between Mg and ions in aqueous environments result in the dissolution of Mg and the crystallisation of $Mg(OH)_2$ passivation layers. The presence of aggressive Cl^- ions in physiological media leads to the dissolution and breakdown of passivation films, enhancing corrosion in film free areas. The presence of PO_4^{3-} ions can enhance the passive behaviour of Mg surfaces if the hydroxide layer is stable. Accordingly, this thesis seeks to gain improved understanding of the corrosion mechanisms of pure Mg, at the fundamental level, in relation to its applicability for stent applications. A feasibility study on the use of nanostructuring technologies, *i.e.* magnetron sputtering, combined with post-deposition thermal treatments, for the manufacture and grain refinement of Mg minitubes, with the aim of improving mechanical and electrochemical properties, will be described. Further, controlling of corrosion rate of bulk Mg by the application of PVD coatings will be reported on, along with a detailed investigation of the corrosion mechanisms. An in depth discussion on the effects of rapid solidification processing, include electron beam and laser processing, on the morphology and corrosion resistance of Mg will also be presented. The main issues concerning the effects of grain refinement on the corrosion performance of Mg will be discussed.

CHAPTER 3 Experimental methodology

3.1 Introduction

The experimental procedures used for the preparation and characterisation of Mg samples investigated in this thesis are outlined in this Chapter. Table 3-1 provides an overview of the sample sets investigated, being a summary of the processes, samples and nature of each process development investigation. Sections 3.2 and 3.3 describe the source materials and the commercially available Mg stent investigated for benchmarking purposes; along with the magnetron sputtering conditions used to fabricate a minitube stent and the post fabrication thermal annealing treatments applied. Section 3.4 describes the sample handling, *i.e.* the polishing protocols for bulk Mg and the surface modification processes applied; including i) the physical vapour deposition (PVD) of Al-H and Si-H coatings; and ii) the near surface modification techniques of electron beam modification (EBM) and laser surface melting (LSM). Sections 3.5 & 3.6 describe the bases of the sample characterisation techniques and corrosion tests applied.

Table 3-1 Overview of sample sets investigated

Chapter / Section	Process	Sample	Investigation
Chapter 4	**Mg-stent fabrication**	Mg-alloy	Reference, commercially prototype Mg-alloy stent: Characterisation and corrosion testing
		Mg	PVD Mg stent fabrication - feasibility study
Chapter 5	**PVD Coating**	Al/Mg	PVD coated Al/Mg in Ar: As deposited and annealed
		Al-H/Mg	PVD coated Al/Mg in Ar/H_2 mixture: As deposited and annealed
		Si-H/Mg	PVD coated Si/Mg in Ar/H_2 mixture
Chapter 6-1	**EBM**	Mg	Electron beam surface modification as a function of cathode voltage and number of pulses
Chapter 6-2	**LSM**	Mg	Laser surface modification as a function of scan speed, power and spot size

3.2 Materials

The source materials and gases used in this study are summarised in Table 3-2.

Table 3-2 Materials, suppliers and purity

Material	Supplier Name	Form	Purity %
Mg	Testbourne Ltd, UK	Sheet	99.99
Mg	Testbourne Ltd, UK	Target	99.98
HA	Testbourne Ltd, UK	Target	-
Al	Boguan vacuum applied materials, China	Target	99.95
Si	Testbourne Ltd, UK	Target	99.999
CrO_3	Sigma Aldrich, UK	solution	-
PBS	Sigma Aldrich, UK	solution	-
Ar	BOC Pure shield, UK	Gas	99.998
H_2	BOC Pure shield, UK	Gas	99.99
N_2	BOC Pure shield, UK	Gas	99.998
Cover glass slip	Agar scientific, UK	Round glass No.5	-

3.3 Mg-stent fabrication

Stent sample codes and heat-treatment conditions applied are tabulated in Table 3-3.

Table 3-3 Samples code and heat-treatment conditions applied to the Mg stents

Sample code	Stent	Post deposition thermal treatment	
		T(°C)	gas
St-0	As-supplied stent	-	-
Tu-0		-	-
Tu-300		300	
Tu-400		400	He/H_2
Tu-450	Mg coating	450	
Tu-500		500	
Tu-550		550	Ar
Tu-600		600	

3.3.1 As-supplied Mg alloy stent

A commercially prototype Mg-alloy stent (Arterius Ltd, UK) was characterised, as a reference sample, being a benchmark for the in-house processed Mg minitubes produced by magnetron sputtering PVD.

3.3.2 Pure-Mg minitubes

3.3.2.1 Substrate preparation

Commercially available stainless steel spinal needles (Becton Dickinson-BD) were used as substrates. The needles, with outer diameter (OD) of 1.2 mm and length (L) of ~ 80 mm, were covered with a very thin sacrificial layer of silicone-based high vacuum grease (Dow Corning). This sacrificial layer was prepared by simple manual application of a fine layer of vacuum grease, with gloved fingers, whilst avoiding any uneven grease trails.

3.3.2.2 Pure Mg coating deposition
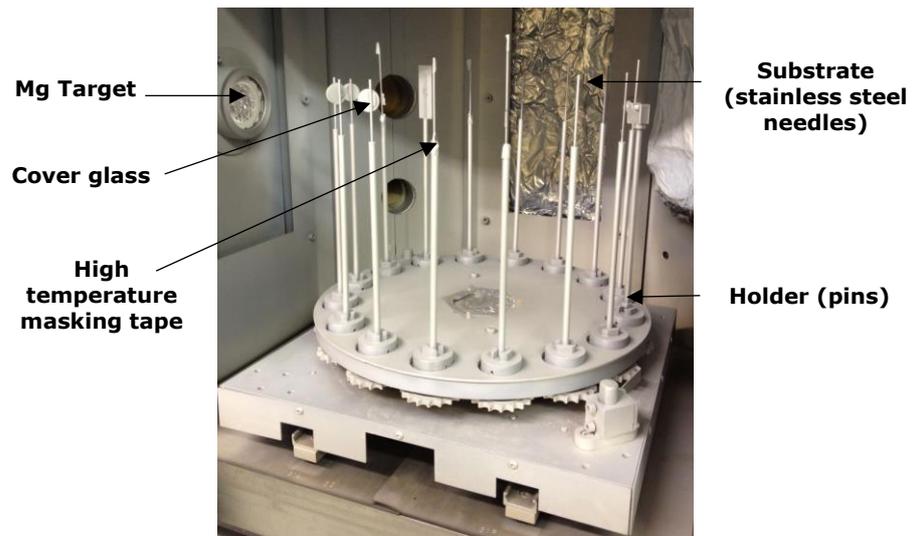
Figure 3-1 Sample stage and holders used for the fabrication of Mg-minitubes

Sequential Mg coatings were deposited using a PVD coating system (Teer Coatings Ltd. UDP 650/4). Two opposed circular magnetrons, upon which pure Mg targets (57 mm diameter; 3 mm thick) were mounted, were used to deposit Mg coatings onto stainless steel substrates. The samples were mounted on supporting pins, held on a twin axis jig connected to a rotary fixture on the chamber base, to facilitate even, 360° coating of the needle

samples held within the plasma fields of two magnetrons. Additional fixation, using Kapton™ high temperature masking tape, was employed to ensure full sample rotation (Figure 3-1).

Before deposition, the chamber was pumped to a base pressure of 2.0×10^{-5} torr, or better. When the base vacuum was achieved (typically after 1 - 1.5 h of pumping time), a controlled flow of Ar (50 sccm) was admitted into the chamber, such that the chamber pressure was maintained at $\sim 1 \times 10^{-3}$ torr. Sample rotation was set at 2 rpm and a DC current of 0.3 A was applied to both Mg targets, in order to strike a deposition plasma, resulting in a target voltage of $\sim$ 600 - 370 V DC, depending on the level of target depletion during deposition. Samples were rotated within the deposition plasma for a period of 8 h, which was judged to be a safe useful lifetime for the Mg targets, to avoid any breakthrough to the Cu magnetron beneath, which would result in sample contamination and possible damage to the magnetron. Each 8 h deposition phase added $\sim$ 9-10 μm of Mg thickness to the sample surface. Upon completion of the deposition phase, following a 30 minute cool down period, the chamber was vented, the twin axis sample stage removed and fresh Mg targets were mounted on both magnetrons; the sample stage was re-admitted to the chamber and pump-down recommenced prior to deposition of the next Mg layer. A total of 10 such Mg depositions were conducted in order to build up a minitube layer thickness $\sim$ 100 μm. Samples were then capped with a final layer of hydroxyapatite (HA), of $\sim$ 100 nm thicknesses, using a similar sized HA target, using radio frequency (RF) magnetron sputtering. Table 3-4 summarises the sputtering conditions for the Mg and HA coatings.

Table 3-4 Sputtering conditions applied to produce Mg minitubes

Sample	Current / A	Ar pressure / torr	Duration / min	Estimated thickness / μm
Mg	0.3	1.0×10^{-3}	480	$\sim$ 10
HA	RF-120	1.7×10^{-3}	30	$\sim$ 0.1

3.3.2.3 Post deposition heat-treatment

After sequential deposition of the Mg layers, the Mg minitubes were subjected to post deposition heat-treatments, up to 450°C for time up to 24 hours, using Sieverts apparatus (Figure 3-2), to promote densification of the Mg. The system consisted of a stainless steel sample cell, fitted into a ring heater (Watlow, UK), capable of temperature control stability of ± 1°C; a Druck PMP 4010 pressure transducer with accuracy of 0.04 %FS and 10 bar absolute pressure; a switchable manifold volume; He and H_2 gas inlet lines; and an oil-free diaphragm pump vacuum system; all sealed in an acrylic glass box equipped with heaters, two fans and thermocouples to maintain a constant temperature of 35 ± 0.5°C inside the glass box.
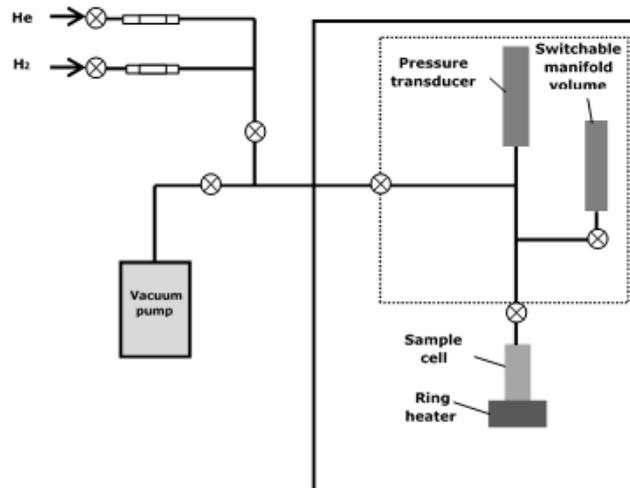
Figure 3-2 Key components of the Sieverts heat-treatment apparatus, adapted from [228].

The Mg minitubes were loaded into an Ar glove-box in a sealed sample cell which was then mounted in a Sieverts apparatus. Once the enclosure temperature had stabilised, the system was subjected to an initial leakage test by slowly filling the cell with 10 bar of He and monitoring the pressure for ~ 1 - 3 h. If a drop in gas pressure was observed, the joint between sample

cell and manifold was tightened and the gas rechecked until a steady pressure was maintained. The sample cell was then filled with H_2 gas, at first to 0.1 bar, followed by a flow of He to reach a total pressure of ≥ 1.0 bar. The system was heated to the specified temperature and held for 24 h. The samples were then allowed to cool to room temperature under an H_2/He atmosphere.

In order to encourage stronger grain regrowth, the Mg minitubes were annealed also up to 600°C using a tube furnace (Lenton Thermal Design, UK) under an Ar atmosphere. The Ar-filled sample cell was admitted into the tube furnace which was then ramped to the specified temperature, under an Ar flow of 1 L/minute, and held for 24 h. The samples were then allowed to cool naturally under the treatment atmosphere. Samples codes and post-treatment conditions are summarised in Table 3-3.

3.4 Bulk Mg surface modification

3.4.1 Mg substrate preparation

High purity Mg sheet was cut by wire erosion (Electric Discharge Machining (EDM)) into 20×20 mm^2 by 3 mm thick blocks, or 20 mm diameter by 3 mm thick discs. The samples were cleaned in acetone prior to mounting on a hot Cu holder covered with a thin layer of wax, and then left to cool to room temperature. The holder was fixed in a semi-automatic LaboPol-5 (Struers, Germany) polisher, with a rotation speed of 150 rpm and an applied force of 20 N. The Mg samples were ground on one surface using an MD1200 disc and then polished with diamond paste (down to 0.25 μm) to a mirror finish. The polished samples were cleaned after each grinding and polishing stage, using cotton balls wetted in IMS and acetone, followed by drying under a flow of

cold air. Care was taken not to use water in any of the grinding, polishing and cleaning stages. Table 3-5 summarises the established polishing protocol for the preparation of Mg surfaces.

Table 3-5 Mg surface preparation protocol

Grinding/polishing	FG	P1	P2	P3
Disc/cloth	MD1200piano	MD-Cloth	MD-Cloth	MD-Cloth
Abrasive type	Diamond	Diamond	Diamond	Diamond
Grit or grain size (μm)	P1200	6	1	0.25
Lubricant type	IMS	White spirit	White spirit	White spirit

3.4.2 Al and Si thin film deposition:
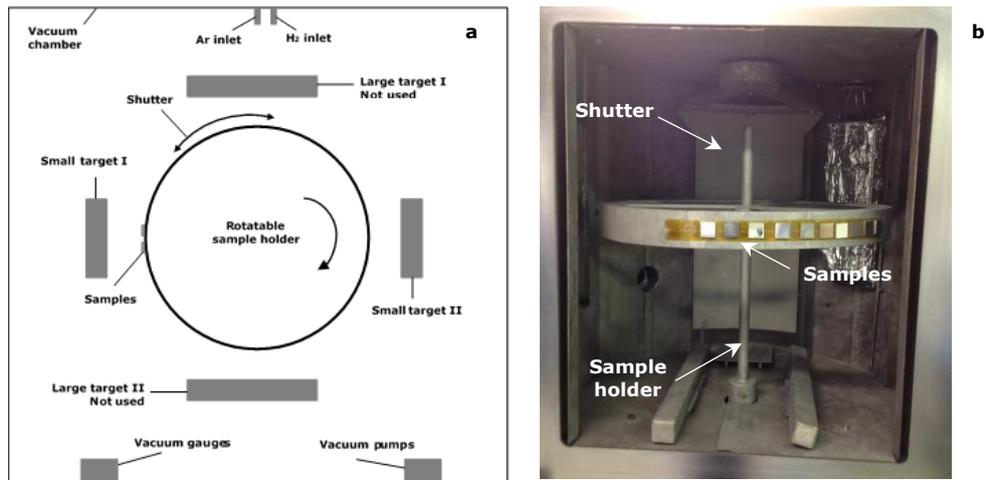
Figure 3-3 (a) Schematic diagram showing targets and sample arrangement inside the PVD system (adapted from [228]); and (b) Mg samples mounted on the sample holder, prior to PVD coating.

Table 3-6 Sample codes and coating process parameters.

Sample code	Coating	Mode/ Power / W	Chamber pressure/ torr	Bias / V	Gas	Flow rate / sccm	Estimated thickness / μm	Annealing Temp / °C
Al	Al	RF-150	1.4×10^{-3}	40	Ar	47.6	>1	-
Al$_{300}$								300
Al$_{450}$								450
AlH	Al	DC-629	1.6×10^{-3}	-	Ar/H$_2$	35.6 / 31.6	≈1	-
AlH$_{300}$								300
AlH$_{450}$								450
SiH	Si	RF-100	3.0×10^{-3}	-	Ar/H$_2$	34.9 / 28	≈1	-

Coatings were deposited using a commercial-scale, closed-field, unbalanced, magnetron Physical Vapour Deposition (PVD) system (Teer Coatings Ltd. UDP 650/4, UK). The system (Figure 3-3 (a)) was equipped with two direct current (DC) radio frequency (RF) power supplies with a pulsed DC bias supply. The inner chamber was ~ 450 mm in diameter and ~ 450 mm high. The external wall of the chamber comprised a double layer stainless steel plate, with a gap to allow the flow of cooled water. The front door of the system allowed for convenient sample loading. The system was equipped with two opposing circular magnetrons; holding sputtering targets of 57 mm diameter, and other two opposing planar magnetrons for 175×380 mm sized targets. In this study, only one circular magnetron was used to deposit single layer coatings, while the others were covered with Al foil to avoid target contamination.

Polished Mg samples and cover glass slips were mounted onto the circular sample stage using Kapton[TM] high temperature masking tape. The samples were statically positioned in front of the target, at a working distance of 6 cm. Figure 3-3 (b) shows the Mg substrates arranged inside the PVD chamber. Before deposition, the chamber pressure was reduced to a base pressure of 1×10^{-5} torr, using a rotary-backed, diffusion pump vacuum system. Vacuum valve operation during pump-down was controlled automatically by the UDP-650 system computer. Once base vacuum was achieved (~ 30 minutes pumping time), a controlled flow of Ar/H_2 was admitted into the chamber, via a feedback control system (MKS Mass-Flo controller and MKS capacitive baratron), such that the chamber pressure was maintained at ~ 1×10^{-3} torr. A shutter was positioned in front of the Mg substrates while the target was pre-sputtered for ~ 10 minutes to remove surface contamination and oxide. Single layer coatings were deposited from the circular target under the sputtering conditions summarised in Table 3-6.

3.4.2.1 Post-deposition thermal oxidation

Post-deposition, thermal oxidation of the Al thin films was performed using a tube furnace (Lenton Thermal Design, UK) in open air atmosphere. The furnace temperature was calibrated for the range 300 - 650°C using a thermocouple. Samples were left to cool naturally (Table 3-7).

Table 3-7 Post deposition heat-treatment conditions of the Al coatings

Sample code	Heating Temp. / °C	Heating rate / °C.min^{-1}	Heating time / h
Al$_{300}$	300	10	5
Al$_{450}$	450	10	2
Al-H$_{300}$	300	20	5
Al-H$_{450}$	450	20	2

3.4.3 Large area electron beam (LAEB) surface modification

A schematic for the EB irradiation process is shown in Figure 3-4. The following principles are provided from literature [193] [229] [230] [231] [232]. Before electron generation, the vacuum chamber was filled within Ar gas at a pressure of 0.05 Pa. After the Ar pressure was reached, a magnetic field was generated through a solenoid coil sited outside the chamber. Once the magnetic field reached maximum intensity, a voltage of 5 kV was applied to the ring anode placed in the middle of the chamber. This high anode voltage extracted electrons from the cathode, and the electrons moved spirally to the anode around the magnetic field flux lines. During travel, the electrons colloided with Ar atoms in the chamber leading to ionisation of the Ar atoms and the generation of a plasma around the anode. After the concentration of generated plasma reached a maximum, an accelerating voltage (maximum of 40 kV) was applied to the cathode. Due to the high cathode voltage, the electrons were accelerated by the high electric field. The accelerated electrons formed a beam with high intensity directed through the

anode plasma to the collector cathode, where the workpiece, *i.e.* specimen, was mounted.
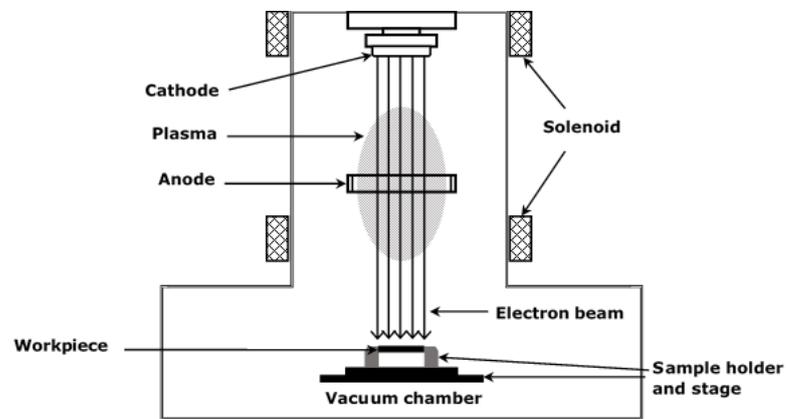
Figure 3-4 Schematic illustration of an Sodick PF32A LAEB machine, adapted from [193].
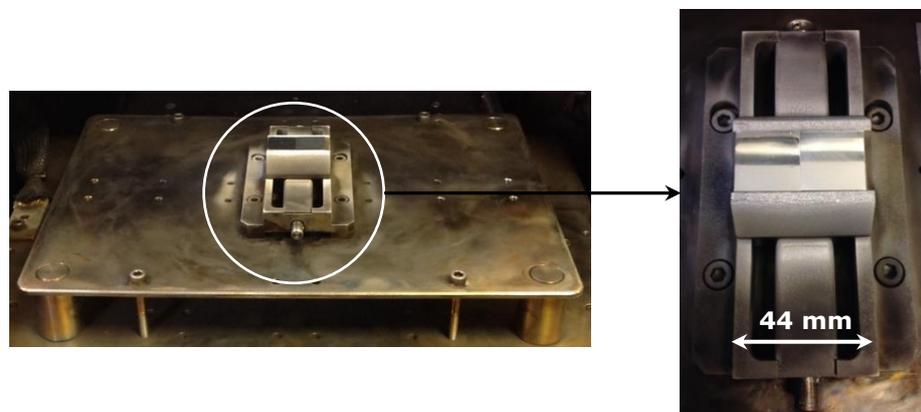
Figure 3-5 Sample stage and holder for the Sodick PF32A LAEB machine.

Accordingly, a Sodick PF32A LAEB machine was used to irradiate Mg sample surfaces (Figure 3-4).

Table 3-8 LAEB sample codes and process parameters

Sample code	Cathode voltage / kV	Number of shots
EB15-1	15	1
EB15-5		5
EB15-20		20
EB25-1	25	1
EB25-5		5
EB25-20		20
EB35-1	35	1
EB35-5		5
EB35-20		20
EB40-1	40	1
EB40-5		5
EB40-20		20
EB40-50		50

Table 3-8 summarises the Mg sample sets investigated by LAEB modification. Ar gas at a pressure of 0.05 Pa was used to build up the plasma required for electron generation. The Ar was supplied from gas cylinders, at pressures of 0.35 MPa. The electron beam diameter was 60 mm, with a pulse time of 2–3 μs, pulse interval of 11 s and energy density of 20 J/cm^2. Two polished Mg samples were clamped onto a sliding sample stage (Figure 3-5) and the surfaces levelled within the sample holder jaws, leaving a 10 mm gap between the Mg surface and holder base. The distance between the electron gun and sample surface was 300 mm, while machine constant anode and solenoid voltages were established at 5.0 kV and 1.5 kV, respectively. In order to establish the effect of irradiation conditions on the Mg surfaces, various cathode voltages and number of pulses were utilised.

3.4.4 Laser surface melting (LSM) modification
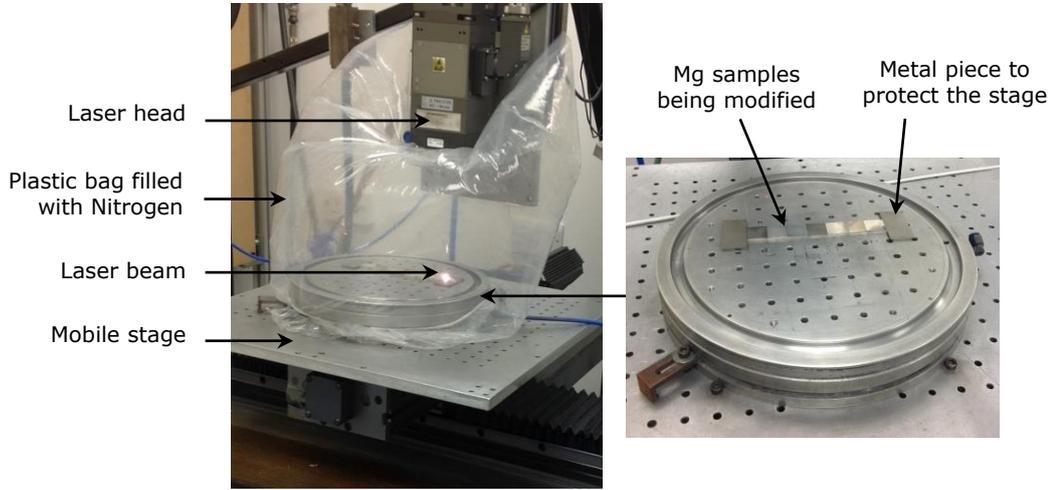
Figure 3-6 LSM processing arrangement.

The samples code and process variables used in the LSM study are summarised in Table 3-9.

Table 3-9 LSM sample codes and processing parameters

Sample code	Scan speed / mm/min	Power / W	Spot size / mm
L3-375	3600	375	2
L3-450		450	
L3-525		525	
L3-600		600	
L4-375	4500	375	2
L4-450		450	
L4-525		525	
L4-600		600	
L5-375	5400	375	2
L5-450		450	
L5-525		525	
L5-600		600	
L5*-375	5400	375	3
L5*-450		450	
L5*-525		525	
L5*-600		600	
L6-1500	6300	1500	3

A continuous laser beam generated by an YLR-2000SM ytterbium fibre laser (IPG, GmbH Germany) with wavelength of 1070 nm and Gaussian beam

profile was used for laser surface treatment. A circular laser spot, measuring 952 μm at the 192 mm focal position, was produced from a 600 μm delivery fibre, with an output power of up to 2000 W. The laser head was fixed at 10 mm and 20 mm positions below the focal point, in order to produce 2 mm and 3 mm beam spot sizes, respectively. The samples were clamped to an X-Y mobile base sealed by a plastic bag, filled with a continuous purge of Ar gas. Multi-track profiles were scanned over the polished samples, using various powers, scan speeds and spot sizes. Figure 3-6 shows the laser processing arrangement.

3.5 Materials characterisation

A range of characterisation techniques were applied to appraise surface topography, chemistry, structure and mechanical properties of the various sample sets; *i.e.* scanning electron microscopy (SEM), energy dispersive x-ray spectroscopy (EDS), X-ray diffractometry (XRD), X-ray photoelectron spectroscopy (XPS), Fourier transform infrared spectroscopy (FTIR) and microhardness (Hv) testing. Additionally, corrosion behaviours of the as-prepared and modified surfaces were investigated, using both mass loss and potentiodynamic corrosion testing techniques.

3.5.1 Metallography

Samples were sectioned using a Brilliant 220 cutter (Germany) and mounted in Struers Epofix cold resin which was left to cure for 12 h. After polishing, samples were etched using acetic glycol (20 mL acetic acid, 1 mL HNO_3, 60 mL ethylene glycol and 20 mL H_2O). Samples were submerged in the etch for 10 s and then rinsed in flowing water, before drying in hot air.

3.5.2 Optical microscopy

Sample surfaces in planar and cross-sectional geometries were examined using a Nikon Eclipse LV100ND (Nikon, Japan) optical microscope, for surface macrostructure and microstructure observations.

3.5.3 Scanning electron microscopy (SEM) and energy dispersive X-ray spectroscopy (EDS)

The interaction of high energy electrons with a material results in a range of signals such as secondary electrons (SE), backscattered electrons (BSE) and characteristic X-rays, Figure 3-7 (a,b).
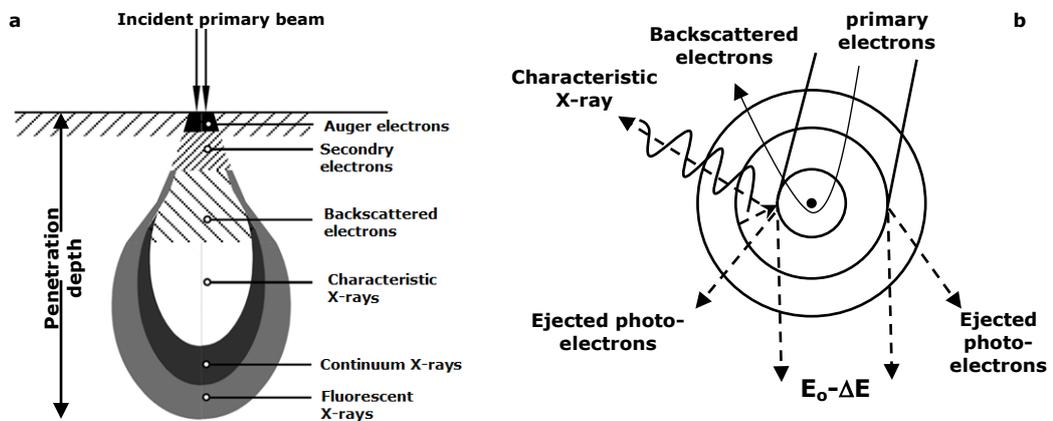
Figure 3-7 (a) Volume of interaction of incident electron beam with material; (b) the origin of backscattered electrons (BSE) and characteristic X-rays.

Secondary electrons SE are generated when inelastic collisions of incident electrons with atoms result in loosely bound electrons being detached, leaving ionised positively charged atoms [233] [234]. The dislodged electrons have

kinetic energy $<$ 50 eV and can be captured by closeby atoms or may overcome the surface barrier energy to escape from the near material surface as secondary electrons [233] [234]. Hence, SEs provide information on surface topography. Backscattered electrons are generated from elastic interactions of incident electrons upon collision with material atomic nuclei, resulting in the backscattering of electrons by $\sim$ 180° [233]. Higher proportions of electrons reflect larger atomic numbers, giving higher brightness levels for heavier elements (locally averaged) in the image. Hence, BSE can provide information on sample composition [235]. A high energy incident electron can also induce the emission of a core shell electron (photo-ionisation). The exited atom can energy relax by filling the inner shell vacancy with an electron from an outer shell orbital, leading to the emission of a characteristic X-ray, defined by the energy difference between the two electron states and hence atomic number. Consequently, sample compositions can be investigated and quantified using EDS.

In this work, processed samples were investigated using FEI XL30 SEM and FEGSEM instruments (15 kV accelerating voltage; spot size 4; working distance 10 mm; SE and BSE operational modes). For samples mounted in resin, the examined surfaces were coated with C or Pt, while other sample surfaces were surrounded with Al tape during SEM analyses. Compositional analyses were performed using an Oxford Instruments EDS system with INCA X-ray microanalysis software.

3.5.4 X-ray diffractometry (XRD)

The scattering of incident X-rays following interaction with atomic outer shell electrons leads to a number of reconstructed intensities in very precise

directions depending on material crystal structure. The geometric criterion for constructive interference (Figure 3-8) is given by Bragg's Law:

$$n\lambda = 2d \sin\theta \qquad\qquad \text{Eq 3-1}$$

Where n is an integer; λ is the X-ray wavelength; d is the lattice spacing; and θ is the diffraction angle.
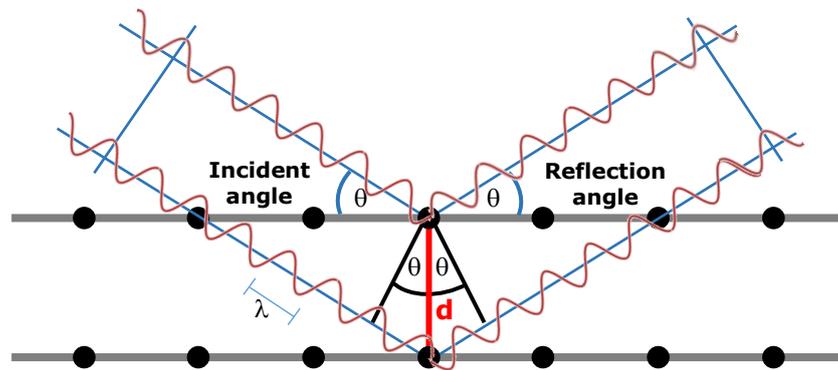
Figure 3-8 Schematic illustration of constructive interference of scattered waves (Bragg diffraction: $n\lambda = 2d \sin\theta$) [236]

Characteristic diffraction patterns for different sample phases may be obtained by plotting intensity as a function of scattering angle (2θ). In this work, XRD patterns for all samples were collected using a D8 Advance X-ray diffractometer (Bruker, German) using a CuKα (λ=1.54060Å) X-ray source run at 40 keV and 35 mA, at room temperature. For the case of EBM, LSM and surface coatings, XRD analyses were performed using XRD mode of operation, fitted with 0.6 mm incidence divergence slit, at an incident angle of 1°, step interval of 0.04° and dwell time of 32 s per step. XRD patterns for the Mg-reference stent and Mg minitubes in their as-deposited and annealed states were collected using conventional $\theta/2\theta$ geometry from 20° to 70°, with step size of 0.01° and dwell time of 4 s per step.

The size of crystallites within the PVD coatings was estimated by applying Scherrer's equation:

$$\boldsymbol{\beta_{hkl}} = \frac{0.9\,\lambda}{L_{hkl}\cos\theta_{hkl}} \qquad\qquad \text{Eq 3-2}$$

Where β_{hkl} is the peak broadening width at half maximum intensity (*i.e.* full width at half maximum (FWHM)) in radians; λ is the wavelength of the XRD source; and L_{hkl} is the crystallite size. Peak broadening β_{hkl} comprises contributions from crystallite size *(β_{size})*, instrumentation *(β_{inst})* and strain *(β_{strain},* considered negligible).

3.5.5 X-ray photoelectron spectroscopy (XPS)

XPS is a surface-sensitive technique used for chemical, compositional and electronic state analysis. A sample surface is irradiated in an ultra-high vacuum environment with monochromatic X-rays, usually Al Kα(1486.6eV) or Mg Kα(1253.6 eV). An interaction between an X-ray photon and a core shell electron results in photoelectron emission with kinetic energy (K.E) determined experimentally and used to calculate the characteristic elemental binding energy (Figure 3-9). A spectrum consisting of a dispersion of photoelectron peak intensities may be used to identify surface elements. The chemical state of elements at the surface may be determined from high spectral resolution data and careful measurement of shifts in elemental binding energies.
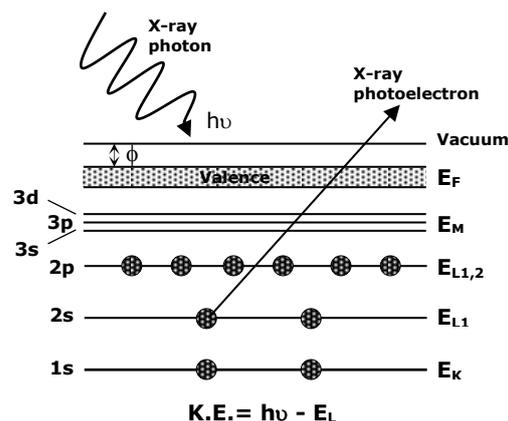
Figure 3-9 Emission of a photoelectron; $h\upsilon$ is the X-ray photon energy and E_L is the binding energy of the photoelectron from an inner core shel [237]

In this study, a VG Scientific ESCALAB 2 with a Kratos AXISULTRA X-ray photoelectron spectrometer, equipped with a non-monochromatic Al Kα X-ray source, was used to analyse the chemical composition of coating surfaces. The X-ray source was held at an anode potential of 12 kV with the chamber vacuum maintained at $< 10^{-9}$ mbar. Survey spectra were collected across a binding energy range of 0-1100 eV, using a pass energy of 50 eV, a dwell time of 0.2 s and step size of 1 eV. High resolution scans for elements of interest were recorded using a pass energy of 20 eV, a dwell time of 0.4 s and a step size of 0.4 eV. All spectra were analysed and charge calibrated using the CasaXPS program. Chemical bonding states and compositional data for the coatings were obtained by subtracting the background and fitting peak components within each peak envelope and then comparing positions and profiles to known reference standards.

3.5.6 Fourier transform infrared spectroscopy (FTIR)

Infrared (IR) spectroscopy utilises electromagnetic radiation (EMR) to detect and identify covalent bonds within a material. An IR spectrum is obtained when a fraction of the incident radiation is absorbed at specific energy [238].

The absorption of EMR in the IR region relates to molecular vibrations. The energy of each peak present in an IR spectrum is associated with the vibrational frequency of functional groups in the sample molecules [238]. Each functional group in the molecule absorbs IR radiation at particular energies or frequencies [238]. The modes of vibration can be stretching, *i.e.* change in bond length; or bending, *i.e.* changing in bond angle [239]. An FTIR spectrometer uses an interferometer to collect and measure IR frequencies, to produce an 'interferogram' which is converted into a wavelength against absorbance/ transmittance spectrum [238]. In this study, IR spectra were collected using a Tensor FTIR spectrometer (Bruker, German) and the data analysed using *OPUS* software.

3.5.7 Surface Roughness

A Photomap 3D Wave light interferometer (Fogale nanotech, USA), with a spatial resolution of 1 μm, was used to measure surface roughness. An average of three measurements was made, from the middle and edge of each sample.

3.5.8 Microhardness testing

Vickers microhardness of the Mg-minitubes was determined using a LECO microhardness testing machine (Buehler, Germany), at a load of 10 gf and force dwell time of 15 s. All hardness measurements were performed on polished sample cross-sections. The average values of more than twelve indents were calculated from the load value (P) and the area of tip contact (A), along with their standard error.

$$H_V = \frac{P_{max}}{A} \qquad \text{Eq 3-3}$$

3.6 Corrosion testing

In this study, the corrosion behaviour of materials was studied through mass loss and potentiodynamic polarization testing.

3.6.1 Mass loss testing

The corrosion resistance of a modified Mg surface was tested and compared with as-prepared materials. The tests were performed in accordance to ASTM standard G31 in PBS solution at $37\pm1°C$ [101]. Only modified surfaces were exposed to PBS, while other surfaces were painted with lacquer. The development of corrosion was examined over exposure times of 1, 3, 5 and 7 days. The samples were then recovered; DI-water rinsed and investigated using optical microscopy, SEM and EDS. Corrosion products were removed by immersion of the samples in 20 vol% chromic acid for 10 minutes at $60°C$, prior to the measurement of weight loss.

3.6.2 Potentiodynamic polarisation testing

Cyclic testing was used to investigate the corrosion behaviour of samples, by studying their anodic and cathodic electrochemical activity, The tests were performed in accordance to ASTM standard F2129 [240] . All tests were performed in a system consisting of three electrode cells; a reference saturated calomel electrode (SCE), a counter electrode of 1 cm^2 Pt sheet, and a working electrode of the surface modified sample being tested. The test solution was 700 mL N_2 aerated PBS at $37°C$.

An ACM potentiostat (Grill 8, UK), accompanied by sequencer software, was used to measure the electrochemical activity of EM modified, LSM modified and PVD coated Mg surfaces. The corrosion behaviour of as-deposited and

heat treated Mg-minitubes was investigated also using a potentiostat (VoltaLab PGZ 100, UK). Open circuit potential (OCP) scans were collected for 1 h after a minute settlement time, followed by potentiodynamic polarization tests. Anodic and cathodic scans were conducted from a potential of -200 mV to +500 mV, with respect to sample OCP, using a sweep rate of 5 mV/minute. After each polarization test, samples were rinsed under a flow of deionised water, dried and the corrosion products examined using SEM/EDS and XRD. Corrosion test measurements were made for both as-prepared and modified surfaces.

3.6.3 Sample preparation

EB modified, LSM modified and PVD coated Mg surfaces were prepared in the form of working electrodes by clamping one sample edge with a metallic clip. The sample-clip attachment area was sealed by rapid settling, waterproof resistant glue (Araldite, UK), while the clip main body was shielded with a plastic cover and connected to the potentiostat through an isolated copper wire. Further protection from the test solution was obtained by painting the sample back, edges and the attached clip with a stop-off lacquer, leaving a minimum exposed area of 1.5 cm^2. Figure 3-10 (a,b) show a schematic diagram and a photograph of the working electrodes used.
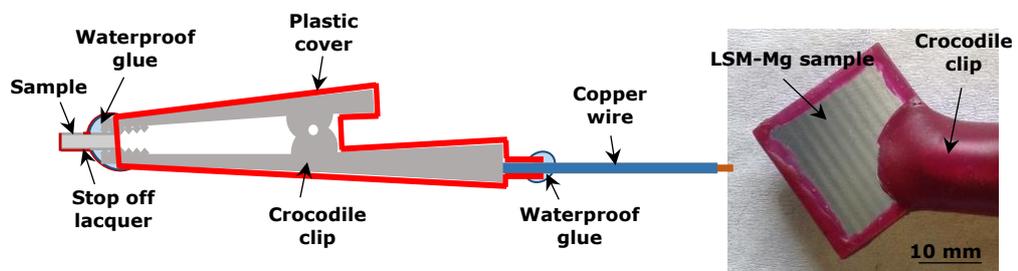
Figure 3-10 (a) Schematic diagram of LSM, EBM and PVD coating working electrodes; and (b) photograph of an LSM working electrode.
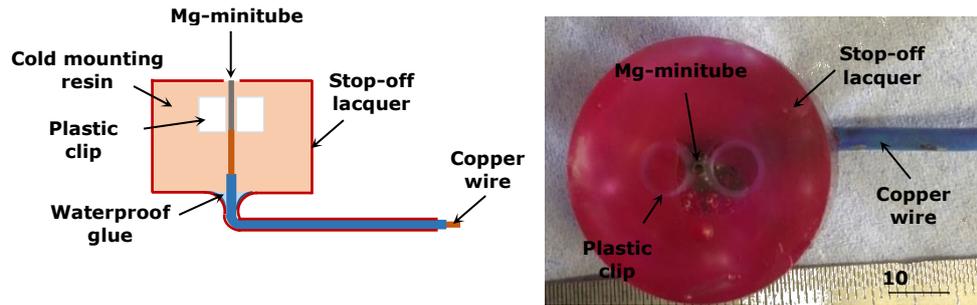
Figure 3-11 (a) Schematic diagram; and (b) photograph of an Mg minitube working electrode.

Corrosion tests for the as-deposited and annealed Mg-minitubes were performed on the samples in cross-section geometry, due to their brittle nature. The minitubes were mounted in a cold resin and polished using the protocol described above. The samples were connected electrically to the potentiostat via a Cu wire, attached to the sample back. Figure 3-11 (a,b) show a schematic diagram and photograph of this type of working electrode.

3.7 Summary

The experimental procedures used for the fabrication of Mg minitubes, and Mg surface modification and characterisation have been presented. A commercial scale, close-field, unbalanced magnetron sputtering PVD system was used to fabricate novel Mg minitubes for stent applications. Stainless steel spinal needles were used as substrates to deposit 10 sequential layers from pure Mg targets with a capping layer of HA. After the deposition process, the Mg minitubes were subjected to post deposition annealing, up to 450°C, under He/H$_2$ conditions and up to 600°C under Ar atmosphere.

Bulk pure Mg samples were used as templates for the investigation of surface modification processes. Al or Si based coatings were deposited using PVD on

Mg surfaces under Ar/or H_2 sputtering gas, and subjected to annealing to obtained an oxide layer.

The rapid solidification processing (RSP) techniques of EB and LSM were applied to Mg surfaces for the purpose of near surface modification of the Mg microstructure. The irradiation treatments were performed under different conditions of cathode voltage and number of pulses for EB, and various scanning speeds and irradiation power for LSM.

A range of complementary topographical, chemical and structural characterisation techniques were used to examine the minitubes, and modified Mg surfaces. Optical microscopy and SEM imaging were used to apprise surface topography, while XRD allowed for bulk and surface structural characterisation. EDX and XPS provided information on the composition of Mg samples and their modified surfaces. The covalent bonding of Si-H coatings was appraised by FTIR.

The corrosion performance of all samples was investigated under PBS test solution at 37°C, using potentiodynamic polarization for all samples, with further immersion testing conducted for Si-H coatings, and EB and LSM modified Mg surfaces.

CHAPTER 4 Mg-stent fabrication

4.1 Introduction

This Chapter presents a feasibility study of Mg-minitube fabrication, produced by PVD, as a route towards the development of a biodegradable minitube stent. This would be a commercial potential route to stent manufacture rather than normal extrusion methods [241], followed by laser cutting of the stent for a particular geometry [50]. The manufacturing cost of laser cut tubes is of the order of a few pounds while PVD would be 10s of pounds per stent. However, the major cost of such an implant is the quality control, validation, sterilisation and packaging, with a likely retail cost of hundreds of pounds, thus the difference in manufacturing method cost is not crucial. The advantages PVD offer are: (1) to be able to be deposited in a controlled manner, allowing for fine control of thickness and geometry (with an appropriate template); (2) the capability of blending in other elements during deposition rather than from the melt provides for graded structures; and (3) the capability of providing multilayered structures which could be utilised to modify the mechanical and in particular the corrosion behaviour of the final product. The work presented in this Chapter starts with an investigation of the structure and mechanical properties of a prototype commercial Mg-alloy stent produced by extrusion and laser cutting, as a reference material. Then the feasibility of fabricating Mg narrow-walled tubes (Mg minitubes), for stent applications, is explored using magnetron sputtering of pure Mg onto a simple tubular stainless steel pin with a silicone oil interface to allow stent removal, as detailed in Chapter 3. Hence, this study includes a detailed characterisation of the as-deposited structure, followed by the effects of post-deposition heat-treatments on the grain structure, using range of characterisation techniques, *i.e.* SEM/EDS, XRD and hardness testing. In

94

addition, the corrosion behaviours of the respective structures, conducted using potentiodynamic polarization tests, were examined and compared. Table 4-1 summarise the samples sets investigated in this section.

Table 4-1 Summary of sample sets investigated during the feasibility study of Mg-stent fabrication: including sample codes, post treatment processing conditions and Mg stent and minitube corrosion rates determined by potentiodynamic corrosion test

Sample	Stent phase	Post thermal treatment		Corrosion rate
		T(°C)	Gas	mm/year
St-0	As-supplied stent	-	-	3.30
Tu-0		-	-	270
Tu-300		300		45.2
Tu-400		400	He/H₂	67.1
Tu-450	Mg coating	450		17.3
Tu-500		500		4.57
Tu-550		550	Ar	3.65
Tu-600		600		16.0

4.2 As-supplied Mg-alloy stent

A Dy-Mg alloy commercial prototype stent, made from extruded tube and laser cut into the desired pattern, was supplied by Arterius Ltd. Morphological investigations of the as-supplied stent are presented in following section. The corrodibility of the stent in aerated PBS was appraised using potentiodynamic polarization corrosion tests, as described in section 4.2.2.

4.2.1 Characterisation of commercial prototype Mg-alloy stent

4.2.1.1 Optical and electron microscopy

OM and SEM were used to investigate the 3D physical form, geometry and structure of the prototype Mg-alloy stent. The OM image of Figure 4-1(a) illustrates the designed shape and dimension of a tubular slotted stent, formed by laser cutting from a single tube of Mg-alloy. Complementary SE images (Figure 4-1 (b,c)) showed that the Mg-stent was designed with a

helical structure, exhibiting a zigzag pattern with links between the loops. The stent had length of 14 mm, an outer diameter of 1.78 mm prior to expansion, a wall thickness of 152.2 ± 0.5 μm, and a strut width of 130.4 ± 0.4 μm. The overall stent structure had 14 loops with 8 zigzags in each loop.
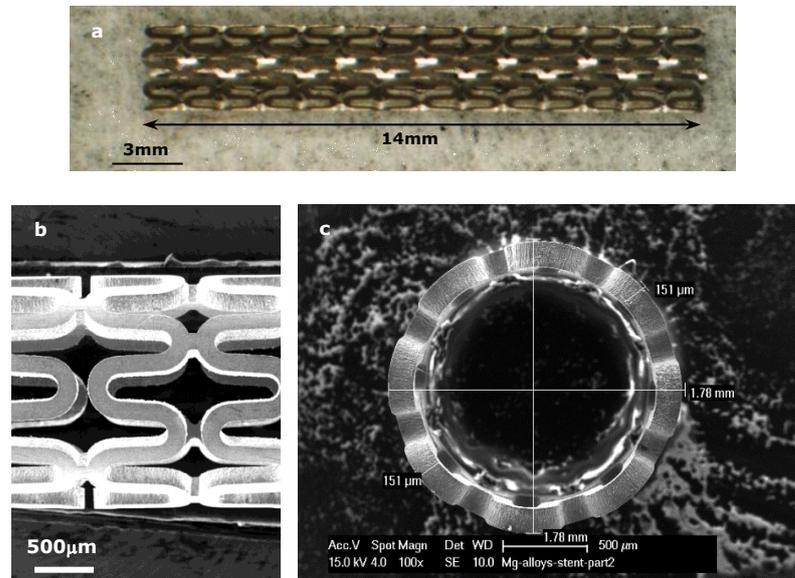
Figure 4-1 Images of a commercial prototype Mg-alloy stent: (a) OM image of laser-cut stent made from Mg-alloy tube; (b) SE image of stent zigzag loops before expansion; and (c) SE image of circular end showing dimensions of the stent.

EDS data from the as-received stent surface in plan-view orientation (Figure 4-2a) indicated the present of Magnesium (Mg), Dysprosium (Dy) and Oxygen as the main constituent elements, in addition to a very low amount of Barium (Ba) and Neodymium (Nd). The stent cross-section was then etched in acetic glycol, prior to further chemical analysis in cross-sectional orientation. SE images and corresponding EDS data (Figure 4-2(b)) revealed that the stent material was not a uniform alloy.

96

Z/at%	Mg	Dy	O	C	Br	Nd
A	66.83	2.99	28.84	-	0.42	0.83
B	40.08	34.68	25.24	-	-	-
C	66.66	0.85	4.58	27.90	-	-
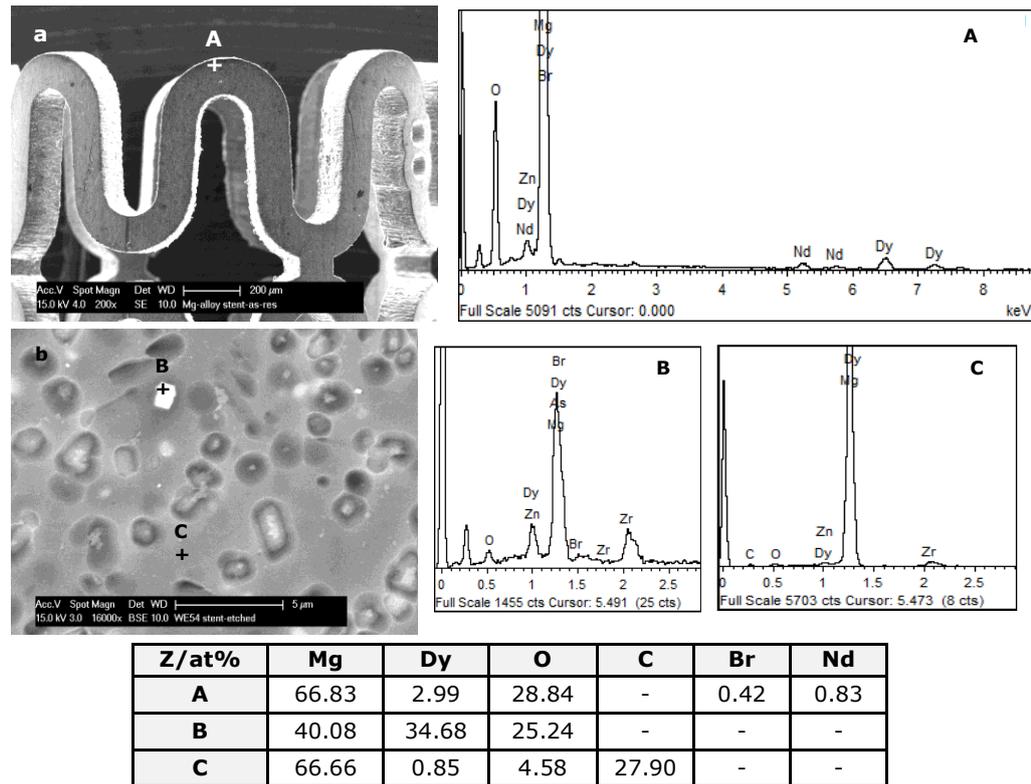
Figure 4-2 EDS analysis of a commercial Mg-alloy stent: (a) as-received surface in plan-view orientation; (b) surface etched in acetic glycol, in cross-sectional orientation.

4.2.1.2 XRD and hardness measurements

The corresponding XRD pattern of for the as-received stent demonstrated the presence of diffraction peaks consistent with the polycrystalline Mg phase (Figure 4-3), with no evidence of a shift of $2\theta°$ diffraction peaks to higher or lower angles. In addition, peaks that matched the crystal structure of Dysprosium zirconium oxide ($Dy_{0.5}Zr_{0.5}O_{1.75}$), with faced centred cubic (FCC) structure and Fm3m space group, were also detected. The Scherrer equation (Section 3.3.4), as applied to the FWHM of the Mg 0002 diffraction peaks indicated an average crystal size of 83 ± 2 nm. The diffraction peaks for $Dy_{0.5}Zr_{0.5}O_{1.75}$ had very low intensity and were not able to provide adequate FWHM values. A broad peak at $2\theta = 25.5°$ was detected also, but could not be assigned.

Vickers micro-hardness of the stent struts, viewed in cross-section, was determined to be 86.3 ± 2.5 HV/10.
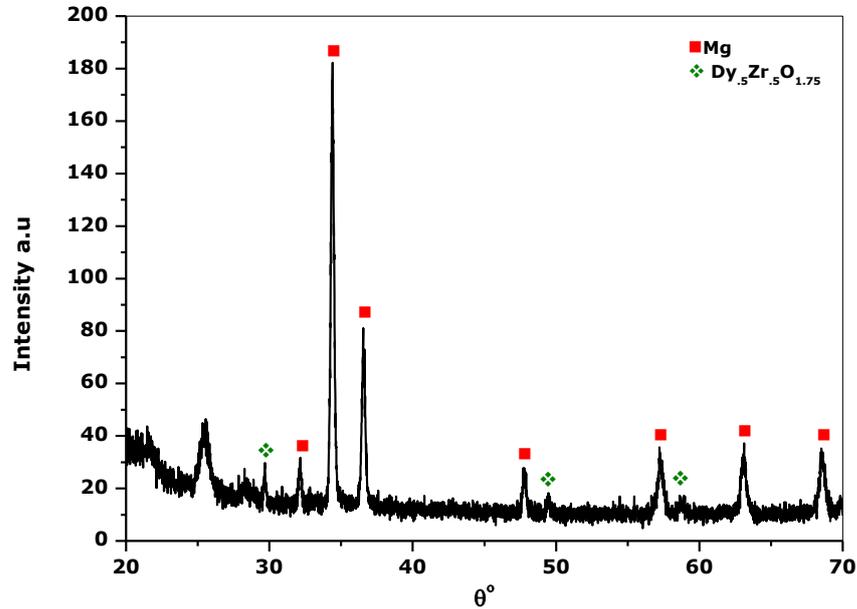
Figure 4-3 XRD pattern from a commercial prototype Mg-alloy stent. Showing strong diffraction peaks for Mg and lower intensities matching $Dy_{0.5}Zr_{0.5}O_{1.75}$ (data card number: 01-078-1293)

4.2.2 Corrosion behaviour of the Mg-stent

A complete potentiodynamic polarization test to find the corrosion potential, current density, and active-passive regions of the Mg stent was performed in 125 mL of PBS in a corrosion cell at 37°C. The OCP behaviour of the Mg-alloy stent is shown in Figure 4-4(a) and was recorded for one hour, prior to the electrochemical test. Figure 4-4(b) illustrates the polarization curve for the stent with an indication of the characteristic electrochemical parameters. It can be seen that when the polarization potential was below the *Flade potential* (E_F) of -1.39 V, the Mg-stent exhibited anodic dissolution at a rate of 3.30 ± 0.02 mm/year, at a corrosion potential E_{corr} of -1.57 V. Once the polarization potential passed the E_F value, the anodic current density decreased gradually as the stent surface underwent passivation. In the passive region from E_F of -1.39 V to -1.10 V, the polarization potential

reached the limited maximum value, before the onset of the trans-passive region. The results extracted from the OCP and polarization curve for this Mg-stent are summarized in Table 4-2.
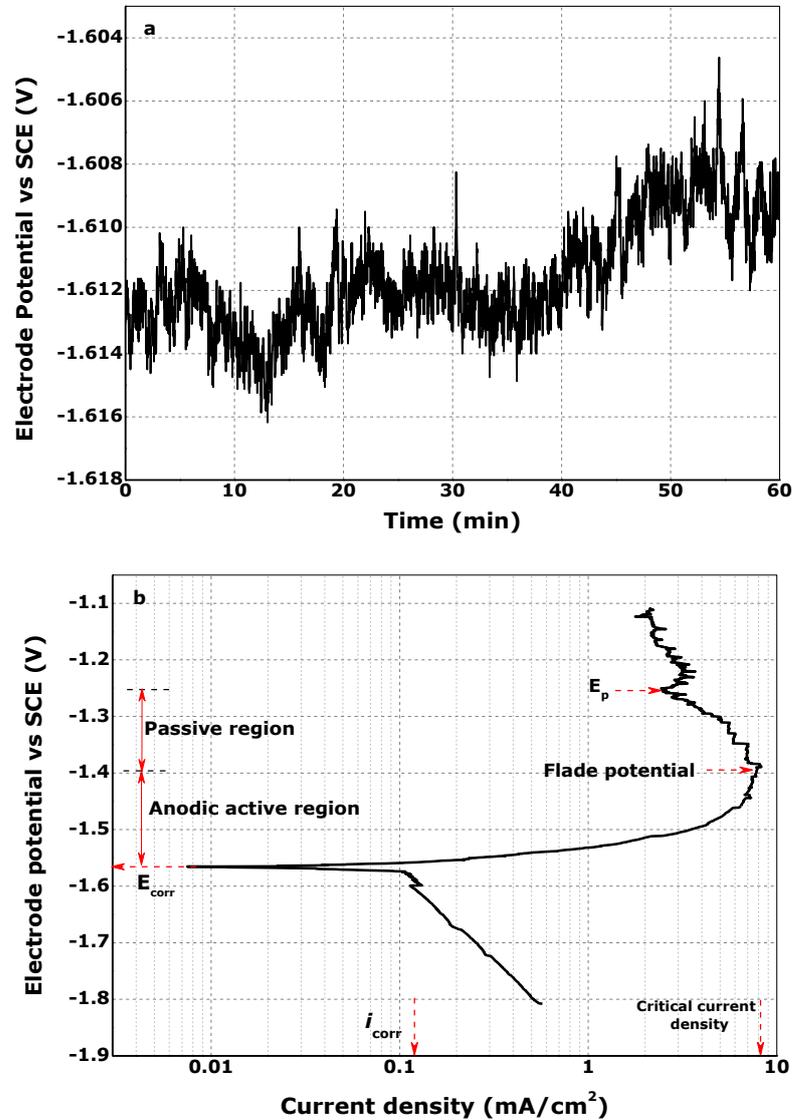
Figure 4-4 (a) OCP; and (b) Potentiodynamic polarization curves for the commercial prototype Mg-alloy stent, in PBS at 37°C.

Table 4-2 Characteristic corrosion parameters of the as-received Mg-alloy stent (potentiodynamic polarization test, in deaerated PBS at 37°C).

OCP / V	E_{corr} / V	i_{corr} / mA/cm²	CR / mm/year	MR / g/m²d	E_F / mV	E_p / mV
-1.60	-1.57	0.12±0.01	3.30±0.02	17.03 ±1	-1.38	-1.25

The formation of oxide, hydroxide and phosphate corrosion products on the Mg-stent surface can inhibit anodic reaction through passivation. Figure 4-5(a-b) presents a BSE image of the Mg-alloy stent after the potentodynamic polarization test in aerated PBS (from -250 mV to 500 mV relative to OCP). It can be seen that stent surface suffered severe corrosion and broke into small fragments. The high magnification BSE image of Figure 4-5(b) shows a thick layer of corrosion product covering the stent struts. EDS analysis after corrosion testing revealed the degradation products to comprise mainly Mg, O, P, Ca, Na and Cl, as shown in Figure 4-5 (Table inset). A high amount of O in the degradation layer may be attributed to hydroxide and phosphate (PO_4) components, in the form of $Mg(OH)_2$ and hydroxyapatite, respectively. There was no evidence of any interaction between Dysprosium or other elements and the PBS media.

Element	Composition / at.%
O	73.7
Na	1.0
Mg	13.6
P	9.2
Cl	0.6
Ca	2.0
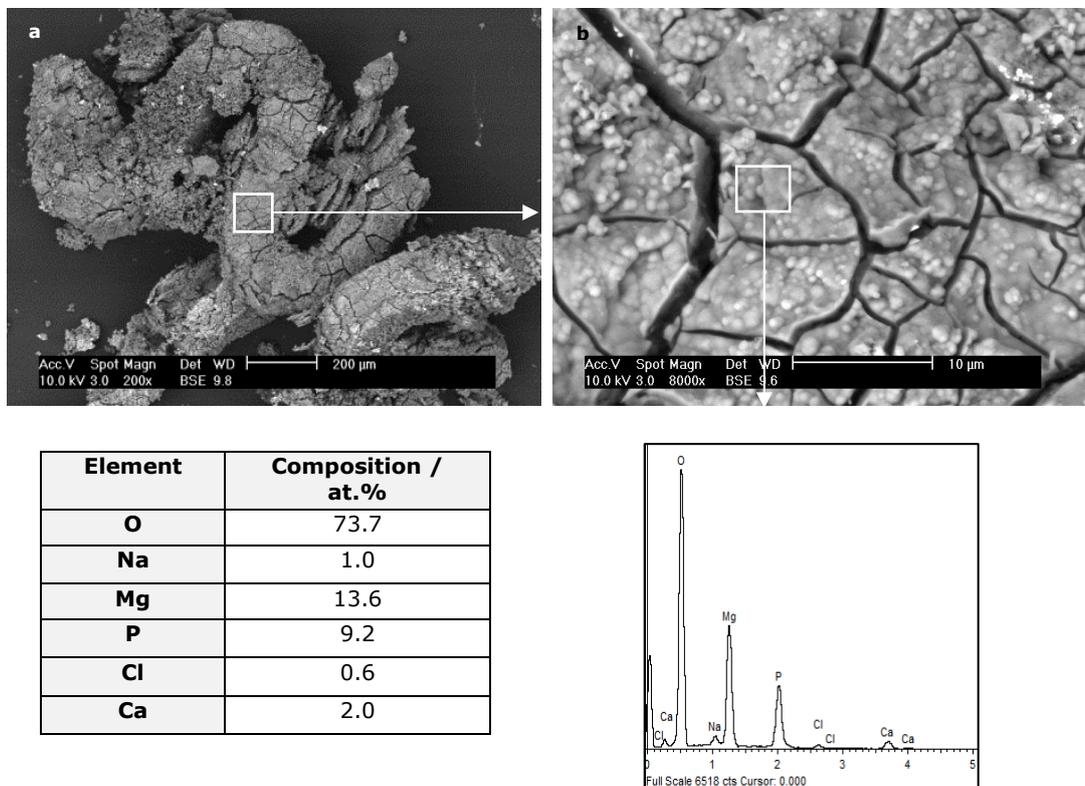
Figure 4-5 BSE images and associated ED spectrum of a commercial prototype Mg-alloy stent after potentiodynamic polarization testing.

4.3 Structural enhancement of Mg minitubes

Pure Mg-minitubes were produced successfully by RF-magnetron sputtering as detailed in Section 3.3.2.2. The as-deposited minitubes were then annealed at temperatures ranging from 300°C to 450°C under an H_2/He atmosphere, and also 500°C to 600°C under an Ar environment to encourage some densification and grain refinement. Morphological characterisations of the as-deposited and annealed Mg-minitubes were performed along with complementary potentiodynamic polarization tests, to appraise the corrosion behaviour of these Mg-stents.

4.3.1 Microstructural characterisation of Mg-minitubes

4.3.1.1 SEM/EDS investigation of as-deposited Mg-minitubes

Figure 4-6 shows an as-deposited Mg-minitube, after separation from the stainless steel substrate. In general, the minitubes exhibited a shiny metallic surface, but were brittle in nature such that they had to be handled with care. SE micrographs of Mg–minitube fracture cross-sections, and the outer and inner surfaces of various small fragments, were collated to appraise the structure of these sequentially deposited PVD Mg layers. The SE images of Figure 4-7(a,b) shows an as-deposited Mg minitube of 1.2 mm inner diameter, formed from ten ~ 10 μm discrete Mg layers. The total thickness of the minitube wall was 99.6 ± 0.5 μm, which met the target thickness for this study. The deposited Mg had developed a porous columnar structure, with the suggestion of some preferred orientation.
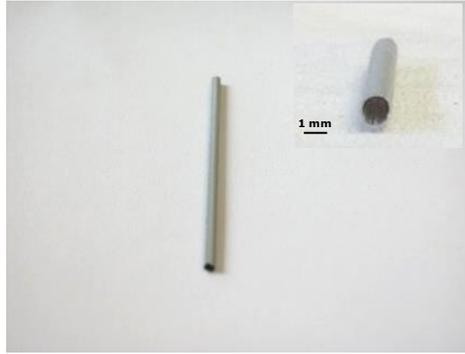
Figure 4-6 Photograph of an as-deposited Mg minitube.

The SE images of Figure 4-7(c,d) illustrate the topography of the external and internal surfaces of the Mg minitubes, in their post-deposition state. The outer surface of the Mg minitubes adopted a rough surface with voids and cracks (Figure 4-7(c) inset). The internal surfaces, on the other hand, exhibited wrinkles and folds (Figure 4-7(d) arrowed), attributable to the effect of the silicone grease sacrificial layer and the minitube stainless steel former.
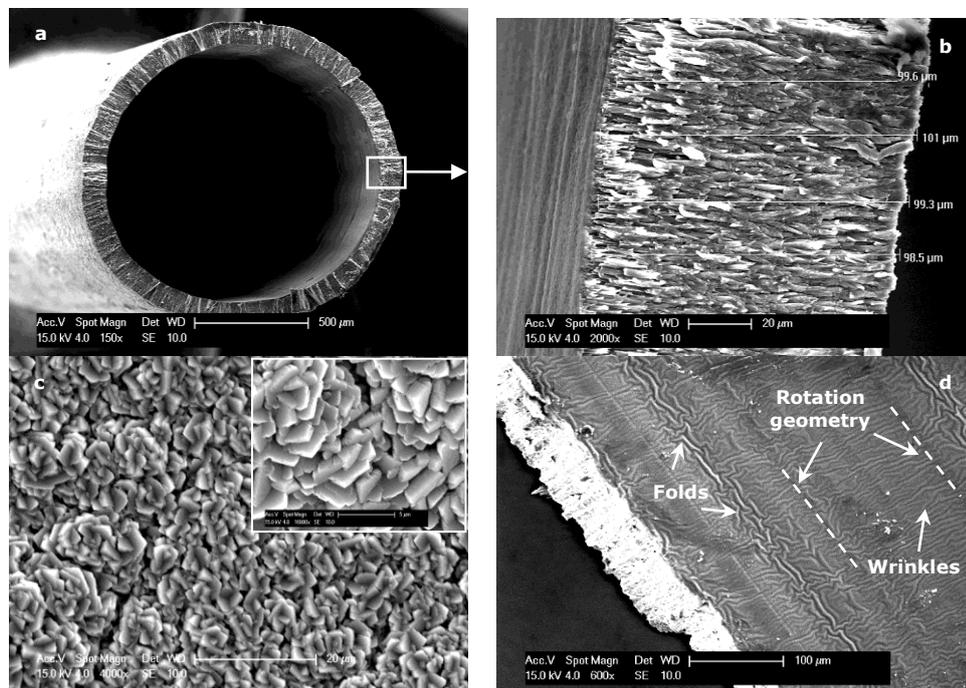
Figure 4-7 SE images of an as-deposited Mg minitube; (a) fractured cross-section, (b) higher magnification image of the fractured minitube wall; (c) minitube outer surface (with higher magnfication image inset); and (d) minitube internal surface.

All the Mg deposited layers exhibited Mg grains with large length to width ratios, resulting in a sharp needle like appearance. Figure 4-8(a,b) are representative of the etched Mg minitubes in cross-sectional geometry, showing that the thickness of each Mg layer was in the range of 10 μm, while the widths of the Mg columnar grains were ~ 0.5μm - 2.15μm. The bright (charging) contrast on the tip and edges of the fractured Mg columnar grains suggested some localised enhancement of oxide.
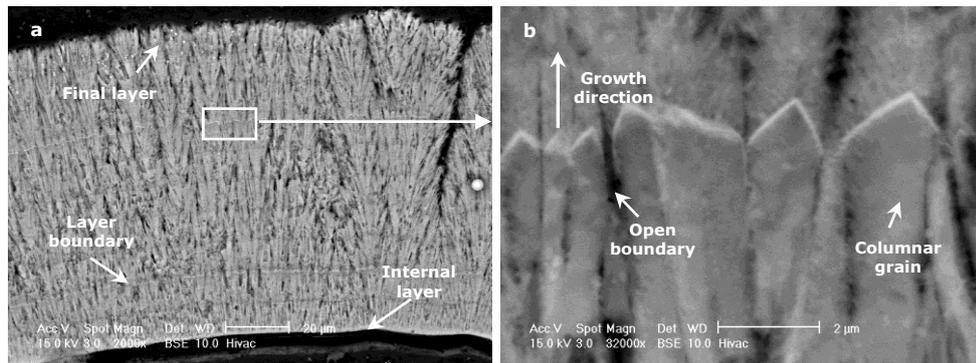
Figure 4-8 BSE images of an as-deposited Mg minitube, etched with acetic glycol.

EDS data was collected for the internal and external surfaces of the as-deposited Mg minitubes, and the cross-section. Figure 4-9(a,b) summarizes the constituents present. For all the Mg minitube surfaces analysed, the Mg content was always > 70 at% along with an amount of O_2 in the form of oxide. The outer surface of the as-deposited Mg minitubes also showed phosphorous (P) and calcium (Ca), from the deposition of the HA capping layer. The inner surface showed high levels of Si and O from the sacrificial grease. Further, EDS elemental mapping of the minitube cross-section (Figure 4-10) demonstrated a small distribution of Si and C, originating from the sacrificial grease layer, throughout the Mg minitube wall. The content of Si and C decreased gradually from *ca.* 11.1 and 41.1 at% at the internal layer, to *ca.* 0.03 and 14.4 at% at the outer surface, respectively.

Element	at. %
O	20.0
Mg	73.4
Si	0.3
P	2.6
Ca	3.7
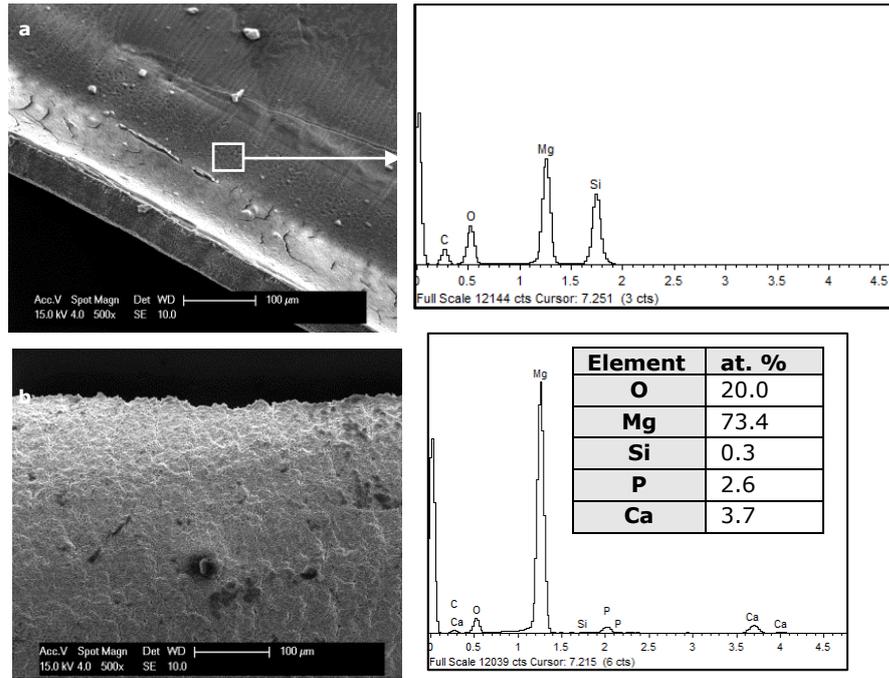
Figure 4-9 ED spectra acquired from the (a) internal surface; and (b) outer surface of a fragment of an as-deposited Mg minitube
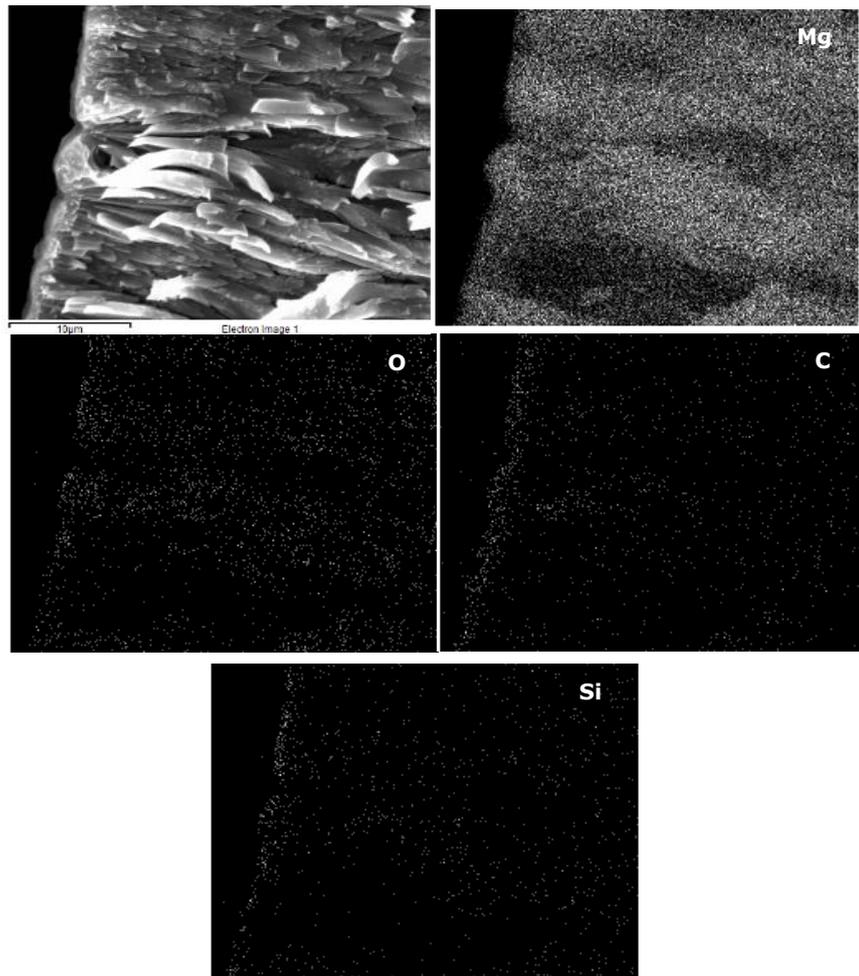
Figure 4-10 EDS elemental map for an as-deposited minitube in cross-section, showing Mg and the enhancement of Si, C and O at the internal edge (associated SE image).

4.3.1.2 SEM/EDS of annealed Mg minitubes

In an attempt to refine the crystallinity of the Mg minitubes, from columnar to equiaxed, the minitubes were annealed using a Sievert apparatus. A mixture of H_2/He was used as an ambient gas during annealing, to inhibit oxidation of Mg at elevated temperature. Figure 4-11(a-f) shows SE micrographs of fractured cross-sections of Mg minitubes annealed at 300°C, 400°C and 450°C. The average tube thicknesses were 95.1 ± 0.9 μm, 91.3 ± 0.7 μm and 93.3 ± 0.1 μm, respectively. For each case of annealing, there were some indications of microstructural densification and oxidation, as illustrated in a reduction of wall thickness and the details of the Mg layers (Figure 4-11 (b,d,f)). From the magnified SE images of Figure 4-11 (a,b), it can be seen that the minitube annealed at 300°C exhibited a brittle fracture mechanism and a columnar grain structure, similar to that of as-deposited minitubes. However, a change of microstructure following annealing became apparent for the Mg minitubes annealed at 400°C and 450°C (Figure 4-11(c-f)), whilst also revealing details of the layered structure. High magnification imaging of the higher temperature annealed minitube wall (Figure 4-11(d,f)) showed dark regions of Mg columnar grains separated by bright boundaries, indicative of oxidation at the interfaces between sequential Mg deposits, whilst also suggesting a less brittle fracture mechanism.
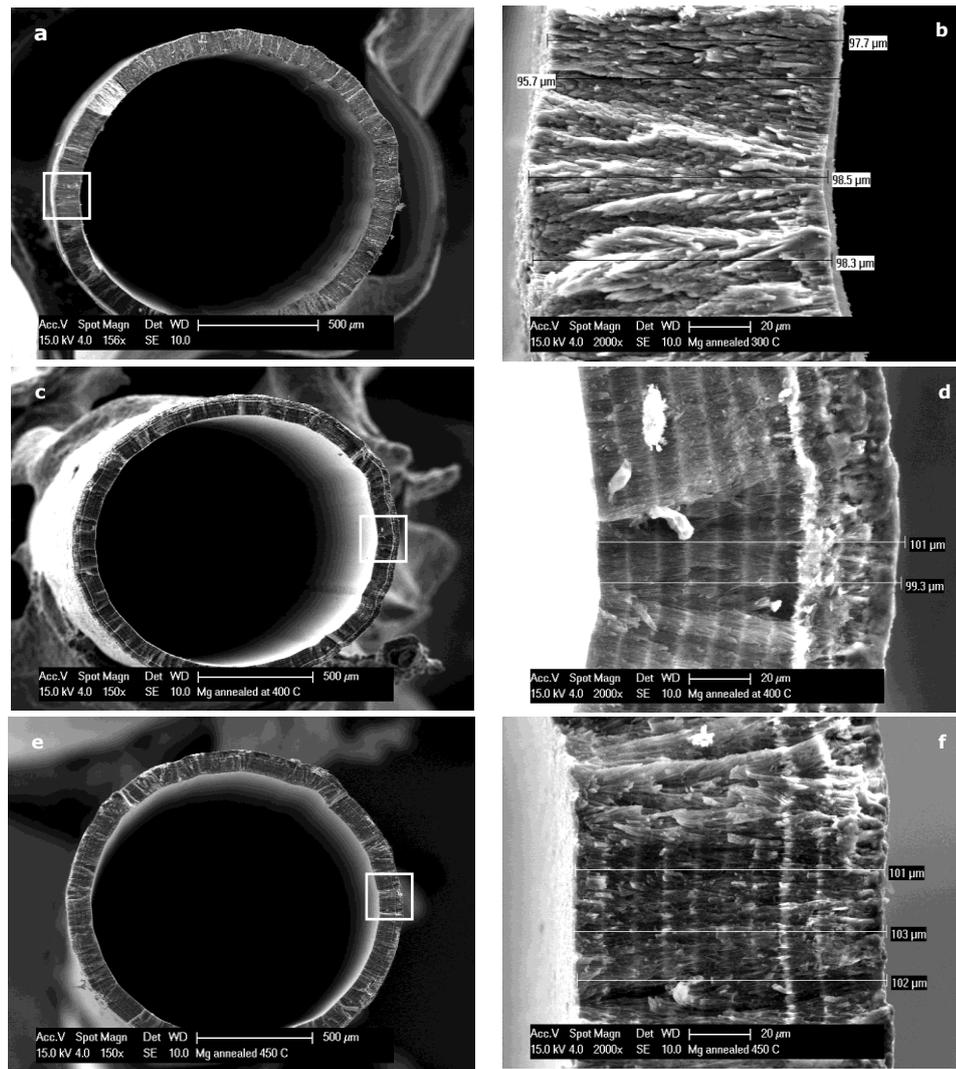
Figure 4-11 SE images of Mg minitubes annealed at: (a,b) 300°C; (c,d) 400°C; and (e,f) 450°C, respectively.

The Mg minitubes were also heat-treated up to 600°C under Ar, to encourage recrystallisation and grain growth. Figure 4-12(a-f) presents SE images showing the Mg minitube morphologies after annealing at 500°C, 550°C and 600°C, respectively. Although all the minitubes retained their original columnar structures, denser structures were associated with minitubes processed at the higher temperatures of 500°C and 550°C. Some alterations from anisotropic to isotropic grain growth were indicated from the high magnification SE images of Figure 4-12(b,d). The annealed tubes exhibited also regions of strong oxidation at the layer boundaries (Figure 4-12(b,f), arrowed). However, full re-crystallisation of the Mg-minitubes at the elevated

temperature of 600°C was not achieved, although the fracture mechanism revealed smoother Mg grains, indicative of a less brittle nature (Figure 4-12(e,f)).
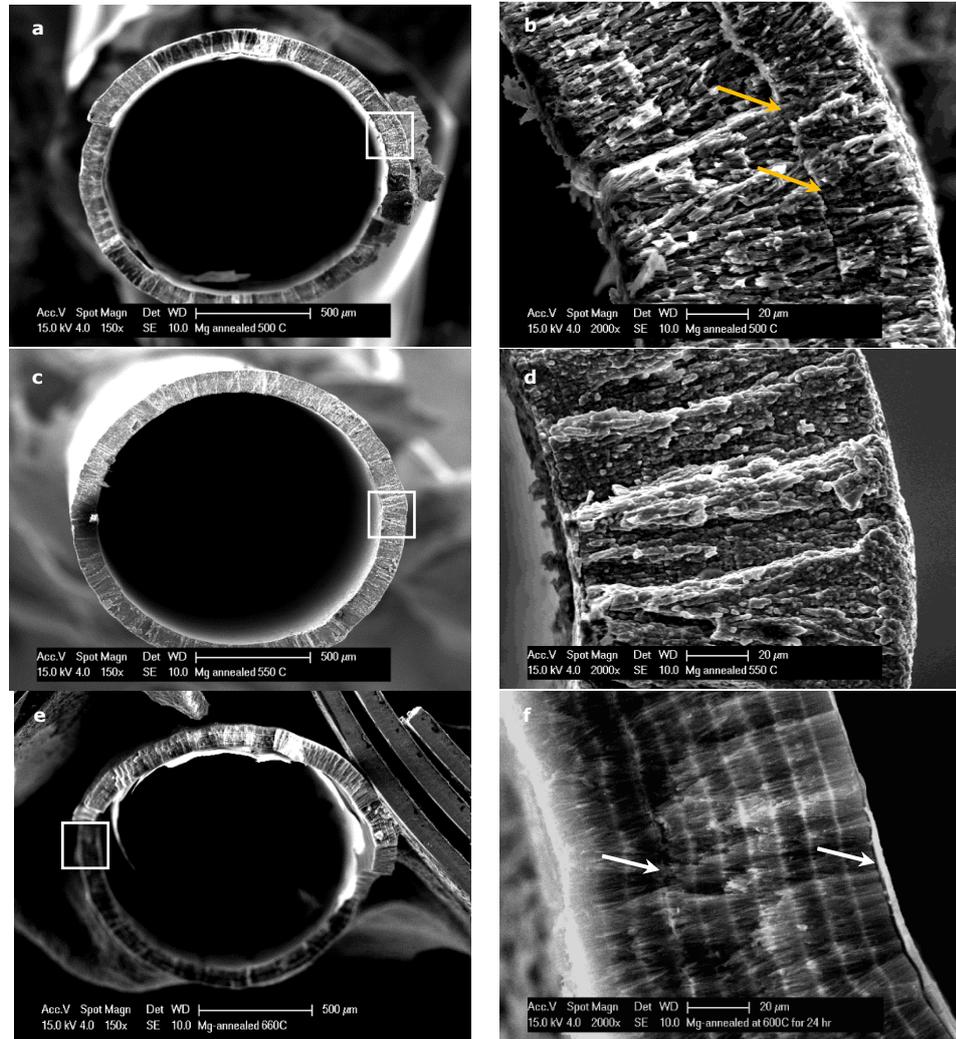
Figure 4-12 SE images of Mg minitubes annealed for 24 h: at (a,b) 500°C; (c,d) 550°C; and (e,f) 600°C, respectively.

A rough topography, combining voids and cracks was observed on the outer surfaces of all the annealed Mg minitubes. Figure 4-13(a,b) presents SE images and corresponding EDS spot analyses for the external and internal surfaces of an Mg-minitube fragment annealed at 550°C, by way of example. The outer surface suggested some level of delamination of the coating layer, whilst the internal surface was characterised by flow lines arising from

separation of the tube from the wire substrate. The Mg:O content now approached one, indicative of thick MgO layer formation as the EDS analysis depth at 15 kV is typically ~ 1-2 microns. The concentration of Si from the sacrificial layer of vacuum grease decreased gradually from 2.7 at.% on the internal surface, to 1.1 at.% on the external surface.

Element	Chemical Composition at.%
O	37.1
Mg	55.5
Si	1.1
P	2.8
Ca	3.5

Element	Chemical Composition at.%	
	A	B
C	19.1	-
O	34.6	48.9
Mg	43.1	49.4
Si	2.7	1.7
Ag	0.4	-
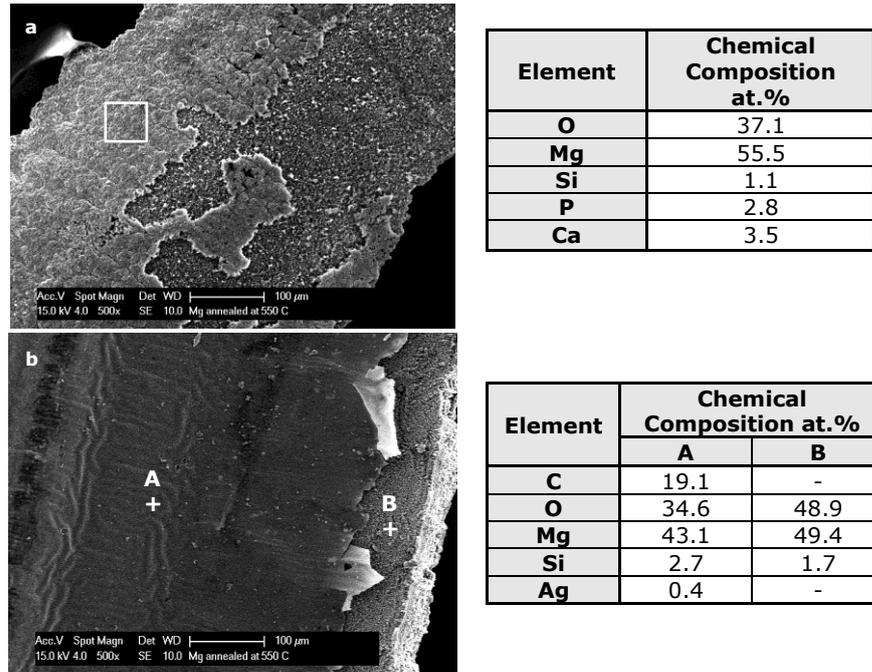
Figure 4-13 SE images and EDS analyses of: the (a) external surface; and (b) internal surface of a PVD deposited Mg minitube annealed at 550°C.

4.3.1.3 XRD of as-deposited and annealed Mg minitubes

Complementary XRD patterns were collected as part of the investigation of microstructural changes in the Mg minitubes, following annealing at elevated temperature. Where it is possible, the grains size of minitubes were apprised optically, otherwise XRD was used. Figure 4-14 presents diffraction patterns of the Mg-minitubes in their as-deposited and annealed states (300 – 600°C for 24 h).

All samples showed clear diffraction peaks from $\{10\bar{1}0\}$, $\{0002\}$ and $\{10\bar{1}1\}$ planes, consistent with single phase polycrystalline Mg. The as-deposited tube exhibited an intense 0002-reflection at 2θ of 34.4° suggesting some preferred

orientation along the c-axis (<0001> direction). In the case of minitubes annealed up to 450°C, the Mg peak at 32.2° was not present while some other peaks for example the peak at 63.1° had varying intensity as a function of annealing conditions, demonstrating the anisotropic nature of the restructuring.
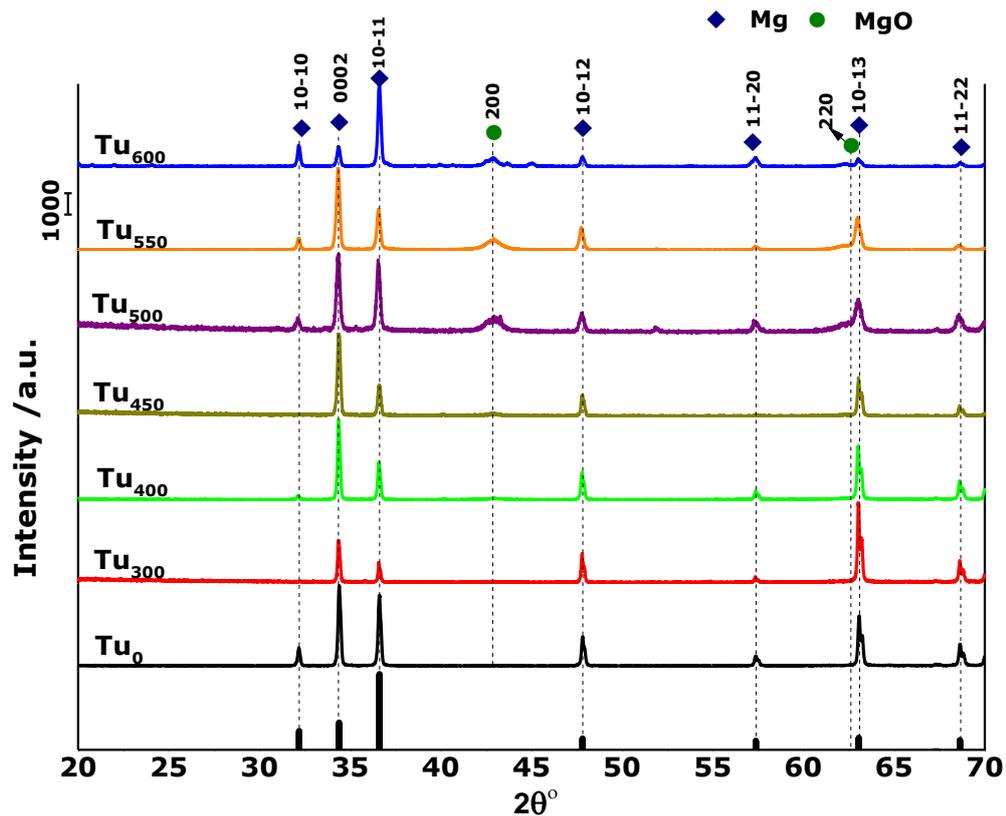
Figure 4-14 XRD patterns of the Mg minitubes, as-deposited and following annealing for 24 h (300 – 600°C). (Expected intensities for polycrystalline Mg peaks presumably for equiaxed grains: $10\bar{1}0$, 25; 0002, 36; $10\bar{1}1$, 100; $10\bar{1}2$, 15; $11\bar{2}0$, 12; $10\bar{1}3$, 16; and $11\bar{2}2$, 13).

Peak broadening was calculated from the measured FWHM values from the Mg diffraction patterns, by subtraction of instrument broadening (FWHM-ins), determined from a coarse-grained, microstrain-free LaB_6 reference sample. Hence, whilst the peak broadening calculations illustrated in Figure 4-15 are accurate, the values returned are outside of the applicable range of the Scherrer equation, which requires a peak broadening value of 0.083° to return a grain size of 100 nm. Hence, this data is treated with caution and

used only to infer a trend in support of the suggestion of some measure of grain refinement with increasing temperature of annealing. Grain size measurements , using the Scherrer equation for the respective diffraction peaks of 10$\bar{1}$0, 0002 and 10$\bar{1}$1 (Table 4-3, Figure 4-15), returned values for Mg grain sizes outside the general applicability (> 100 nm) of this equation, and so this data set can only be interpreted with caution, with a tentative suggestion of a decrease in average Mg grain size after annealing up to 450°C, consistent with the onset of some grain recrystallisation (Table 4-3, Figure 4-16). The broad diffraction peak at 2θ ~ 43° formed after annealing of 450°C was attributed to MgO$_{200}$. The corresponding MgO crystal size calculation (Table 4-3) indicated that grains within the oxide layer increased in size, from ~ 9 to ~ 18 nm, with increasing temperature. The ~ 100 nm thick HA capping layer was expected to be amorphous for the as-deposited Mg minitubes and hence did not feature on the XRD patterns. However, there was no evidence for the development of crystalline HA upon annealing at elevated temperature, but such as thin layer might be at the limits of XRD sensitivity.
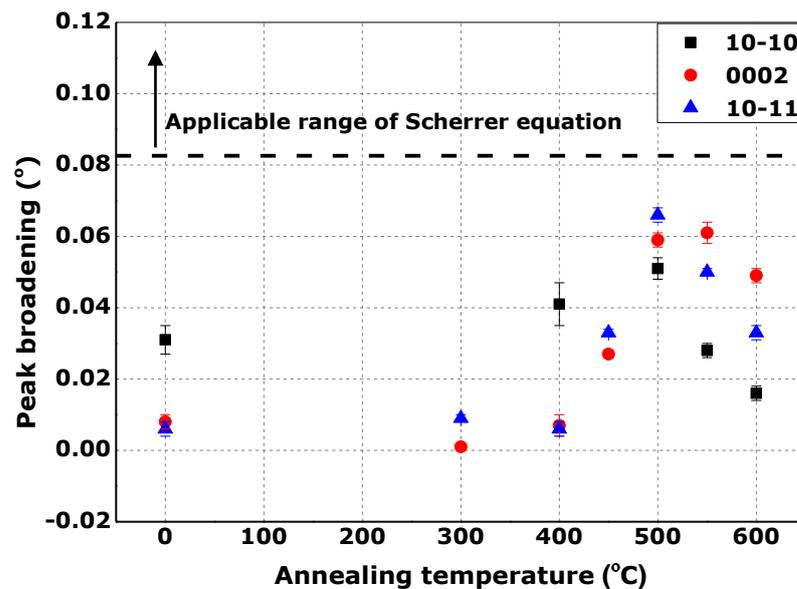
Figure 4-15 Peak broadening of Mg 10$\bar{1}$0, 0002 and 10$\bar{1}$1 diffraction peaks for different annealing temperatures.

Table 4-3 Variation of grain size determined from three different planes of as-deposited and annealed Mg-minitubes

sample	Grain size/ nm			
	Mg			MgO
	$10\bar{1}0$	0002	$10\bar{1}1$	200
Tu$_0$	265	1014	1350	-
Tu$_{300}$	-	8315	930	-
Tu$_{400}$	201	1155	1349	-
Tu$_{450}$	-	306	252	9±1
Tu$_{500}$	161	140	127	10±1
Tu$_{550}$	293	136	167	12±1
Tu$_{600}$	510	169	252	18±3
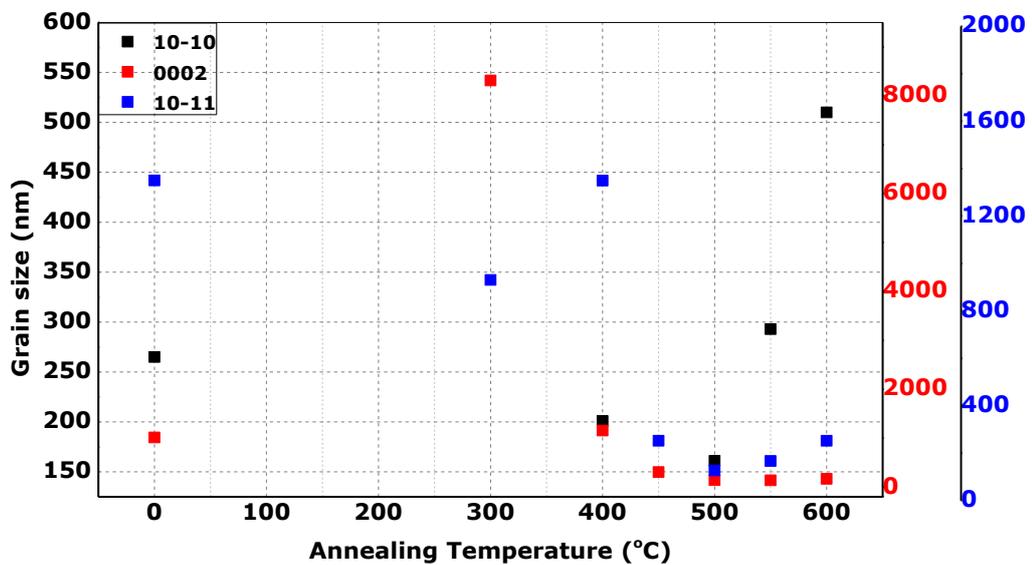
Figure 4-16 Grain size variation of Mg for as-deposited and annealed Mg minitubes, determined from three different planes.

4.3.1.4 Micro-hardness of as-deposited and annealed Mg minitubes

The as-deposited and annealed Mg minitubes were appraised using Vickers micro-hardness testing. Table 4-4 summarises the average Vickers micro-hardness values and corresponding standard error for more than 10 measurements. The averages hardness of the as-deposited samples was 38.1 ± 0.9 Hv, whereas, hardness values were variable, with a maximum of 52.1 ± 1.5 Hv upon annealing at 500°C (Figure 4-17(a)). Figure 4-17(b) shows an SE image of Vickers indentations on an as-deposited Mg minitube, in cross-

section. The loading did not induce cracking and indentations were made in

the middle of Mg layers, a best position as shown in Figure 4-17(b), arrowed.

Table 4-4 Vickers micro-hardness data and corresponding standard error for as-deposited and annealed Mg-minitubes.

Minitube	Annealing temperature / °C	Hv / gf/cm^2
Tu_0	0	38.1 ± 0.9
Tu_{300}	300	40.0 ± 1.2
Tu_{400}	400	51.6 ± 0.7
Tu_{450}	450	31.9 ± 1.9
Tu_{500}	500	52.1 ± 1.5
Tu_{550}	550	33.4 ± 2.6
Tu_{600}	600	32.6 ± 2.2
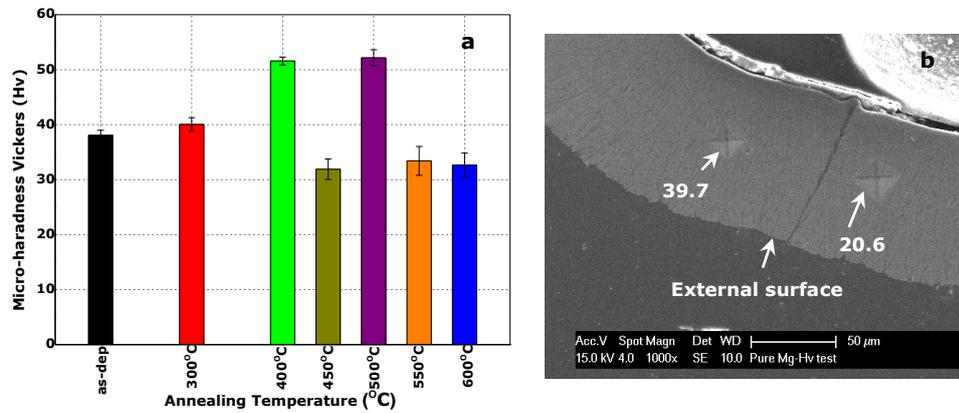
Figure 4-17 (a) Micro-hardness values for as-deposited and annealed Mg-mintubes, as a function of annealing temperature and corresponding standard error; (b) SE image of Vickers micro-hardness indentation patterns on an as-deposited Mg minitube.

4.3.2 Corrosion performance of the Mg-minitubes

Figure 4-18 presents OCP data for the as-deposited and annealed Mg

minitubes in aerated PBS, at 37°C, for one hour. Due to the small number of

Mg minitube samples and difficulties with sample handling and geometry,

corrosion tests could be performed only once for each condition. The as-

deposited minitube achieved a steady state OCP of -1.69 V with respect to

SCE within 20 minutes. Minitubes annealed in both H_2/He and Ar

environments showed nobler onset OCP, with the minitube annealed at 600°C

showing the noblest behaviour at -1.38 V, while the minitube annealed at

550°C showed a more negative OCP.

Figure 4-19 compares the potentiodynamic polarization curves for the as-deposited and annealed Mg minitubes. Characteristic values for the onset potential and corrosion rates extracted from the polarization curves are summarised in Table 4-5. The as-deposited minitube showed normal hydrogen evolution in the cathodic region, with the development of a typical Tafel region (I). Fast passivation acted to slow down the generation of Mg^+ ions during rapid anodic passivation (region II). The corrosion rate of the as-deposited sample, corresponding to an E_{corr} of -1.66±0.01 V and a corrosion current density of 11.8±0.5 mA/cm^2, was 270±9 mm/year. The voltage reached the limited value of the polarization test, before trans-passive region formation. The passive current density of the as-deposited minitube was 128 mV/cm^2.
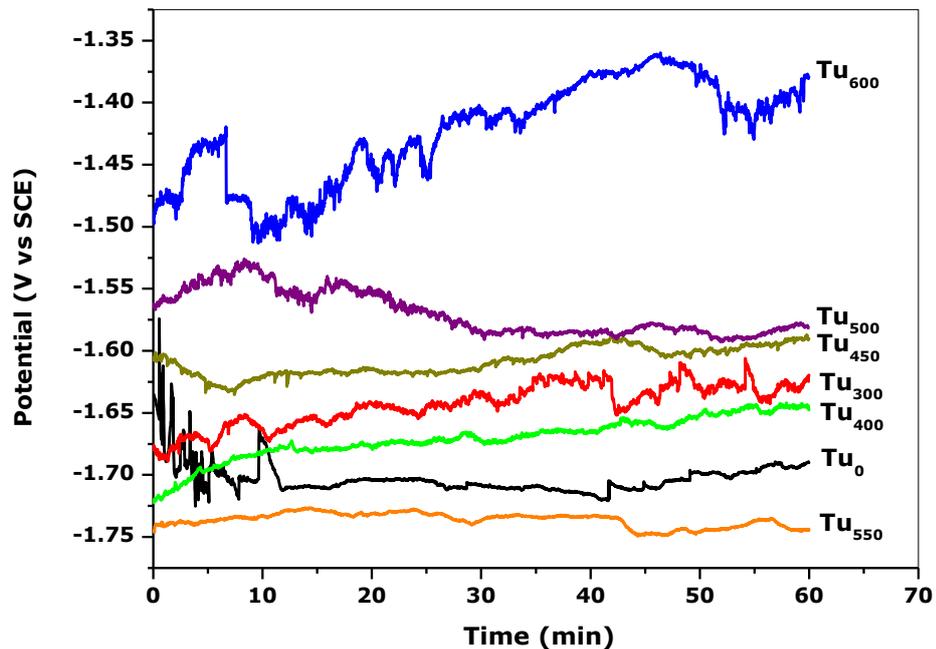
Figure 4-18 OCP data for as-deposited & annealed Mg-minitubes in PBS at 37°C.
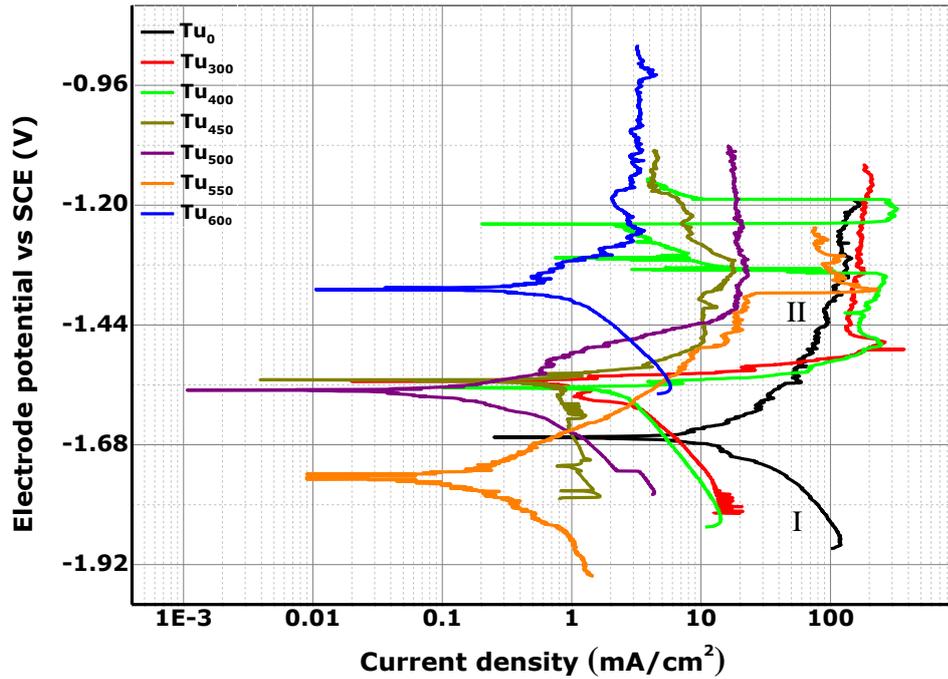
Figure 4-19 Potentiodynamic polarization curves for as-deposited & annealed Mg-minitubes in PBS at 37±1°C.

Table 4-5 Characteristic corrosion parameters of the as-deposited and annealed Mg minitubes, from potentiodynamic polarization tests in deaerated PBS at 37±1°C.

Sample	Annealing temp / °C (±5)	E_{corr} / V (±0.01)	i_{corr} / mA/cm²	E_b / V (±0.01)	CR / mm/year	MR / g/m²d
Tu_0	-	-1.66	11.83±0.5		270±9	1287±45
Tu_{300}	300	-1.55	1.98±0.3	-	45.2±5	216±24
Tu_{400}	400	-1.57	2.94±0.1	-	67.1±1	320±7
Tu_{450}	450	-1.55	0.76±0.1	-	17.3±1	82±3
Tu_{500}	500	-1.57	0.20±0.01	-	4.57±0.2	22±1
Tu_{550}	550	-1.74	0.16±0.01	-1.38	3.65±0.1	17±0.1
Tu_{600}	600	-1.37	0.70±0.1	-	16.0±0.1	76 ±1

In comparison to the corrosion performance of as-deposited Mg minitubes, the annealed minitubes showed generally increased noble behaviour, *i.e.* increasing resistance to the onset of corrosion, consistent with the OCP curves. A general reduction in the rate of corrosion was also measured as a function of increasing annealing temperature. The polarization curves for the Mg minitubes annealed at 300°C and 400°C showed rapid anodic dissolution of 45.2±5 mm/year and 67.1±1 mm/year, respectively, before the Mg surfaces reached passivation, at a current density of 168 mV/cm² and 270

mV/cm^2, respectively. Unlike the as-deposited samples, the minitube annealed at 400°C showed trans-passive behaviour beyond the passivation region, from -1.48 V to -1.23 V. Further reduction in corrosion current density and corrosion rate was more pronounced for minitubes annealed at 450°C and over. The minitube annealed at 550°C showed the lowest corrosion rate of 3.65±0.1 mm/year, slightly less than that for the hardest minitube annealed at 500°C. After a short passivation region of 0.11 V, the 550°C annealed sample showed rapid dissolution of the passivation film at a breakdown potential of -1.38±0.01 V.

The BSE images of Figure 4-20(a,b) are illustrative of the surface topography, with associated EDS data, for an Mg minitube annealed at 400°C, after anodic polarization measurements in aerated PBS at 37°C (from -250 to 500 mV relative to OCP). The Mg minitube suffered uniform degradation, and a white corrosion product completely covered the exposed minitube surface. The degradation products were adhered strongly to the surface and did not wash away under flow of DI water. The high magnification BSE image of Figure 4-20(b) indicates the corrosion products took the form of a thick, cracked, rough layer, with a spread of porous mineral structure agglomerates on top.

Complementary EDS analyses at *e.g.* spot A (flat layer) and spot B (agglomerates) indicated a significant amount of O (61.9 and 55.6 at%, respectively) and P (14.6 and 17.7 at%, respectively) in both cases, suggesting the formation of Mg(OH)$_2$ and PO$_4$ components. The agglomerates contained Ca and P see Figure 4-20. An EDS line profile analysis, not shown, was also conducted on the Mg-minitube annealed at 400°C and the data was consistent with the EDS spot analyses.

Element	Composition at different spots	
	A	**B**
O	61.92	54.58
Na	2.22	2.29
Mg	15.30	5.76
P	14.55	17.94
Ca	3.81	17.45
Cl	2.20	1.98
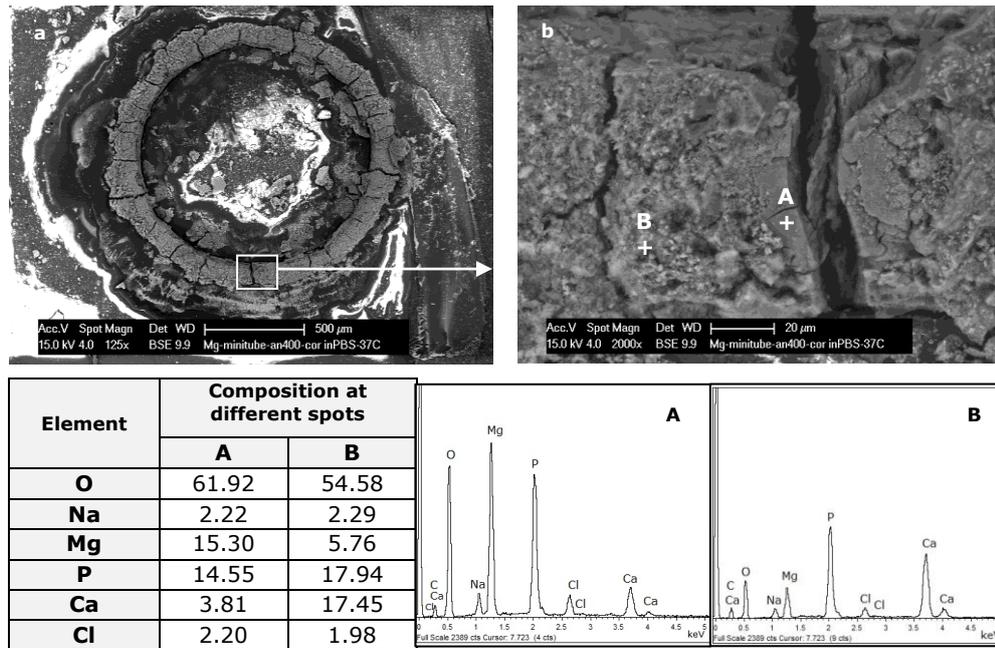
Figure 4-20 (a,b) BSE images of the corrosion topography of an Mg-minitube annealed at 400°C, after potentiodynamic polarisation testing.

4.4   Discussion

Modern day metal degradable stents are made using bulk metal tubes. These stents are relatively large and have a wall thickness > 100 μm. There is a growing demand to obtain smaller, thinner stents that can be delivered and implanted into very narrow blood vessels [242]. Sputtering deposition techniques such as PVD are suitable for deposition of a high quality metal films, as thin as a few micrometers, at commercial rates [166] and have the important advantage that by using multiple targets, blended compositions or multilayer structures not possible by melt processing can be produced. In this manner, PVD techniques can be used to produce three-dimension devices with desired thicknesses, using 3D-substrates. This can solve the welding problem that is needed for stents produced from planer films. In addition, the advantage of using PVD techniques is the use of high purity target

materials and a refined PVD deposited film microstructure is expected due to the high cooling rate of $\sim 10^{12}$ K/s [243] [244] which can enhance the coating corrosion resistance [245]. Other new methods such as selective laser sintering (SLS) require Mg sphere precursors that are safe to handle with a certain size distribution, to be able to be spread evenly on an additive manufacturing layer bed. Below 30 μm diameters, Mg particles are reactive and have to be handled in an inert atmosphere and when combined with the low density of Mg, this makes them difficult to handle and fluidise in terms of delivery to the SLS bed. This imposes a limitation on how thin and complex a part can be made by SLS [246], with the requirement for homogenous powders limiting composition variation, as compared with PVD methods.

4.4.1 Structural characteristics of PVD deposited Mg layers

In order to understand the structural change within as-deposited Mg-minitubes under thermal annealing, the series of SE images as illustrated in section 4.3.1 highlight the morphological evolution of Mg-minitubes during thermal processing. The SE images of the as-deposited Mg-minitubes show the tube walls to comprise grains with large height to width ratios (5:1 to 20:1), resulting in a needle like appearance (Figure 4-7). Comparison with BSE images (Figure 4-8) indicates further that each deposited layer underwent columnar growth. Plan-view imaging of the as-deposited surface showed rough morphologies at the top of columns. Such structures are typical for PVD films deposited under low temperature conditions, as summarised by the Movchan and Demchishin (MD) model [247].

The MD model divides film growth structures into three zones, as a function of substrate and melting temperature of the coating material (T/T_m), which determines the different adatom diffusion processes. Zone I consists of a

tapered structure, with dome-shaped tops increasing in width with temperature. In this zone, the adatoms do not have enough energy to diffuse and overcome the vapour flux shadowing effect, because of substrate roughness [244]. Zone II consists of dense columnar grain structures in the growth direction, with smooth surfaces resulting from the high mobility of adatoms diffusing along the surface. Zone III consists of equiaxed grains, caused either by recrystallisation or grain growth controlled by bulk diffusion [244]. The Thornton model [248], as shown in Figure 4-21, added a transition region (zone T) between zone I and zone II, consisting of densely packed fibrous grain structures, with preserved initial nuclei orientation, and also includes the effect of argon pressure. In addition, Zone II columnar grains have a tendency to be faceted, whilst Zone III shows equiaxed grains [249].
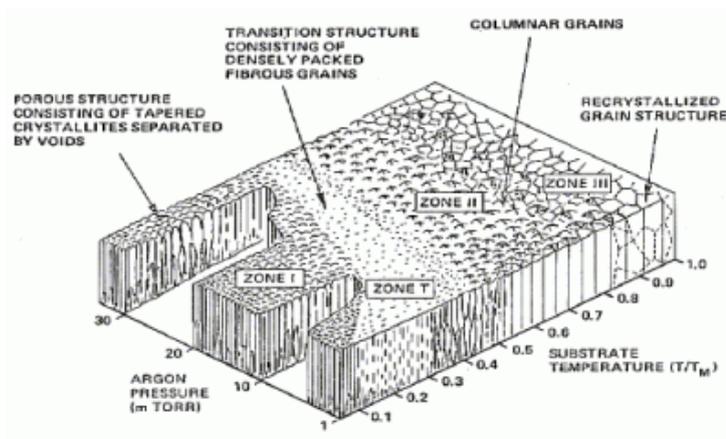
Figure 4-21 Thornton-Messier structure zone model for sputter deposited films [248].

The current to the Mg target was 0.3A, with a target bias that varied from -600 to -370 V, as the target became depleted. This means that 180 – 111 W were utilised heating the chamber, and despite water cooling to the double skinned vacuum chamber and to the targets, the chamber temperature

reached > 100˚C. In addition, the sputtered Mg atoms would provide localised energy on the surface, hence the rotating target was positioned 10 cm away to minimise this. Normally, a negative bias would be applied to the substrate to aid coating adhesion, but this was not applied in this case, as removal of the coating was required and so no additional accelerating electric field was applied. Hence, taking these considerations into account, it would be expected that the structure should, at the very least, be above a T/T_m of 0.4 on the Thornton diagram. Allowing from an Argon partial pressure of *ca*. 1 mTorr, then one would expect a structure at the top end of zone T on the Thornton diagram (Figure 4-21). The SE images for the fractured cross-section, and in plan-view, revealed that the as-deposited Mg-minitubes were consistent with zone T of the Thornton model. The surface topography and fractured cross-section of these brittle Mg minitubes showed, near the substrate, small grains randomly oriented, out of which emerged columns, closely packed, with faceted column tops. The grain size was initially small, but increased with increasing thickness, while voids or boundaries between columns became more open [250]. This resulted in cracks which propagated on the Mg-minitube surface, along weak and low-density columnar regions. This description of Mg-film morphology has been reported by Stormer *et al.* [245], who deposited 3 μm pure Mg films onto silicon wafers, and noticed that the film growth was influenced by a lack of adatom diffusion during deposition.

Thornton [248] claimed that open boundary structures formed as a result of insufficient mobility of incoming atoms, to overcome the substrate surface, so incident atoms adhered where they impacted. Hence, shadowing developed when the atom flux reached high points on the growing surface, before valleys [249]. This happens particularly when the coating flux is oblique and/or the substrate is rotated [248]. However, when initial nuclei are

faceted, the crystal faces that receive a high coating flux grow quicker than other faces. The crystals then become isolated with sharp surface features composed of slow growth rate planes [248].

The as-deposited Mg minitubes were found to be oriented with their {0002} planes predominantly parallel to the substrate, as shown also by Gautam *et al.* [251], being consistent with the SE images of columnar growth. Mg has an hexagonal structure, and the basal plane has low energy configuration which favours the tendency to grow parallel to the substrate surface [245] [252]. This crystal orientation, along the c-axis, allows the coating to avoid high strain. When the thickness of the deposited film increases, texture develops due to growth competition between different planes [244]. The growth velocity of planes should be similar to the strain energy, so that planes with low strain energy grow faster. When more atoms arrive on the surface, strain increases and drives the film in a preferentially oriented direction [253], which favours in the case of Mg to {0002} film growth. Such textured growth has been widely reported in literature, for pure Mg [243] [245] [254] as well as binary Mg-alloys [244] [252] [255].

Post-deposition heat treatment was performed in an attempt to recrystallise the Mg-coating structure, towards an equiaxed grain structure. The intention was to take the coating through recrystallisation and grain growth, which for most metal is in the region of 0.4 to 0.6 T/T_m and for Mg is reported to be 0.6 T/T_m [256]. Strain in the coating can further reduce the recrystallisation temperature, however this would have been relaxed after removal from the stainless steel former, combined with the ductility of Mg [248]. Accordingly, the annealing temperature was chosen to be in range of ($T/T_m > 0.6$), with the aim to alter the structure the as-deposited Mg-minitubes from columnar, open grain boundaries, to a denser, more equiaxed structure.

In practice, a T/T_m range of 0.6-0.78 (300-450°C) was applied, whilst a mix of hydrogen and helium in Sieverts apparatus was used to avoid oxidation of the Mg during the annealing stage - initial annealing attempts under inert (Ar) conditions resulted in oxidation of the Mg minitubes, due to outgassing of the tube furnace and residual oxygen contamination. SE images of fracture cross-sections (Figure 4-11) indicated that the Mg-grains became denser with increasing temperature and this resulted in less brittle fracture surfaces. Microstructural densification was also reflected in an increase of Hv values, with increase annealing temperature (Figure 4-17), whilst a decrease in hardness at 450°C attributed tentatively to a loss of some Mg material during annealing under the H_2/He mixture.

At $T/T_m > 0.8$ (500-600°C), under Ar in the tube furnace, even though the Mg-minitubes retained their original columnar structures (Figure 4-12), the annealed minitubes developed some refined microstructures. Some compression between the widths and heights of columnar grains, under these condition, indicated a trend from anisotropic to isotropic grain growth, consistent with the SE image of Figure 4-12, and in grain size values in Table 4-3. Denser boundaries and more refined grains (Figure 4-16) developed at 500°C, being related to the increase the hardness, from 38.1±0.9 in the range for bulk cast Mg [257], to 52.1±1.5. Annealing at higher temperature (550-600°C) was associated with a further increase in grain size and hence a slight decrease in hardness [258] to 33.4±2.6 and 32.6±2.2.

The onset of recrystallization temperature of 450˚C ($T/T_m = 0.78$), as evidenced by a reduction of grain size, is relatively high for Mg (Mg recrystallisation temperatures < 300°C) [259]. This was surprising since coatings often contain residual stress that, if anything, tend to lower the recrystalisation temperature [260] [261]. However, in the case of this

coating, stress would have been relieved upon removal from the stainless steel former. Hence, the increase in the recrystallization temperature must be due to some stabilisation effect. Since the as-deposited and annealed samples showed columnar grains extending over the sample thickness, these could act to stabilize and inhibit recrystallisation. Another possibility is that limited recrystallisation may occur within any type I, T zone, due to the presence of voids and open grain boundaries [248]. Another possibility may be a substructure of MgO pinning grain boundaries and preventing recrystallisation. Hence, the potential impact of oxidation at the Mg interfaces is discussed in the following section.

4.4.2 Impact of oxidation at the Mg interfaces

As described previously in Chapter 3, during the deposition of sequential Mg coatings, upon completion of each Mg layer, the sample stage was removed from the chamber and new Mg targets mounted on magnetrons. This led to exposure of freshly deposited Mg layers to air which would cause the spontaneous formation of an oxide layer of thickness $\sim$ 3 nm [262] (Figure 4-8). Due to the porous nature of the as-deposited Mg-minitubes, it is likely that the oxide layer also locally covered columnar Mg grains and any exposed voided areas.

Oxidation of the Mg grains was observed noticeably after annealing at elevated temperature (450-600°C) (Figure 4-14), even though the annealing process was conducted under inert conditions. For both annealing processes, under He/H$_2$ or Ar environments, samples were loaded into a stainless steel sample cell, back-filled with Ar, to further ensure a good seal from atmosphere. In the case of the Sieverts apparatus, the system was subjected to a leakage test, up to 3 h, to reduce oxygen contamination during annealing (24 h). However, it is noted that any reduction in pressure inside the sample cell might be responsible for air species (oxygen) moving inwards towards the

sample cell, facilitating a source for oxygen contamination which would be more pronounced for samples annealed at 450°C. In the case of the tube furnace, it was not possible to do a full leakage test and it is possible that complete isolation of the sample cell from air was not achieved, in which case, possible oxygen contamination would be higher upon annealing at 500-600°C.

At high temperatures, the kinetics of dissociation of molecular to atomic oxygen occurs more rapidly and the diffusion coefficient is sufficiently large to allow MgO to form [263] [264]. Thus, the oxide layer became thicker with increasing temperature, coupled with increasing grain size (Table 4-3). Growing MgO at the interfaces between sequentially deposited layers would act to enhance layer separation (Figure 4-12). It is considered that the oxide layer might act as an additional barrier for columnar grains undergoing recrystallization, thus delaying the recrystallisation temperature to 450˚C, as discussed in the previous section.

4.4.3 Corrosion mechanisms

Electrochemical corrosion tests using PBS media have been used to determine the corrosion rates of the as-deposited and annealed Mg minitubes. It is evident that heat treatment of the Mg minitubes reduced considerably the corrosion current density and hence corrosion rate. Both the shift of E_{corr} towards a more positive potential and a decrease in current density i_{corr} of the annealed minitubes may be associated with an increase in the densification and oxidation of the Mg grains.

The annealed minitubes showed a significant noble corrosion potential E_{corr} compared to the as-deposited minitube, with the exception of the sample annealed at 550°C (Figure 4-18). This increase in the onset of corrosion of the annealed Mg-minitubes, with increase temperature, maybe attributed to the

densification and grain refinement of columnar Mg grains. In addition, the annealed Mg minitubes showed an increase in oxidation with temperature, with the formation of protective MgO layers enhancing passive activity, *i.e.* the formation of $Mg(OH)_2$ on Mg grains in the corrosion environment.

It is worth mentioning that E_{corr} recorded for the as-deposited and annealed Mg-minitubes, with a noblest potential of -1.37 V for the Mg-minitube annealed at 600°C, and the lowest corrosion potential of -1.74 V measured for the Mg-minitube annealed at 550°C, were in the range of corrosion potentials for extruded Mg (-1.539 V) [245]. This finding is opposite to the results obtained by Stormer *et al.* [245], who reported that all Mg-coatings deposited at various deposition angles (0-70°) and Ar-pressures (0.001-0.005 torr) showed a lower free corrosion potential than as-cast or extruded Mg. However, the lowest E_{corr} value of annealed (at 500°C) Mg minitubes recorded here was close to the potential recorded for Mg-coating prepared at 0° deposition angle and 0.001 torr Ar-pressure in the studies reported by Blawert *et al.* [243] and Stormer *et al.* [245].

A similar trend of improving the onset of corrosion, after annealing, was observed for the corrosion rate (Figure 4-19 and Table 4-5). The high corrosion rate of the as-deposited Mg minitube was attributed to the open boundaries between columnar grains, acting as pinholes, and providing pathways for the electrolyte to cause more corrosion attack around the Mg grains, *i.e.* increasing the effective surface area which cannot be considered in the calculation of corrosion rate. This calculation assumed an identical surface area exposed to PBS which is probably not the case for Mg columnar grains, resulting in the exceptionally high corrosion rate for the as-deposited minitube. The observed decrease in corrosion rate with increasing the temperature is likely to result from a decrease of effective surface area, due to the densification of Mg grains. Closing the boundaries between isolated Mg

columnar grains decreases the area exposed to electrolyte and hence provide for more corrosion resistance. This can be seen in the decrease in cathodic and anodic kinetics for the annealed Mg minitubes. The decrease in cathodic kinetics indicates a slow-down in the cathodic reaction rate of Mg and hence a decline in hydrogen evolution at cathodic sites. The annealed Mg-minitubes also experienced a decrease in anodic kinetics, *i.e.* a slowdown in the dissolution of Mg ions within PBS by a shift of the anodic current density to smaller values compared to the as-deposited Mg-minitube, with the exception of the low temperature annealed samples (300°C and 400°C).

It is speculated that the shift in cathodic and anodic kinetics and associated decrease in corrosion rate of the annealed Mg-minitubes may also reflect a change in the extent of preferred orientation within the Mg films. A refinement of the microstructure towards a more equiaxed distribution combined with densification could change the overall density of grain boundaries exposed to media and hence affect the overall corrosion resistance of the annealed Mg minitubes.

Enhanced oxidation after annealing may also play role in reducing the corrosion rate of the Mg minitubes, as indicated above. The MgO layer covering Mg grains can act as a barrier within the electrolyte, because less Mg ions are exposed to ions in PBS. This can enhance the passivation behaviour of the Mg columnar grains by consuming quickly the Mg ions in media in the formation of the passivation layer (Figure 4-22). Moreover, MgO is relatively stable due to its strong ionic bonds (79±7 kcal/mol), made of Mg^{+2} and O^{-2} ions, making the oxide layer less soluble in media [265]. In addition, the interaction between MgO and water molecular in PBS ($MgO + H_2O \rightarrow Mg(OH)_2$) results in hydrolysis to hydroxide, which further enhances the minitube passivation layer [173] [266] (Figure 4-22). This is reflected in the fast passivation of the Mg minitubes annealed from 450 to

600°C (Figure 4-19) - the same samples showed the presence of MgO peaks in the XRD data (Figure 4-14).
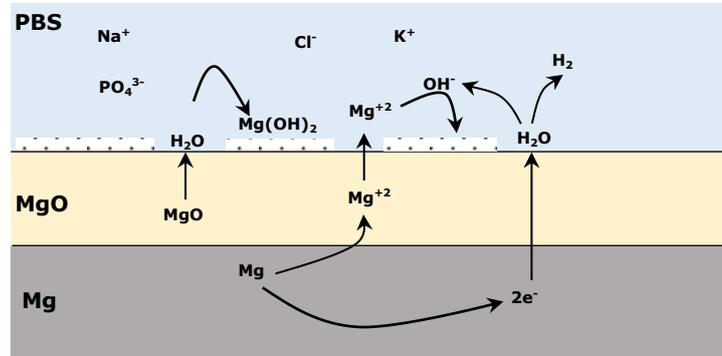
Figure 4-22 Schematic showing the competing processes of dissolution and film formation on an MgO/Mg surface.

It should mentioned that the best corrosion rate of 3.65 mm/year was recorded for the minitube annealed at 550°C, being higher than that reported by Blawert *et al.* [243] who reported a dissolution rate of 0.260 mm/year at a corrosion potential -1.738 V for an Mg coating with columnar structure corroded in 0.5% NaCl solution. This difference may be related to the lower concentration of Cl⁻ ions in their test solution compared to PBS used in the current study.

4.4.4 Comparison with the commercial stent

Mg-alloys are gaining increased research attention for use as degradable implant materials, but their application remains limited due to their low corrosion resistance. However, rare earth (RE) elements have a strong influencing effect on Mg and its alloy corrosion properties. Corrosion resistance can be improved through the link with impurities and the alteration of second phase distributions which incorporate into the passivation film during the corrosion process [267]. Accordingly, RE with high solubility in Mg can be a good choice to form Mg-alloys with improved corrosion resistance, through the formation of inter-metallic phases that can enhance strength;

combined with grain refining, which influences ductility and thereby assists in the manufacture and shaping of Mg-alloys [99]. Dysprosium (Dy) has a high solubility in Mg of 25.3 wt.% at 561 °C [267] [268], so it is used to promote grain refinement and solid solution strengthening in Mg:Dy-alloys [112]. Indeed, microstructural analysis of the prototype commercial stent revealed the use of Mg:Dy-alloy, to aid with grain refinement and extrusion [99]. No uniform or second phase alloy was formed, with the stent only containing a matrix of Mg with segregated particles of Dy (Figure 4-2). This was confirmed further by XRD (Figure 4-3), where the $Dy_{0.5}Zr_{0.5}O_{1.75}$ phases was detected, in addition to Mg and some unknown minor phases.

It is suggested that Dy can influence the corrosion resistance of Mg, by enhancing the passivation behaviour of Mg. Yang *et al.* [267] claimed that an increase the amount of Dy in the Mg matrix can improve corrosion resistance by blocking the propagation of filiform corrosion, thereby enhancing the formation of high corrosion resistance passivation films. In their study, the corrosion resistance of Mg-xDy (x=5, 10, 15, 20) alloy in 0.9 wt% NaCl, after one-day hydrogen evolution, showed that Mg-10Dy alloy had the lowest corrosion rate of 0.18 mm/year (0.35 mg/cm^2/h). This low corrosion rate was fairly comparable with the value of 3.30 mm/year for the Mg-Dy alloy recorded in the present study, with the difference being attributed to differences in the test solution components and the sample geometries. It is worth mentioning that the corrosion rate of extruded WE43 alloy, used in degradable Mg implants, is reported as 1.35 mm/year [4], in between these Mg:Dy alloy and prototype Mg-Dy stent corrosion rates.

However, the present study has shown that the use of heavy and expensive Dy metal in Mg-alloys does not significantly influence the corrosion resistance of Mg-stents. Direct comparison between the annealed pure Mg-minitubes, produced by PVD, and the prototype Mg:Dy stent indicates that the two

devices have a similar corrosion potential, in the range of -1.57 V, and a breakdown potential of -1.38 V. Generally, the Mg-minitube surfaces were more prone to degradation than the Mg:Dy stent, being attributable to the more rapid dissolution and release of Mg^+ ions from these in-house fabricated devices. However, the very best corrosion performance of grain refined Mg-minitubes (annealed at 550°C) had a corrosion rate of 3.65 mm/year, comparable to the 3.30 mm/year for the commercial prototype Mg:Dy stent. Chemical examination of the corrosion products formed on the Mg:Dy stent revealed that no indication of incorporation of Dy, or other alloy elements, into the passivation layer, which refutes claims that the addition of RE can enhance the passivation of Mg by incorporation into the $Mg(OH)_2$ film.

PBS is a water based-salt solution, containing sodium phosphate (Na_2HPO_4), sodium chloride (NaCl), potassium chloride (KCl), potassium phosphate (KH_2PO_4), calcium chloride ($CaCl_2$) and magnesium chloride (Mg Cl_2). Hence, the main ions in PBS are Ca^{2+}, Na^+, K^+, Mg^{2+}, HPO_4^{2-}, $H_2PO_4^-$ and Cl^-, in addition to water molecules. The reaction of the Mg surface with water results in the formation of $Mg(OH)_2$ and H_2 bubbles. In addition, phosphate components such as calcium phosphate ($CaHPO_4$) and calcium carbonate ($CaCO_3$) formed from dissolved CO_2 are usually formed on the Mg-surface after immersion in body solution [269]. In this study, both the Mg-Dy stent struts and the Mg minitubes surfaces were covered with normal corrosion layers, consisting of $Mg(OH)_2$ and PO_4-components. Just after immersion, Mg dissolved in the PBS electrochemically, in the form of Mg^{2+} ions, while electrons were consumed at cathodic sites by decomposition of H_2O molecules in PBS. The anodic and cathodic reactions proceeded as follows:

$$Mg \rightarrow Mg^{2+} + 2e^- \qquad \text{(anodic reaction)} \qquad\qquad \text{Eq 4-1}$$

$$2H_2O + 2e^- \rightarrow 2OH^- + H_2 \qquad \text{(cathodic reaction)} \qquad\qquad \text{Eq 4-2}$$

Thus, the interaction of Mg with H_2O resulted in the just the formation of magnesium hydroxide ($Mg(OH)_2$), the total reaction for which is given by:

$$Mg + 2H_2O \rightarrow Mg(OH)_2 + H_2 \qquad \text{Eq 4-3}$$

With increasing concentration of pH and Mg^{2+} ions, a Mg-containing calcium phosphate may precipitate on the Mg surface, by the following reaction [270] [42]:

$$Ca^{2+} + HPO_4^{2-} + 2H_2O \rightarrow CaHPO_4 . 2H_2O \qquad \text{Eq 4-4}$$

$$10Ca^{2+} + 6HPO_4^{2-} + 8OH^- \rightarrow Ca_{10}(PO_4)_6 (OH)_2 + H_2O \qquad \text{Eq 4-5}$$

or

$$(10-x)Ca^{2+} + x\,Mg^{2+} + 6PO_4^{3-} + 2OH^- \rightarrow (Ca_{(10-x)}Mg_x)(PO_4)_6 (OH)_2 \quad \text{Eq 4-6}$$
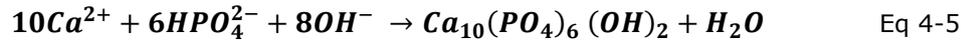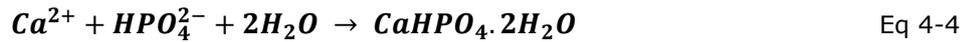
Hence, other phosphate components may form on a Mg-Dy stent, *i.e.* $Na_4Mg(PO_4)_2$, $Mg(PO_4)OH$ and $Mg_3(PO_4)_2$ [271], whilst high contents of Ca^{2+} and Mg^{2+} ions in solution might accelerate the deposition of calcium phosphate ($CaHPO_4$). The presence of phosphates as corrosion products within the degradation layer is associated with the composition of the corrosion solution [33].

The hydroxide and phosphate layers precipitated from reaction of the Mg surface with solution acted to reduce local corrosion attack, leading to fast passivation of the Mg minitubes. $Mg(OH)_2$, however, has a micro-porosity nature, hence the Mg corrosion can be reduced but not completely inhibited [272].

4.5 Summary

The morphologies and corrosion properties of a commercial prototype Mg-Dy-alloy stent and Mg minitubes produced by PVD and then grain refined by annealing, have been studied. The prototype stent had a zigzag pattern

formed by laser cutting from a single tube of Mg-alloy. The microstructure of this as-received stent consisted of $Dy_{0.5}Zr_{0.5}O_{1.75}$ segregated in an Mg matrix. The Mg-Dy-alloy stent showed straightforward dissolution properties before passivation in PBS under potentiodynamic polarization corrosion test conditions.

Structural enhanced Mg-minitubes were successfully produced by PVD-magnetron sputtering followed by annealing at varied temperatures. The microstructure, hardness and corrosion properties of the as-deposited and annealed Mg-minitubes, as a function of temperatures and environment conditions were investigated. The microstructure of the as-deposited Mg-minitube was characterised by columnar structures with porous and open grain boundaries. Differences in the annealing behaviours of the minitubes, processed under varied environment and temperatures, were revealed. Annealed Mg-minitubes, in the temperature range of 300-450°C, showed slight densification and recrystallization, being less brittle and having improved hardness. At an annealing temperature of 500°C, the Mg minitubes underwent grain refinement, leading to improved microhardness, while grain growth and slightly decreased microhardness was observed for Mg-minitubes annealed at 550-600°C. It is suggested that oxidation at the interfaces between the sequentially deposited Mg layers acted to stabilise the Mg columnar grains and limit recrystallisation of these zone T structures.

Large differences in the corrosion properties of Mg-minitubes, as a function of annealing temperatures, were found, when densification, recrystallisation and oxidation are considered. The as-deposited Mg-minitubes showed comparable high corrosion rates, due to the presence of columnar and open boundary structures. Significant improvement in the corrosion rate of annealed Mg minitubes was achieved by structure densification, combined with grain refinement and possibly oxidation of the Mg grains. The corrosion behaviour

of the Mg-minitubes investigated here showed that minitubes annealed at 550°C had the best corrosion resistance, comparable to that of the prototype Mg:Dy-alloy stent. The corrosion products covering the Mg:Dy stent and the Mg minitubes consisted of $Mg(OH)_2$ and PO_4-components.

In summary, it is clear that the corrosion performance of the Mg:Dy stent was determined by its microstructure, which may be improved further by suitable surface treatment, *e.g.* PVD coatings. The Mg-minitubes fabricated by PVD process here could provide performance to the commercial alloy stent, in terms of corrosion behaviour, due to the ability to densify, refine and homogenise the microstructure. Nevertheless, the Mg minitubes remain limited for practical use because of their brittle nature and high dissolution rates which are presently insufficient for long term, clinical function.

It is evident that there are many factors influencing the development and performance of biodegradable stents. The RF-MS fabrication method offers a wide degree of freedom, for the production of tailored microstructures, to improve Mg mechanical properties and corrosion behaviour. The next stage of the investigation relates to the potential of appropriate coating and near surface modification procedures, to impart improved corrosion performance. Accordingly, attention is now given to bulk pure Mg, subjected to various PVD coatings and near surface modification procedures, to achieve appropriately defined microstructures with electrochemical properties to delay the onset of corrosion and reduce the rate of corrosion, *e.g.* through enhanced passivation.

CHAPTER 5 PVD coatings on Mg

5.1 Introduction

The modification of surface characteristics using coatings is a common strategy for many technological applications [273]. For example, ceramic alumina (Al_2O_3), in thin film form, may be used as a diffusion barrier and for corrosion and wear protection [274]. The applicability of alumina coatings in different environments requires that appropriate functional properties be developed, which can depend strongly on the process parameters applied [275]. For example, thin ($<$ 10 nm) amorphous alumina is the most common form of aluminium oxide [276], whilst oxidation at temperatures above 400°C in a reactive (oxygen containing) environment can lead to the development of films in the form of crystalline structures of α-, κ- and χ-Al_2O_3 (of the α- Al_2O_3 series) and δ, η and γ-Al_2O_3 the (of γ-Al_2O_3 series) [277, 278]. In certain cases, metastable crystalline oxide phases may be preferred thermodynamically, *e.g.* due to the low surface energy of γ-Al_2O_3 compared to α-Al_2O_3 [279].

Direct current (DC) reactive sputtering of Al in an oxygen/argon atmosphere can produce stoichiometric Al_2O_3 [280]. However, aluminium oxide is electrically insulating and tends to charge and discharge during the DC reactive sputtering process, which can result in arcing [280]. Hence, radio frequency magnetron sputtering (RF-MS) is attracting attention as a promising technique for the deposition of thin film materials, due to its applicability to insulating materials, as well as metals and alloys, along with high deposition rates making it suitable for large-scale film deposition. The approach investigated here involves the direct deposition of Al followed by subsequent annealing *ex situ*, to convert the near surface layer to Al_2O_3.

Hydrogenated amorphous silicon (a-Si:H) is another interesting system for Mg coating applications, with Si being an essential trace element in tissue formation and other metabolic processes [281]. For example, Dahmen *et al.* [282] found that a-Si:H and sub-oxide silicon films are biocompatible, whilst Liu *et al.* [283] concluded that a-Si:H could enhance the precipitation of bone like apatite. The RF-MS technique may be used to deposit uniform, high quality a-Si:H films on metal surfaces [281].

This Chapter presents a fundamental investigation of Al- and Si-based coatings on Mg surfaces, PVD formed in Ar or Ar/H_2 environments, followed by heat treatment in air, as a route towards the development of biocompatible oxide coatings. To increase further the propensity of Al to oxidise, H_2 was used with Ar as the sputtering gas. Thin films of Al and Al-H, and a-Si:H, deposited by RF-MS onto Mg substrates were investigated. The effects of different gases and applied substrate bias on the phase stability of the developed Al films were explored, along with their thermal oxidation in open atmosphere, as a function of temperature. The developed coating morphologies were investigated using the combined techniques of SEM/EDS, GA-XRD, XPS and FTIR, and correlated with the corrosion behaviours of the respective sample sets investigated, using potentiodynamic and/or immersion tests in phosphate buffered saline (PBS) solution. Table 5-1 summaries the sample sets investigated in this PVD coatings section.

Table 5-1 Summary of PVD coated Mg sample sets investigated.

Sample code	Coating	Deposition mode	Working gas	Flow rate / sccm	Annealing temp / °C	Corrosion rate mm/year
Mg	-	-	-	-	-	0.91±0.1
Al					-	1.60±0.3
Al$_{300}$	Al	RF	Ar	47.6	300	6.62±0.3
Al$_{450}$					450	0.23±0.1
Al-H					-	5.48±0.6
Al-H$_{300}$	Al	DC	Ar / H	35.6 / 31.6	300	5.71±1.8
Al-H$_{450}$					450	7.76±1.1
Mg	-	-	-	-	-	0.11±0.01
a-S:H	Si	RF	Ar / H	34.9 / 28.0	-	0.05±0.02

5.2   Al and Al-H coatings

Al and Al-H coatings were deposited on Mg substrates by RF-MS, as described in Section 3.3.2.2. The as-deposited coatings were annealed in air at 300°C for 5 h, or 450°C for 2 h (samples denoted as Al_{300}, Al_{450}, $Al-H_{300}$ and $Al-H_{450}$, respectively). Morphological investigations of the as-deposited and thermally annealed coatings are presented in following section. Complementary potentiodynamic polarization corrosion tests, performed for both Al and Al-H sample sets, are described in section 5.2.2.

5.2.1 Characterisation of Al and Al-H coatings

The as-deposited and thermally annealed coatings were characterised using the combined techniques of XRD, SEM/EDS and XPS, in a mixture of plan-view and cross-sectional geometries.

5.2.1.1 XRD of Al and Al-H coatings

Figure 5-1 presents XRD patterns of the as-deposited and heat-treated Al and Al-H coatings. In all cases, the patterns indicated the presence of face centred cubic (fcc) Al grains on polycrystalline Mg. Slight evidence for the presence of some Al_2O_3 was noted for the Al coating following heat-treatment at 300°C, whilst Al and Al-H coatings heat-treated at 450°C were dominated by the presence of MgO.

Intensity variations within these XRD patterns reflect a random distribution of grain orientations within the coatings and substrate. The XRD peaks for the as-deposited samples were found to be shifted slightly from their standard positions, towards lower 2θ angles for the case of as-deposited Al coatings and towards higher angles for as-deposited Al-H coatings (Figure 5-1). The

shift in 2θ values, indicative of slight lattice distortions, returned lattice parameters of 4.0715 Å and 4.0413 Å for Al and Al-H, respectively, as compared to the standard Al lattice parameter of 4.0494 Å [72] (Table 5-2).
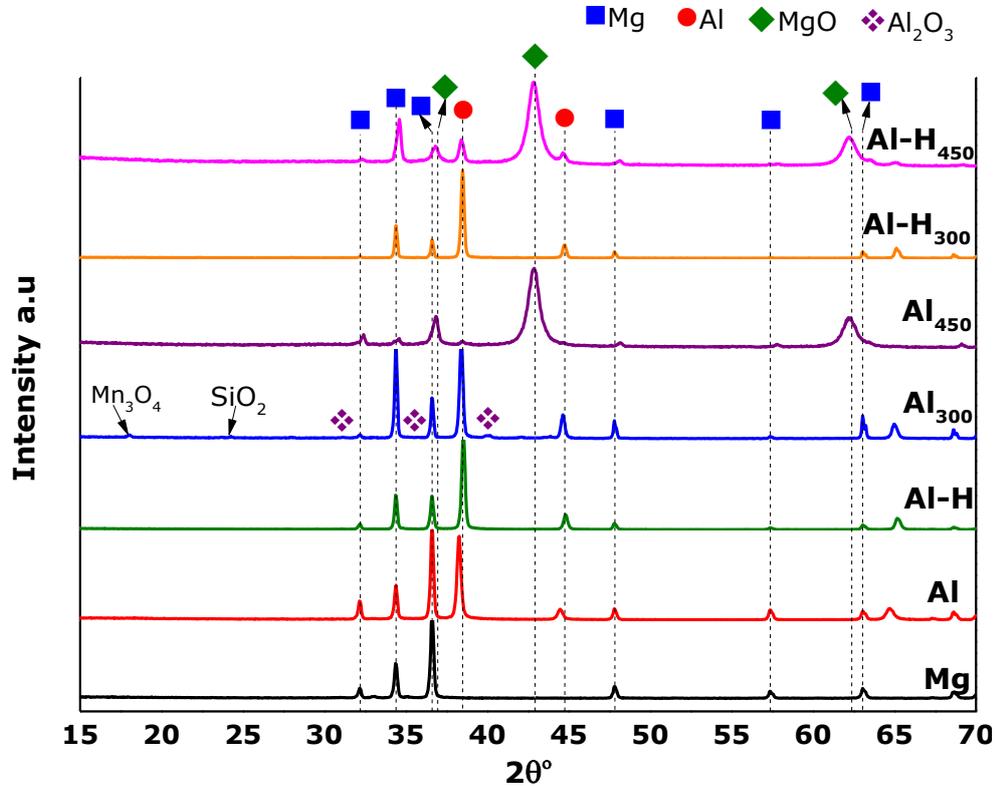
Figure 5-1 XRD patterns of as-deposited and heat-treated Al and Al-H coatings on Mg.

In order to promote the growth of a surface oxide film, the Al and Al-H coated samples were annealed in air at 300°C and 450°C.

Figure 5-1 shows XRD patterns for Al_{300} and Al-H$_{300}$ coatings heat-treated at 300°C, with slight evidence for the formation of some crystalline Al_2O_3 for the Al_{300} sample, but no evidence for the case of the Al-H$_{300}$ sample contrary to expectation. The Al XRD peaks were shifted slightly from their as-deposited positions, returning lattice parameters of 4.0554 Å and 4.0462 Å for Al_{300} and Al-H$_{300}$, respectively (Table 5-2).

The average grain sizes of the as-deposited Al and Al-H coatings were 64 ± 1.0 nm and 94 ± 13 nm, respectively, as determined using the Scherrer equation (Table 5-2). The grain sizes for the Al_{300} and Al-H$_{300}$ coatings were

found to have increased slightly with heat treatment, to 89 ± 1.0 nm and 136 ± 10 nm, respectively, indicative of a certain level of grain growth.

In addition to Mg, Al and some small peaks attributable to low levels of Al_2O_3, evidence for the presence of small quantities of Mn_3O_4 and SiO_2 were also detected (being attributed, tentatively, to the substrate polishing process and some unknown source of cross-contamination) (Figure 5-1 (Al_{300}), arrowed), with these species being detectable also for the as-deposited coatings (see SEM/EDS analyses – section 5.2.1.2).

Conversely, XRD patterns of the annealed Al_{450} and $Al-H_{450}$ coatings demonstrated the dominance of MgO, whilst no Al_2O_3 was observed. The calculated grain sizes of MgO associated with these Al_{450} and $Al-H_{450}$ samples were 39.7 ± 0.2 nm and 30.3 ± 0.1 nm, respectively.

The XRD peaks for the Mg substrate were very sharp, making it impracticable to estimate grain size from peak broadening, being indicative of grain sizes $\gg 100$ nm, *i.e.* beyond the grain size limit that can be determined by the Scherrer equation. Also, the Mg peaks at $10\bar{1}0$, 0002 and $10\bar{1}1$ showed a small shift in their position to higher angle, as compared with that of the starting material, attributed to slight lattice distortion of the near surface Mg, following annealing at $450°C$ and growth of an MgO layer at the coating/substrate interface.

In all these samples, there was no direct evidence for the partial hydrogenation of Al or the Mg substrate, with just a number of small peaks from the heat-treated coatings being consistent with the development of a slight amount of polycrystalline Al_2O_3, most clearly in the case of the Al_{300} coating. The estimated grain sizes, lattice parameters and lattice distortions of the main phases in these Al/Mg and Al-H/Mg samples are summarised in Table 5-2.

Table 5-2 Lattice parameter, lattice distortion and average grain sizes for Al and Al-H coatings on Mg substrates, as deposited and following annealing.

Samples	Phase	Structure	Lattice parameter / Å	lattice distortion	Grain size / nm
Al	Al	fcc	4.0715	0.0055 ± 0.0002	64 ± 1.0
Al$_{300}$			4.0554	0.0018 ± 0.0003	89 ± 1.0
Al$_{450}$			4.0514	0.0005 ± 0.0001	90 ± 4.8
	MgO	halite	4.2212	-	39.7 ± 0.2
Al-H	Al	fcc	4.0413	-0.0020 ± 0.0009	94 ± 13
Al-H$_{300}$			4.0462	-0.0004 ± 0.0002	136 ± 10
Al-H$_{450}$			4.0547	0.0013 ± 0.0001	49.1 ± 0.1
	MgO	halite	4.2233	-	30.3 ± 0.1

MgO adopts the halite (rock salt) structure of NaCl

Unclear why there is a decrease in Al-H$_{450}$ grain size

5.2.1.2 SEM/EDS of Al and Al-H coatings

Figure 5-2 (a-d) presents SE images showing generalised topographic features of these Al and Al-H coatings, as-deposited on polished Mg surfaces in Ar and Ar/H$_2$ environments, respectively. The coatings followed the Mg surface profiles resulting from substrate preparation, *i.e.* striations / grooves and polishing marks (*e.g.* Figure 5-2(c), arrowed). Further, the Al-H coating morphology was found to be affected by the sputtering gas, with the suggestion that dark, buckled regions distributed over the Al-H/Mg surface (Figure 5-2 (b), arrowed) were caused by trapped H$_2$O\H$_2$ within the deposited coating escaping after exposure to air. In addition, the high magnification SE images of Figure 5-2(b,d) indicate a random distribution of small particles on these Al and Al-H coatings. EDS investigation showed these particles to be SiC artefacts, *i.e.* polishing debris from the abrasive paper, along with other contaminant particles, emphasising the practical difficulty of preparing pristine surfaces of mechanically polished, soft Mg. The as-deposited Al and Al-H coatings were found also to be not strongly adhered to the Mg substrates, with peeling-off of coating material observed towards the edges of the Mg discs being attributed to the effects of residual strain. The

poor adhesion of Al coatings to these polished Mg surfaces suggests that additional chemical cleaning protocols might be beneficial, prior to coating.
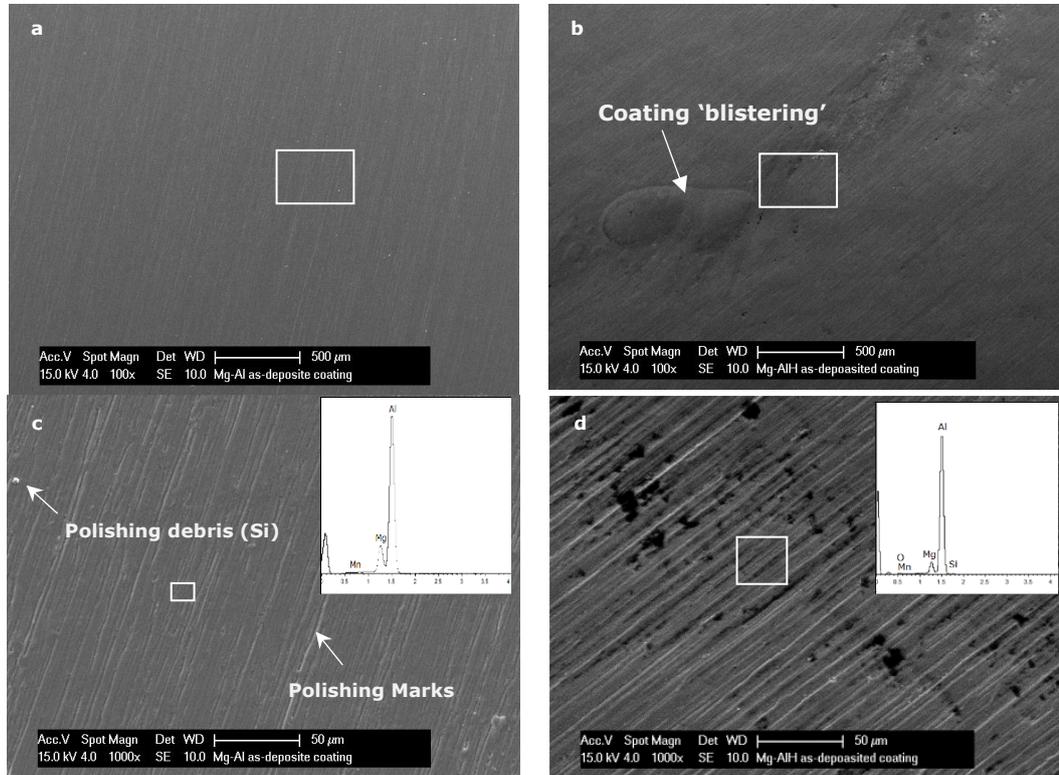
Figure 5-2 SE images of as-deposited coatings on polished Mg substrates: (a) Al deposited in Ar; (b) Al-H deposited in Ar/H$_2$; (c) high magnification of as-deposited Al with EDS inset; and (d) high magnification, as-deposited Al-H, with EDS inset.

The Al and Al-H deposits were heat-treated in air at 300°C and 450°C, with a view to converting the coatings to ceramic Al$_2$O$_3$. Figure 5-3(a-d) are representative of the Al$_{300}$, Al$_{450}$, Al-H$_{300}$ and Al-H$_{450}$ surface morphologies, after thermal treatment. After heating at 300°C for 5 h, the Al$_{300}$ coating surface (Figure 5-3(a)) showed bubble-form morphology, not seen for the as-deposited coatings, and some delamination, being attributed tentatively to the release of adsorbed gas (O$_2$/Ar) from the Al/Mg interface during heating. In comparison, the Al$_{450}$ coating treated at the elevated temperature of 450°C had the appearance visually of a very brittle, grey layer, with enhanced levels of coating cracking and delamination (Figure 5-3(b)), leaving the substrate

surface unprotected. SE images of Al-H$_{300}$ samples annealed at 300°C for 5 h (Figure 5-3(c)) showed the development of smoother, more continuous coatings, with good adherence to the substrate. However, Al-H$_{450}$ coatings heat-treated at 450°C were found to be very patchy, showing aggregated surface particles that detached easily from the Mg substrate (Figure 5-3(d)).
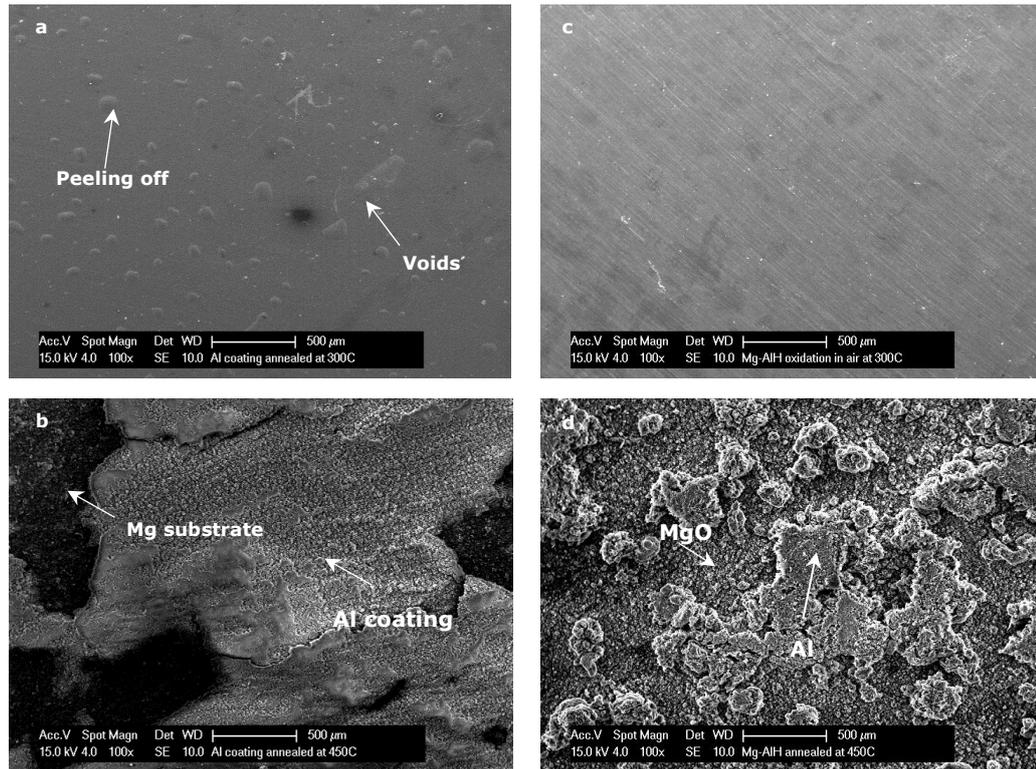
Figure 5-3 SE images of Al and Al-H coatings annealed in open air, at 300°C for 5 h and 450°C for 2 h: (a) Al$_{300}$; (b) Al$_{450}$; (c) Al-H$_{300}$ and (d) Al-H$_{450}$.

Figure 5-4(a,b) presents representative SE micrographs of fractured cross-sections of as-deposited Al and Al-H coatings on coverslip glass, showing their thicknesses to be 2.2 ± 0.02 μm and 1.2 ± 0.02 μm, respectively, for the RF-MS process parameters used in this instance. Complementary SEM and EDS analyses indicated also that Al coating thicknesses were dependent on the deposition gas and time.
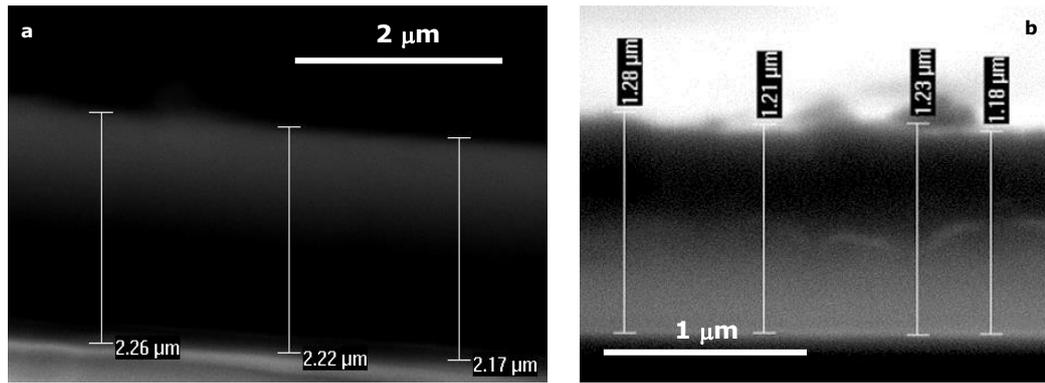
Figure 5-4 Cross-sectional SE images of as-deposited: a) Al, and b) Al-H coatings, showing how thickness measurements were performed.

EDS data was collected for the as-deposited and thermally treated Al and Al-H coatings in plan-view orientation, in order to assess the compositions of the coatings as a function of temperature (Table 5-3). No oxide was associated with the as-deposited Al coating, whilst a small amount of Al_2O_3 was associated with this coating annealed at 300°C, consistent with XRD data. The as-deposited Al-H coating showed signs of an initial Al_2O_3 layer, but not after annealing at 300°C, again consistent with XRD data. Conversely, both Al and Al-H sample sets annealed at 450°C were dominated by the presence of MgO, demonstrating that care is need to avoid 'over-processing' of these Mg samples. Trace levels of Si and Mn were detected also, being attributed to SiO_2 and Mn_3O_4 contamination artefacts.

Complementary EDS elemental maps of the Al-H$_{300}$ coating after thermal treatment at 300°C are shown in Figure 5-5, in cross-sectional geometry, illustrating the fairly uniform distribution of Al throughout this coating; some intermixing of Al and Mg, *i.e.* a level of alloying of Al with the near surface of the Mg substrate, providing for good coating adhesion; and a uniform distribution of O throughout the Al coating and into the Mg substrate.

Table 5-3 Compositions of the Al and Al-H coatings, as-deposited and thermally treated (EDS data; plan-view sample geometry).

Element	Composition at%					
	Al	Al_{300}	Al_{450}	Al-H	$Al-H_{300}$	$Al-H_{450}$
O	-	2.65	60.61	3.91	3.80	58.65
Mg	19.14	12.81	38.16	6.79	5.47	36.82
Al	80.46	84.06	1.24	88.36	90.73	4.53
Si	-	-	-	0.63	-	-
Mn	0.40	0.48	-	0.30	-	-
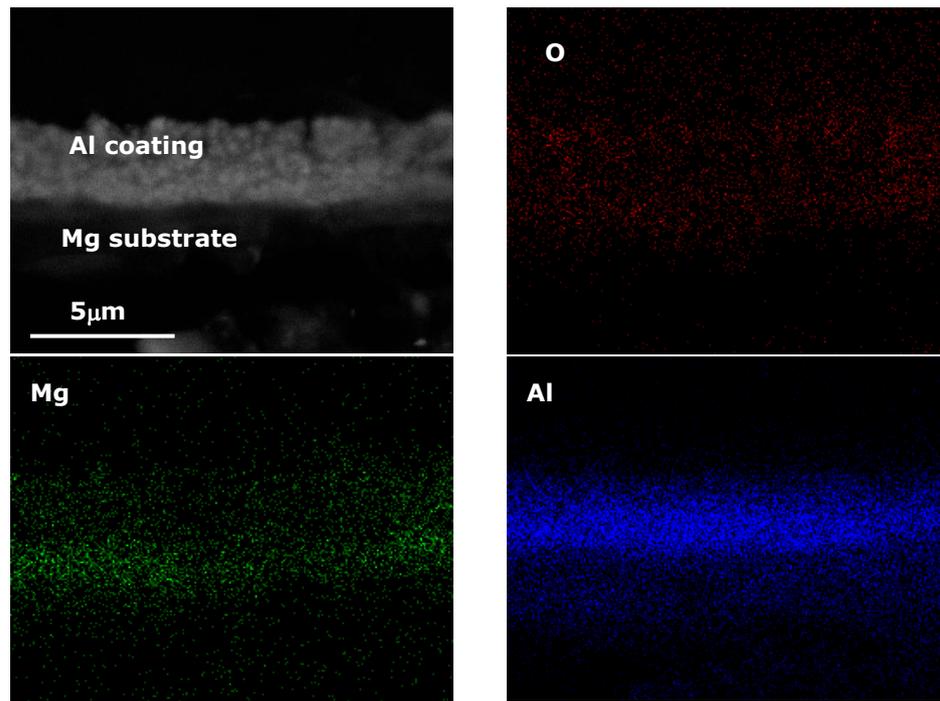
Figure 5-5 EDS elemental maps of $Al-H_{300}$ coated Mg in cross-section, after heat treatment at 300°C

5.2.1.3 XPS of Al and Al-H coatings

Appraisal of the chemistry of the top surfaces of the as-deposited and heat-treated Al and Al-H coatings was performed using XPS, to complement the XRD observations. Figure 5-6(a-h) presents a survey scan and detailed Mg_{2p}, Al_{2p} and O_{1s} spectra for the as-deposited coatings. Both sample sets provided evidence for the presence of Al, Mg and high intensity O peaks (Figure 5-6(a,e)). High-resolution scans allowed these peaks to be attributed to Al_2O_3, MgO and Al-Mg alloy at the surface.

The Al_{2p} scans (Figure 5-6(c,g)) indicated the spontaneous formation of Al_2O_3 at the Al and Al-H surfaces, with associated binding energies (BE) at 74.33 eV and 74.42 eV, respectively, in addition to varying levels for an Al-Mg alloy (Figure 5-6(c,g)), attributed predominantly to metallic Al (BE of 72.7 eV) slightly shifted to 71.88 eV (for Al) and 72.13 eV (for Al-H) due to the presence of small quantities of Mg in solid solution.

The Mg_{2p} high resolution scans (Figure 5-6(b,f)) confirmed also the presence of surface MgO, for both Al and Al-H coatings, at BE of 50.49 eV and 50.39 eV, respectively. Signatures due to O_{1s} (Figure 5-6(d,h)) revealed also the oxide phases of Al and Mg, with major peaks for Al_2O_3 at 532.15 eV and 531.87 eV, and minor peaks for MgO at 530.99 eV and 531.18 eV, respectively. The peak intensities associated with Al_2O_3 and Mg-Al for the as-deposited Al-H coating were reversed to that observed for the Al coating (Figure 5-6(e)), suggesting that the presence of H_2 acted to restrict the development of Al-Mg and was associated with a slight increase in the proportion of Al_2O_3, at the sample surface.

X-ray photoelectron spectra for the Al and Al-H coatings, heat-treated at 300°C and 450°C, are presented in Figure 5-7(a-h) and Figure 5-8(a-h), respectively. The oxidation levels for Al_2O_3 were enhanced slightly following annealing at 300°C (Figure 5-7(a,e)), whilst MgO dominated the spectra following annealing at 450°C (Figure 5-8(b,f)).
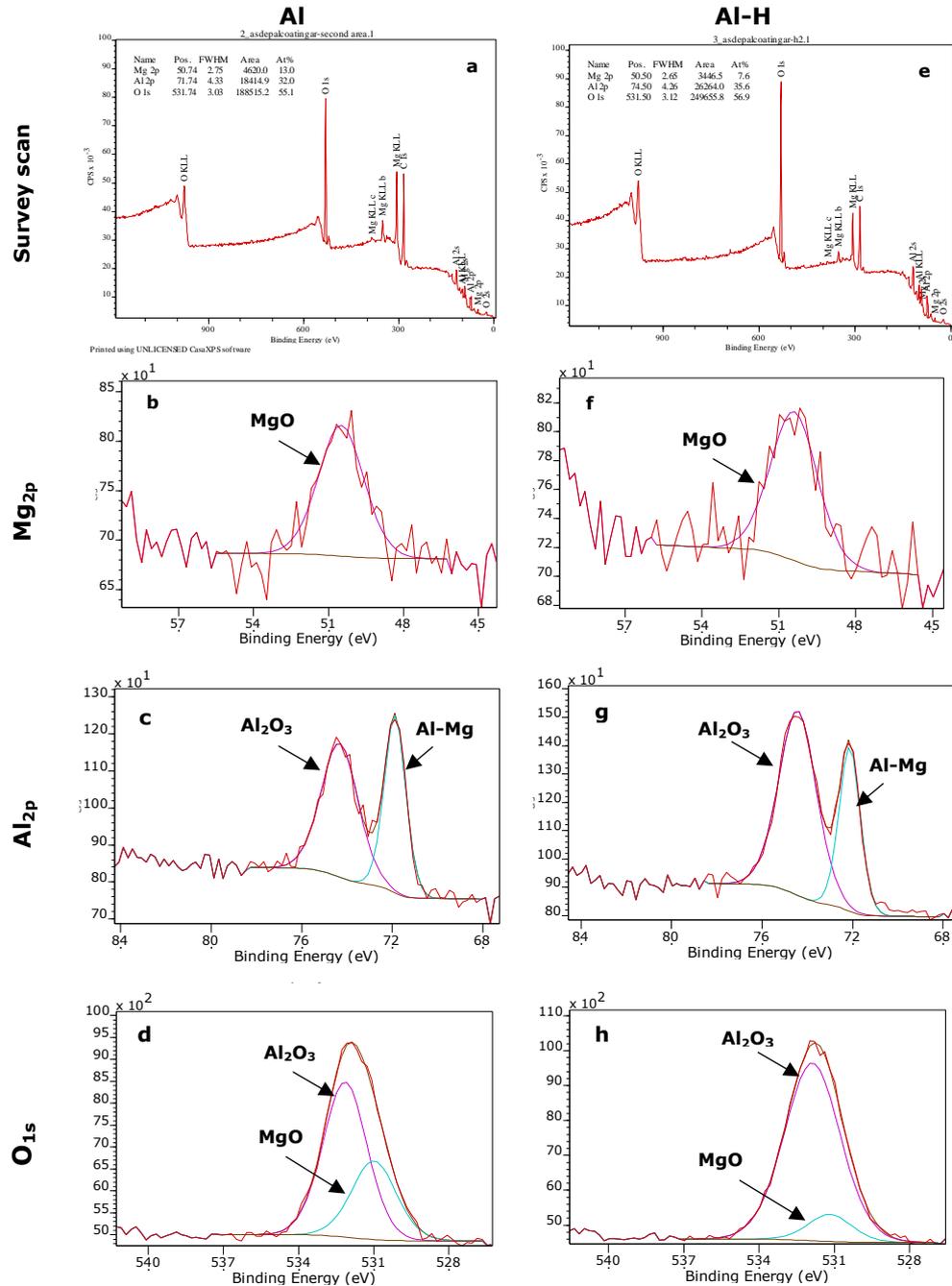
Figure 5-6 Survey and HR-XPS of as-deposited Al: (a) survey scan; (b) Mg$_{2p}$; (c) Al$_{2p}$; and (d) O$_{1s}$; and Al-H: (e) survey scan; (f) Mg$_{2p}$; (g) Al$_{2p}$; and (h) O$_{1s}$.

In particular, Al was found in both metallic and oxide forms. Figure 5-7(c,d,g,h) confirmed the formation of Al$_2$O$_3$ from both Al$_{2p}$ at BE of 71.51eV and 71.73eV, and O$_{s1}$ peaks at BE of 531.92eV and 531.87eV, for both Al and Al-H coatings annealed at 300°C, respectively. Deconvolution of the Mg$_{2p}$ peak (Figure 5-7(b,f)) indicated the presence of some Mg(OH)$_2$ and

143

Mg-Al solid solution, again for both Al_{300} and $Al-H_{300}$ surfaces. However, the levels of Al-Mg alloy formed during deposition were found to decrease for both coatings when annealed at 300°C.

Figure 5-7 Survey scan and HR-XPS of coatings annealed at 300°C: (a-d) Al_{300}; and (e-h) $Al-H_{300}$.
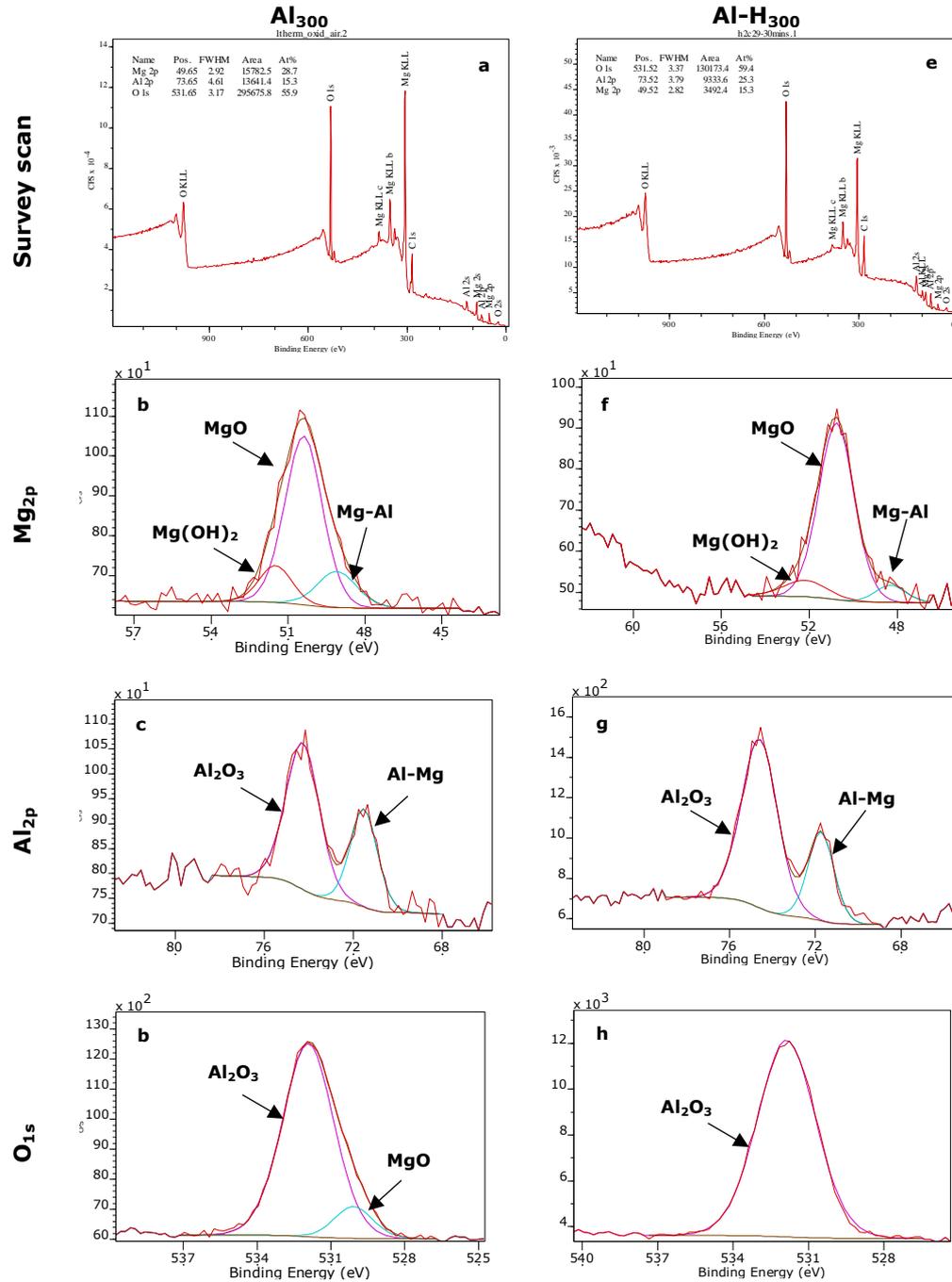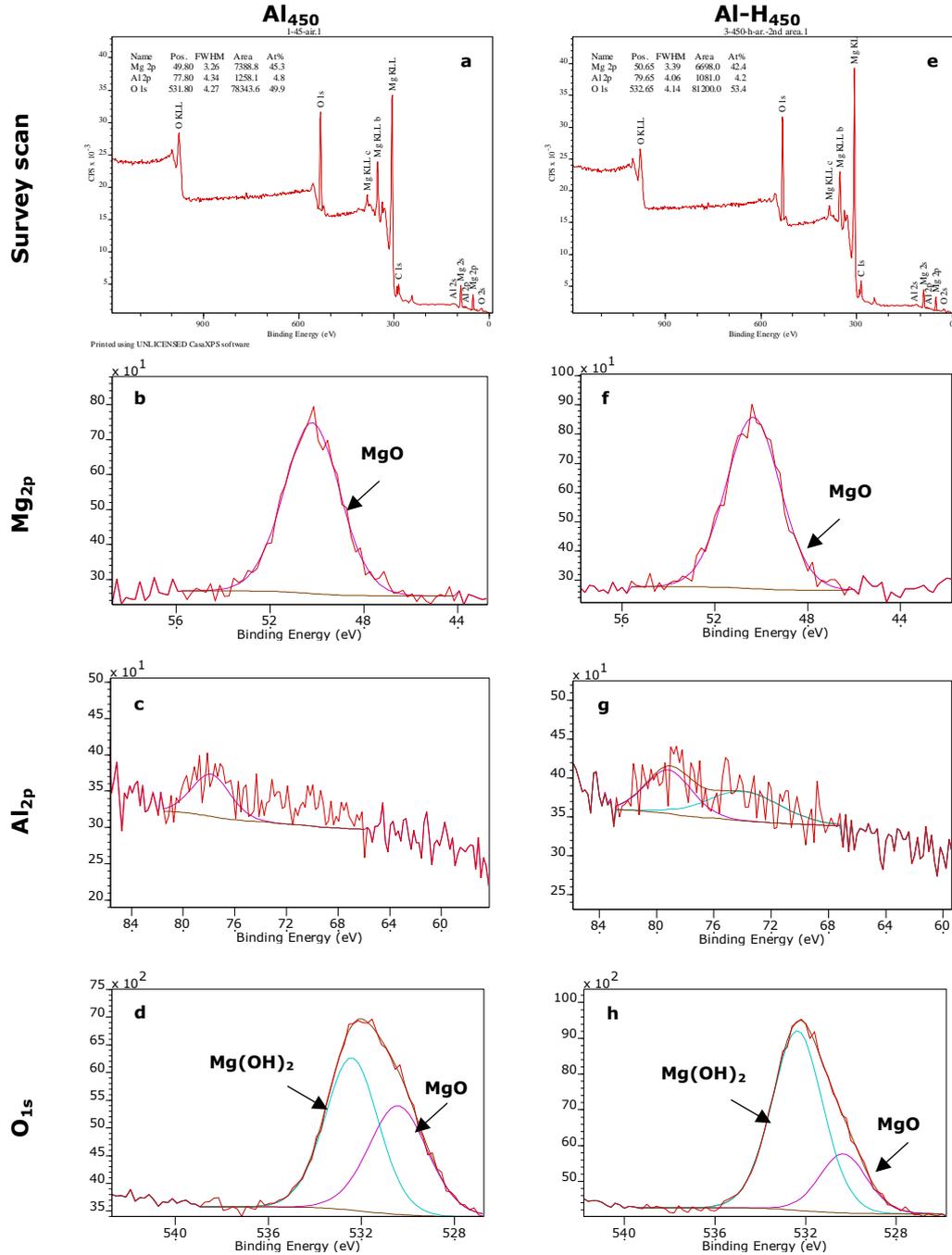
Figure 5-8 Survey and HR-XPS spectra of (a-d) Al_{450} and (e-h) $AlH_{450,}$ annealed at 450°C.

The survey and HR-XPS scans for both Al_{450} and Al-H$_{450}$ samples annealed at 450°C were very similar (Figure 5-8(a-g)), with Mg_{2p} and O_{1s} peaks being dominated by MgO and Mg(OH)$_2$ (Figure 5-8(b,f,d,h)). There was no indication of the presence of metallic Al or Al_2O_3 at the sample surfaces, with the Al_{2p} signal being reduced to the background level (Figure 5-8(c,g)). This finding was also consistent with the tendency for the Al coatings to

delaminate under these annealing conditions, combined with the dominance of MgO formation at these elevated temperatures.

Table 5-4 presents a summary of the BE assignments for the main surface components of these as-deposited and annealed Al and Al-H coatings.

Table 5-4 Summary of binding energy assignments for these Al and Al-H coatings.

Sample ID	BE / Mg_{2p}			BE / Al_{2p}		BE / O_{1s}		
	Mg-Al	MgO	$Mg(OH)_2$ $Mg\,CO_3$	Al-Mg	Al_2O_3	MgO	Al_2O_3	$Mg(OH)_2$
Al	-	50.49	-	71.88	74.33	530.99	532.15	-
Al-H	-	50.39	-	72.13	74.42	531.18	531.87	-
Al$_{300}$	49.09	50.39	51.48	71.51	74.27	530.08	531.92	-
Al-H$_{300}$	48.31	50.67	52.19	71.73	74.60	-	531.87	-
Al$_{450}$	-	50.35		-	-	530.34	-	532.36
Al-H$_{450}$	-	50.44		-	-	530.33	-	532.41

5.2.2 Corrosion performance of Al and Al-H coatings

5.2.2.1 Potentiodynamic polarization tests

Potentiodynamic polarization tests were used to appraise the corrosion behaviour of the as-deposited and heat-treated Al and Al-H coated Mg samples. Figure 5-9(a,b) presents typical open circuit potential (OCP) and potentiodynamic polarization curves for polished Mg; as-deposited Al and Al-H coatings on Mg; and furnace annealed Al$_{300}$, Al-H$_{300}$, Al$_{450}$ and Al-H$_{450}$ coatings on Mg, immersed in aerated PBS (comprising KCl, NaCl, KH_2PO_4 and Na_2HPO_4, free of Ca and Mg for stability), at 37°C. Technical values extracted from these curves are summarized in Table 5-5. The OCP data showed that polished Mg substrates exhibited the lowest rest potential of -1910±5 mV, becoming stable after 20 minutes. All the coatings as-deposited and after annealing showed more noble behaviour, demonstrating increased resistance to the onset of corrosion, with the as-deposited Al-H and heat-treated Al-H$_{450}$

having the most resistance at -1483±2 mV and -1435±2 mV, respectively. The polarization curves demonstrated significant variation in the behaviour of the coatings during corrosion (Figure 5-9 b). The polished Mg surface showed normal cathodic hydrogen evolution, with the development of a typical Tafel region (I). Fast passivation without the effect of any galvanic cell acted to slow down the generation of Mg^{2+} ions during the onset of corrosion (II), whilst rapid anodic current generation (III) correlated with the breakdown of the $Mg(OH)_2$ passivation film.

The coated Mg surfaces all showed positively offset corrosion potentials as compared to the polished Mg substrates (Figure 5-9(b)). The as-deposited Al and Al-H coated samples both showed anomalous Tafel regions consistent with a mixture of initial corrosion and passivation processes (IV), followed by rapid anodic current generation and extensive corrosion (V). The heat-treated $Al-H_{300}$ and $Al-H_{450}$ coatings similarly showed an anomalous Tafel region and extensive corrosion response. However, the heat-treated Al_{300} and Al_{450} coatings showed more uniform behaviour, with a conventional Tafel region (VI) prior to rapid corrosion for Al_{300} and an active-passive trend for Al_{450}.

Values for corrosion current density (i_{corr}) were obtained from the polarization curves by extrapolating the Tafel regions, whilst corrosion rates (CR) were determined using the standard equation ($22.85 \times i_{corr}$). Despite having the lowest E_{corr} value, polished Mg surfaces passivated quickly with an i_{corr} of 0.04±0.01 mA/cm^2 before the onset of corrosion at 0.91±0.1 mm/year (Table 5-5). Intriguingly, the i_{corr} values for the as-deposited Al and Al-H coatings and heat-treated Al_{300}, Al_{450} $Al-H_{300}$ and $Al-H_{450}$ coatings showed improved resistance to the onset of corrosion, but much more rapid initial corrosion rates once established, as compared with polished Mg. The heat-treated Al_{450} and as-deposited Al showed the slowest corrosion rates of 0.23±0.1 mm/year and 1.60±0.3 mm/year respectively, as compared to the heat-treated Al_{300}

coating and the as-deposited and heat-treated Al-H$_{300}$ and Al-H$_{450}$ coatings (Table 5-5).
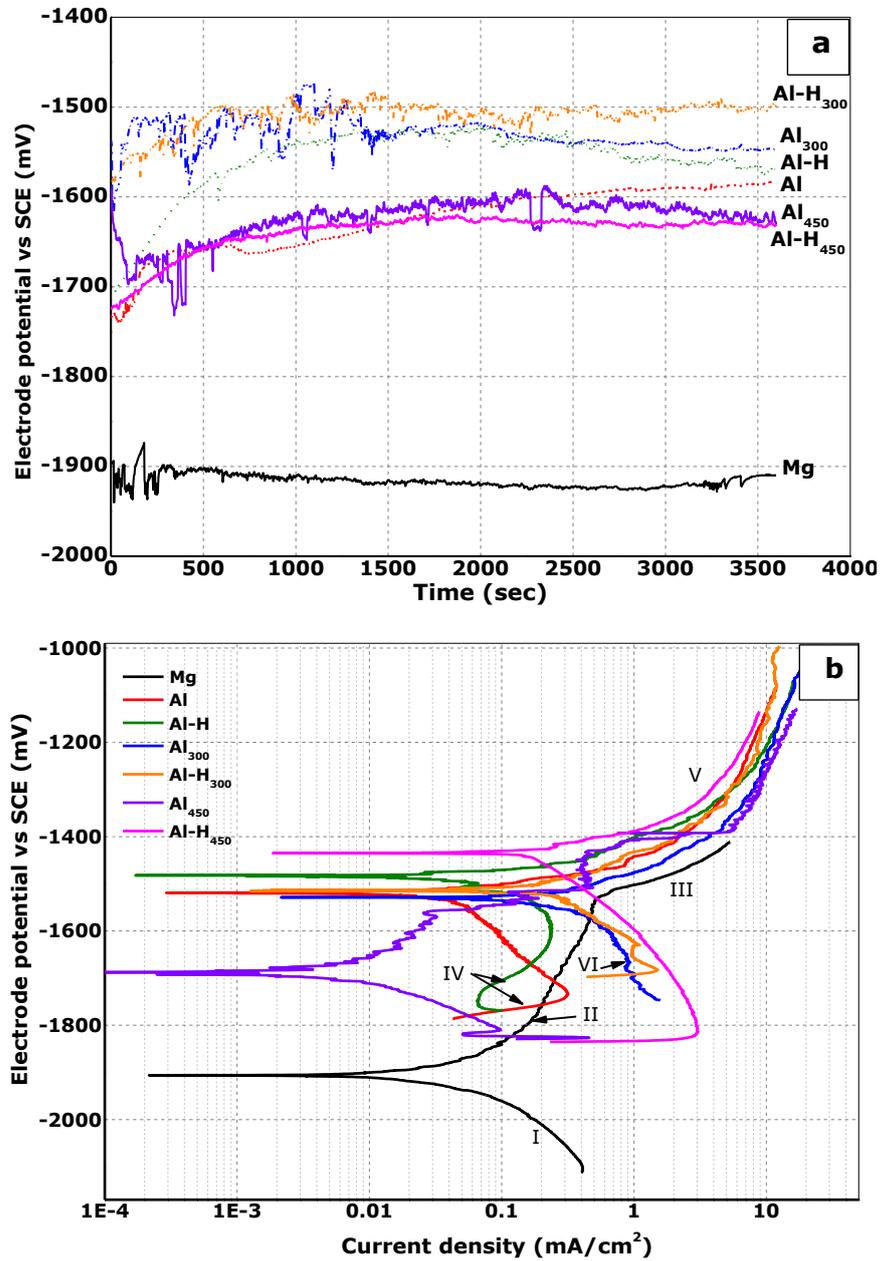
Figure 5-9 (a) Open circuit potential; & (b) potentiodynamic polarization curves for as-deposited Al and Al-H coatings on Mg; and heat-treated Al$_{300}$, Al-H$_{300}$, Al$_{450}$ and Al-H$_{450}$ coatings, furnace annealed in air at 300°C and 450°C; immersed in PBS at 37°C.

Table 5-5 Corrosion parameters for the Mg, as-deposited and heat-treated Al and Al-H coatings on Mg surfaces

Sample	OCP mV	E_{corr} mV	i_{corr} mA/cm^2	CR mm/year
Mg	-1910±5	-1907±2	0.04±0.01	0.91±0.1
Al	-1584±5	-1519±2	0.07±0.01	1.60±0.3
Al-H	-1570±5	-1483±2	0.24±0.02	5.48±0.6
Al$_{300}$	-1547±5	-1530±2	0.29±0.01	6.62±0.3
Al-H$_{300}$	-1505±5	-1515±2	0.25±0.01	5.71±1.8
Al$_{450}$	-1624±5	-1435±2	0.01±0.01	0.23±0.1
Al-H$_{450}$	-1632±5	-1686±2	0.34±0.04	7.76±1.1

Mg represents the corrosion rate of the as-polished surface without the galvanic effect of the Al coating.

5.2.2.2 Characterisation of as-deposited Al and Al-H coatings following corrosion

The BSE images of Figure 5-10(a,b) illustrate the corrosion morphologies of the as-deposited Al and Al-H coatings on Mg, in plan-view and cross-sectional geometries, respectively, after potentiodynamic polarisation corrosion tests in aerated PBS (from -200 mV to +500 mV relative to OCP).

The Al-H surface exhibited more uniform corrosion and developed a thicker layer of corrosion products. EDS investigation showed the presence of a high content of oxygen and Mg, indicative of Mg(OH)$_2$ (Figure 5-10(a) (Spot 1)), along with a significant amount of phosphate (PO$_4$), but much less Al, suggesting the formation of a protective layer of Mg$_2$(PO$_4$)OH (Figure 5-10 (a) (Spot 2)). Remnant patches of the Al-H coating revealed an Al(OH)$_3$ corrosion product (Figure 5-10(a), arrowed regions).

Figure 5-10(b) presents a BSE image of the as-deposited Al coating, in cross-section, following corrosion. The associated EDS line profile indicted that the near surface layer comprised a mixture of Mg(OH)$_2$ and Al(OH)$_3$ corrosion products. Hence, the evidence suggests that the Mg substrate corroded first and formed an Mg(OH)$_2$ corrosion product at the Al/Mg interface, in turn leading to delamination of the Al coating. It is likely that pin-holes on the Al

coating acted as anodic sites, facilitating direct exposure of the Mg substrate to PBS. The $Mg(OH)_2$ passivation layer had a porous nature (Figure 5-10(b), arrowed), making it unable to protect effectively the Mg substrate from the penetration of harmful Cl^- ions. Na was detected also throughout the corrosion layer.
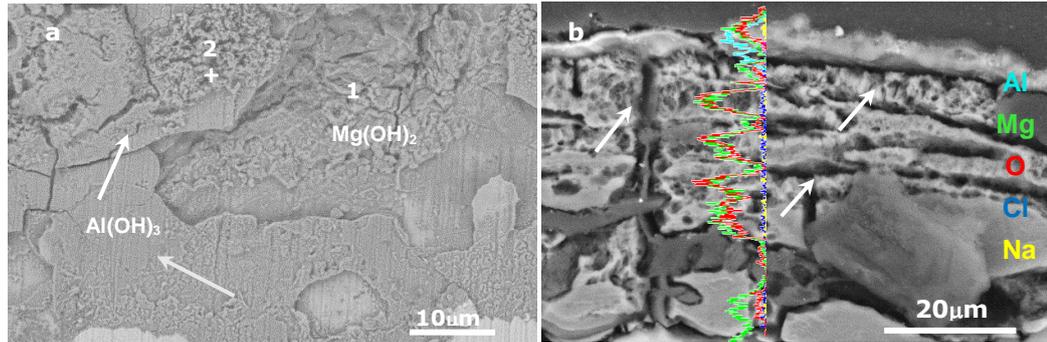
Figure 5-10 BSE images of corrosion morphologies of: (a) as-deposited Al-H in plan-view; and (b) as-deposited Al coating in cross-sectional view, after potentiodynamic polarization corrosion testing.
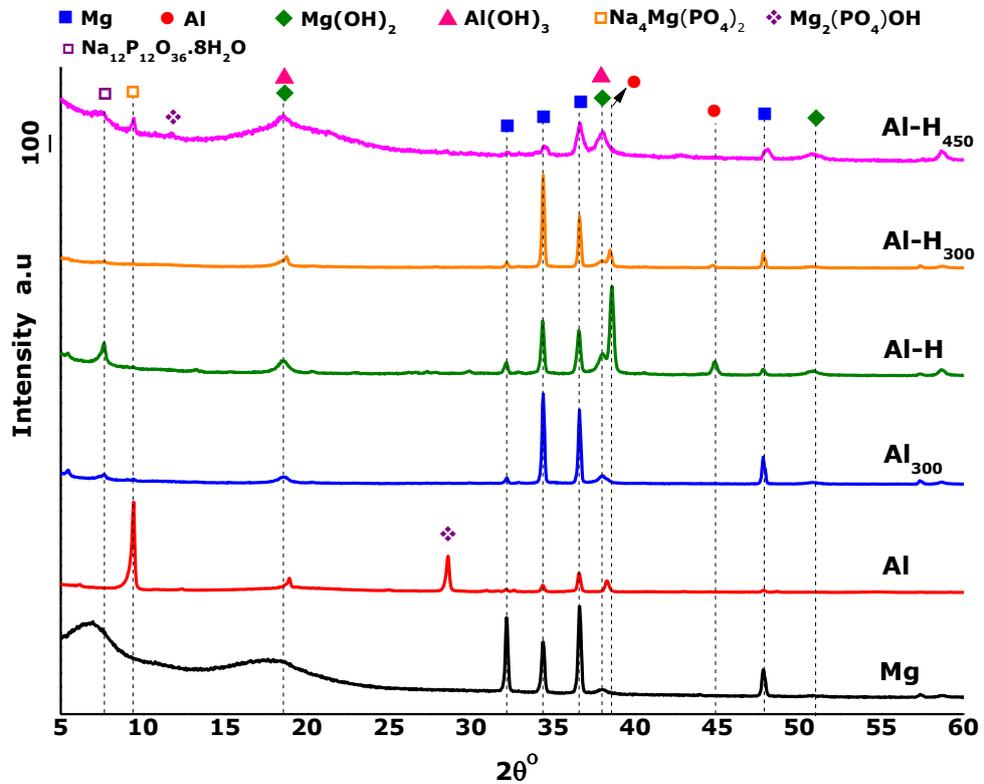
Figure 5-11 XRD patterns of as-deposited and heat-treated Al and Al-H coatings on Mg substrates after potentiodynamic polarization corrosion tests in PBS at 37°C.

Figure 5-11 presents complementary XRD patterns of the Mg substrate, and the as-deposited and annealed Al and Al-H coatings, after potentiodynamic polarization testing. In addition to diffraction peaks corresponding to the Mg substrate and the Al coating, the patterns indicate the presence of Mg(OH)$_2$ corrosion products, for all the corroded surfaces. No clear diffraction peaks for Al(OH)$_3$ coating corrosion products were detected, due to the problem of peak overlap. Intriguingly, a series of sharp intense peaks attributable to phosphate species such as Na$_4$Mg(PO$_4$)$_2$ and Mg$_2$(PO$_4$)OH were detected, mainly on the as-deposited Al and Al-H$_{450}$ and Na$_{12}$P$_{12}$O$_{36}$.8H$_2$O on Al-H and Al-H$_{450}$ corroded surfaces.

5.2.3 Discussion

5.2.3.1 Overview

As outlined in the literature review (Section 2.8), a good strategy for the protection of Mg and Mg-alloy surfaces from wet environments is to apply a physical barrier, such as a PVD coating. Ceramic layers are promising examples of this type of coating, *e.g.* alumina (Al$_2$O$_3$), to delay the onset of corrosion of Mg as well as improve overall corrosion and wear properties. However, in order to achieve a favourable coating system, optimised deposition conditions need to be identified. The direct deposition of insulating materials, such as alumina, using sputtering techniques is problematic generally due to low deposition rates [284]. Further, the DC deposition of Al in a reactive atmosphere of Ar/O, to produce Al$_2$O$_3$, leads to the formation of an electrically insulating aluminium oxide "poisoning" layer on the Al target surface which charges and discharges during the deposition process [280, 284]. Accordingly, an alternative approach has been investigated here - to develop a near surface layer of Al$_2$O$_3$ by depositing Al on to Mg by RF-MS and

transforming it to Al_2O_3 by annealing *ex situ* after deposition. To increase further the propensity of Al to oxidise, H_2 was used with Ar as the sputtering gas.

This section reviews the experimental data presented above, with a view to clarifying and gaining improved understanding of how coating material structures develop during PVD deposition and after thermal oxidation, and how coating structures affect the corrosion performance of Mg in the context of degradable stent applications.

5.2.3.2   Deposition and oxidation of Al and Al-H PVD coatings

Figure 5-12 provides an overview of the PVD deposition of an Al coating on Mg and the formation subsequently of Al_2O_3 and MgO after *ex situ* annealing in air at 300°C and 450°C, respectively.

(a) Deposition of Al on Mg

Al^{3+}

MgO

Mg

800μm

(b) Development of Al coating

Al_2O_3

Al

Al > 60 nm

Interface Mg/Al

Mg

800μm

(c) Annealing at 300°C

Al_2O_3

Al

Al > 90 nm

Mg/Al

Mg

800μm

(d) Annealing at 450°C

Al

MgO > 30 nm

MgO

Mg

800μm
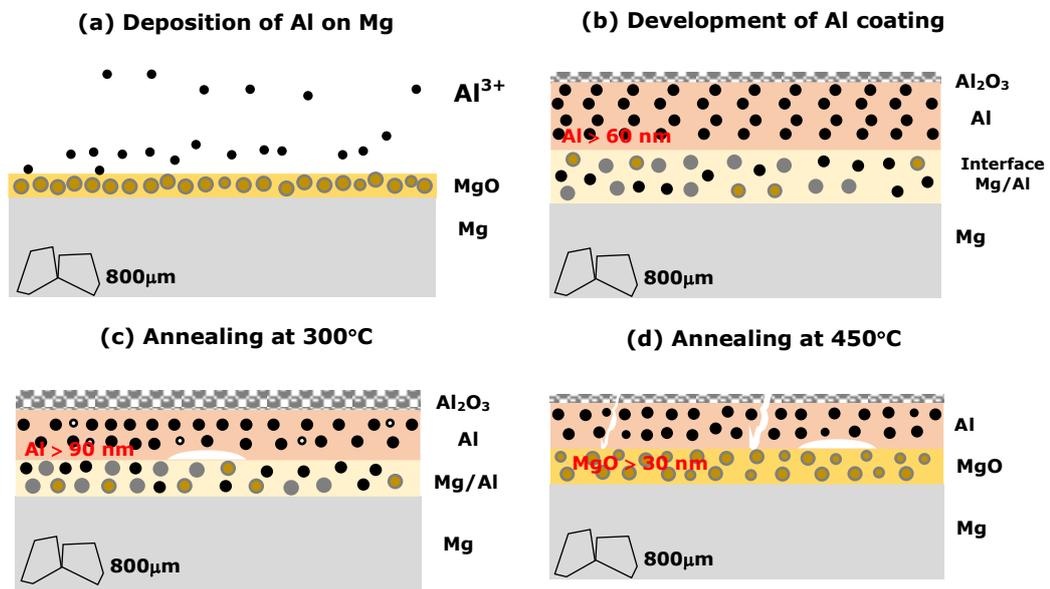
Figure 5-12 Schematic diagrams illustrating the deposition and evolution of Al deposited coatings on Mg, as a function of annealing.

As detailed in Section 3.2.5, the Al and Al-H coatings were deposited from a pure Al target in the presence of Ar or Ar/H_2 sputtering gases, respectively.

These two different sputtering environments were reflected, slightly, in the XRD patterns of the as-deposited Al and Al-H coatings (Figure 5-1). The diffraction patterns for the Al and Al-H coatings were very similar, in that they showed a dominant, intense sharp peak at $2\theta \sim 38°$ and a secondary peak $2\theta \sim 44.5°$ corresponding to {111} and {200} planes of Al, respectively. The data indicate strong preferred orientation of the Al grains in the <111> direction, to minimize the coating surface free energy [285]. The directional growth of Al is widely reported in literature, [276] [167] [286] [287] [288] [289].

In particular, XRD scans showed a small shift of the {111} Al diffraction peaks to an angle of $2\theta \sim 38.26°$ for the as-deposited Al coating, compared to standard 2θ value of $38.475°$ for Al, indicating an increase in lattice parameter for Al from 4.0494 Å to 4.0715 Å. This effect is attributed tentatively to the incorporation of Mg from substrate within the Al coating to form a dilute Al-Mg alloy [290], given the high atomic radius of Mg (145 pm) compared with that of Al (118 pm) - this would cause an increase in lattice parameter and shift of the Al peaks to lower 2θ values. The formation of a randomly distributed Al-Mg phase was suggested also by the shift of the Al_{2p} HR-XPS scan (Figure 5-6 (c)). If small quantities of Mg were present in the Al coating, it is probable that Mg atoms (BE of 49.40 eV) bonding with Al atoms (BE of 72.7eV) would cause of Al peak shift to a lower binding energy (71.88 eV).

Conversely, the as-deposited Al-H thin films showed a small shift in the position of the {111} XRD peak towards the higher angle of $2\theta \sim 38.52°$ (Figure 5-1), indicating a contraction in lattice parameter to 4.0412 Å. The presence of a considerable amount of H_2 in the chamber, in addition to the Ar sputtering gas, would lead to the incorporation of small amounts of hydrogen (atomic radius of 53 pm) within the Al coating layer. Hydrogen within the Al matrix may result in the formation of defects, *e.g.* vacancies and voids [291]

leading to surface "blisters" appearing on the Al-H coating surface (Figure 5-2 (b)).

Furthermore, for the case of Ar/H_2 used as a deposition gas, the relative intensities of the XPS peaks associated with Al_2O_3 and Al-Mg for the Al-H coating, compared to the Al coating (Figure 5-6), suggested that the presence of H_2 acted to restrict the development of Al-Mg and favour the formation of Al_2O_3, at the surface.

The as-deposited Al and Al-H coatings were found not to be strongly adhered to the Mg substrate, with peeling-off of coating material, observed towards the edges of the Mg discs, being attributed to strain effects. The poor adhesion of Al coatings to these polished Mg surfaces might be related to a component of mechanical bonding between Al and the Mg substrate, which is weaker than the ionic bonding of Al-Al and Mg-Mg, combined with a tendency for a spontaneous thin layer of MgO to form on the Mg substrate which could act as a chemical and physical barrier for alloy bonding of the Al coating into the Mg substrate.

5.2.3.3 Partial conversion of Al and Al-H coatings to alumina

After thermal oxidation, the shiny metallic Al_{300} and $Al-H_{300}$ surfaces annealed at 300°C produced XRD patterns (Figure 5-1) similar to those of the as-deposited coatings, in terms an intense Al peak at $2\theta \sim 38°$ corresponding to {111} planes and a small peak at $2\theta \sim 44.5°$ assigned to {200} planes. The sharpness of the Al diffraction peaks combined with an increase in average grain size (Scherrer) to ~ 89 nm for Al_{300} and to ~ 136 nm for $Al-H_{300}$ (Table 5-2) indicated some refinement of the crystallinity of the Al coatings. Figure 5-13 illustrates the variability of lattice parameter, lattice distortion

indicative of residual strain, and grain size for this sample set as a function of annealing.
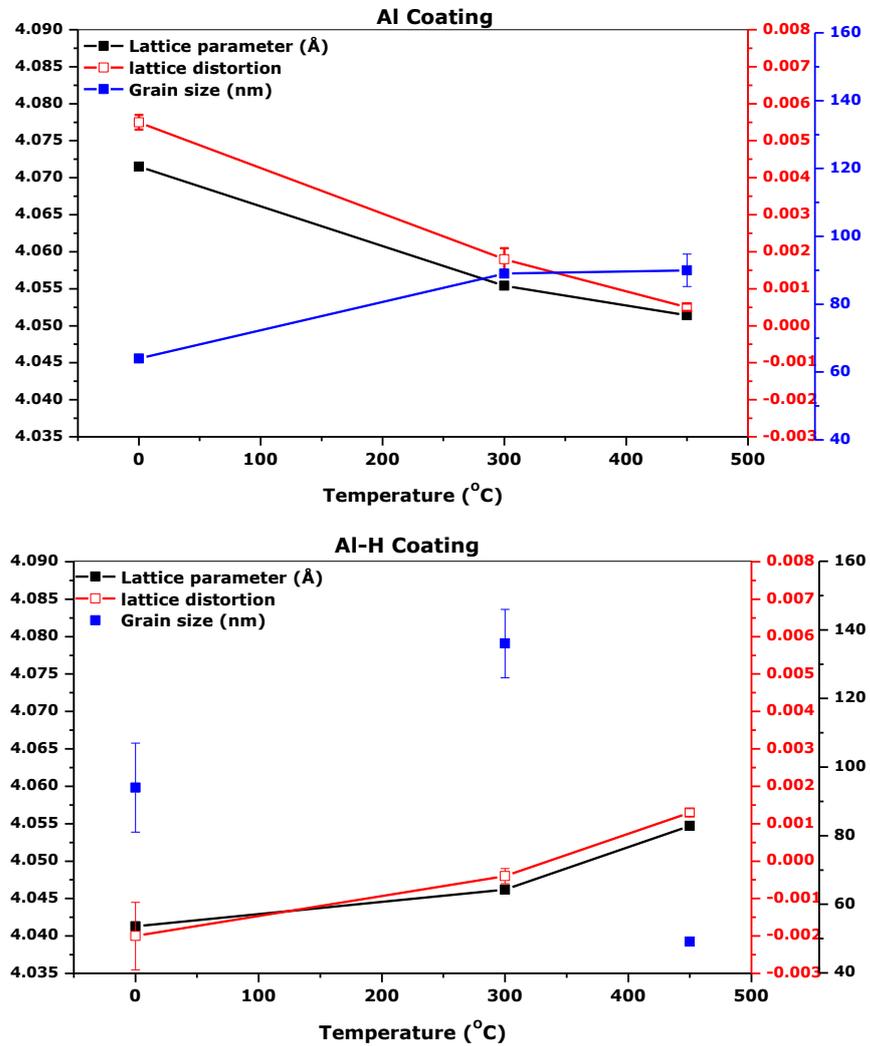
Figure 5-13 Variation of Al lattice parameter, lattice distortion and grain size as a function of annealing temperature.

Partial conversion of the Al_{300} coating near surface to a crystalline Al_2O_3 layer was achieved at 300°C, as shown by XRD observations, while Al_2O_3 formed on the Al-H_{300} surface, as evidenced by XPS, was presumably amorphous. XPS data also showed increased Al oxidation, for both Al_{300} and Al-H_{300} surfaces in preference to Al-Mg alloy formation (Figure 5-7 (c,d,g,h)), in view of a decline or disappearance of Al-Mg, MgO and $Mg(OH)_2$ signals at the surface [292].

The mobility of oxygen on a metal (M) surface, Al or Al-H in this case, and it's incorporation into the metal sub-surface, increases with increasing temperature [293]. The oxidation reaction follows the chemical formula:

$$2Al + 3/2\, O_2 \rightarrow Al_2O_3 \qquad \Delta H_f = -1675\, \tfrac{kJ}{mol}, \; \Delta LE = -15916 \, kJ/mol \quad \text{Eq 5-1}$$

Where ΔH_f and ΔLE are the standard heat of formation and lattice energy of Al_2O_3, respectively. This process is divided into two steps, in which Al forms an ion by the release of electrons:

$$Al \rightarrow Al^{3+} + 3e^- \qquad \Delta H^\circ = 5139 \, kJ/mol \qquad \text{Eq 5-2}$$
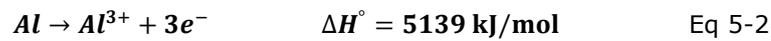
Where ΔH° is the ionisation energy of Al to become Al^{3+}; and the released electrons diffuse and become absorbed by oxygen to form O^{2-} ions:

$$O + 2e^- \rightarrow O^{2-} \qquad \Delta H^\circ = -141 \, kJ/mol \qquad \text{Eq 5-3}$$
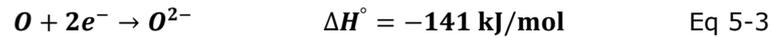
Where ΔH° is the electron affinity of O released to form O^{2-}, at the metal-air interface. Either oxygen in the atmosphere diffuses inwards and reacts with M^{n+} ions (Al^{3+}) at the near surface, or Al^{3+} and $3e^-$ diffuse outwards through the developing oxide film to react with O^{2-} at the surface. This results in the fast formation of a thin oxide layer of Al_2O_3 on the Al surface.

However, the increase in thickness of a developing aluminium oxide layer, during thermal oxidation, can impede the differential cross-diffusion of Al^{3+} and O^{2-} ions through the oxide layer, slowing down the oxidation process, explaining why only partial oxidation of the Al coating was achieved, by the end of the processing time of 5 h [294].

Samples were then oxidised in air at 450°C, with the intention of increasing the formation of crystalline Al_2O_3. However, the formation of MgO was found to dominate (Figure 5-1). At both 300°C and 450°C, pin-holes and cracks were observed on both Al and Al-H surfaces that would provide sites for the supply of oxygen to the Mg substrate. It is noted that activation energy for

the oxidation of Mg is 148 kJ/mol [295] and for Al is 414.22 kJ/mol [296], respectively. The higher reactivity of Mg suggests it is able to overcome the activation energy required for reaction with oxygen to form MgO at 450°C, with initial material consumption via the pin-holes. It is worth noting that:

$$Mg \rightarrow Mg^{2+} + 2e \qquad \Delta H^{\circ} = 2188.4 \text{ KJ/mol} \qquad \text{Eq 5-4}$$

$$Mg + 1/2\, O_2 \rightarrow MgO \qquad \Delta H_f = -601\,\frac{\text{kJ}}{\text{mol}}, \ \Delta LE = -3889 \text{ kJ/mol} \qquad \text{Eq 5-5}$$
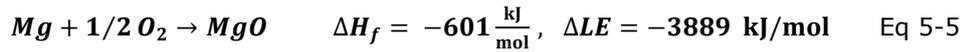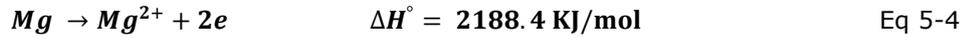
Where ΔH_f and ΔLE are the standard heat of formation and lattice energy of MgO, respectively.

The tendency of a material to react with oxygen to form a metal oxide is governed by the Gibbs free energy ΔG° ($\Delta G = \Delta H - T\Delta S$, where ΔH is the enthalpy; T is absolute temperature; and ΔS is entropy). If ΔG° has a negative value, then the oxidation reaction occurs spontaneously and the more negative ΔG° the more the metal tends to oxidize.

According to the ΔG° (kJ/mol) values for Al and Mg, from the Ellingham Diagram of metal oxide (Table 5-6), MgO has more free energy than Al_2O_3. In addition, the ionisation energy of Mg^{2+} (ΔH°=2188 kJ/mol) is less than Al^{3+} (ΔH°=5138.9 kJ/mol). Hence, the propensity of oxygen to dissociate and bond with one Mg^{2+} ion and form MgO is higher than three O^{2-} ions to bond with two Al^{3+} ions and form Al_2O_3.

Table 5-6 Chemical bonding parameters for Al_2O_3 and MgO

Compound	Bond	Lattice energy ΔLE kJ/mol	Ionisation energy kJ/mol	Bond dissociation energy, ΔH_{f298}, kJ/mol	ΔG° (kJ/mol)		
					25°C	300°C	450°C
MgO	Mg-O	3889	2188.4	394(35)	-1170	-1110	-1075
Al_2O_3	Al-O	15916	5139	512(4)	-970	-1000	-1050

At the lower temperature of 300°C, the absorbed oxygen has low activation energy to enter the Al lattice structure, and hence leads to just oxidation of the near surface of the coating. Conversely, the high substrate oxidation

levels at 450°C act to degrade strongly the Al coating crystallization, observed in both SEM (Figure 5-3) and {111} peak broadening of Al-H$_{450}$ in XRD (Figure 5-1). In this case, the absorbed oxygen atoms have enough energy to diffuse and enter Mg lattice position, although desorption can also occur with the escape of O/H atoms leading to the formation of vacancies [297, 298].

The residual strain calculated within Al-H {111} planes indicates a change of residual stress, from compressive to tensile stress, with increasing temperature of annealing (Figure 5-13,Table 5-2). This supports also the suggestion of the creation of point defects and vacancies [298].

5.2.3.4 Corrosion mechanisms

OCP and potentiodynamic polarization tests have been used widely to study the corrosion behaviour of bulk Mg [270] [299]. For highly pure Mg, corrosion is attributed mainly to the dissolution of Mg^{2+} ions from the bulk into PBS. In this part of the study, the corrosion resistance of these processed Al and Al-H coatings is appraised, with the anticipation that uniform coatings would delay the onset of corrosion of the Mg substrate.

As shown in Figure 5-9, the Al and Al-H coated Mg surfaces, in both as-deposited and annealed conditions, showed positively offset corrosion potentials, and nobler OCP and E$_{corr}$ values, compared to the polished Mg substrate (E$_{corr}$ ~ -1907±2 mV). According to the corrosion thermodynamic and voltage scale of metals, the tendency of Al (E°=-1663 mV) to corrode is less than Mg (E°=-2370 mV). Hence, Al and Al-H adopt a more passive surface, as shown in the shift of OCP and E$_{corr}$ to more noble values.

The Al, Al$_{300}$ and Al-H$_{450}$ coatings adopted a steady OCP that indicated better protection of the Mg surfaces when the coatings were less defective.

However, for the Al-H, Al-H$_{300}$ and Al$_{450}$ coatings, the OCP decreased after ~ 2500 sec in PBS, being attributed to the development of an unstable oxide layer and penetration of the test solution to reach underneath the Al coating.

The potentiodynamic polarisation scan (Figure 5-9) of the Al and Al-H coatings (with the exception of Al$_{300}$ and Al$_{450}$) resulted in an anomalous cathodic Tefal region, consisting of an initial corrosion and passivation trend (region IV), being attributed to the initial dissolution of the Al coating followed by rapid anodic corrosion. Conversely, the heat-treated Al$_{300}$ and Al$_{450}$ coatings exhibited a more conventional Tafel region, prior to rapid dissolution for Al$_{300}$ and an active-passive trend for Al$_{450}$.

Basis on this, the corrosion mechanism of the as-deposited and annealed Al and Al-H coatings (in PBS at 37°C) is illustrated schematically (Figure 5-14). In general terms, and by way of example, the Al / Al-H coatings interact with H$_2$O molecules in the PBS solution to form Al(OH)$_3$ reaction products on the coating surface (Figure 5-14 (a)). The electrochemical reaction involved here is the oxidation of Al and the oxygen reduction reaction:

$$Al \rightarrow Al^{3+} + 3e^- \qquad \text{Eq 5-6}$$

$$O_2 + 2H_2O + 4e^- \rightarrow 4OH^- \qquad \text{Eq 5-7}$$

$$Al^{3+} + 3OH^- \rightarrow Al(OH)_3 \qquad \text{Eq 5-8}$$
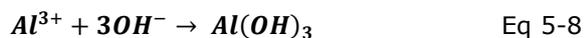
The solution becomes more alkaline because of a local increase in pH, and this can be balanced by the formation of Al hydroxide [300]: The general reaction of Al with water in PBS is:

$$2Al + 6H_2O \rightarrow 2Al(OH)_3 + 3H_2 \qquad \text{Eq 5-9}$$

a

Mg^{2+} Al^{3+}

OH^- Al^{3+} Al^{3+} OH^- PO_4^{3-}

$2H_2O+O_2+4e^-\rightarrow 4OH^-$ Al(OH)$_3$ MgPO$_4$OH   Al(OH)$_3$

$Al\rightarrow Al^{3+}+3e^-$ Mg(OH)$_2$ Mg(OH)$_2$ **Al**

Cl^-

$Mg^{2+}+2OH^-\rightarrow Mg(OH)_2$ OH^- Mg^{2+} $Mg\rightarrow Mg^{2+}+e^-$

Mg(OH)$_2$ $2H_2O+2e^-\rightarrow 2OH^-+H_2$

Mg

b

Al^{3+} Mg^{2+} Al^{3+}

OH^- Al^{3+} OH^- PO_4^{3-}

MgPO$_4$OH

Al(OH)$_3$ Al(OH)$_3$ **Al$_2$O$_3$**

$Al+3H_2O\rightarrow Al(OH)_3+H_2$ Mg(OH)$_2$ **Al**

Cl^-

OH^- Mg^{2+}

$Mg^{2+}+2OH^-\rightarrow Mg(OH)_2$ Mg(OH)$_2$ $Mg\rightarrow Mg^{2+}+e^-$

$2H_2O+2e^-\rightarrow 2OH^-+H_2$

Mg

c

Mg^{2+} Al^{3+} Al^{3+}

OH^- Al^{3+} OH^- PO_4^{3-}

Mg(OH)$_2$ Al(OH)$_3$ MgPO$_4$OH $MgO+H_2O\rightarrow Mg(OH)_2$ **Mg(OH)$_2$**

MgO

Cl^-

OH^- Mg^{2+}

$Mg^{2+}+2OH^-\rightarrow Mg(OH)_2$ Mg(OH)$_2$ $Mg\rightarrow Mg^{2+}+e^-$

$2H_2O+2e^-\rightarrow 2OH^-+H_2$

Mg

Figure 5-14 Schematic illustration of the corrosion process of Al/Al-H coated Mg upon immersion in PBS at 37°C: (a) as-deposited; (b) annealed at 300°C; and (c) annealed at 450°C.

When Al_2O_3 oxide layer had formed already on the Al surface, the resistance of Al coating to corrosion may increase, with the oxide layer acting to isolate the Al/Mg surface from further interaction with ions in the PBS (Figure 5-14(b)). This is shown in the typical cathodic evolution of the Al_{300} sample, with the development of crystalline surface Al_2O_3 compared to the as-deposited Al coating. The samples annealed at 450°C were dominated by MgO, prior to immersion in PBS. The MgO reacted with water in the PBS to form $Mg(OH)_2$, (Figure 5-14(c)) which further enhanced the passivation

behaviour of the exposed surface, consistent with the improved corrosion resistance of Al_{450} (Figure 5-9 (b) and Table 5-5)

The Al coating could be susceptible to stress corrosion cracking (SCC), with fracture and crack growth in Al and Al-H coatings in aqueous solution occurring due to hydrogen embrittlement. Hydrogen evolution during cathodic reaction combined by residual stress in an Al coating results in a high concentration of hydrogen in crack tips [291]. The hydrogen atoms enter the Al lattice, leading to the production of brittle region supporting crack propagation. Diffusion of hydrogen to Al grain boundaries can also lead to a decrease in strength between adjacent grains, again resulting in embrittlement and crack growth.

Meanwhile, aggressive Cl^- ions and H_2O present in the PBS solution can migrate through the coating layer via cracks, pin-holes and regions of coating delamination (Figure 5-2 and Figure 5-3) to react with the Mg substrate. The wet corrosive medium leads to the formation of a galvanic cell at the Al/Mg interface, resulting in the localised attack of MgO/Mg at the substrate and the formation of $Mg(OH)_2$ [300]:

$$Mg \rightarrow Mg^{2+} + 2e^- \qquad\qquad \text{Eq 5-10}$$

$$2H_2O + 2e^- \rightarrow 2OH^- + H_2 \qquad\qquad \text{Eq 5-11}$$

$$Mg^{2+} + 2OH^- \rightarrow Mg(OH)_2 \qquad\qquad \text{Eq 5-12}$$
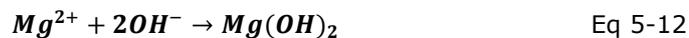
The BSE image of the as-deposited Al surface, following corrosion in PBS, in cross-sectional view (Figure 5-10 (b)) shows the presence of the substrate corrosion product $Mg(OH)_2$ underneath the Al coating and its corrosion product $Al(OH)_3$. Both these $Mg(OH)_2$ and $Al(OH)_3$ components were detected on all the coated surfaces, following corrosion, as revealed by XRD (Figure 5-11) and EDS analysis, *e.g.* the BSE image of the corroded as-deposited Al-H coating (Figure 5-10 (a)). This supports the suggestion that

the growing $Mg(OH)_2$ layer applied stress to the Al/Al-H coatings, resulting in damage or delamination, leaving the Mg substrate unprotected (Figure 5-10 (a,b)). Furthermore, hydrogen bubble evolution may lead to rupture of the Al/Al-H coatings, thereby introducing additional sites for corrosion initiation. Hang and Yang [170, 289] reported the same corrosion mechanism for an Al coating deposited on AZ31B Mg-alloy using DC magnetron sputtering, and tested in 3.5% NaCl solution.

In addition to $Mg(OH)_2$ and $Al(OH)_3$, the presences of phosphate species in PBS, in the form of KH_2PO_4 and Na_2HPO_4, may lead to the formation of phosphate ions leading to a localised increase in pH:

$$H_2PO_2 \rightarrow HPO_4^{2-} \rightarrow PO_4^{3-} \qquad \text{Eq 5-13}$$
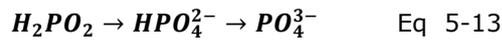
The dissolution of Mg from the substrate in PBS and the presence of $Mg(OH)_2$ could result in the formation of a Mg-phosphate, in form of $Na_4Mg(PO_4)_2$ or $Mg_2(PO_4)OH$, by the following reaction:

$$2Mg^{2+} + PO_4^{3-} + OH^- \rightarrow Mg_2 PO_4OH \qquad \text{Eq 5-14}$$

$$4Na^+ + Mg^{2+} + PO_4^{3-} \rightarrow Na_4Mg(PO_4)_2 \qquad \text{Eq 5-15}$$
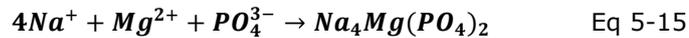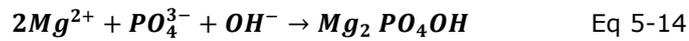
The precipitation of Mg-phosphate phases is in agreement with both the EDS (Figure 5-10) and XRD data (Figure 5-11).

5.2.4 Recommendations for process control

The Al and Al-H coatings in this study were deposited on Mg surfaces by magnetron sputtering in an Ar or Ar/H_2 atmosphere. Thermal annealing at 300°C and 450°C was used to encourage the growth of an oxide layer on the Al and Al-H coatings, with the aim of converting the coatings to alumina. However, the poor adhesion of the Al coatings to the polished Mg surfaces

suggests that additional substrate cleaning protocols might be beneficial, prior to coating. The attempt to convert Al/Al-H to alumina, by increasing the temperature of oxidation up to 450°C led to coating delamination and brittleness, making them unsuitable for practical use. However, annealing at a more moderate temperature of 300°C (or slightly higher) for a longer time, may impart better control over the development of Al_2O_3.

The relatively low corrosion resistance performance of the as-deposited and annealed Al/Al-H coatings suggest that improved Mg substrate preparation, combined with an increase in coatings thickness, would provide for better corrosion protection. The incomplete conversion of Al and Al-H to alumina resulting from the processing conditions investigated here raises the question about the practicalities of such Al-based coatings within stent applications, due to the association of Al ions dissolved in body being linked clinically to Alzheimer disease. An alternative approach would be to coat Mg with a more biocompatible coating, which still acts as a physical barrier between Mg and PBS (or body solution), for delaying the onset of corrosion of biodegradable stents. On that basis, the applicability of the a-Si:H coating system is now investigated.

5.3 a-Si:H coatings

Coating materials on Mg substrate should possess biocompatible as well as passivation properties for use with implant devices. Silicon, for instance, has been considered, being also a trace element involved in metabolic processes [301]. Liu *et al.* [283] reported on the formation of carbonate-containing hydroxyapatite (bone-like apatite) when 100 nm thick hydrogenated amorphous silicon (a-Si:H) films, deposited by plasma-enhanced chemical vapour deposition (PECVD), were immersed in a simulated body fluid (SBF)

for 28 days. A related study by Dahmen *et al.* [282] concluded that hydrophilic surfaces of amorphous silicon or silicon suboxides (a-SiOx:H), deposited by PECVD, were largely biocompatible.

In addition to PECVD, the technique of PVD may be used to deposit a-Si films at low temperature, making it suitable for use with Mg substrates (melting point of 650°C). A growing layer of silica (Si_2O) on Si needs ordinarily a very high temperature of $\sim$ 1200°C [302]. However, with reference to the development of Al-H coatings, it is suggested that deposition in the presence of H_2 could increase the tendency of the near surface of an a-Si coating to oxidise, to provide a suitable additional insulating layer for corrosion resistance.

Hence, Si coatings were deposited on Mg substrates by RF magnetron sputtering (RF-MS) in the presence of Ar/H_2 deposition gas (Section 3.2.5). In the following section, morphological investigations of as-deposited Si:H coatings are reported. Complementary potentiodynamic polarization corrosion data and immersion tests for both Mg substrates and a-Si:H coatings are then presented in section 5.3.2.

5.3.1 Structural characterisation of a-Si:H coatings on Mg

SE and BSE images illustrating the topographies of a-Si:H coatings, as-deposited by RF-MS on Mg, in an Ar/H_2 environment, are presented in Figure 5-15(a,b). The coatings again followed the Mg substrate preparation profiles, of striations, grooves and polishing marks (Figure 5-15(a), arrowed). The Mg substrate surface roughness prior to coating was 0.09 $\pm$ 0.01 μm, becoming 0.13 $\pm$ 0.01 μm after a-Si:H layer deposition. The high magnification BSE image of Figure 5-15(b) also showed some randomly distributed small, bright particles (arrowed).
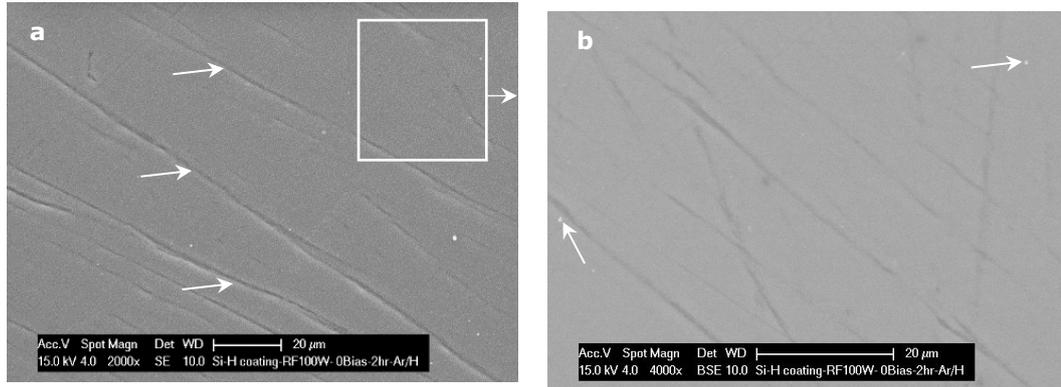
Figure 5-15 (a) SE and (b) BSE images of RF-MS coated a-Si:H /Mg.

Figure 5-16(a) presents an XRD pattern of an as-deposited a-Si:H coating on Mg. The pattern indicates the presence of polycrystalline Mg with no evidence of Si:H, consistent with the coating being amorphous.

The covalent bonding nature of the coating was investigated using FTIR spectroscopy. Figure 5-16(b) presents an FTIR spectrum obtained from an as-deposited a-Si:H layer on Mg, showing a peak at 874.2 cm^{-1} attributed to Si-H bonding, while absorption peaks at 1033.8 and 1161.8 cm^{-1} were attributable to Si-O (stretching) bonds [303]. Strong absorption peaks at 1416.9 cm^{-1} were associated with H-O-H [304], while the broad band at 2850.4 - 2619.6 cm^{-1} band was attributed to O-H groups [303]. A peak at 3693.6 cm^{-1} was attributed to Si-OH bonding [303]. It should be mentioned also that no peak was detected for Si-Si, which would appear in the 600-620 cm^{-1} range [305] [306].
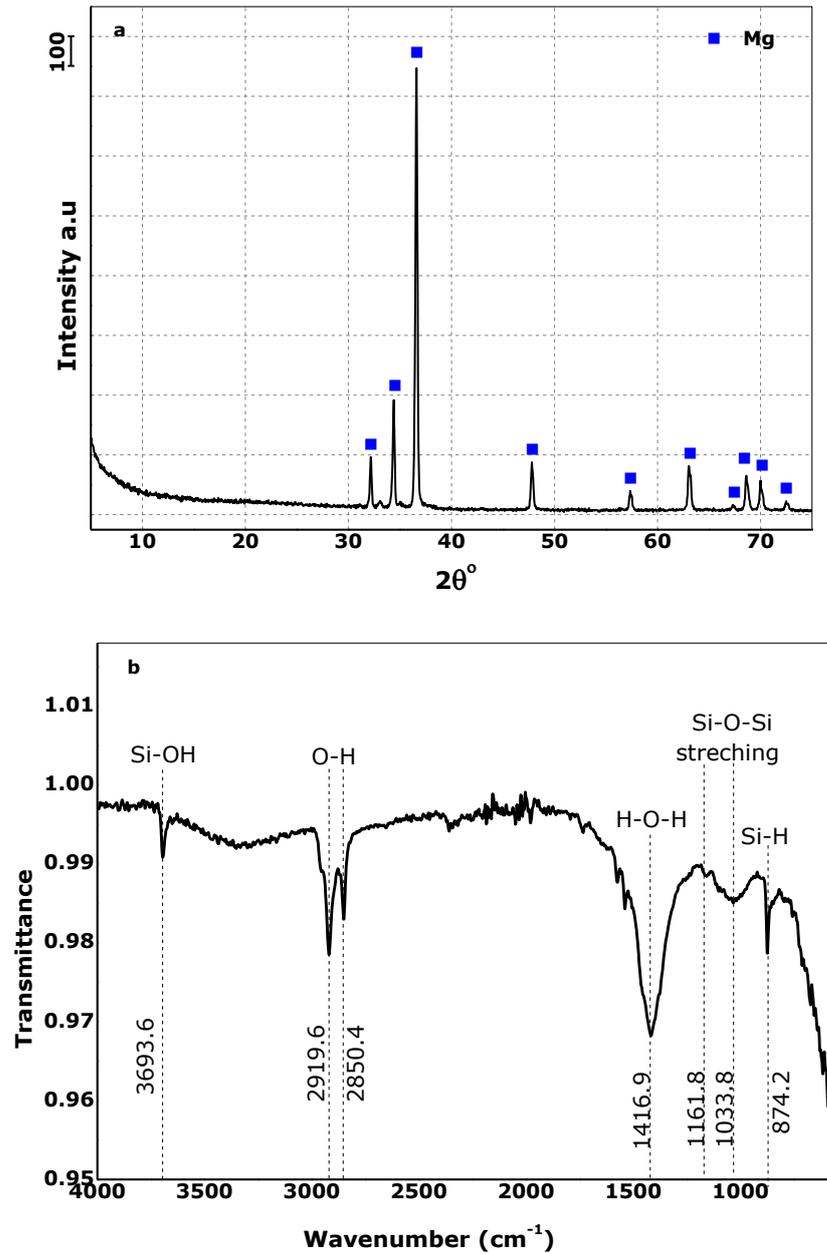
Figure 5-16(a) XRD pattern of an a-Si:H coating on Mg; (b) representative FTIR absorption spectrum of an a-Si:H coating on Mg.

Figure 5-17(a,b) presents representative EDS analyses of the as-deposited a-Si:H coatings, in plan-view and cross-sectional orientations, respectively. EDS spot analysis (Figure 5-17(a)) indicates the presence of Si and Mg, as well as an O peak. The randomly distribution of small surface particles were identified as Ag particles, attributed tentatively to cross-contamination from the PVD chamber. Figure 5-17(b) presents an SE micrograph of a fractured cross-section, showing the crack free Si coating with thickness of 1.22 ± 0.02 μm.

Element	at.%
O	33.03
Mg	54.48
Si	12.19
Ag	0.30

Element	at.%
O	13.87
Si	21.58
Cl	5.18
K	29.76
Ca	29.61
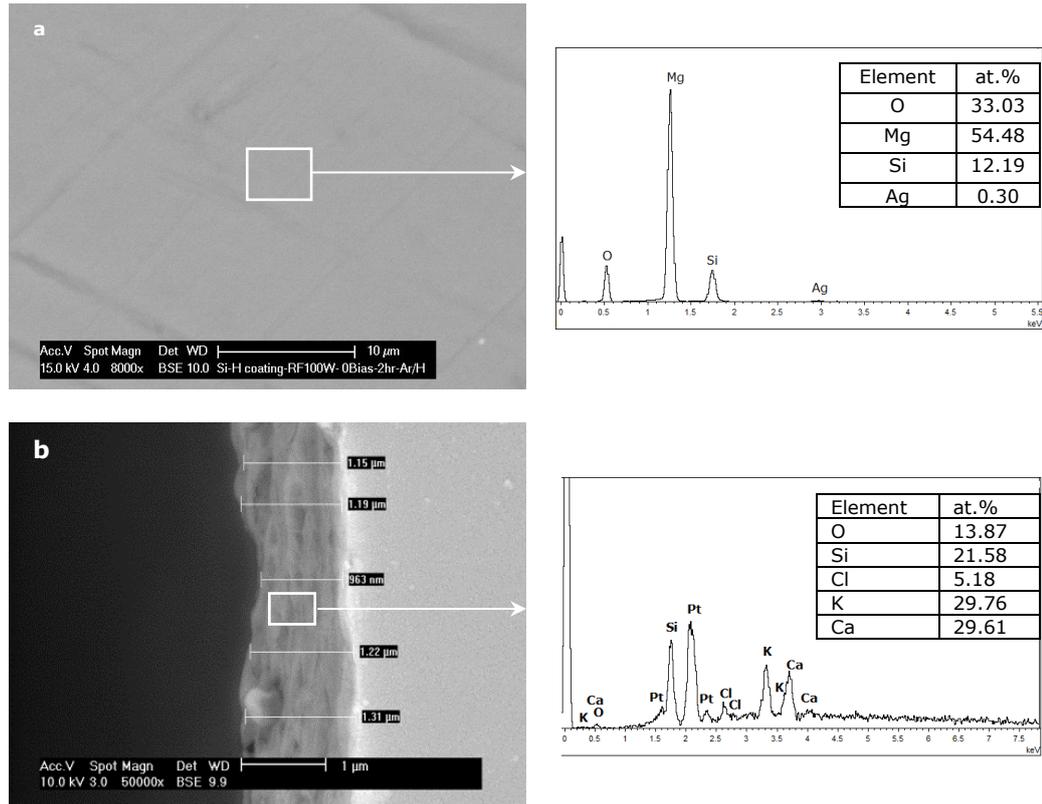
Figure 5-17 BSE images and associated EDS spectra for: (a) a-Si:H coated Mg in plan-view orientation; (b) a-Si:H coated Mg in cross-sectional orientation.

XPS survey scans for the Mg substrate and a-Si:H coated Mg, complementary to the FTIR observations, are presented in Figure 5-18(a-c) and Figure 5-19(a-c), respectively. The survey scan of the as-prepared Mg substrate reveals the presence of strong oxide peaks, confirming the spontaneous formation of MgO at the near surface. The O_{1s} spectral peak (Figure 5-18(b)) could be fitted with peaks of binding energies: 529.54 - 531.63 eV and 533.26 eV, corresponding to MgO and H_2O, respectively. The Mg_{2p} spectral peak (Figure 5-18(c)) was fitted with two peaks at 49.92 eV, assigned to Mg, and 47.67 eV which could not be assigned. The XPS survey scan (Figure 5-19(a)) for the as-deposited a-Si:H coating again indicated the presence of a surface oxide. The O_{1s} peak (Figure 5-19(b)) illustrates a major peak at 533.13 eV, assigned to SiO_2, and two other minor peaks at 535.01 eV and 530.65 eV, corresponding to H_2O and Ag_2O (again attributed to cross-

contamination from the RF-MS chamber). There were no peaks attributable to pure Si on the coated surface. The SiO_2 signature at 103.80 eV was consistent with the FTIR and EDS analyses.
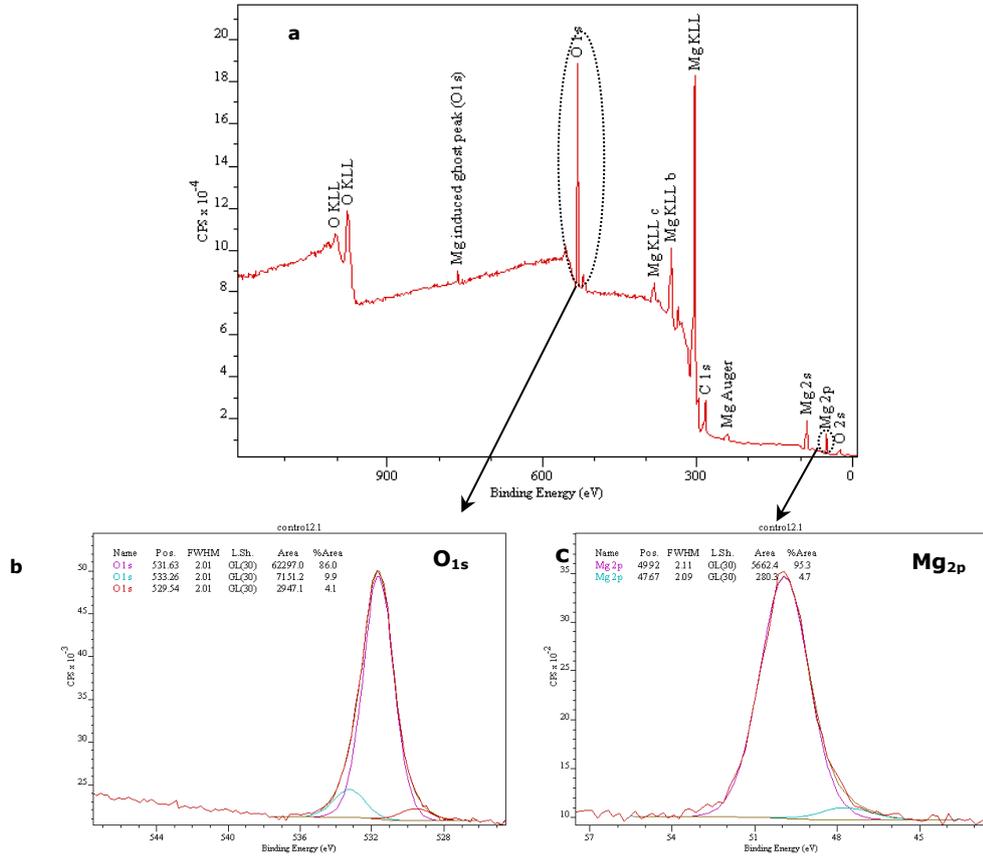
Figure 5-18 XP-survey scan and high-resolution O_{1s} and Mg_{2p} spectra of the Mg substrate.
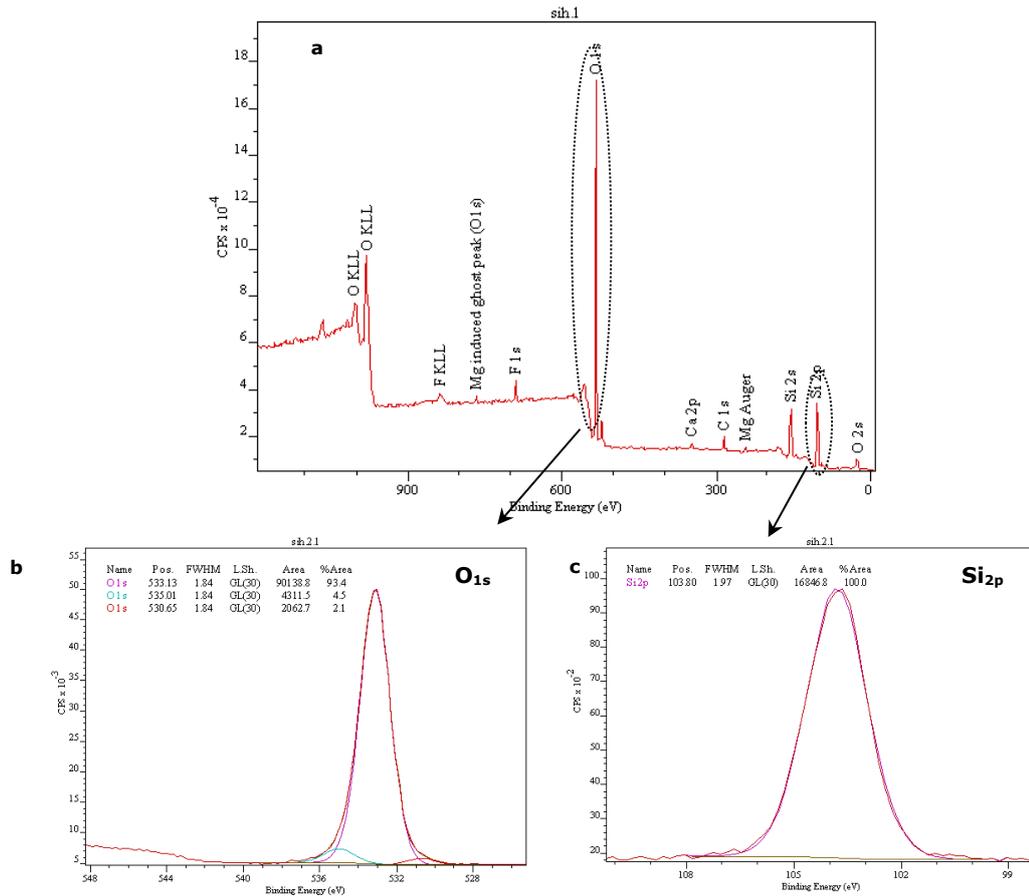
Figure 5-19 XP-survey scan and high resolution O_{1s} and Si_{2p} spectra of as-deposited a-Si:H on Mg.

5.3.2 Corrosion behaviour of a-Si:H

5.3.2.1 Potentiodynamic corrosion tests

Figure 5-20(a,b) presents OCP and potentiodynamic polarization curves for as-polished Mg and an as-deposited a-Si:H coating on Mg, in PBS at 37°C, respectively. The OCP of the a-Si:H coating (Figure 5-20(a)) showed a slightly more active and stable trend after 3000 s, to a value of -1739.8 mV, as compared to -1736.0±3 mV for the Mg surface, with OCP drop-out caused by the counter electrode connection. The corrosion behaviour of the polished Mg substrate (Figure 5-20(b)) exhibited a typical potentiodynamic polarization curve for normal cathodic hydrogen evolution and slow anodic dissolution of 0.11 ± 0.01 mm/year at an E_{corr} value of -1718.7±2 mV, before fast corrosion

at a break-down potential of -1563.7±3 mV. Conversely, the a-Si:H coating showed slow anodic dissolution of 0.05±0.02 mm/year at an E_{corr} value of -1602.8±2 mV, which increased with potential before self-passivation. Corrosion values extracted from the OCP and potentiodynamic curves are presented in Table 5-7.
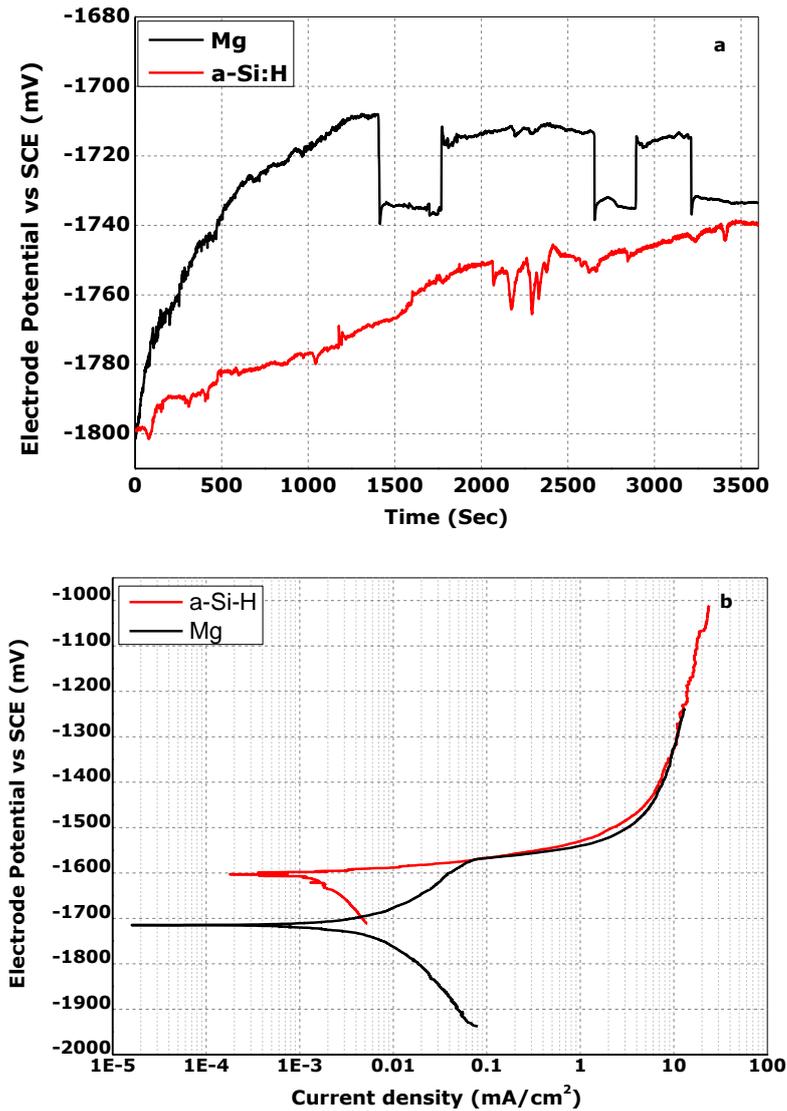
Figure 5-20 (a) OCP and (b) potentiodynamic polarization curves for as-polished Mg and a-Si:H coated Mg

Table 5-7 Corrosion parameters from the polarization behaviours of polished Mg and as-deposited a-Si:H on Mg.

Sample	OCP (mV)	E_{cor} (mV)	i_{cor} (mA/cm²)	E_b (mV)	CR (mm/year)
Mg	-1736.0±3	-1718.7±2	0.005±0.001	-1563.7±3	0.11±0.01
Si-H	-1739.8±3	-1602.8±2	0.002±0.001	-	0.05±0.02

5.3.2.2 Immersion testing

Immersion tests were conducted on one side of the polished Mg substrates (control samples) and the a-Si:H coated surfaces, in PBS at 37°C, for durations of 1, 3, 5 and 7 days. Figure 5-21 shows a comparison of corrosion rates for the Mg substrate and the a-Si:H coated Mg. After the first day, the a-Si:H coated surfaces showed improvements in corrosion rate, from 4.7±0.1 mm/year to 2.4±0.1 mm/year. After five days, the a-Si:H sample corrosion rate showed a minimum value of 1.4±0.02 mm/year, compared to 1.90±0.01 mm/year for the control sample. After the passivation layer on the Mg surface dissolved, further corrosion took place, at levels of 4.2±0.01 mm/year and 2.8±0.02mm/year for the control Mg and a-Si:H coated Mg, respectively.
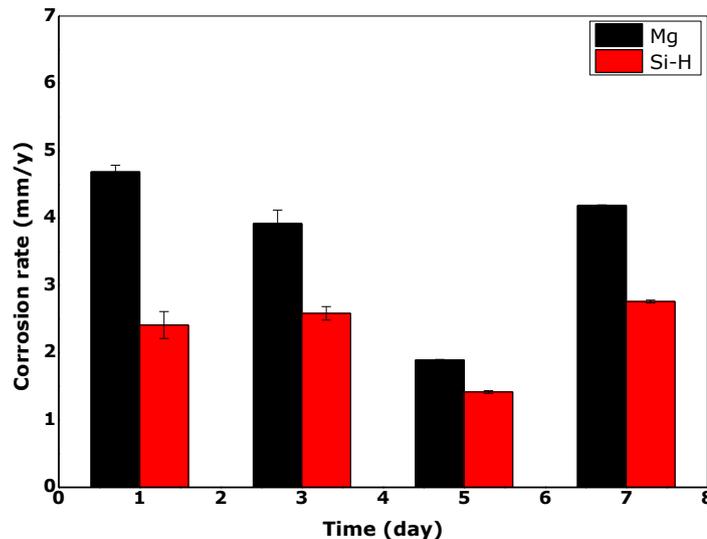
Figure 5-21 Corrosion rates of the as-polished Mg substrate and a-Si:H coated Mg, after 1, 3, 5 and 7 days.

Figure 5-22(a-c) presents OM and SEM images of the surface topography of a-Si:H coated Mg, after immersion in PBS at 37°C for 7 days, along with an associated EDS spectrum. It was evident that crevice corrosion had become established on the lacquer side that may have had an effect on corrosion rate (Figure 5-22(a), arrowed). However, the corrosion products observed on the

middle of the sample suggested the a-Si:H coating to be dense, very well adhered and continuous. In particular, the a-Si:H coating showed the ability to resist the effect of Cl^- ions, isolating the Mg surface from the PBS media.

A spot EDS analysis of the corroded a-Si:H surface (Figure 5-22(c)) indicated the present of Na, Ca and P, in addition to Si, O and an Mg peak from the substrate. Complementary XRD observations (Figure 5-23(a)) revealed small peaks related to the corrosion products of $Mg(OH)_2$, as well as PO_4-components attributable to calcium hydrogen phosphate ($CaHPO_4$), magnesium phosphate in the form of ($Na_4Mg(PO_4)_2$, $Mg(PO_4)OH$) or magnesium carbonate ($MgCO_3$). FTIR analysis (Figure 5-23(b)) for an a-Si:H corroded surface, after 3 days' immersion in PBS, showed peaks at 669.2 cm^{-1} and 962.9 cm^{-1}, corresponding to HPO_4^{2-} and PO_4^{3-} ions, respectively. Carbonate (CO_3^{2-}) species were detected also at 1446.9 cm^{-1}.
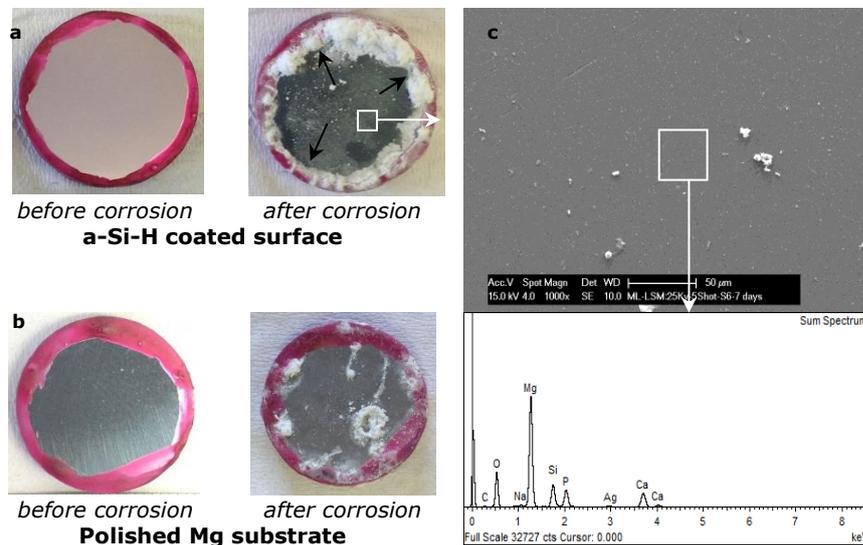
Figure 5-22 OM images, SE image and ED spectrum for corroded a-Si:H coated Mg, after immersion in PBS at 37°C for 7 days.
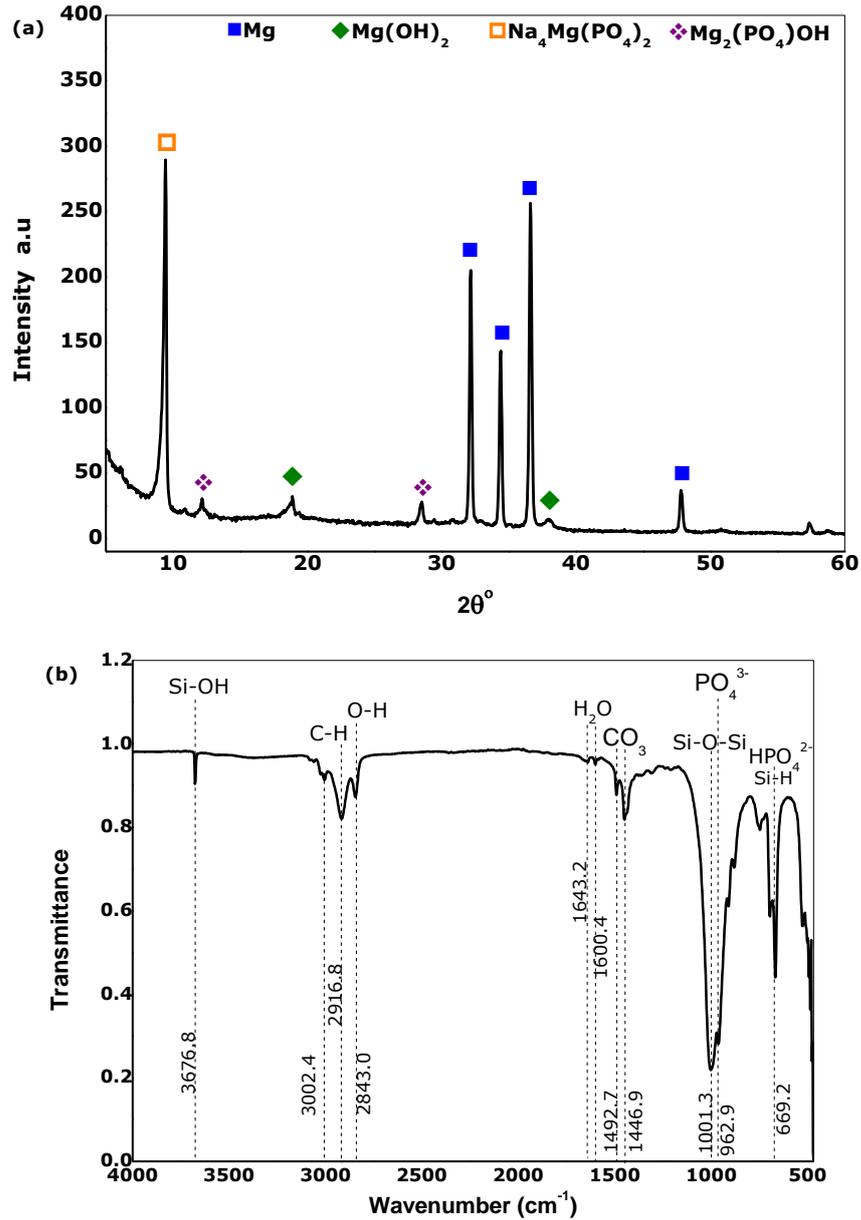
Figure 5-23 (a) XRD pattern (b) FTIR spectrum for an a-Si:H coating on Mg, corroded in PBS at 37°C.

5.3.3 Discussion

5.3.3.1 Overview

Amorphous silicon, compared to the crystalline phase, has a large band-gap leading to a reduction in the generation of thermal carriers [282]. In addition,

improved passivation properties of a-Si can be achieved by the incorporation of hydrogen [283]. Accordingly, hydrogenated amorphous silicon (a-Si:H) is a promising material with potential for use in biomedical and biosensor devices [283]. RF-MS is a suitable technique to prepare a-Si thin films without using toxic gases such as phosphine (PH_3) and diborane (B_2H_6) [307]. However, investigations of the corrosion resistance of a-Si:H on Mg are still in the early stages.

The ambition of the present work was to obtain amorphous hydrogenated silicon coatings on Mg surfaces to improve corrosion resistance. The data obtained clarified the morphology of the coating material, after PVD deposition, and its affects on the corrosion performance of Mg in PBS.

5.3.3.2 a-Si:H coating morphology

Successful deposition of these RF-MS Si-based coatings on finely polished Mg substrates was revealed by EDS (Figure 5-17), with the detection of Si and O peaks, along with the Mg substrate. XRD investigations (Figure 5-16) showed no crystalline signatures for the Si:H coating layer, consistent with its predicted amorphous state. Wang *et al.* [308] cited XRD data for the deposition of an a-Si layer on quartz glass, at RT, by MS. A related study by Fukaya *et al.* [307] similarly found no crystalline XRD peaks for a-Si deposited under an Ar/H_2 atmosphere by RF-MS, consistent with its amorphous nature.

FTIR provided valuable evidence for the nature of the as-deposited a-Si:H coating in the presence of an Ar/H_2 sputtering gas. Figure 5-16(b) confirmed the absorption of air species on the Si surface, indicative of the presence of amorphous silica (SiO_2), whilst a narrow FTIR peak at 874.2 cm^{-1} was assigned to Si-H. This latter assignment was in agreement with Savvides [309] who reported on a-Si:H films deposited by DC-MS, at 200°C, known to

enhance the formation of SiH_2 species at a bending mode of 875 cm^{-1} and polysilane species $(SiH_2)_n$ at bending modes of 845 and 890 cm^{-1}. Similar observations were made by Lucovsky *et al.* [310] who detected SiH_2 at 875 cm^{-1} after growing a thin film of a-Si:(H,O), prepared by the glow-discharge decomposition of SiH_4 in a gas ambient containing both H_2 and O_2. The presence of Si-H at 875 cm^{-1} was attributed to isolated SiH_2 in which hydrogen atoms were not bonded to common Si sites.

A wide FTIR peak around 1033.8 cm^{-1} and a small peak at 1161.8 cm^{-1} were assigned to stretching Si-O-Si bonds, indicative of the presence of residual oxygen in the PVD chamber. Gunde [311] also reported the presence of a-SiO_2 after the deposition of a silicon oxide film by CVD, at 350°C, as identified by FTIR peaks at 1064 and 1165 cm^{-1}. Lucovsky *et al.* [310] considered that the structure of Si-O-Si consists of four oxygen atoms bonded to two Si atoms, with two other bonding positions attached to Si or H neighbours. This arrangement is different from crystalline silica, consisting of a central Si atom surrounded by four oxygen atoms (tetrahedral groups) [312].

A related study by Pai *et al.* [313] recorded the presence of an Si-O-Si stretching band at 1075 cm^{-1} and a broad shoulder centred at ~ 1150 cm^{-1} for SiO_x films growth by PECVD. A linear relationship of IR frequency for the Si-O-Si stretching vibration, as a function of oxygen composition (x in SiO_x) was reported (Figure 5-24). Based on this relationship, SiOx detected at a stretching mode of 1033.8 cm^{-1} could probably reflect the form of $SiO_{1.5}$. Further, the absorption of oxygen/hydrogen in the chamber and the formation of silica is consistent with XPS data (Figure 5-19), from both O_{1s} at 533.13 eV and Si_{2p} at 103.8 eV.
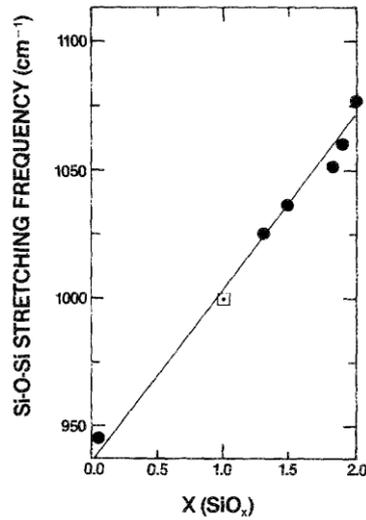
Figure 5-24 Si-O-Si stretching vibrations as a function of oxygen composition in SiO_x [313].

Although FTIR and XPS observations indicated the presence of a-SiO_2, EDS analysis (Figure 5-17(b)) of these as-deposited Si-based coatings in cross-section indicated that the content of oxygen decreased deeper into the Si layer, as compared to the top surface (Figure 5-17(a)). Hence, the model proposed for the deposited Si coating (Figure 5-25, adapted from [314]) indicates that the deposited film may comprise different layers: *i.e.* a transitional sub-oxide layer ($\sim$ $SiO_{1.5}$) and partial conversion of a-Si to a-SiO_2 upon contact with the air.
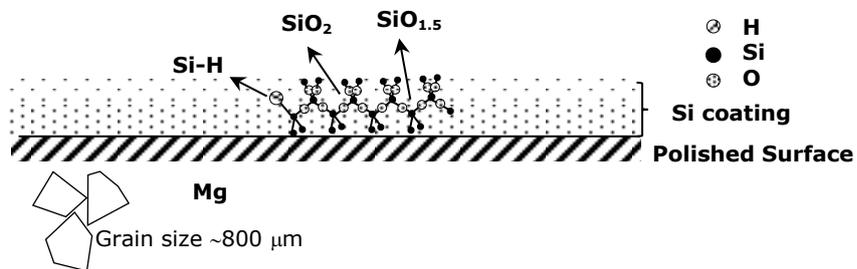
Figure 5-25 Schematic illustration of a-Si:H coating of Mg.

176

5.3.3.3 Corrosion mechanisms

The OCP (Figure 5-20(a)) of the as-prepared Mg surface showed a fluctuation of the corrosion potential with time, indicating that the $Mg(OH)_2$ passivation layer had yet to establish equilibrium with the PBS. This was attributed tentatively to the sensitivity of the Mg surface to localised corrosion enhanced by the presence of Cl^- ions in PBS.

On the other hand, the as-deposited a-Si:H surface showed a steady increase in potential, with time, until becoming slightly more negative than the as-polished Mg surface, at the end of the measurement time. This indicated a more reactive a-Si:H coating surface, becoming stable within the PBS during immersion. By the end of 1 h of stabilisation, the a-Si:H coating showed a nobler E_{corr} behaviour of -1602.8 mV, compared to the uncoated Mg surface at -1718.7 mV. This was attributed to the dissolution of surface components of a-Si:H in PBS. The active surface, progressively covered by corrosion products, showed a rise in surface potential until an equilibrium between corrosion products and coating dissolution in steady OCP was reached. The progressive dissolution of a-S:H coated Mg, immersed in PBS is mediated by the reaction of SiO_2 with H_2O [315]:

$$SiO_2 + 2H_2O \rightarrow H_4Si\,O_4 \qquad\qquad \text{Eq 5-16}$$
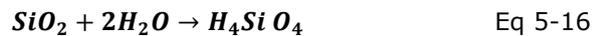
It is considered that a newly formed surface containing silanol, Si-OH, in addition to Si-H, responsible for a sharp FTIR peak at 3693.6 cm^{-1} corresponding to the silanol Si-OH bond, as reported by Cerofolini *et al.* [316] and Weldon *et al.* [317]. The Si-H reaction with H_2O to form silanol is followed by a reaction with hydroxide, to form a negative charged $Si - O^-$ surface [283].

$$Si - H + H_2O \rightarrow Si - OH + H_2 \qquad \text{Eq 5-17}$$
$$Si - OH + OH^- \rightarrow Si - O^- + H_2O \qquad \text{Eq 5-18}$$
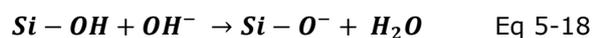
Subsequently, Ca^{2+}, Na^+ and Mg^{+2} ions in PBS solution, attracted to the $Si - O^-$ negatively charged surface, combined with the arrival of carbonate (CO_3^{2-}) and phosphate HPO_4^{2-} ions, leads to the precipitation of amorphous calcium hydrogen phosphate ($CaHPO_4$), consistent with EDS analysis (Figure 5-22), in addition to magnesium phosphate ($Mg_3(PO_4)_2$), in the form of $Na_4Mg(PO_4)_2$ and $Mg_2(PO_4)OH$, as revealed in XRD data (Figure 5-23). The presence of $Si - O^-$ on the corroded surface was confirmed by FTIR at 1001.3 cm^{-1}, attributable to the Si-O-Si vibration. Similar observations by Xin *et al.* [281] reported silicon oxide bands at 1004 cm^{-1} (attributed to Si-O-Si). Furthermore, FTIR signatures around 962.9 cm^{-1} (800-1160 cm^{-1} region) and 669.2 cm^{-1} (Figure 5-23) were consistent with the presence of PO_4^{3-} and HPO_4^{2-}, respectively. A signal for amorphous carbonate CO_3^{2-} was observed at 1446 cm^{-1} [318], in agreement with the corrosion mechanism proposed.

The precipitation of these layers on an a-Si:H surface resulted in a slower anodic dissolution, of 0.05 ± 0.02 mm/year at E_{corr} potential (Figure 5-20 (b)), followed by a straight-forwards corrosion process, fitting that of the Mg substrate. This indicates the penetration of PBS solution through the a-Si:H coating to reach the Mg substrate, with increasing immersion time, presumably assisted by the hydrophilic nature of the a-Si coating. The hydrophilic characteristic nature of as-deposited a-Si-H coating is observed strongly in FTIR data (Figure 5-16 (b)), *i.e.* at 1416.9 cm^{-1} and ~ 2850.4 – 2919.6 cm^{-1} that are associated with O-H groups (corresponding to H_2O). Such hydrophilic surfaces are preferable for biomedical implants since they can initiate protein adsorption/desorption processes, thereby enhancing cell interaction and adhesion [319].

The improved corrosion resistance of a-Si:H coated Mg was confirmed further by immersion testing (Figure 5-21). It is clear that a-Si:H possesses the properties of a barrier like coating, *i.e.* a continuous, dense and crack-free coating, as confirmed by Figure 5-15 and Figure 5-17, achieving a reduced corrosion rate for Mg, from 4.7±0.1 mm/year to 2.4±0.1 mm/year. This slow corrosion continued until the end of the test duration (7 days), confirming the stable dissolution behaviour of a-Si:H coated Mg. This result is in agreement with Xin *et al.* [281], who showed that a 1 μm thick hydrogenated amorphous silicon a-Si:H coating improve the corrosion resistance of coated AZ91 Mg-alloy, in which E_{corr} shifted from -1836 mV to a more positive value of -1507 mV, coupled with a reduction of corrosion current density (i_{corr}) by two orders of magnitude, from 7.05×10^{-4} A/cm^2 to 3.75×10^{-6} A/cm^2.

5.3.4 Recommendations for process control

Based on the results obtained from these a-Si:H coatings, it is suggested that the coating of Mg stents with a-Si:H should be beneficial, in terms of reducing the corrosion rate of bulk Mg and improving cell attachment to Mg stent surfaces. The surface biocompatibility of Si-based coatings should be explored further, *e.g.* by growing polycrystalline Si-H coatings, through alteration of substrate bias and substrate temperature, in addition to subsequent furnace thermal annealing, to enhance the near surface crystallisation. Furthermore, a study of the structured development of Si coatings, under different hydrogen partial pressures, showed the influence of gas pressure on the coating nano-structure and crystallinity [307] and thus may influence corrosion performance. The grow of a stoichiometric oxide layer on top of a Si coating, through annealing in an O_2 atmosphere, should also act to improve the corrosion resistance of Mg.

5.4 Summary

The use of PVD (RF-MS) to deposit Al-based and Si-based coatings on Mg surfaces has been investigated, as a part of a strategy to moderate the corrosion resistance of biodegradable Mg-stents. As-deposited Al and Al-H coatings, processed in Ar and Ar/H_2 sputtering gas atmospheres, were found to be crystalline, with a component of Al-Mg alloy. The involvement of H_2 in the sputtering gas acted to enhance the spontaneous formation Al_2O_3 upon exposure to atmosphere, and restrict the development of Al-Mg alloy. Thermal oxidation, in air at 300°C, led to a partial conversion of the Al coating to a near surface layer of alumina, from XRD observations. Increasing the oxidation temperature to 450°C resulted in the sintering and delamination of the Al/Al-H coating, combined with oxidation of the substrate to form MgO. The corrosion performances of both as-deposited and annealed Al and Al-H coatings were explored. The OCP and E_{corr} values for Al and Al-H coated Mg samples were found to shift positively, compared to Mg corrosion potentials. Under the conditions examined here, as-deposited Al and heat-treated Al_{450} showed the slowest corrosion rates, as compared with Al_{300} coatings and the as-deposited and heat-treated Al-H coatings, on the basis of potentiodynamic polarization corrosion tests. The development of galvanic cells at the Al/Mg interface may lead to poor corrosion resistance of Al and Al-H coatings. It is found that the corroded layer included $Al(OH)_3$ and substrate $Mg(OH)_2$ corrosion products, as well as magnesium phosphate.

In addition, as-deposited PVD coatings of Si, in the presence of an Ar/H_2 gas mixture were examined. XRD and complementary EDS investigations showed the deposited coatings to be amorphous. FTIR investigations on as-deposited a-Si:H coatings provided evidence for Si-H in the form of isolated SiH_2. The

presence of a-SiO$_x$ within the a-Si:H coating was also confirmed by FTIR, with a linear relationship of IR frequency for Si-O-Si stretching, as a function of oxygen composition, suggesting the oxide layer included a non-stoichiometric a-SiO$_{1.5}$ structure. The developed a-Si:H film structure comprised a mix of a-Si, a-SiO$_{1.5}$ and a-SiO$_2$. The corrosion resistance of the coated Mg surface was improved under both potentiodynamic polarization and immersion corrosion tests. The corrosion potential E$_{corr}$ value was found to shift positively compared to the Mg corrosion potential, indicating improved resistance to the onset of corrosion. The corrosion rate reduced to half, by the application of these a-Si-H coatings, indicating their ability to isolate the Mg surface from Cl$^-$ ions in the PBS media. Immersion in PBS turned the surface to negatively charged $Si-O^-$, which promoted the precipitation of a-CaHPO$_4$ and (Mg$_3$(PO$_4$)$_2$) components.

CHAPTER 6 Near surface modification of Mg by LAEB and LSM

6.1 Introduction

Rapid thermal processing (RTP) refers to methods used to produce nanostructures, whereby material temperature is controlled dynamically through high heating and cooling rates [190]. Controllable heat profiles permit the modification of material near surfaces, through fast phase transitions to the surface morphologies, not achievable in conventional furnaces due to their limited heating and cooling rates (few K s^{-1}) [190]. RTP involves the application of electron beams, ion beams, lasers or plasmas, as used to improve a material's surface properties, through localised melting and rapid cooling effects up to 10^9 K s^{-s} [190]. Such processes result in a change in the near surface microstructure, with a view to enhancing wear and hardness, or corrosion and oxidation resistance.

Large area electron beam (LAEB) processing, for example, uses a high energy beam of electrons (1-40 J/cm^2) [190] to create a surface melt pool (with depth of ~10 μm) which then re-solidifies rapidly under ambient conditions. The aim is to achieve a modified surface layer with homogeneous microstructure, with a view to enhancing corrosion resistance through a combination of grain refinement and the removal of impurities and precipitates from the near surface region. In this context, there is need for improved understanding of the interaction of the electron beams (EB) and Mg surfaces, for the purpose of process optimisation.

A change of surface characteristics can be achieved also by laser surface melting (LSM); in which case a laser beam (1-30 J/cm^2) is used to heat and

melt a material's surface (melting pool depth ~ 750 µm), followed by rapid cooling / self-quenching [211]. The refinement of the near surface structure, as a result of fast cooling, can reduce the micro-segregation of impurity elements, and promote the formation of a more homogeneous microstructure. The laser beam / material interaction depends on various processing parameters, such as power density, beam diameter and scanning (traverse) velocity, whilst large area coverage is achieved by overlapping laser tracks (up to ~ 50%). Mg, however, shows high reflectivity to the laser, hence the LSM process parameters need to be selected carefully, in order to achieve a satisfactory layer melting without vaporisation, which could compromise corrosion resistance and lead to enhanced surface roughness.

The aim of this study is to improve the corrosion resistance of Mg by grain refinement and the production of a more homogeneous near surface layer. This requires the melting and rapid solidification of the surface layer, to create a fine-scale microstructure with minimal impurity segregation.

Accordingly, the work presented in this Chapter starts with the effect of electron beam parameters on surface morphology of Mg surface, through applying different cathode voltages and number of pulses (Section 6.2). Then, the effect of laser beam irradiation parameters on the modification of Mg surface morphology and structure is explored (Section 6.3). The study of grain refinement for both EB and LSM was investigated using SEM/EDS and XRD, along with surface roughness measurements and the results are detailed in Sections 6.2.1 and 6.3.1. In addition, the corrosion behaviour and passivation performance of the EB/or LSM modified Mg surfaces were investigated using potentiodynamic polarization and immersion corrosion tests. The alteration of surface morphology under high and low energy of EB/or LSM irradiation and their relation to corrosion performance is discussed in Sections 6.2.3 and 6.3.3.

6.2 LAEB processing of Mg

High purity Mg samples were subjected to electron beam irradiation using a Sodick PF32A large area electron beam (LAEB) instrument, under varying cathodic voltages (15, 25, 35 and 40 kV) and number of shots (1, 5, 20 and 50). Morphological investigations of the as-prepared and modified Mg surfaces are presented in following section. The potentiodynamic polarization and immersion corrosion tests, performed on both the as-prepared and modified samples, are described in Section 6.2.2. Table 6-1 summaries the sample sets investigated, in these near surface LAEB modification experiments, listing their processing conditions and resultant corrosion rates.

Table 6-1 Sample sets processed using LAEB near surface modification and their coding where EB refers to electron beam; the numbers 15,25,35 and 40 refer to cathode voltages; and the numbers 1,5,20 and 50 refer to the number of pulses.

Sample code	Cathode Voltage / kV	Number of shots	Corrosion rate / mm/year				
			Potentiodynamic	Immersion test			
			3 hr	1 day	3 days	5 days	7 days
Mg	0	0	0.11 ± 0.01	6.6 ±0.07	1.8 ±0.1	1.3 ±0.04	1.7±0.03
EB15-1	15	1	0.15 ± 0.01	1.2 ±0.07	2.0 ±0.1	1.1±0.04	0.8±0.03
EB15-5		5	0.12 ± 0.01	1.0 ±0.07	0.4 ±0.1	1.3±0.04	1.6±0.03
EB15-20		20	0.10 ± 0.01	2.9 ±0.07	2.1±0.1	0.6±0.04	0.7±0.03
EB25-1	25	1	0.08 ± 0.01	0.6 ±0.07	0.5±0.1	0.7±0.04	2.1±0.03
EB25-5		5	0.16 ± 0.01	3.5 ±0.07	2.8±0.1	1.3±0.04	0.9±0.03
EB25-20		20	0.16 ± 0.01	1.2 ±0.07	2.3±0.1	1.5±0.04	1.7±0.03
EB35-1	35	1	0.09 ± 0.01	3.3 ±0.07	2.1±0.1	2.0±0.04	1.8±0.03
EB35-5		5	0.13 ± 0.01	5.8 ±0.07	1.5±0.1	1.5±0.04	1.8±0.03
EB35-20		20	0.17 ± 0.01	4.7 ±0.07	2.2±0.1	1.7±0.04	0.9±0.03
EB40-1	40	1	0.14 ± 0.01	3.5 ±0.07	2.0±0.1	1.7±0.04	1.9±0.03
EB40-5		5	0.14 ± 0.01	3.2 ±0.07	1.6±0.1	1.2±0.04	1.2±0.03
EB40-20		20	4.66 ± 0.01	3.3 ±0.07	4.4±0.1	1.4±0.04	1.4±0.03
EB40-50		50	2.30 ± 0.01	6.9 ±0.07	2.2±0.1	3.9±0.04	4.7±0.03

6.2.1 Characterisation of LAEB modified Mg surfaces

6.2.1.1 OM and SEM/EDS of LAEB modified Mg surfaces

Figure 6-1 (a-h) presents optical microscope (OM) and secondary electron (SE) images of as-prepared and EB-irradiated Mg surfaces, processed at 15 kV, with 1, 5 and 20 pulses. The as-prepared Mg surfaces (Figure 6-1 (a-b)) showed residual marks and striations from the mechanical polishing. There was no remarkable change to the Mg surface, as modified by 1 LAEB pulse (Figure 6-1 (c-d)), although slight re-modelling could be observed, with some polishing marks being removed and a tendency for the surface to become more planer. More grain boundaries were observed for samples LAEB processed with 5 and 20 shots (Figure 6-1 (e-h)), suggesting removal of the surface burnished layer, however, deep polishing marks could still be observed, indicating that no melting deeper than the depth of the polishing marks occurred.
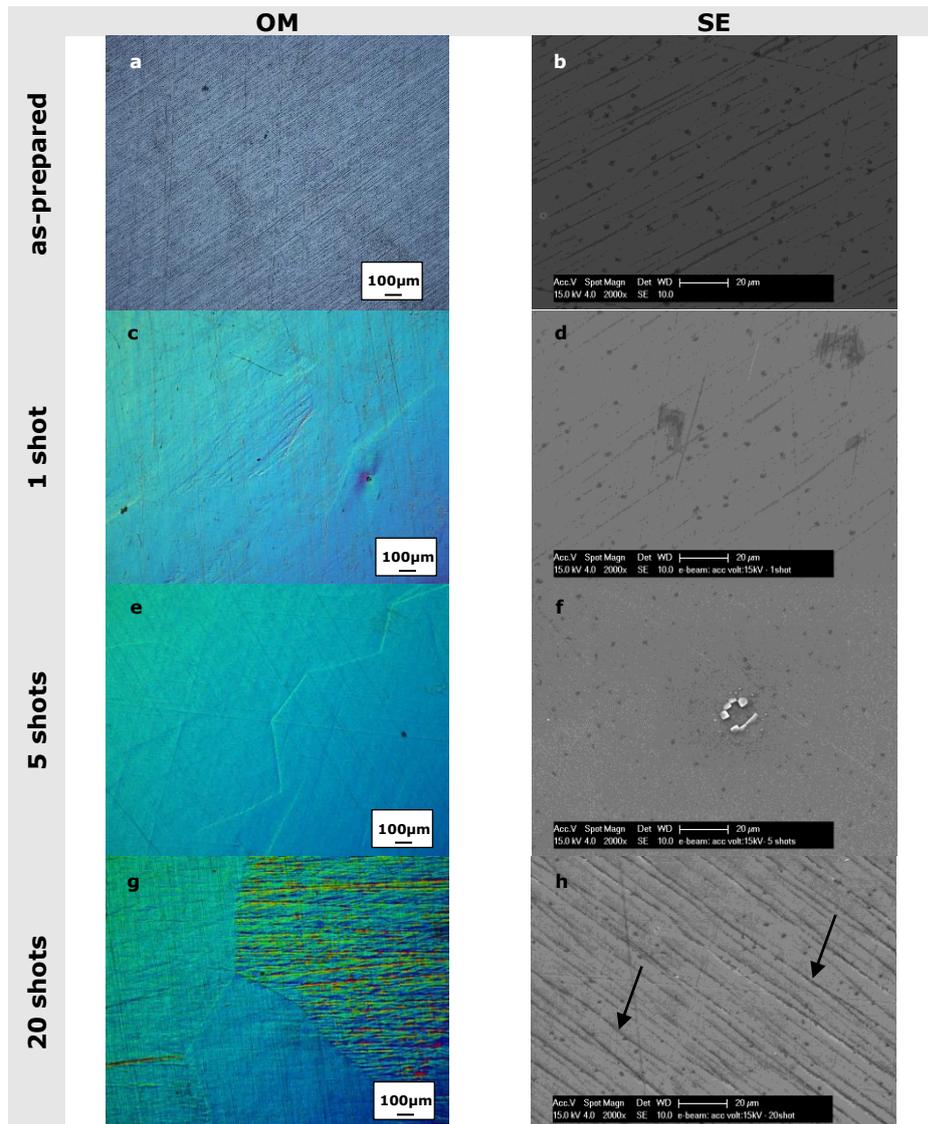
Figure 6-1 OM and SE images of Mg surfaces modified by LAEB processing (15 kV; 1, 5 and 20 pulses), arrows indicate the presence of polishing damage on the Mg surface.

Figure 6-2 (a-f) shows the influence of EB irradiation at 25 kV cathode voltage, after 1, 5 and 20 pulses. With increasing number of pulses, the Mg surfaces experienced increasing amounts of re-modelling and the enhancement of grain boundaries. For the case of 1 pulse (Figure 6-2 (a-b)), numerous small craters of ~ 1.5 - 5.0 μm diameter formed, mainly at polishing marks, indicative of shallow melting on the scale of the depth of the polishing marks, along with localised ablation, leaving the Mg surface covered

with debris showing high brightness levels, indicative of a charging effect, in turn suggesting the formation of MgO which is electrically insulating. For the case of 5 pulses (Figure 6-2 (c-d)), the diameter of these process craters reached an average of ~ 2.2 μm, decorating strips of melted polishing marks. A small amount of remnant debris was present also, indicative of more intensive, localised ablation at peaks on the rough, polished surfaces. For the case of 20 pulses (Figure 6-2 (e-f)), complete melting of near surface material led to the disappearance of polishing marks and ablation debris. However, short-range striations and a mixture of large (~ 24 μm) and small (~ 0.6 - 2.0 μm) diameter craters covered the Mg surface.
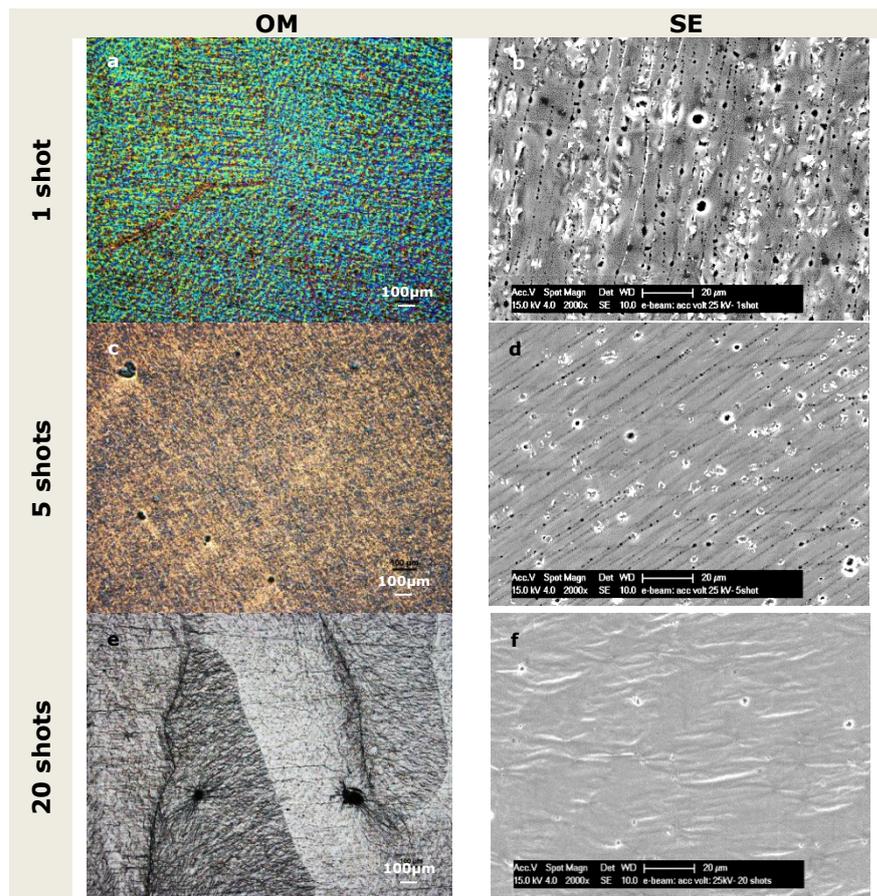
Figure 6-2 OM and SE images of Mg surfaces modified by LAEB processing (25 kV; 1, 5 and 20 pulses)

Mg surfaces LAEB processed at 35 kV showed a similar response to those irradiated at 25 kV, with increasing delineation of grain boundaries with increasing number of pulses (Figure 6-3 (a-f)). Surfaces modified by 1 pulse (Figure 6-3 (a-b)) were covered by craters of varied diameter, from 1.5 - 5.6 μm, combined with the removal of some polishing marks indicative of deep melting, and some residual surface debris. Mg surfaces after 5 pulses (Figure 6-3 (c)) were shiny, indicative of improved planarization following material removal, allowing large Mg grains underneath to become visible, whilst high magnification SE images (Figure 6-3 (d)) revealed numerous small craters with average diameter of 3.0 μm. Some 5-pulse modified surfaces showed also irregular, melted pits of ~ 120 μm diameter (Figure 6-3(c), inset (arrowed)), whilst close examination of SE images revealed that the insides of the pits were porous, indicative of gas-evolution during localised boiling of the Mg surface. In addition, enhanced amounts of debris were present on the periphery of each EB affected area. Surfaces modified by 20 EB pulses (Figure 6-3 (e-f)) showed well-established modulation, with striations at the surface and clear delineation of grain boundaries, as a result of ablation. A bimodal distribution of craters again was evident, of sizes ~ 125 μm and ~ 1 μm.
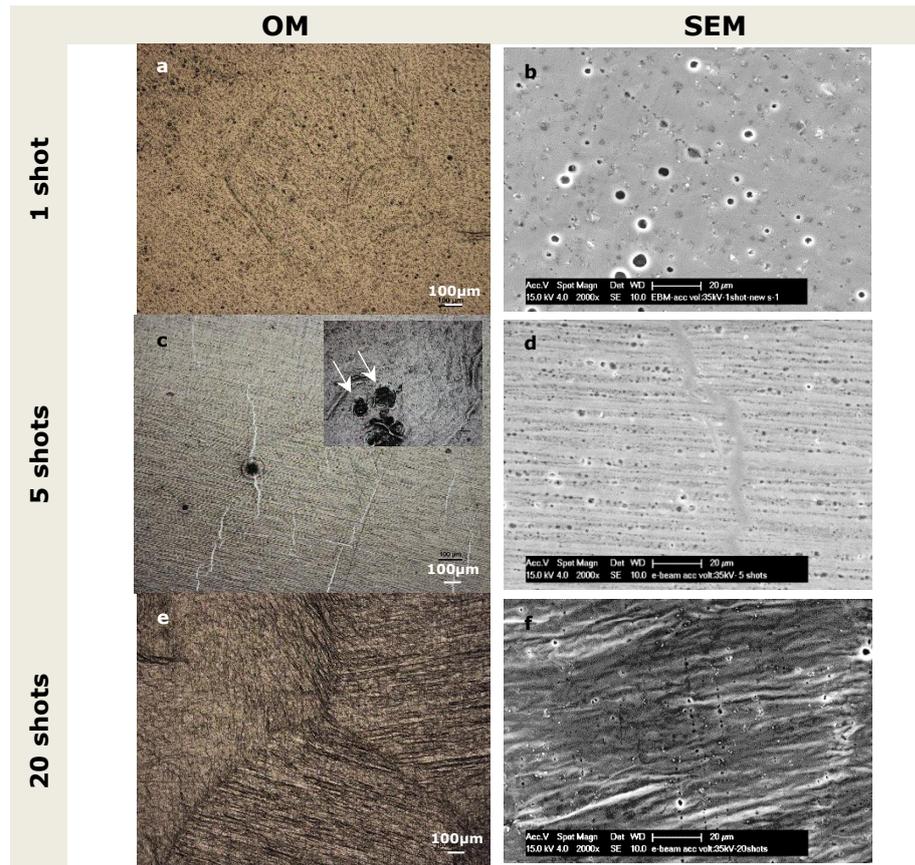
Figure 6-3 OM and SE images of Mg surfaces modified by LAEB processing (35kV; 1, 5 and 20 pulses).

Figure 6-4 (a-h) presents OM and SE images of LAEB processed Mg at 40 kV cathodic voltage, as a function of number of pulses. Again, the modified surfaces exhibited increasing levels of ablation with increasing number of pulses. After 1 pulse (Figure 6-4 (a-b)), the surface layer looked blurry, with evidence for melting as deep as the polishing marks, combined with a distribution of ~ 2.3 - 5.0 μm diameter sized craters. Surfaces processed with 5 pulses (Figure 6-4 (c-d)), showed a polishing finish in the middle of the EB affected area with numerous small craters and bright debris, whilst the periphery showed partial removal of the polishing marks and large ~ 150 μm diameter sized craters. When LAEB processed with 20 pulses (Figure 6-4 (e-f)), the polishing marks completely disappeared and the number of craters decreased, whilst a 'tidal-sand' wavy topography delineated the surface. It is considered that the energy deposited at the surface was sufficient to melt the

top Mg layer and induce a distribution of wavelets upon cool-down. High magnification SE images of these modified surface also showed crack formation, indicative of a discontinuous molten layer, along with a distribution of bright debris deposits in the centrally EB processed area. Surfaces LAEB processed with 50 pulses (Figure 6-4 (g-h)) showed similar features to samples irradiated with 20 pulses. Smooth surfaces with the appearance of grain boundaries defined central regions, whilst wavy features and obscured edge craters decorated the periphery.
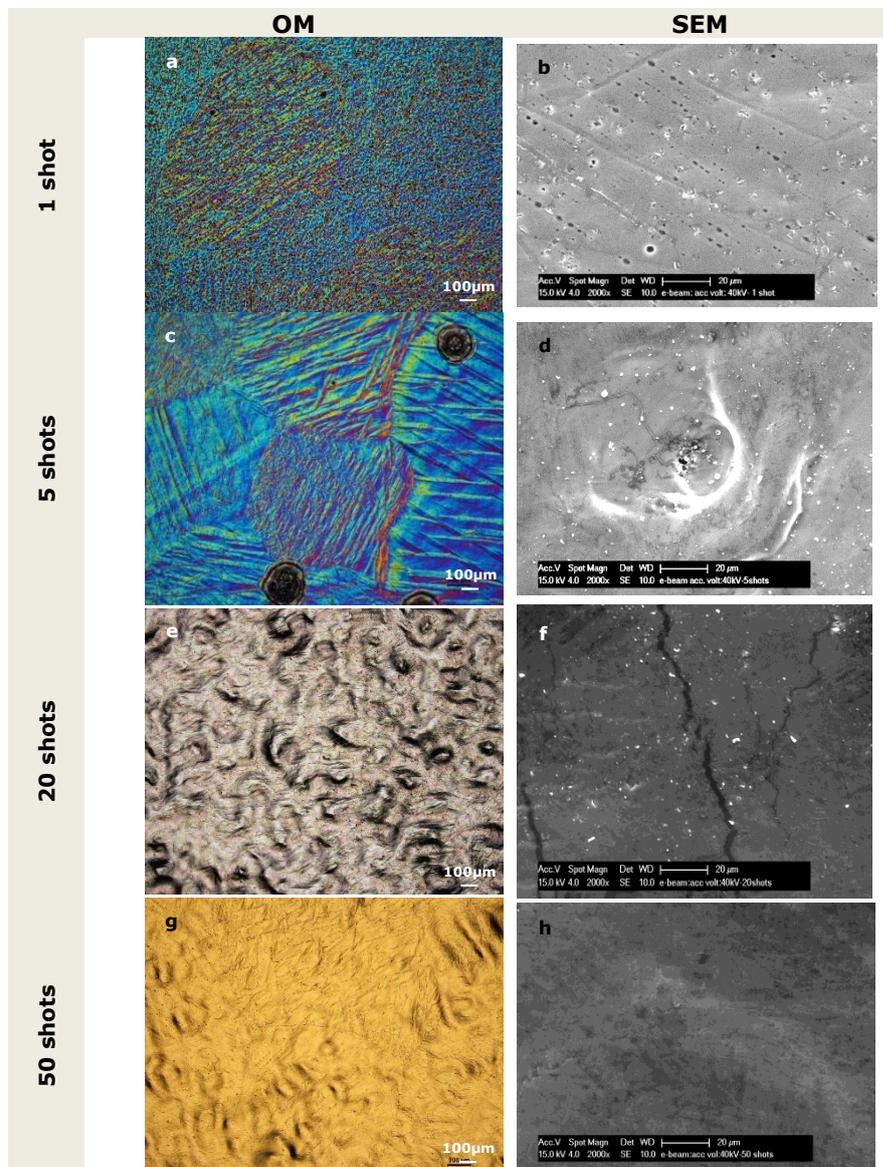
Figure 6-4 OM and SE images of Mg surface modified by LAEB processing (40 kV; 1, 5, 20 and 50 pulses).

Example EDS analyses of the LAEB modified Mg surfaces are presented in Figure 6-5. As-prepared and low energy LAEB processed Mg surfaces showed similar levels of Mg and O content, with O reaching a maximum of 10 at.% in some LAEB cases. Conversely, Mg surfaces LAEB processed at high energy, associated with the formation of craters, showed much higher levels of O (Figure 6-5 (b)) arrowed), with complementary elemental maps (Figure 6-6: 40kV; 5 pulses) confirming the presence of Mg, O, Ca and C, associated with the surface craters. The presence of Ca is tentatively assigned to an unknown source of cross-contamination.
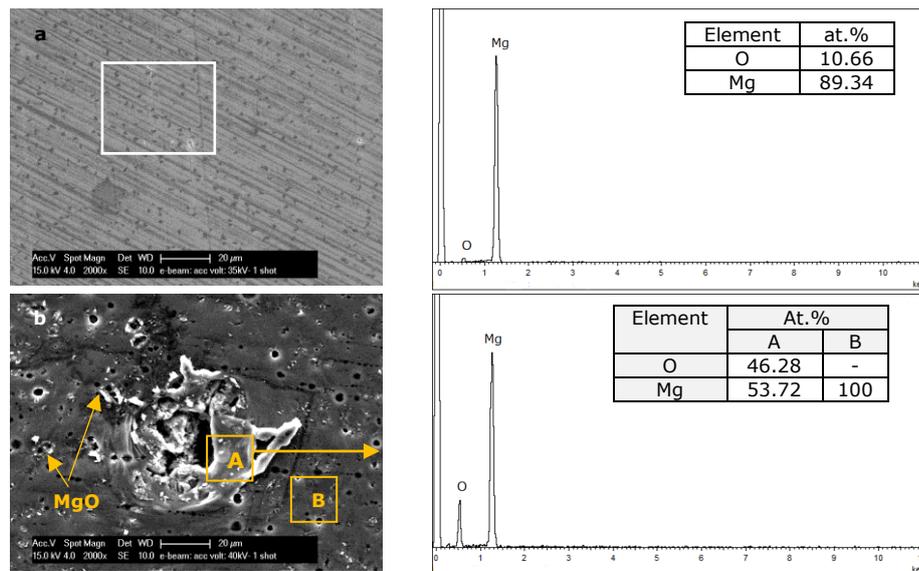
Figure 6-5 EDS analyses of LAEB processed Mg surfaces: (a) 35 kV; 1 pulse; and (b) 40 kV; 1 pulse.
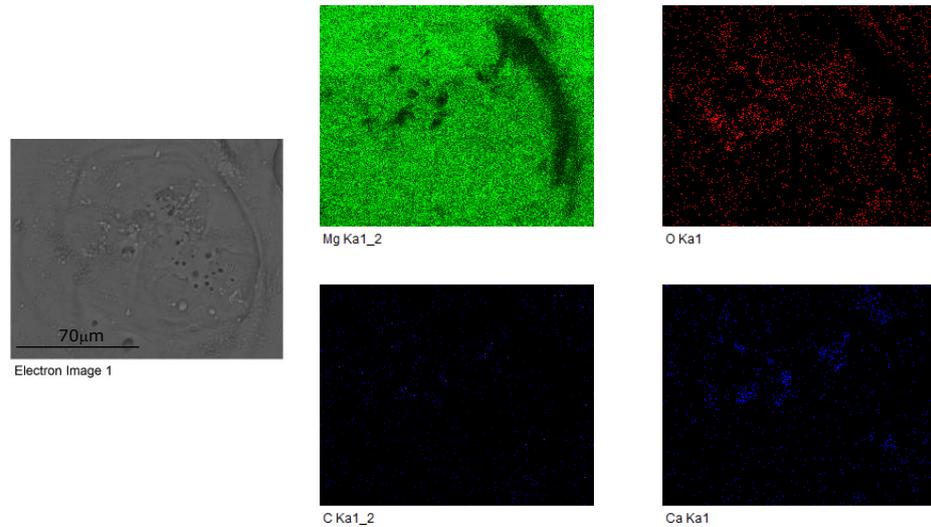
Figure 6-6 EDS elemental maps for LAEB processed Mg (40 kV; 5 pulses). The presence of Ca is tentatively assigned to an unknown source of cross-contamination

6.2.1.2 Cross-sectional morphology

Cross-sections of the Mg surfaces irradiated at varying cathode voltages and number of pulses are presented in Figure 6-7, with corresponding thicknesses summarised in the Table (inset). Generally, the melted layer thickness was similar but the overall topography has a general trend, with increased waviness observed with increasing the cathode voltage and number of pulses. After 1 pulse, the melted layer thickness was in the range of $\sim$ 2 μm. When surfaces were subjected to 5 repeated pulses, the thickness increased to $\sim$ 3 μm, but further pulses had no apparent effect on the melted layer thickness. Some surfaces did not show well-defined layer melting due to ablation, but showed an increase in roughness, due to the formation of small craters and pits, as well as a 'tidal-sand' wavy topography.
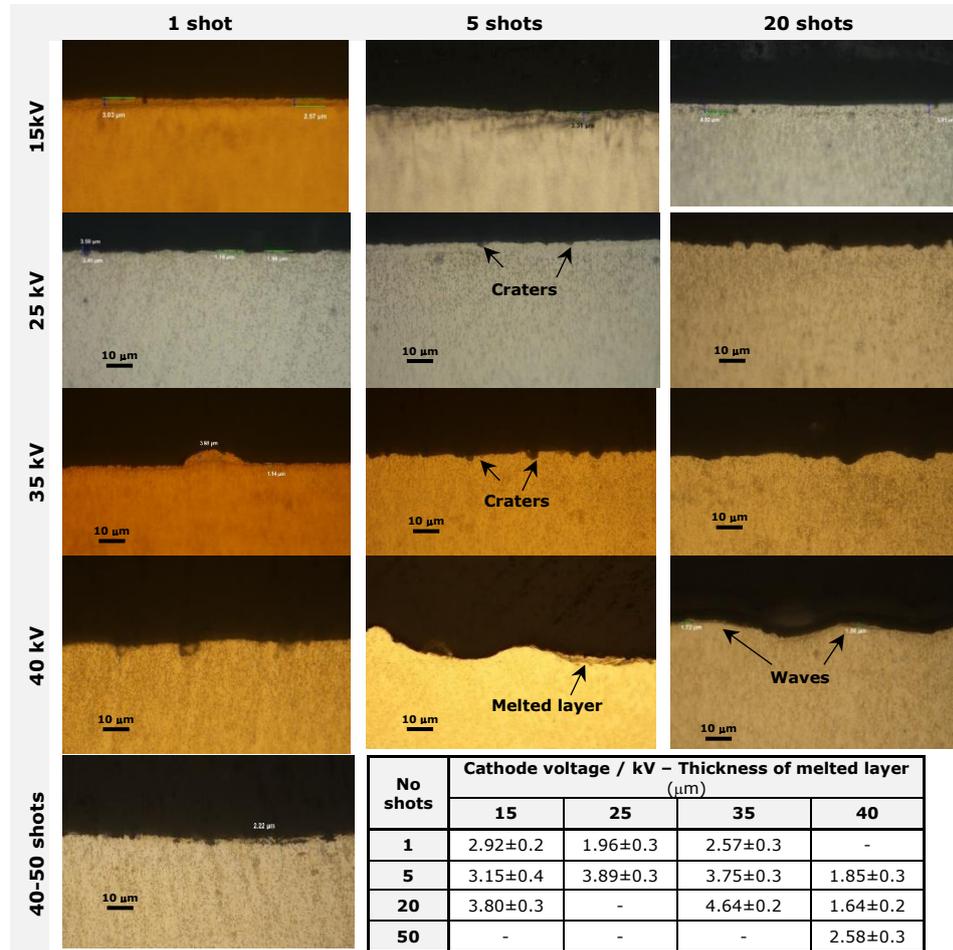
Figure 6-7 OM images showing cross sectional morphologies of LAEB treated Mg; Table summarising melted layer thicknesses in μm. The bar in the images represents 10 μm.

No shots	Cathode voltage / kV – Thickness of melted layer (μm)			
	15	**25**	**35**	**40**
1	2.92±0.2	1.96±0.3	2.57±0.3	-
5	3.15±0.4	3.89±0.3	3.75±0.3	1.85±0.3
20	3.80±0.3	-	4.64±0.2	1.64±0.2
50	-	-	-	2.58±0.3

6.2.1.3 Roughness of LAEB modified surfaces

The topographies of the LAEB modified surfaces were assessed using white light-3D photomapping, over an area of 583 x 783 (μm)^2.

Figure 6-8(a,b) presents surface roughness (Ra) values as a function of cathodic voltage and number of pulses, at the middle and edges of the EB processed areas, respectively. The roughness values were averaged from three measurements made for each EB irradiated area. Generally, Mg surface roughness increased with increasing voltage and number of pulses, compared

to the initial Ra value of 0.13 ± 0.02 μm for mechanically polished surfaces. Slight improvements to surface roughness, by about a third, were achieved under conditions of 15 kV cathode voltage and 1 and 5 pulses, suggesting that low input energy conditions may be beneficial in the remodelling of smoother Mg surfaces, with shallow melting being sufficient to remove some of the polishing marks. However, Ra increased to 0.15 ± 0.02 μm after 20 pulses at 15 kV; and then became raised to ~ 0.2 – 0.3 μm upon irradiation under conditions of 25 kV and 35 kV (1-20 pulses); and then significantly raised to ~ 0.5 μm under conditions of 40 kV (20 pulses), indicating that excessive energy imparted to the sample acted to increase surface roughness. The formation and dispersion of craters across the modified surfaces also impacted upon these surface roughness measurements, in accordance with SEM observations.
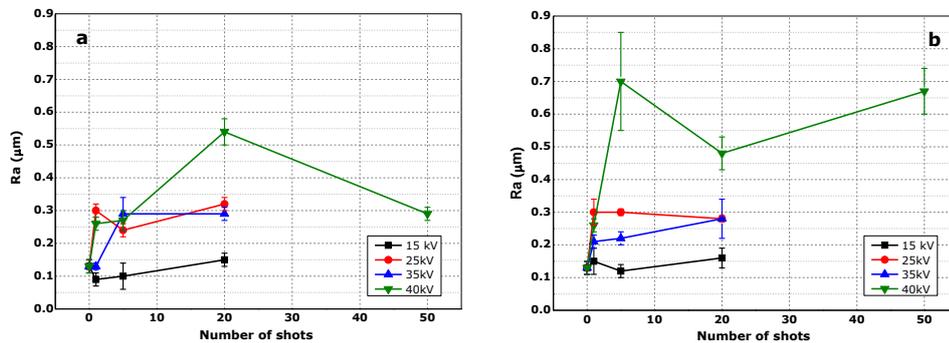
Figure 6-8 Surface roughness (Ra) as a function of cathodic voltage and number of pulses: (a) in the middle; and (b) at the edges of the EB processed areas.

It was noted that considerable differences in surface roughness were returned between the centre and the periphery of LAEB regions, processed under conditions of high 40 kV cathodic voltage, with 5, 20 and 50 pulses at the centre resulting in Ra values from 0.3 to 0.5 μm while at the periphery higher values from 0.5 to 0.7 μm were observed. This may be related to differences in the localised amount of energy received into the sample, or more likely due to reduced diffusion of thermal energy from the hot zones to the low

temperature areas due to the reduction in potential thermal pathways at the edge. This results in higher temperatures and more surface remodelling at the edges.

Figure 6-9(a,b) presents a comparison of surface topographies, LAEB processed under conditions of 40 kV and 50 pulses, at a middle (Ra = 0.30 μm) and edge regions (Ra = 1.3 μm), respectively. The central irradiated area was characterised by high frequency, low amplitude roughness, compared to the edge profile which exhibited wavier features, consistent with the OM and SEM observations.
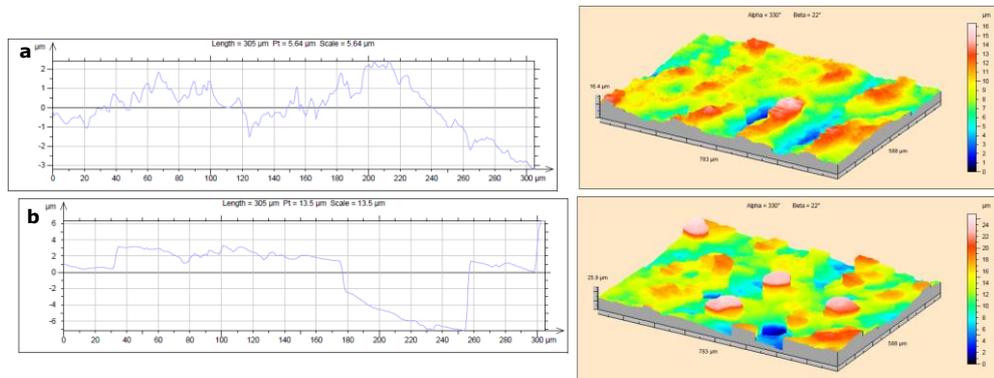
Figure 6-9 Surface roughness profiles for LAEB processed Mg (40 kV cathode voltage; 50 pulses): (a) Middle region; and (b) edge region.

6.2.1.4 XRD of LAEB modified surface

Figure 6-10 presents XRD diffraction patterns of as-prepared and EB modified Mg surfaces, irradiated under conditions of 15, 25, 35 and 40 kV cathodic voltages, as a function of increasing number of pulses. Overall, the patterns are typical of polycrystalline, single phase Mg with no evidence for MgO. However, the intensity of the Mg peaks of the LAEB irradiated surfaces reduced significantly with increasing cathode voltage kV / number of pulses. Mg peak FWHM were measured after LAEB treatment, with significant broadening of the $10\bar{1}0$ peak at 32.2° after irradiation at 35 kV (1 pulse) and

40 kV (20 pulses), being attributable to some measure of grain refinement within the near surface layer combined with relaxation of internal stresses.

Figure 6-11 presents a plot of peak broadening values for the 0002 and $10\bar{1}1$ diffraction peaks, as a function of kV and number of pulses. Variability of these Peak broadening values after LAEB processing may be due to variations in sub-surface damage induced by previous sequential mechanical polishing. The reduction of $10\bar{1}0$ diffraction peaks at 32.2° and 0002 at 34.4°, and the enhancement of the $10\bar{1}1$ diffraction peak at 36.6°, for surfaces modified at 15 kV (5-20 pulses) and 40 kV (Figure 6-10), suggests a certain level of preferred orientation within the recast layers. Scherrer's equation, as applied to estimate grain size within the near surface modified layers (Table 6-2, Figure 6-12) indicated values > 100 nm, *i.e.* beyond the general applicability of the equation.
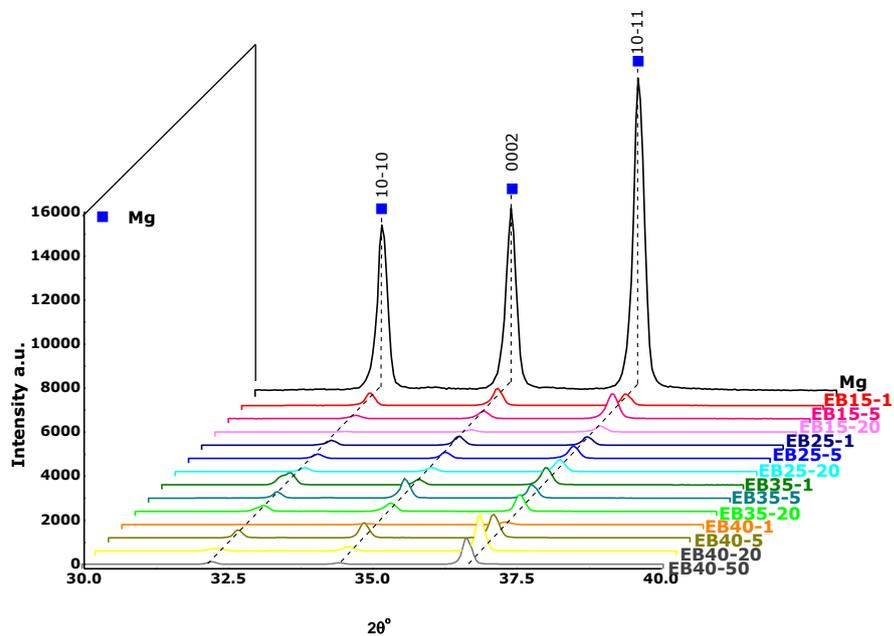
Figure 6-10 XRD patterns of as-prepared and LAEB processed Mg surfaces. Low intensity of EB modified Mg suggests the modified layer had not recovered full crystallinity.
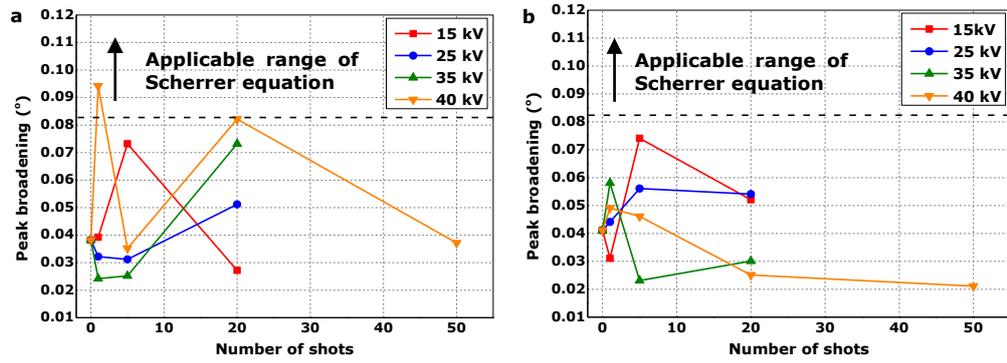
Figure 6-11 Peak broadening of as-prepared and LAEB processed Mg surfaces, as a function of kV and number of pulses: using (a) 0002 and (b) 10$\bar{1}$1 diffraction peaks.

Table 6-2 Average grain size of Mg samples irritated by LAEB

Sample ID	10$\bar{1}$0	0002	10$\bar{1}$1	Average grain size / nm
Mg	551	218	204	255 ± 150
EB15-1	306	212	269	218 ± 63
EB15-5	125	114	113	125 ± 14
EB15-20	138	306	161	180 ± 64
EB25-1	197	258	190	208 ± 39
EB25-5	197	267	149	187 ± 45
EB25-20	318	162	154	225 ± 65
EB35-1	45	343	144	152 ± 101
EB35-5	359	330	362	265 ± 119
EB35-20	72	114	278	138 ± 75
EB40-1	331	88	170	205 ± 88
EB40-5	517	236	182	394 ± 246
EB40-20	44	101	333	183 ± 125
EB40-50	394	224	397	269 ± 110
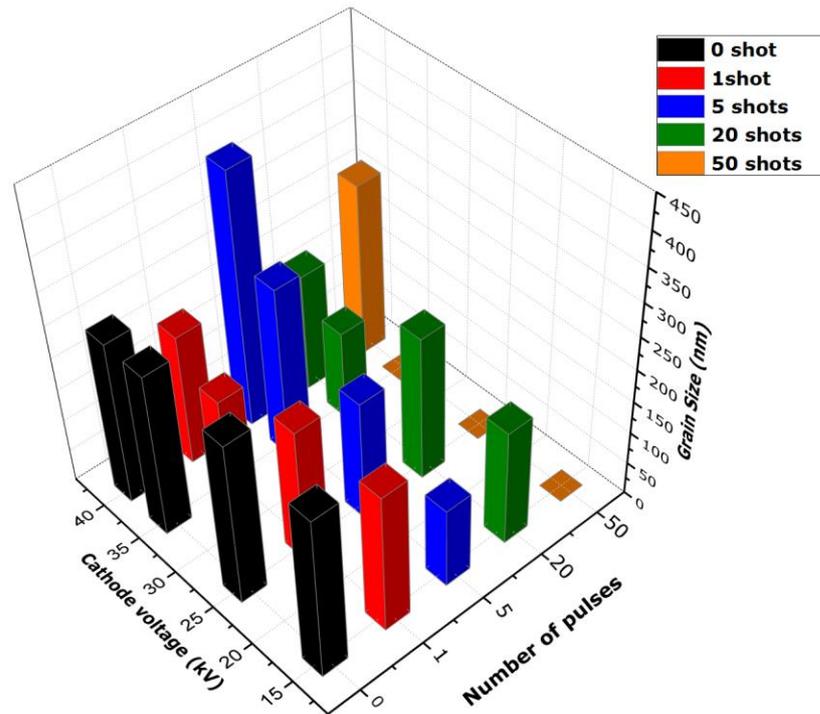
Figure 6-12 Average grain size of Mg samples irritated by LAEB as a function of cathode voltage and number of shots

6.2.2 Corrosion performance of LAEB treated Mg surfaces

6.2.2.1 Potentiodynamic polarization corrosion tests

The corrosion behaviours of LAEB processed Mg surfaces were investigated by potentiodynamic polarization tests, conducted in PBS at 37°C. Figure 6-13(a,b) presents OCP and potentiodynamic polarization tests of the as-prepared and LAEB processed Mg surfaces as a function of cathodic voltage and number of pulses.

Table 6-3 summarises the main corrosion performance values, extracted from Figure 6-13(b). The OCP data showed that the as-prepared Mg substrate exhibited a rest potential of -1802 mV, becoming stable after 30 minutes. After EB processing, the onset corrosion resistance of EB modified surfaces became variable with cathode voltage and number of pulses, but generally increased for surfaces receiving higher power densities. For example, samples

treated under conditions of 40 kV cathode voltage and 50 pulses showed the most resistance, at -1620 mV.

The polarization curves (Figure 6-13(b)) demonstrated similar behaviour of the EB modified Mg surfaces to the as-prepared samples, during corrosion testing. The polished Mg surface revealed typical Tafel regions, with anodic dissolution of 0.11 ± 0.01 mm/year at a corrosion potential of -1756 mV before the $Mg(OH)_2$ passivation broke-down at -1560 mV. Across all the LAEB modified surfaces, samples treated by 20 and 50 pulses at 40 kV showed the most noble E_{corr} values of -1587 mV and -1604 mV, respectively. In contrary to E_{corr}, the same 40 kV and 20 and 50 pulsed samples exhibited no passive region, but a straightforward increase in i_{corr} value with potential, having high values of 0.204 mA/cm^2 and 0.101 mA/cm^2, respectively.

Figure 6-14 summarises corrosion rate as a function of kV and number of pulses for these LAEB modified Mg surfaces. The EB modified surfaces showed significantly higher corrosion rates, which increased with increasing number of pulses, than the as-prepared surfaces. For example, 1 pulse treated samples at 25 kV and 35 kV displayed best corrosion rates of 0.08 ± 0.01 and 0.09 ± 0.01 mm/year, respectively, whilst much higher corrosion rates of 4.66 ± 0.01 and 2.30 ± 0.01 mm/year were returned for surfaces treated by 20 and 50 pulses at 40 kV, respectively.
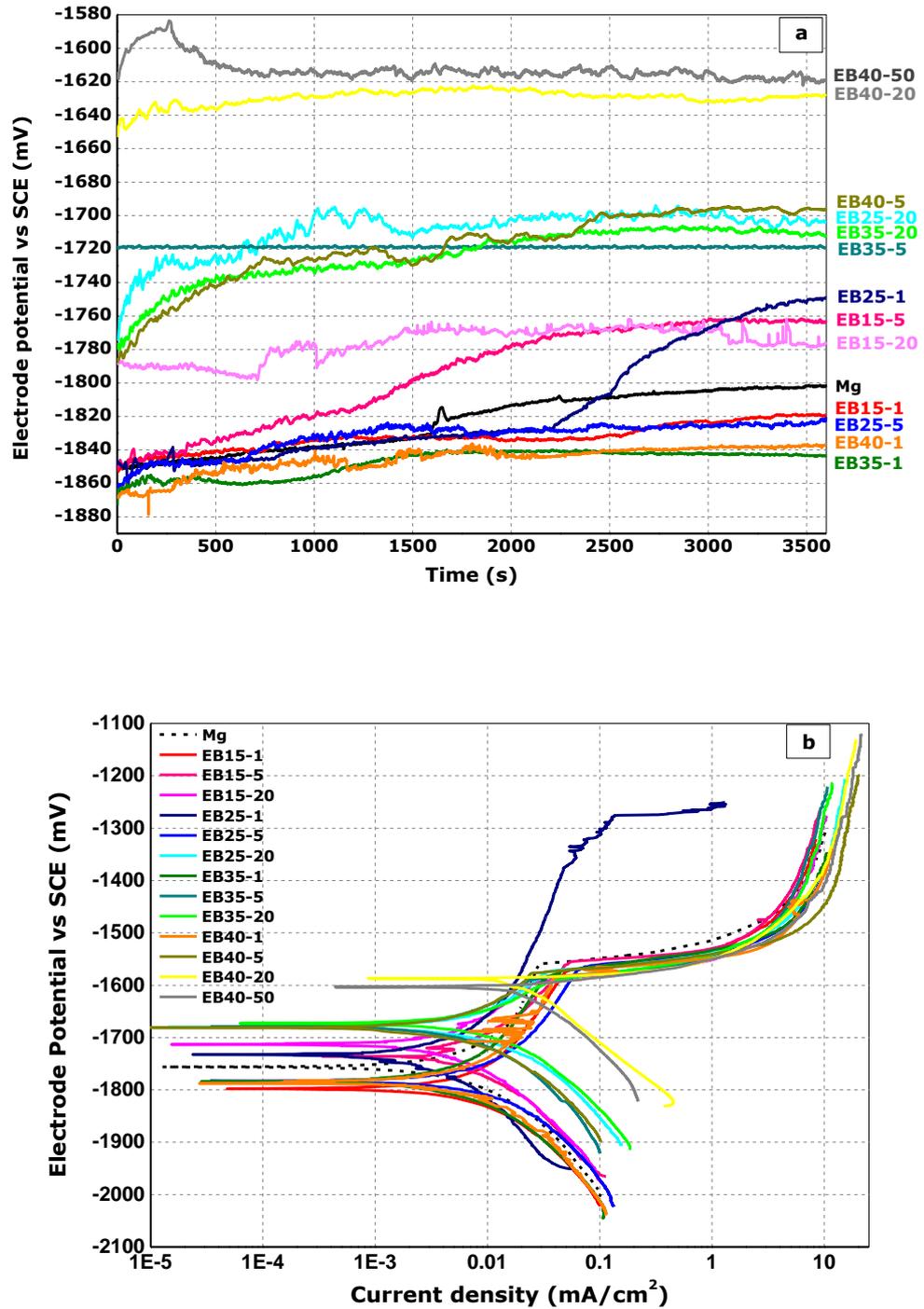
Figure 6-13 Electrochemical corrosion tests of as-prepared and LAEB processed Mg-surfaces, in PBS at 37°C (-200 mV to +500 mV): (a) OCP; and (b) potentiodynamic polarization tests.

Table 6-3 Corrosion parameters of as-prepared and LAEB modified Mg surfaces, from sample polarization behaviours in PBS at 37°C.

Sample	OCP mV	E_{corr} mV	i_{corr} mA/cm²	E_b mV	CR mm/year
Mg	-1802	-1756	0.004	-1560	0.11 ± 0.01
EB15-1	-1819	-1798	0.007	-1574	0.15 ± 0.01
EB15-5	-1764	-1736	0.005	-1556	0.12 ± 0.01
EB15-20	-1776	-1713	0.004	-1598	0.10 ± 0.01
EB25-1	-1749	-1733	0.003	-1377	0.08 ± 0.01
EB25-5	-1820	-1783	0.007	-1572	0.16 ± 0.01
EB25-20	-1705	-1680	0.007	-1575	0.16 ± 0.01
EB35-1	-1844	-1784	0.004	-1583	0.09 ± 0.01
EB35-5	-1719	-1679	0.006	-1591	0.13 ± 0.01
EB35-20	-1712	-1673	0.008	-1593	0.17 ± 0.01
EB40-1	-1837	-1788	0.006	-1585	0.14 ± 0.01
EB40-5	-1697	-1681	0.006	-1577	0.14 ± 0.01
EB40-20	-1629	-1587	0.204	-	4.66 ± 0.01
EB40-50	-1620	-1604	0.101	-	2.30 ± 0.01
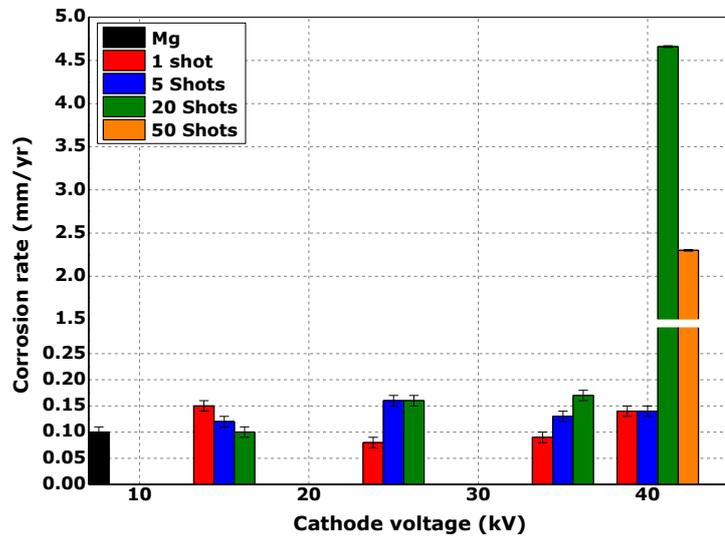
Figure 6-14 Corrosion rate as a function of kV and number of pulses

6.2.2.2 Characterisation of corroded LAEB modified Mg surfaces

Figure 6-15(a-c) presents plan-view micrographs of a corroded surface of LAEB processed Mg (25 kV; 1 pulse), after potentiodynamic polarization testing in PBS. The Mg surface suffered localised pitting corrosion, distributed randomly throughout the immersed surface (Figure 6-15(a)). The high magnification BSE image of Figure 6-15(b) showed that many corrosion products (arrowed) were decorated with clusters. The corrosion of Mg in PBS media usually occurs due to the presence of aggressive chloride (Cl⁻) anions.

The exposed surface was also characterised by layer cracking, along with circular voids / holes surrounded by bright precipitants (Figure 6-15(c, arrowed)).

EDS data from different spots on the high magnification corroded surface is tabulated in Figure 6-15 (d). For spot A, the corrosion products were consistent with the presence of O, Mg and Cl, indicative of MgO / Mg(OH) and possibly $MgCl_2$ / $MgCl_2(H_2O)_x$. The O content was greatly increased compared to the surface before corrosion, consistent with the formation of a hydroxide passivation layer. This sample showed best corrosion performance. Spot B contained mainly O and Mg, in addition to low amounts of P, Na, Cl and Ca corresponding to phosphate (PO_4) components. Spot C, corresponding to the bright corrosion products around open pores showed high amounts of O, Ca and P, with significantly reduced Mg levels, indicating the presence of hydroxyapatite (Ca-P) components.

Element	Composation / at.%		
	Spot A	Spot B	Spot C
O	64.31	50.98	54.05
Na	-	1.97	3.20
Mg	25.38	39.94	7.98
P	-	5.07	14.71
Cl	10.32	1.42	1.01
K	-	-	0.23
Ca	-	0.61	18.81
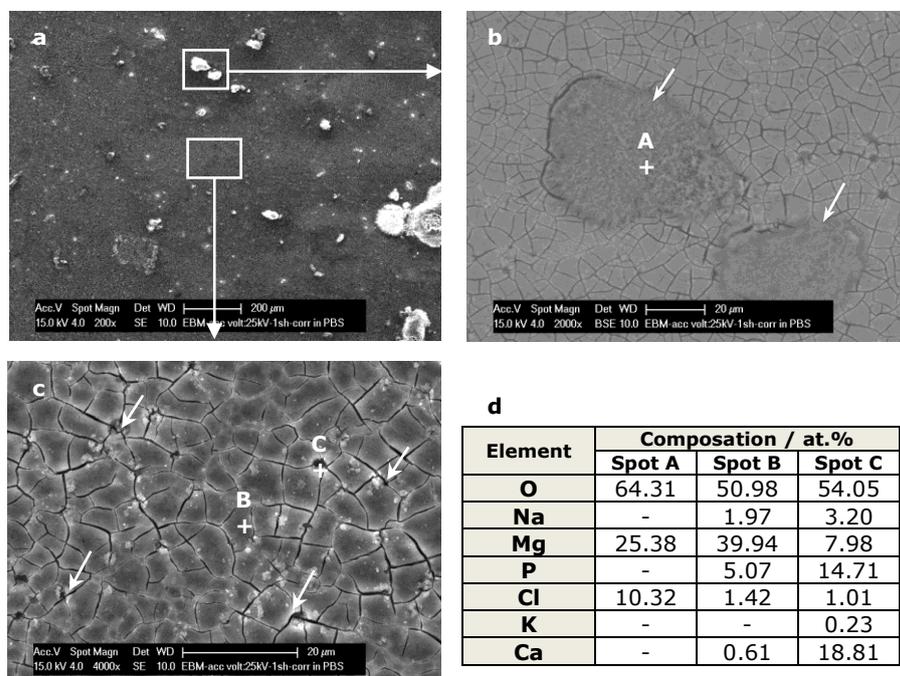
Figure 6-15 Corrosion morphology of an Mg surface, LAEB modified (25 kV, 1 pulse), after potentiodynamic polarization testing in aerated PBS at 37°C. (a) An overview of the corrosion morphology; (b) BSE image of the reaction products; (c) SE image of the passivation layer; and (d) associated EDS data.

6.2.2.3 Immersion testing

Immersion tests was carried out for the as-prepared and LAEB modified surfaces, in PBS at 37°C, for periods of 1, 3, 5 and 7 days.

Figure 6-16 presents corrosion rates as a function of cathode voltage, number of pulses and immersion time. For all specimens, the corrosion rate decreased with immersion time, with the exception of surfaces modified at 40 kV (20 and 50 pulses). For the case of lowest EB-power density, the corrosion rate for the short immersion time of 1 day was lower than that of the as-prepared Mg surface, as minimum as 0.61 ± 0.07 mm/year for sample irradiated at 25 kV and 1 pulse, whereas for case of the highest EB power density (Sample EB40-50), the corrosion rate of 6.9 ± 0.07 mm/year was similar to the 6.6 ± 0.07 mm/year for the as-prepared sample. As the immersion time became longer, the corrosion rate differences between the as-received Mg and EB treated surfaces reduced, with only the sample treated at high energy density (40 kV, 50 pulses), degrading faster with rate of 2.2 ± 0.1 and 3.93 ± 0.03 mm/year compared to 1.8 ± 0.1 and 1.3 ± 0.04 mm/year after 3 and 5 days, respectively. After 7 days of immersion in PBS, the lowest and highest corrosion rates of 0.70 ± 0.03 mm/year (15 kV, 20 pulses) and 4.7 ± 0.03 mm/year (40 kV, 50 pulses) were observed, compared to the value of 1.71 ± 0.03 mm/year for the as-prepared Mg surfaces.
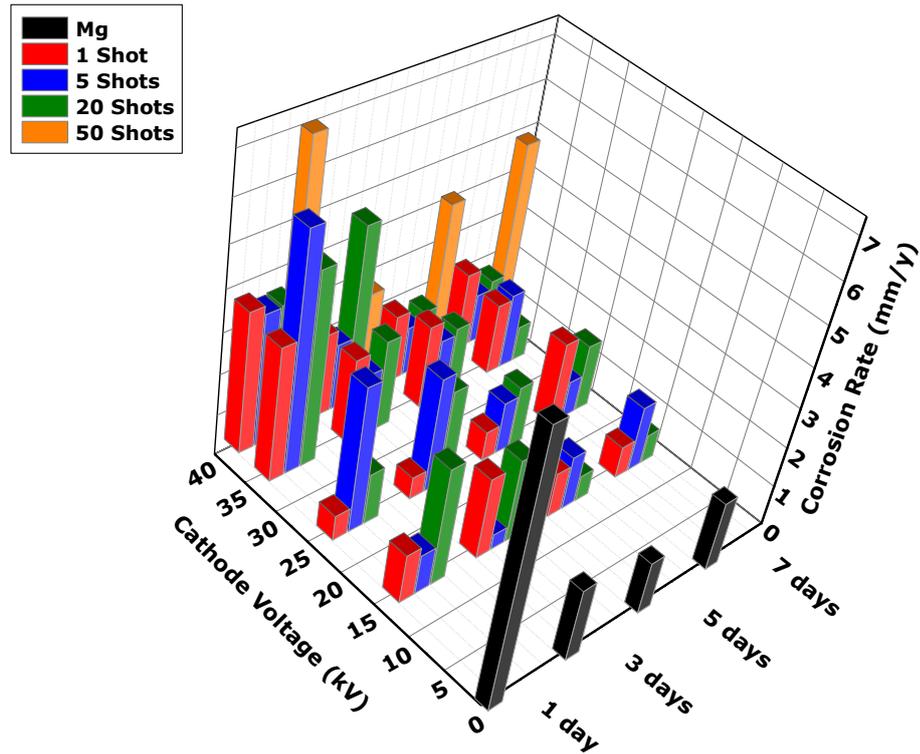
Figure 6-16 Corrosion rates of Mg and LAEB modified Mg surfaces, immersed up to 7 days in PBS at 37°C. Errors not shown for clarity purposes.

6.2.2.4 Characterisation of the corroded surfaces

In order to gain improved understanding of the corrosion mechanism of LAEB treated Mg surfaces, detailed BSE and SE planar-view micrographs of the corroded surfaces were recorded (Figure 6-17 (a-h)). A thin layer of $Mg(OH)_2$ combined with localized corrosion products covered the processed surface after 1-day immersion in PBS (Figure 6-17 (a, EDX inset)). After 3 days, thick films with agglomerations of small round particles were observed (Figure 6-17 (c)). EDS analyses showed the main components to be P, Ca and Na, in addition to Mg and high levels of O. Larger particles formed with increasing immersion times (Figure 6-17 (e,g)). Layer cracking was attributed to hydration, after sample removal from the test solution and exposure to air.

Figure 6-17(b,d,f,h) shows the surface topography of the corroded surfaces after removal of the corrosion products using chromic acid (20% CrO_3 in

water). In addition to uniform corrosion, the Mg surface experienced shallow localized attack, which gradually increased with immersion time. The corrosion preferentially attacked the interior grains, with no evidence of preferential degradation at the grain boundaries. It suggested that high purity Mg has very low levels of impurity precipitation at grains boundaries.
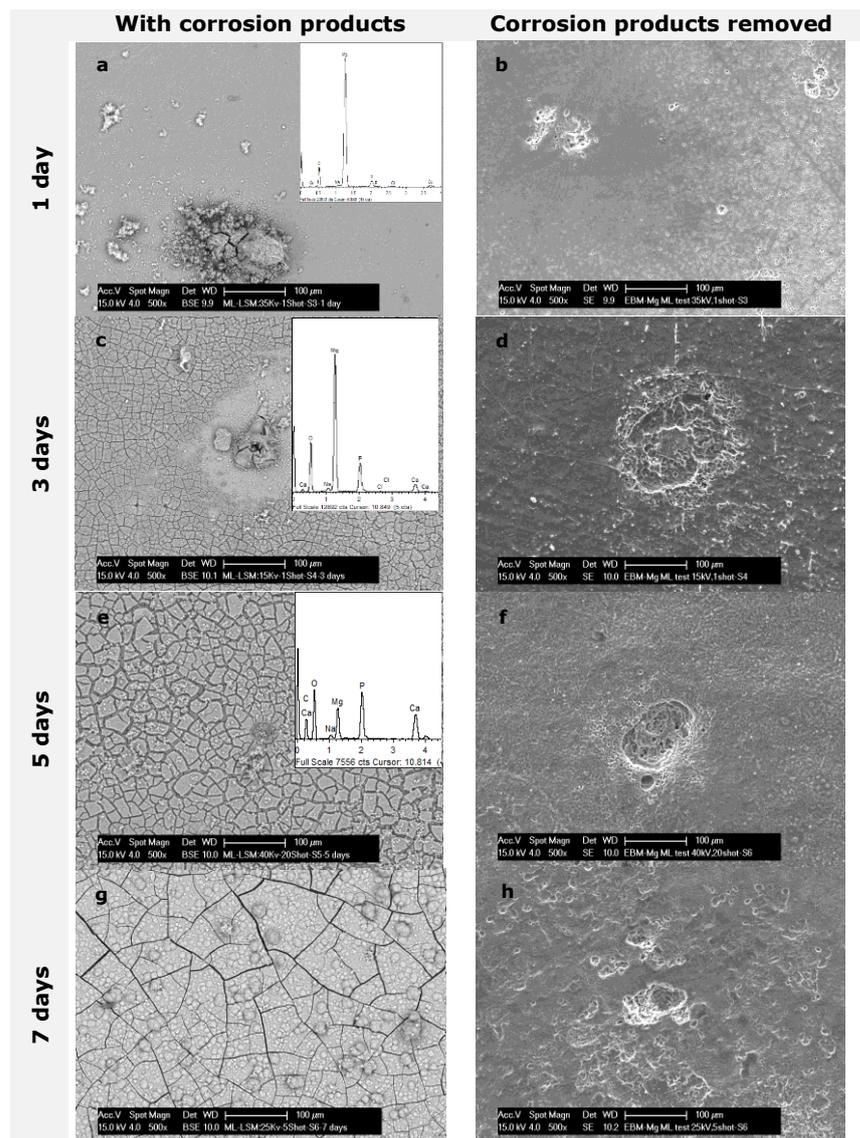
Figure 6-17 BSE and SE images of corroded LAEB-treated Mg surfaces, after immersion in PBS for 1,3,5 and 7 days

6.2.3 Discussion

Processed material by LAEB, subjected to bombardment by accelerated electron under applied cathode voltage, has been investigated. High velocity electrons impact the material surface, causing transfer of kinetic energy into thermal energy which then becomes distributed through the affected surface, leading to an increase in surface temperature for sufficient time to melt and alter the near surface microstructure upon rapid solidification.

In general, the necessary conditions to obtain a homogenous grain sized layer in LAEB processing is that the crystalline Mg surface must melt quickly, reaching temperatures not available in a conventional furnace, and then cool rapidly, to re-crystallise with a fine-scale grain structure [190].

In this study, the EB has an energy density of 2-14 J/cm^2 and the duration of each pulse in range of 2 μs [230], which is extremely short but sufficient to allow rapid melting and cooling of the material surface, with refinement of the structure, and improved surface topography and corrosion rate.

6.2.3.1 Surface morphology of LAEB processed Mg

Due to the short pulse duration of 2−3 μs [320], rapid cooling rate (dT/dt ~ 10^7-10^9 K/s) and high temperature gradients (∇T ~ 10^9 K/m) at the irradiated near surface [321], the Mg surface will melt, cool and solidify through rapid heat transfer into the bulk underneath. This rapid processing leads to melting, vaporisation, ablation, and re-solidification of the sample surface [322]. The temperature distribution under EB irradiation can be simulated by solving the heat conduction equation, with the interior heat source being the incident EB energy [198, 323, 324]. For example, Ye *et al.* [205] applied 1-D heat transfer equations to pure Mg and found that the Mg surface reached a plateau temperature of ~ 1350°C, which is significantly higher than the

boiling point of Mg ($1107°C$) [300]. As a consequence, evaporation can occur, as the heat of evaporation for Mg of 127.4 kJ/mol is relatively low.

The mechanism of surface modification under EB irradiation, shown schematically in Figure 6-18, can be summarised as follows: After metal sectioning and polishing, micro-protrusions are present on the surface along with contamination and spontaneous oxide layer MgO (Figure 6-18 (a)).

(a) As-polished surface

MgO
2-5 nm
0.5µm
Surface damage
Bulk Mg

Ra=0.13 µm
Mg
Contamination

(b) Low energy EB processed surface

Pits
Ra~ 0.1 µm
Melting layer
2-5 µm

(c) High energy EB processed surface

Crater   Cracks   MgO
Ra~0.3-0.5 µm   Ra~0.7
Recasting layer
< 5µm
Mg
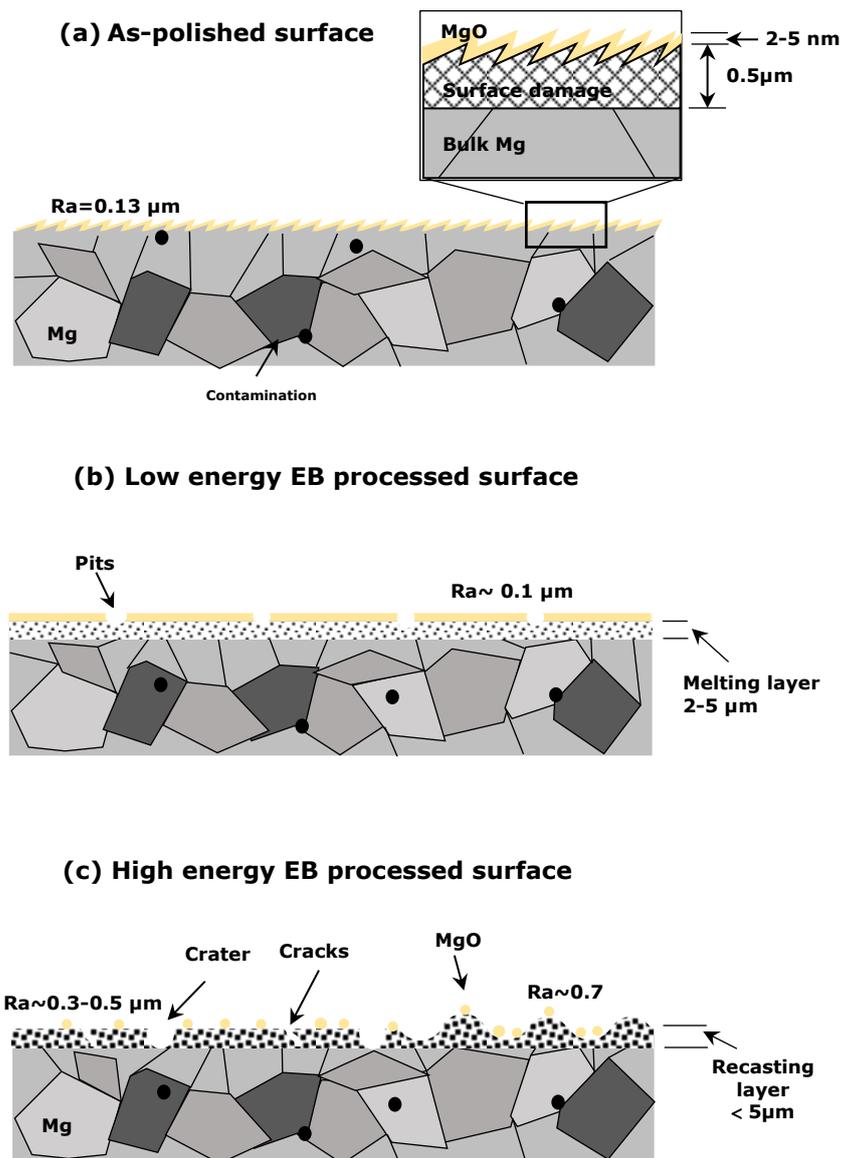
Figure 6-18 Schematic of LAEB modification of Mg surface: (a) as-polished Mg surface; (b) low energy EB processed Mg surface; (c) over processed - high energy EB processed Mg surface. Note in (c) the RHS represents the edge region while the LHS of the schematic represents the central region.

Under low energy EB irradiation (Figure 6-18 (b)), the metal melts rapidly and flows from micro-protrusions to hollows, leading to surface smoothening, whilst contamination diffuses into the bulk. During the early stages of EB treatment, *e.g.* 5 pulses at 15 kV (Figure 6-1(e)), the evidence indicates shallow melting and selective ablation, induced by EB irradiation, associated with micro non-uniformities of the original surface (polishing marks). Mg debris is not seen on the Mg surface even after treatment with 5 & 20 pulses at 15 kV, as illustrated by the SE images of Figure 6-1(f,h). The condensation of Mg vapour would not ordinarily be anticipated, given the working pressure in the vacuum chamber of 0.05 Pa. Under conditions of higher cathode voltage (25 kV) and increased number of pulses, the increased energy deposition leads to higher levels of evaporation and more intensive selective ablation. This results in more extensive melting of polishing marks (Figure 6-2(b,d)) and increased delineation of grain boundaries at the surface, (Figure 6-2(e). Further, shallow pits no deeper than the melting layer covered the surface due to local melting.

Roughness evolution is evidential of changes to the surface process conditions, from heating to melting (smoothening) and evaporation (Figure 6-18 (a,b). The roughness of mechanically polished Mg surfaces can either decrease or increase, depending on the process parameters applied. For the case of low energy density (15 kV; 1 - 5 shots) the surface roughness of the modified surfaces decreased from 0.13 μm to 0.1 μm (Figure 6-8), however this is within the error of measurement. The limitations of using a single Ra value to detail this subtle modification are clear. The SEM images in Figure 6-1 show a clear melt region but the average roughness remain similar. This melting and evaporation occurs just near surface, and more specifically at the peaks of polishing marks (Figure 6-1 (d,f)). The distribution

of heat into a rough surface becomes intensively located at the areas of micro-protrusions, leading to smoother, more planerised surfaces as can be seen in Figure 6-7 although not making significant difference to the Ra value. Improvements of surface roughness by LAEB processing has also been reported by Uno *et al.* [193], with application of up to 10.7 J/cm^2 to metal mould steel leading to highly finished surfaces (Ra $\sim$ 0.7 μm). A related study by Okada *et al.* [194] showed improvement in the surface roughness of Ti-alloy (Ti–6Al–4V) from 10 μm to 0.7 μm, when treated under conditions of 7.8 J/cm^2 by LAEB. Both these references are at the higher end of the range explored here.

Under excessive EB processing (Figure 6-18(c)) Mg evaporation becomes dominant, leading to a reduction in the melting layer. Due to the nature of Mg evaporation, a wavy topography may delineate the irradiated surface, in addition to the re-deposition of Mg particles. Indeed, an increase in cathode voltage (to 40 kV) leads to selective ablation (Figure 6-7) with more intensive dispersions of droplets at the periphery (Figure 6-4(d,f)). The ablation process acts to reduce the molten layer thickness, counter balancing the increased thickness of the molten layer after irradiation under an increased number of pulses [200]. Accordingly, increasing the cathode voltage and number of pulses has little effect on the resultant thickness of the recast layer (Figure 6-7). The evaporation and removal of molten material has been reported for AZ31-Mg alloy treated under repeated number of pulses (10 and 15 pulses) at 2.5 J/cm^2 by HCPEB [204].

Bright particles observed at the surface indicate some re-deposited of ablated Mg particles, localised around the centre of EB processed region, attributed to condensation after significant evaporation [200]. This phenomenon has been reported for surface modified pure Ti [325] and Al [326] under high-intensity pulsed ion beam (HIPIB) irradiation, with large numbers of Ti/Al-ablated

droplets being deposited on the processed surfaces. The ejection of material droplets by ablation only happens when the power density (P) reaches a threshold values (P_1) of 50 MW/cm^2 [325] [327] for these materials. Furthermore, the pressure in the chamber may increase due to an increase in evaporation with increasing number of pulses, and this is consistent with the SE images of Figure 6-3 (d,f).

Surfaces receiving high pulsed energy densities showed an increase in surface roughness, due to the severe evaporation (ablation) of the Mg. For example, the surfaces of Mg processed using conditions of 35 kV and 20 pulses exhibited many surface modulations, with striations and a dispersion of differently sized craters, causing a rise in surface roughness to reach Ra ~ 0.3 μm. One suggestion is that the differences in the thermal expansion coefficients between the molten surface and the relatively cold bulk underneath could promote the development of modulated surfaces [328]. The distribution of energy deposited onto an EB irradiated Mg surface is expected to be fairly uniform, with a beam diameter of 60 mm covering the area of two samples. This is commensurate with samples treated under low or moderate cathode voltage conditions showing similar surface roughness Ra values in the central area and at the sample edge. However, with increasing energy density, the Mg surface responds differently, with local energy deposition into the sample affected by surface features upon cool-down. The deposited energy is sufficient to melt and ablate the top layer of Mg, reducing polishing marks and exposing grain boundaries in the central area while wavelet features decorate the periphery (Figure 6-18 (c)). Indeed, Uno *et al* used LAEB to polish mould steel surfaces and reported the energy density at the centre of electron beam to have the highest value, becoming lower away from the centre at a distance of 20 mm [320]. Accordingly, the differences in Mg morphology under conditions of high energy density are attributed to

differences in localised heating and cooling rates of under the pulsed EB. The suggestion being that molten Mg has insufficient time to cool and evaporates in the central region, where it received the highest energy, while lower energy deposition at the edges provides for sufficient cooling time with the development of modulated surface features. Wave-like features have been associated with pure Mg [208] [329] and AZ31 surfaces [204] irradiated under high current pulsed electron beam (HCPEB) conditions.

In addition to ablation phenomena, surfaces processed under high EB energy conditions showed surface cracks, *e.g.* under high cathode voltage (40 kV) (Figure 6-4(f)). The rate of contraction of the molten layer upon rapid solidification will be higher than the relatively colder bulk material underneath . This results in tensile stress on the near surface layer, leading to cracking if the tensile stress exceeds the fracture strength of Mg. Further, the EB processed layer may enhance the formation of MgO, from reaction with residual oxygen in the low vacuum pressure EB chamber. If which case, then the brittle characteristic of this MgO layer, combined with differential thermal expansion, could act to enhance crack initiation and propagation.

Accordingly, it is recognised that LAEB treatment can induce a variety of changes in the near surface microstructure of Mg. XRD data (Figure 6-10) indicates a notable reduction in Mg peak intensity, attributable to a decrease in the crystalline state of Mg, with increasing number of pulses for fixed cathode voltage. Increasing the number of pulses also leads to an increase in thickness of the near surface modified layer, with re-crystallisation of the melted layer showing signs of preferred orientation, as for the case of surfaces modified at 15 kV (5-20 pulses) and 40 kV (Figure 6-10).

Mg peak broadening was noticeable in XRD (Figure 6-11(a,b)), particularly for the case of high power EB (high kV and 20 pulses). The broadening of the

diffraction lines generally indicate the development of a very fine grain structure, as a consequence of rapid-quenching [201]. Even though the application of Scherrer's equation (Table 6-2), indicated grain sizes > 100 nm, the measurement indicates tentatively a reduction in grain size of the recast layer, especially under low EB energy (Figure 6-12). In addition to grain refinement, it is recognised that the near surface layer cools rapidly at the end of an EB pulse, causing the development of residual tensile stress [199].

It has been established that EB treated surface in cross-section comprise three regions; a melted layer, a heat affected zone, and the matrix of the bulk material [196]. The modified layer increases in thickness with increase in energy density (cathode voltage and number of pulses), consistent with the temperature equations. As a result of the non-equilibrium thermal field in the material, the EB treated Mg surfaces experienced shock thermal stresses of several hundred MPa [197]. The shocks usually develop during the melting/eruption process, propagate along the beam direction and then decline when the eruption process finish. A temporal change in stress continues when the martial cools rapidly, until reaching equilibrium [189], cause deformation in the Mg in the form of planar defect formation and dislocations [197] [192]. Hence, the broadening of diffraction peaks may also be attributed the introduction of defects, such as dislocations and vacancies [195].

6.2.3.2 Crater formation and reaction products on Mg

In addition to the effects of ablation, surface roughness measurements were also influenced by the formation of craters / pits on the Mg surface, Figure 6-18 (b,c), caused by inhomogeneous localised melting and eruption of

the EB irradiated surfaces. LAEB processing under conditions of 25, 35 and 40 kV (Figure 6-2, Figure 6-3 and Figure 6-4, respectively) showed the formation of craters, occasionally decorated with spherical particles (Figure 6-4(c)). The LAEB process induced thermal effects leading to heating and melting of the near surface layer prior to rapid solidification [330]. The electron range (r), *i.e.* the maximum penetration depth of electrons into the material can be calculated using [330]:

$$r = 2.1 \times 10^{-5} \frac{U^2}{\rho} \qquad \text{Eq 6-1}$$

Where ρ is the material density ($\rho_{Mg} = 1.74 \times 10^{-3}$ kg/cm^3); and U is the acceleration voltage (kV). The calculated electron ranges for LAEB irradiated Mg, for 1 pulse, are listed in Table 6-4.

Table 6-4 Electron range (r) in LAEB irritated Mg

Acceleration voltage / kV	r / μm
15	2.72
25	7.54
35	14.8
40	19.3

The profile of energy deposition into Mg forms an approximate Gaussian distribution [205], with the maximum absorbed energy below the surface located at a distance ~ 1/3 of the electron penetration depth [205] [331]; the position of which depends on acceleration voltage and material density [201].

When the deposition energy is sufficient, it is anticipated that sublayer material will melt before the top surface. Further, an existing irregular microstructure might provide sites for impurities and hence low, localised melting temperatures [201]. With continued, excessive heating, these molten sites erupt and rupture the covering surface material, leading to surface craters of varied size, from nanometers to hundreds of micrometers, under conditions of repetitive melting and evaporation [330, 331] (Figure 6-2,

Figure 6-3 and Figure 6-4 (b,d,f). This is in agreement with the mechanism of crater formation proposed by Qin *et al.* [331], who suggested that an extreme change in material temperature resulted in a varied temperature gradient along the incident beam direction, while expansion was restricted in the vertical direction. With increasing temperature, the sublayer melts with the formation of small droplets, and these droplets expand to a degree such that the covering solid cannot resist the developing pressure leading to localised eruption at the material surface. Similar crater surface morphologies have been reported for many alloys subjected to EB irradiation. For example, Al and steel H13 by Qin *et al.* [330]; in 316L stainless steel by Qin *et al.* [332]; carbon steel T8, mould steel D2 and Mg-alloy AZ91HP by Hao *et al.* [201]; in NiTi-alloy by Zhang *et al.* [333], as well as in pure Mg and AZ31B by Ye *et al.* [205].

Increasing the number of shots led to a decrease in the number of craters, combined with an increase in their average size, as a result of repeated melting and evaporation events under the EB [328], as illustrated by the Mg surface processed with 20 pulses at 25 kV (Figure 6-2 (e,f)) and 5 pulses at 40 kV (Figure 6-4 (c)). However, surfaces treated by 20-50 pulses at 40 kV showed a noticeable reduction in the number of craters which adopted more blurred shapes. Material subjected to a very high energy density undergo deeper melting with the positon of the molten sublayer further away from the surface, making it more difficult to rupture the surface. Further, microstructural irregularities, which account for localised, elective eruption, tend to become more homogenous, through dissolution into the melt after multiple pulses, again reducing the tendency for crater formation.

Evidence for surface contamination providing sites for localised melting and enhanced crater formation is provide by the EDS elemental map of Figure 6-6 for the case of a crater formed after treatment by 5 pulses at 40 kV, which

revealed a surface composition containing Ca and C, attributed to polishing debris from the diamond disc used during surface preparation.

Significant changes in surface morphology was also associated with the presence of small droplets showing bright contrast; with EDS analysis (Figure 6-5(b)), indicating high oxygen levels suggesting MgO formation. After crater eruption Mg droplets ejected from the surface may react with the atmosphere, become negatively charged using the electron beam, and return to the surface electrostatically [205].

6.2.3.3   Corrosion behaviour of LAEB irradiated Mg surfaces

Potentiodynamic corrosion test can be a useful test for the very early stage of response of EB Mg-modified surface to the ions in PBS. The evolution of the OCP with time provided evidence for stabilisation of the passivation layer on the Mg surface, during the initial stage of immersion in the test solution. Even though OCP for low energy EB processed surface showed variation in level of passivation, from Figure 6-13 (a), the high energy EB processed surfaces showed significantly higher potential, *i.e.* OCP and nobler E_{corr}, than the starting potential of the as-prepared Mg surface, consistent with the rapid formation of passivation layer. This indicated that the passivation layer did not break or dissolve during this stage of immersion in PBS, providing longer protection for LAEB treated surfaces compared to as-prepared surfaces. Hence, the recast molten layer may have a more homogenous polycrystalline nature, acting to enhance the formation of a more stable passivation layer [334]. Improvements of passivation behaviour due to the presence of a recast molten layer was reported also by Zhang *et al.* [335] who treated coarse grained NiTi-alloy with HCPEB irradiation and recorded increased noble potential of the surface when immersed in simulated body fluid. Okada *et al.*

[194] reported a decrease in the OCP and current density of Ti–6Al–4V irradiated by LAEB, under anodic polarization current curves using 1M HCl solution, with the improvement in corrosion resistance attributed to the amorphous structure of the re-solidified surface layer.

An increase of oxygen content of the Mg surfaces processed under high EB treatment may contribute to the initial improvement in Mg onset of corrosion. In this work, surfaces treated by at 40 kV (1 pulse) showed MgO at the surface (Figure 6-5), acting as a protective layer and enhance the formation of $Mg(OH)_2$ when the sample was immersed in PBS. A similar improvement of Mg corrosion resistance due to MgO formation under EB treatment was reported by Gao *et al.* [197] for AZ91HP-Mg alloy HCPEB processed with beam energy density of 3 J/cm^2 and 10 pulses, under 5% NaCl immersion testing. The existence of an MgO layer on the recast layer was cited as having a positive effect on the onset of corrosion of the EB irradiated surface [192].

Enchantment of the passivation behaviour of LAEB processed Mg is shown by the polarisation curve of Figure 6-13(b), which can reflect the quality of recasting layer of earlier corrosion. Mg processed at 25 kV under 1 pulse, for example, has a break-down potential E_b being more noble than that of the untreated surface, giving longer passivation before breakdown at -1377 mV. This acted to decrease the corrosion rate to 0.08 mm/year (Table 6-3) with the $Mg(OH)_2$ passivation layer (Figure 6-15 (a)) protecting more continuously the Mg surface for longer times. Oscillations in the corrosion current density, between passive and active regions before the breakdown potential, may be attributed to a competition between passivation layer formation and dissolution.

Mg surfaces receiving the highest energy deposition, under conditions of 40 kV (20 and 50 pulses) showed a straightforward increase in current density

i_{corr} with increasing potential, with a sharp rise in anodic current i_a just above the E_{corr} being indicative of pitting corrosion, hence, the pitting potential E_p was trapped with the E_{corr} [336]. The OCP and E_{corr} for these processed surfaces (Table 6-3) reached their noblest values with a breakdown potential of -1600 mV. But, under these processing conditions, it is considered that the passivation layer is largely ineffective, with ease of breaking leading to fast dissolution of Mg ions into the PBS.

The response of EB modified surface to the ions in PBS for longer time can be extracted from immersion test data, conducted for different times. The corrosion mechanism of EB modified surface under immersion tests is schematically illustrated in Figure 6-19(a-c).

In general, the corrosion behaviour of LAEB irradiated Mg was mediated by the dissolution of Mg ions into PBS and donation of electrons. Then, water decomposes by electron capture leading to formation of hydroxide ions and hydrogen evolution. Presence of Mg^{2+} and OH^- ions in solution results in formation of $Mg(OH)_2$ layer. The reaction of Cl^- ions with $Mg(OH)_2$ leads to the formation of dissolved $MgCl_2$. The Mg ions react with phosphate ions (PO_4) in PBS and results in formation of phosphate components such as amorphous hydroxyapatite (Ca-P), crystalline $Mg_2(PO_4)OH$ and $Na_4Mg(PO_4)_2$.

Corrosion behaviour of low energy LAEB-irradiated Mg surface under immersion testing for short time (Figure 6-19 (a)) showed that the surface exhibited a lower corrosion rate after one-day immersion in PBS compared to the as-prepared Mg (Figure 6-16), again consistent with the mechanism proposed that LAEB treatment acts to enhance the formation of a continuous, more stable, homogenous passivation layer [208].
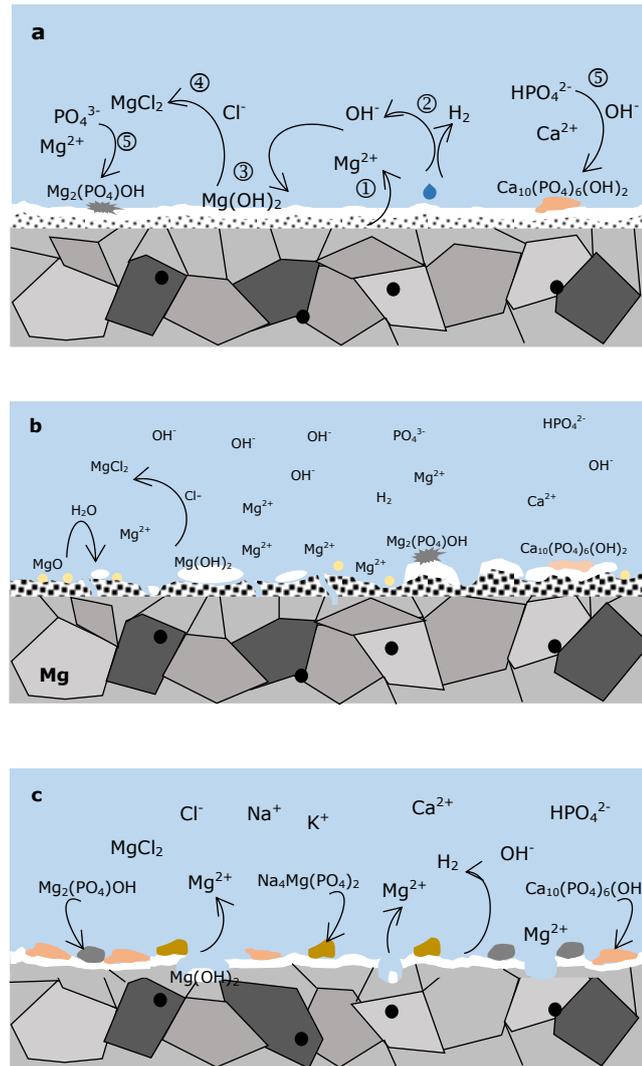
Figure 6-19 Schematic illustration of corrosion mechanism of EB- Mg modified surface: (a) Low energy EB processed surface at initial stage of corrosion; (b) high energy EB processed surface at initial stage of corrosion; (c) corrosion of Mg after dissolution of modified layer

However, higher energy EB processed Mg surfaces corroded faster during one-day immersion (Figure 6-19 (b)). These surfaces showed a mixture of topographies, ranging from smooth in the middle to wavy feature on the sides, which may act to reduce the continuity of the passivation layer. Further, the presence of differently sized craters and cracks on the EB processed Mg surfaces may also affect corrosion performance. The craters and cracks will provide sites for localised pitting corrosion (Figure 6-17),

allowing the electrolyte to penetrate through recasting layer and reach the Mg bulk beneath, leading to enhanced local dissolution, instead of more uniform corrosion characteristic for pure Mg. Additionally, under high energy EB, the modified region becomes deeper, however, structure defects may also increase which degrade the surface quality [197]. These weak points, associated with vacancies, dislocations or inclusions in the Mg provide sites of discontinuity for localised dissolution of the underlying Mg, leading to the formation of pits (Figure 6-17 (b,d,f,h)).

The corrosion rate calculated from immersion testing may be used to determine approximately the penetration depth of the corroded surface as a function of processing conditions (Table 6-5).

Table 6-5 Penetration depth of corrosion in comparison with the remaining recast layer after ablation

Sample ID	Penetration depth (μm)				Recast layer / μm
	1 day	3 days	5 days	7 days	
Mg	18.1	14.7	17.7	32.8	**-**
EB15-1	3.3	16.4	15.1	15.0	**2.9**
EB15-5	2.6	3.1	18.0	31.1	**3.5**
EB15-20	7.9	16.9	8.6	13.5	**3.8**
EB25-1	1.7	4.4	9.8	39.6	**2.0**
EB25-5	9.7	23.1	17.5	17.4	**3.9**
EB25-20	3.4	19.1	20.5	32.0	**-**
EB35-1	9.0	17.2	28.0	33.6	**2.6**
EB35-5	15.8	12.7	20.8	35.4	**3.8**
EB35-20	12.9	18.1	22.8	16.4	**4.6**
EB40-1	9.5	16.6	22.6	36.5	**-**
EB40-5	8.9	13.4	16.5	23.7	**1.9**
EB40-20	9.0	35.8	19.8	27.6	**1.6**
EB40-50	18.8	20.6	53.8	89.4	**2.6**

This revealed that, in general, the molten layer completely dissolved after approximately one-day immersion, with the exception of surfaces irradiated at 15 kV (5 pulses), and at 25 kV (1 pulse) which showed the lowest corrosion rate and protected the Mg immersion in PBS. Hence, even though EB treatments induced many competing effects on the Mg, it is evident that

certain processing conditions (*e.g.* cathode voltage 25 kV / 1 pulse) can act to lower the initial Mg surface corrosion rate which is consistent in both potentiodynamic and immersion tests.

After long immersion times of 3-7 days (Figure 6-19(c)), the recast layer already dissolved and the corrosion rate returned to its original value, *i.e.* upon dissolution of the coarse grained Mg bulk underneath the LAEB processed layer.

Hence, LAEB microstructure refinement, induced by melting and rapid solidification, leads to various corrosion behaviours depending on the amount of energy into the surface. For the case of surfaces able to develop a passivation layer, *i.e.* under conditions of low energy EB, the tendency to form an amorphous surface or a refined, fine-grained polycrystalline surface with a high density of grain boundaries could act to accelerate the formation of a more continuous $Mg(OH)_2$ passivation layer, acting to improve the initial corrosion resistance. However, surfaces processed under conditions of higher EB energy tend to show a more unstable passivation layer, leading to fast Mg dissolution and more rapid corrosion. Hence, balancing the surface homogenisation, for both topography and microstructure, becomes the main consideration for controlling corrosion performance.

6.2.3.4   Recommendations for process control

LAEB irradiation of pure Mg was performed in order to explore the EB interaction with Mg and identify conditions which might lead to an improvement in corrosion resistance. The Mg surfaces experienced rapid melting, evaporation and re-solidification under EB treatment. Shallow melting and slight ablation along with improve surface roughness was observed on Mg surfaces modified by low energy EB. Severe ablation, craters

formation and crack initiation along with deposition of ablated MgO particles occurred for conditions of over-processing.

According to corrosion test results, the surface processed under low energy EB exhibited better corrosion performance than over-processed surfaces, being attributed to the enhanced passivation behaviour of the modified layer. Hence, it is recommended that Mg surfaces should be processed under lower energy EB irradiation, 15 kV for example, with long processing times, more than 20 shots, in order to gain improved corrosion resistance of Mg. These conditions can also enhance the formation of a deeper melting layer with refined polycrystalline grain structure, and enough thickness to resist corrosion for longer times in test solution.

6.2.4 Summary

The effects of LAEB surface treatment on the surface topography and corrosion performance of Mg have been investigated as a function of cathode voltage and the number of pulses. The starting material showed micro-protrusions due to mechanical polishing process.

Under low energy EB irradiation, the Mg surfaces experienced rapid melting causing flow of metal from micro-protrusions to hollows leading to surface smoothening. With increase the EB energy, the Mg surfaces observed selective ablation, with increase the delineation of grain boundaries on the surface, in addition to shallow pits which acted to increase the surface roughness.

Under high energy EB irradiation, the Mg surfaces showed severe ablation, cracks, wavy topography and re-deposition of MgO particles delineating the periphery of the irradiated surfaces, in addition to different sized craters as

big as hundreds of micrometers, all of which account for an increase in surface roughness.

The EB modified Mg near surface developed a refined microstructure with a recast layer thickness of ~ 2-5 µm.

The corrosion performance of EB irradiated surfaces initially improved in terms of increase the onset of corrosion under potentiondynamic test, which may be attributed to the rapid formation of the passivation layer. Low energy EB processed surfaces showed corrosion rates slightly lower or within the range of the as-prepared surface. The long corrosion performance under immersion tests indicates a similar trend of improved corrosion resistance for the first day of immersion in PBS and then increased corrosion, to within the original values, due to the complete dissolution of the melted layer after 7 days. Over processed surfaces experienced high corrosion rates, in both potentiodynamic and immersion testing, which may due to inclusions, craters, cracks, *etc* on the modified surface, accounting for the formation of a discontinuous passivation layer, and hence rapid dissolution.

6.3 Laser surface melting of Mg

Laser surface melting (LSM) followed by rapid solidification may be used also to refine the near surface grain structure of Mg. This section presents an investigation of Mg-surface morphologies processed by YLR-2000SM ytterbium fibre LSM, as a function of the operating parameters of laser power, spot size and scan speed, with a view to inducing microstructural changes to improve corrosion performance. High purity Mg samples were polished to a final finish using 1 μm diamond paste. In order to refine the near-surface grain structure, Mg samples were subjected to overlapping, multi-tracks of laser melting in continuous wave mode, under an Ar atmosphere. The microstructural alterations of the LSM processed surfaces, compared to as-prepared Mg samples, were appraised using the combined techniques of SEM/EDS, 3D photo-mapping and XRD. The corrosion behaviours of the samples were studied using potentiodynamic polarization and immersion corrosion testing. A summary of the sample sets investigated, their LSM processing conditions and corresponding corrosion rates extracted from potentiodynamic and immersion tests is presented in Table 6-6.

Table 6-6 Summary of the LSM Mg sample sets investigated and their coding.

Sample	Scan speed / mm/min	Power / W	Spot size / mm	Corrosion Rate mm/year				
				Potentiodynamic	Immersion test			
				3 hr	1day	3 days	5 days	7 days
Mg	-	-	-	0.12 ± 0.01	6.46±0.1	1.56±0.1	1.29±0.1	1.69±0.1
L3-375	3600	375	2	0.69 ± 0.08	4.17±0.4	1.92±0.4	1.58±0.4	1.29±0.4
L3-450		450		0.43 ± 0.08	6.31±0.4	2.12±0.4	1.67±0.4	1.30±0.4
L3-525		525		0.12 ± 0.08	6.22±0.4	3.26±0.4	1.21±0.4	1.18±0.4
L3-600		600		0.45 ± 0.08	5.17±0.4	2.55±0.4	2.12±0.4	1.70±0.4
L4-375	4500	375	2	0.04 ± 0.02	3.87±0.6	1.44±0.6	1.36±0.6	1.48±0.6
L4-450		450		0.08 ± 0.02	3.84±0.1	2.69±0.1	1.69±0.1	1.37±0.1
L4-525		525		0.08 ± 0.02	3.15±0.5	1.34±0.5	2.19±0.5	1.88±0.5
L4-600		600		0.06 ± 0.02	5.70±0.1	2.34±0.1	1.88±0.1	1.36±0.1
L5-375	5400	375	2	0.18 ± 0.01	4.48±0.1	2.40±0.1	0.72±0.1	0.85±0.1
L5-450		450		0.15 ± 0.01	3.21±0.1	2.65±0.1	1.43±0.1	1.04±0.1
L5-525		525		0.14 ± 0.01	3.99±0.1	1.23±0.1	2.10±0.1	1.22±0.1
L5-600		600		0.14 ± 0.01	6.17±0.1	1.85±0.1	1.18±0.1	1.31±0.1
L5*-375	5400	375	3	0.07 ± 0.01	3.23±0.4	2.42±0.4	1.93±0.4	2.11±0.4
L5*-450		450		0.12 ± 0.01	1.62±0.1	0.96±0.1	0.94±0.1	1.90±0.1
L5*-525		525		0.05 ± 0.01	5.00±0.3	2.27±0.3	2.30±0.3	2.91±0.3
L5*-600		600		0.06 ± 0.03	7.11±0.7	3.65±0.7	2.62±0.7	2.60±0.7
L6-1500	6300	1500	3	0.86 ± 0.03	14.00±0.7	3.16±0.7	1.95±0.7	2.20±0.7

6.3.1 Characterisation of LSM processed Mg-surfaces

6.3.1.1 OM and SEM/EDS of LSM modified Mg-surfaces

Figure 6-20 presents optical microscope (OM) images of the Mg samples following laser irradiation (spot size 2 mm) as a function of scan speed (3600, 4500 and 5400 mm/minute) and laser power (375, 450, 525 and 600 W). The Mg surface was found to be highly influenced by laser power, for a given scan speed and spot size. By increasing the laser power from 375 to 600 W, the line profile (presumed to be Gaussian) of the laser beam tracks became wider, providing for more uniform coverage, as indicated by the narrowed overlapping regions (Figure 6-20, vertical bands). There was no significant change in the Mg surface appearance after 450 W laser irradiation, although more grain boundaries appeared (Figure 6-20, arrowed).

Increasing the power to 525 and 600 W for a given scanning speed led to more obvious morphology refinement, with surface modification occurring more strongly at the centre of each beam track [218].
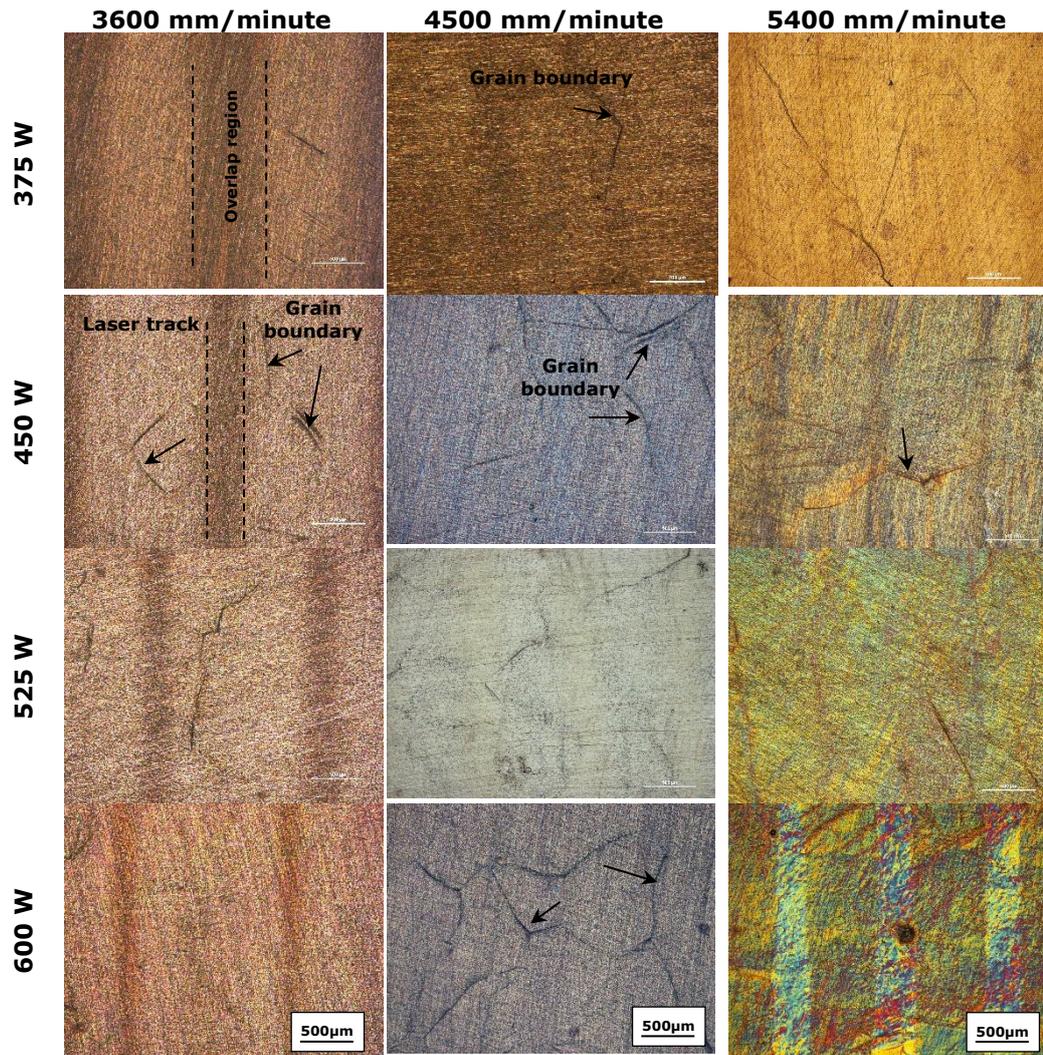
Figure 6-20 OM images of Mg surfaces following LSM modification.

Figure 6-21 presents SE images of LSM processed Mg surfaces, at scan speeds of 3600, 4500 and 5400 mm/minute; spot size of 2 mm; and laser powers of 375, 450, 525 and 600 W, respectively. Surfaces processed at 375 W laser power showed residual grooves of damage from the starting surface, polished using 1 µm diamond paste. Inducing a certain level of surface damage was found beneficial, to reduce the reflection of laser beam on the Mg surface during the initial stages of processing. For laser power processing conditions of 525 - 600 W, the SE images indicated a refinement of surface morphology, centred along the laser beam track, with the perception of ≤ 35 µm sized grains (Figure 6-21, arrowed), being much smaller in size compared to the as-polished Mg surfaces. The presence of remnant deep polishing

227

marks after laser treatment (Figure 6-21, arrowed) indicates shallow melting, generally of the near Mg surface. Some areas of the 600 W processed samples showed long cracks (not shown here). It was found that crack density at the surface initiated and increased with increasing processing power, being attributable to higher input energy and high thermal stress, leading to cracking along grain boundaries.
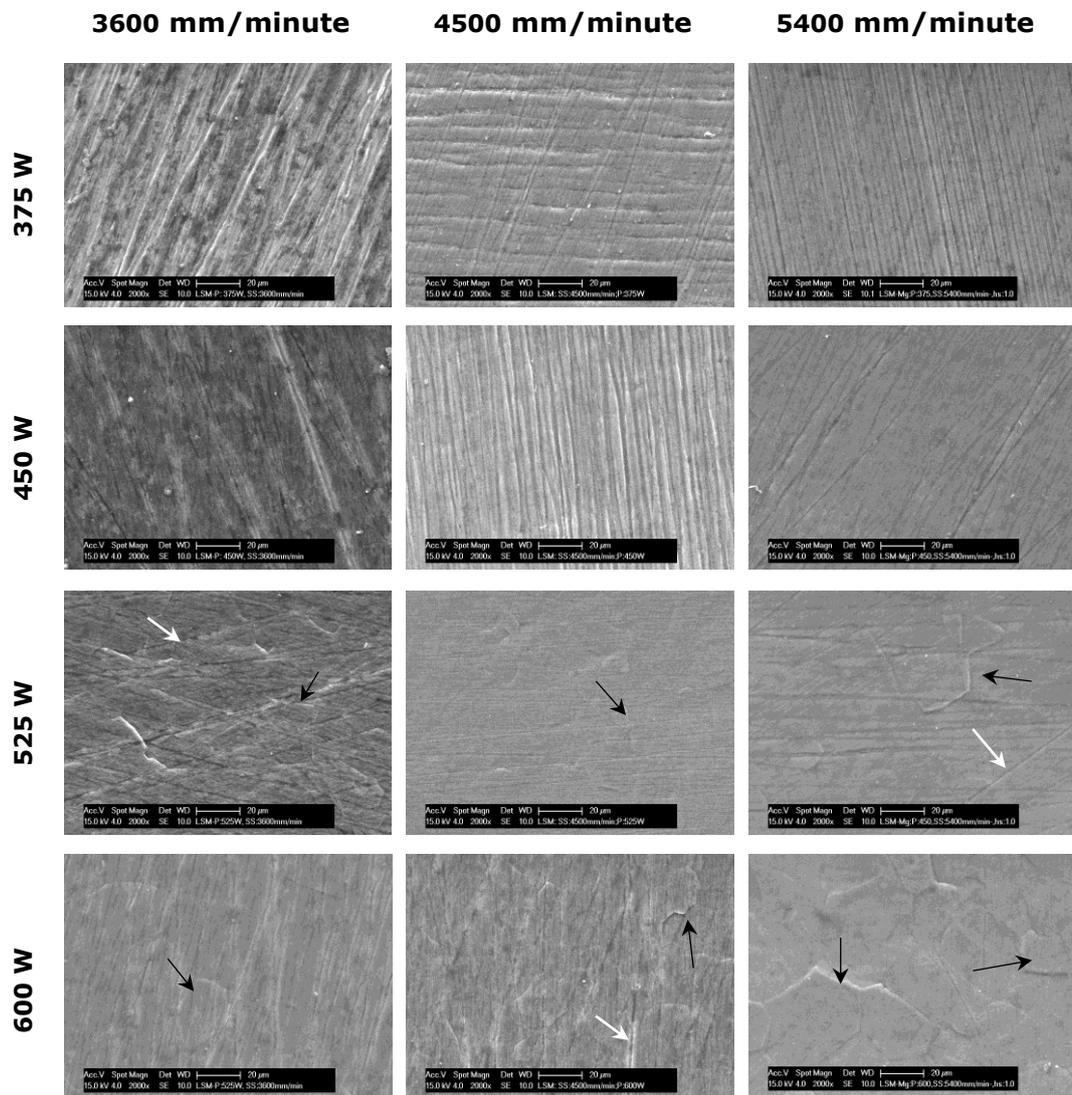
Figure 6-21 SE images of Mg surfaces following LSM surface processing. The black arrowed areas indicate a refinement of surface morphology with the perception of small sized grains. The white arrows indicate presence of remnant deep polishing marks

By increasing the laser spot size to 3 mm, Figure 6-22, it was found that the laser beam track pattern disappeared, indicative of much more uniform surface processing. However, remnant surface mechanical damage from polishing remained, even after raising the laser power to 600 W (Figure 6-22).
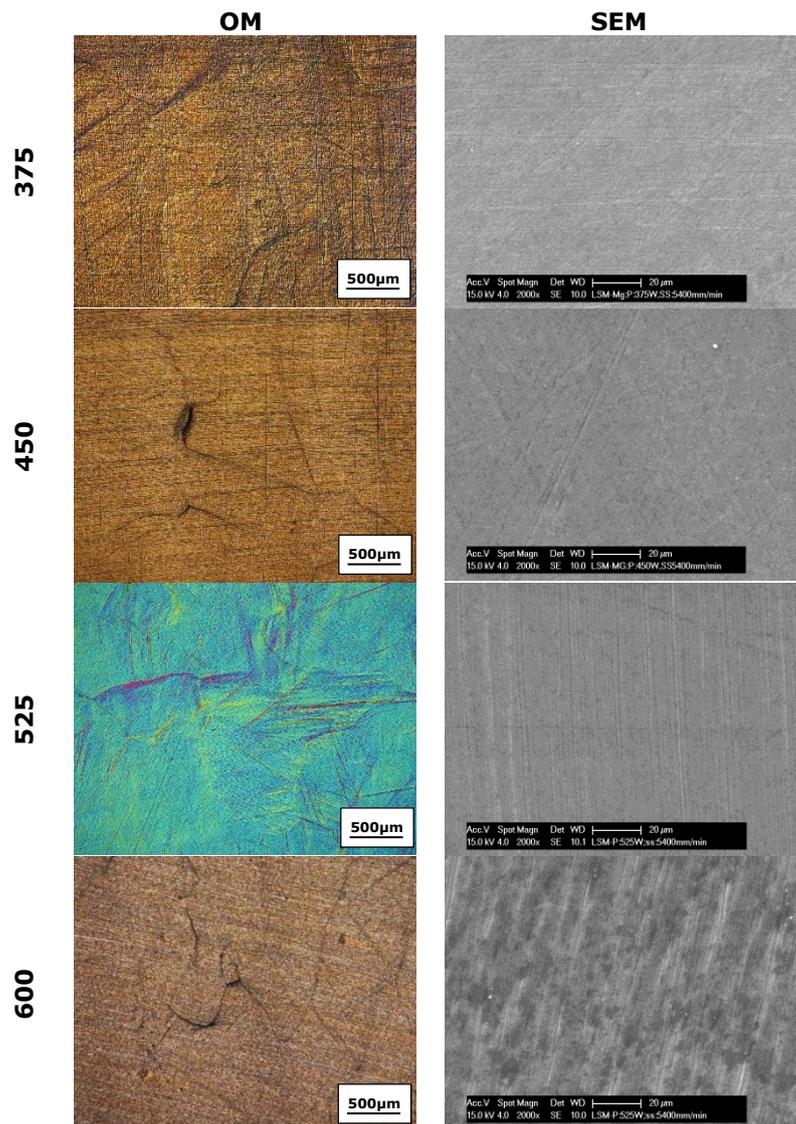
Figure 6-22 OM and SE images of Mg surfaces LSM processed at 5400 mm/minute with a laser spot size of 3 mm.

Figure 6-23 (a,b) shows the Mg surface morphology following LSM processing at a scanning speed of 6300 mm/minute with a laser power of 1500 W and 3

mm spot size. In this case, a conventional laser melting ripple pattern formed, combined with surface craters (Figure 6-23(a), arrowed). In addition, SE imaging indicated that the modified surface underwent a process of evaporation and condensation, leaving Mg particles deposited on the surfaces. Long cracks were also observed, indicative of high thermal stresses during solidification.

Figure 6-23(c,d) illustrates the LSM Mg processed surface, in cross-sectional geometry, for a scan speed of 6300 mm/minute with a laser power of 1500 W. In this case, the laser melted trucks overlapped indicating that the melt pool had a maximum depth of ~ 300 μm, and the track width of 1500μm. At high magnification, the SE image of Figure 6-23(d) revealed that the overlapping melt pool regions had recast to form a cellular microstructure with voids along the HAZ boundaries.
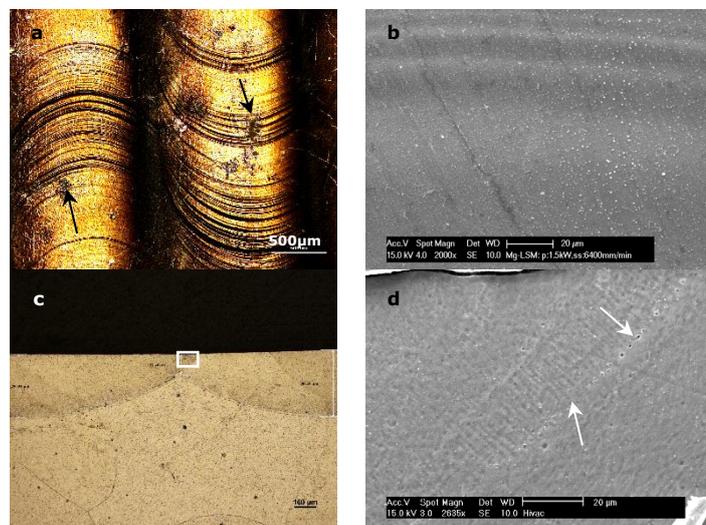
Figure 6-23 OM and SE images of Mg surfaces LSM processed at 1500 W, 6300 mm/minute with a laser spot size of 3 mm: (a) overlapped laser track width; in plan view (b) SE of Mg particles and cracks on laser tracks; in plan view (c) OM image showing cross section of tracks depth; and (d) SE inset of cross-section of ovelapped region.

In the present work, it was found that all the LSM processed specimens exhibited minor concave curvature of the surface, attributable to the

development of tensile stresses caused by volume contraction upon melt layer solidification.

6.3.1.2 Roughness (Ra) of as-prepared and LSM processed Mg surfaces

Surface roughness data for the LSM processed Mg samples, acquired using white light-3D photomapping are presented in Figure 6-24. Overall, the laser melted surfaces showed improved Ra values, in terms of reduction, compared to the original, as-prepared surfaces (Ra ~ 0.27 μm). Shallow melting, under 5400 mm/minute processing conditions such as 375 W, reduced Ra value by up to ~ 30% (Ra ~ 0.17 μm for the case of the L5-375 sample). The input energy in this case was sufficient to melt the surface, whilst recasting left a few surface defects, *i.e.* craters and cracks. For other combinations of power and scan speed, the trends are mixed. This indicates a careful balance is needed between laser power and scan speed to reduce the roughness of the recast layer, whilst increasing levels of input energy are associated with an increase in surface roughness. For example, the sample processed at 1500 W and 6300 mm/minute showed the highest Ra value of ~ 0.51 μm.
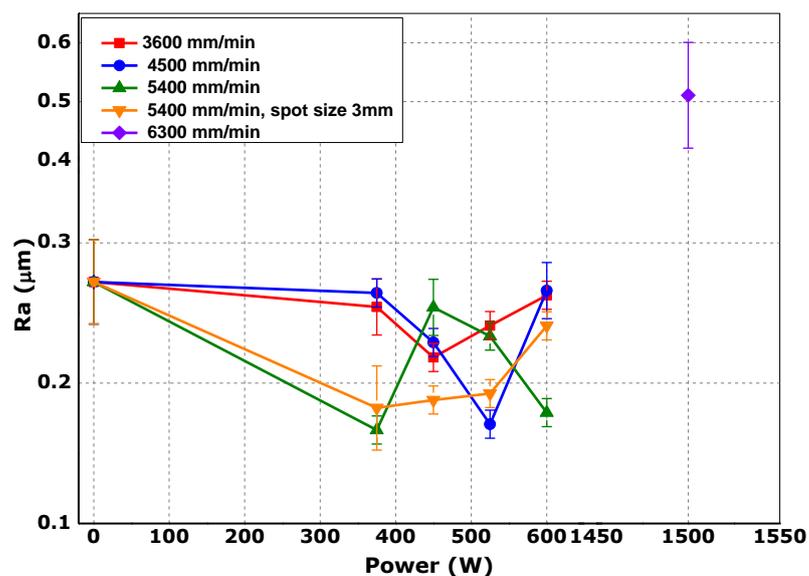
Figure 6-24 Mg surface roughness (Ra) as a function of laser power and scan speed.

6.3.1.3 XRD investigations of LSM processed Mg surfaces

Figure 6-25 presents XRD diffraction patterns and grain size data for as-prepared and LSM modified Mg surfaces, as a function of laser power, at an example scan speed of 3600 mm/minute. All patterns were typical of polycrystalline, pure Mg single crystal for all the LSM modified surfaces (Figure 6-25(a)). Grain sizes were estimated using the Scherrer equation using $10\bar{1}0$, 0002 and $10\bar{1}1$ diffraction peaks, all of which returned values > 100 nm and hence this data set again is beyond the general applicability of the Scherrer approach, however a few tentative trends might be implicated. The intensity of the Mg 0002 diffraction peak for the LSM processed surfaces increased significantly, compared to the as-polished surface, suggesting a certain amount of preferred orientation as a result of recasting. The grain sizes values (Figure 6-25(b-d)) (Table 6-7) for Mg $10\bar{1}0$, 0002 and $10\bar{1}1$ diffraction peaks were variable but generally decreased of $10\bar{1}0$ was more apparent for conditions of low input energy, whilst grain size values for 0002 and $10\bar{1}1$ increased generally with increasing laser power for all scan speeds. The data is tentatively interpreted to indicate changes in grain shape during recasting, in line with the suggestion of the development of some preferred orientation. However, it is noted that the penetration depth of the X-rays was likely to be higher than the LSM modified layer thickness of 100 μm, so the XRD data would retain a component of information from the Mg grains in the bulk. Hence, the Scherrer equation has limited applicability in this case for the appraisal of grain size within the near surface modified layer. The grain size measured from OM and SE images for surface that exhibited grain refinement on the centre of the laser track is presented in Table 6-7, for comparison.
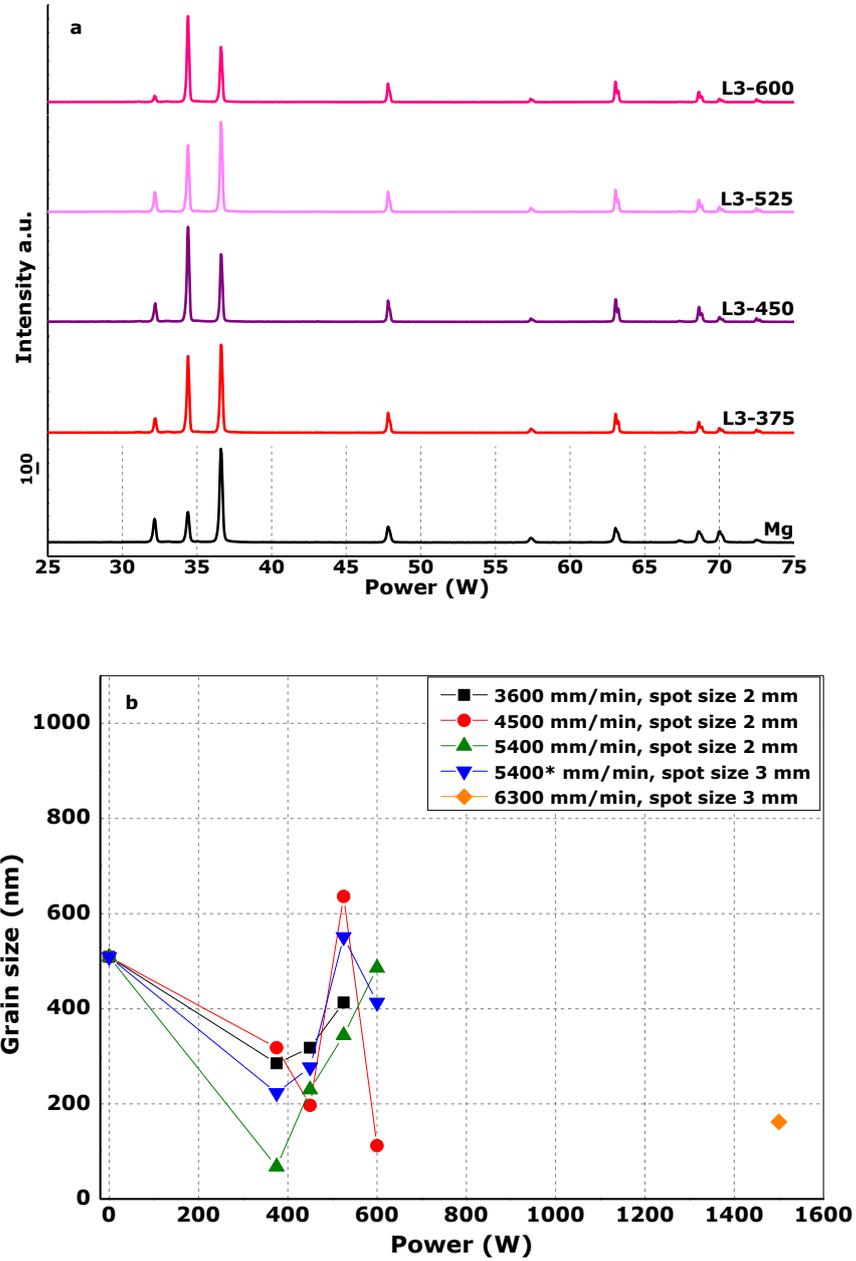
Figure 6-25 (a) XRD patterns of as-prepared and LSM processed Mg surfaces, as a function of laser power (at 3600 mm/minute scan speed); and grain size values from: (b) $10\bar{1}0$, (c) 0002 and (d) $10\bar{1}1$ diffraction peaks.
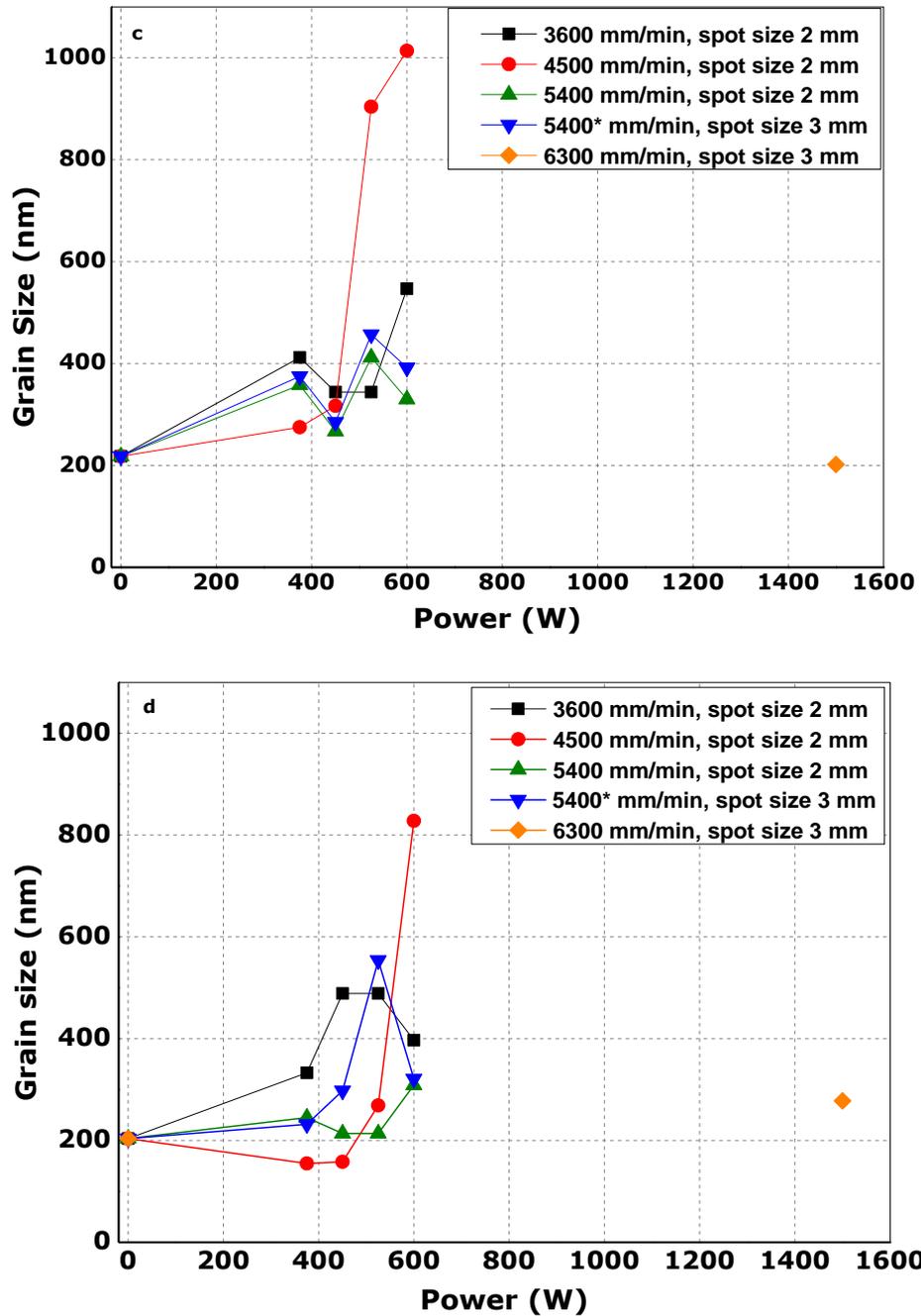
Figure 6-25 continued... Grain size values from: (c) 0002 and (d) $10\bar{1}1$ diffraction peaks.

Table 6-7 Average grain size of LSM-Mg recast surface, it is noted that this is not the best way to measure modified layer large grain sizes, as all values returned are above the applicability of the Scherrer equation.

Sample ID	$10\bar{1}0$	0002	$10\bar{1}1$	Average grain size	
				Scherrer /nm	OM-SEM / µm
Mg	509	218	204	310±81	~821
L3-375	285	412	333	343±30	-
L3-450	318	344	489	384±44	-
L3-525	413	344	489	415±34	~17
L3-600	-	547	397	472±53	~25
L4-375	318	275	155	249±40	-
L4-450	197	317	158	224±39	-
L4-525	636	904	269	603±150	~12
L4-600	112	1014	828	651±224	~20
L5-375	68	358	245	224±69	-
L5-450	230	267	214	237±13	-
L5-525	344	412	214	323±47	~20
L5-600	486	330	309	375±46	~43
L5*-375	223	375	232	277±40	-
L5*-450	277	285	298	286±5	-
L5*-525	551	457	554	521±26	-
L5*-600	413	392	321	375±23	-
L6-1500	162	202	278	214±28	-

6.3.2 Corrosion performance of LSM processed Mg surfaces

6.3.2.1 Potentiodynamic polarization tests

The corrosion performance of LSM processed Mg surfaces was examined by potentiodynamic polarization testing, conducted in PBS at 37°C. Figure 6-26 (a-e) presents OCP and potentiodynamic polarization test data for as-prepared and LSM treated Mg surfaces, as a function of laser power and scan speed. A summary of the main parameters extracted from these data sets is presented in Table 6-8. In general, the LSM modified surfaces showed nobler onset of corrosion, becoming stable after ~ 40 minutes of processing, with the sample treated at 375 W and 4500 mm/minute showing most resistance, at -1595 mV.

The polarization curves for the laser melted surfaces, compared to the as-polished surfaces, revealed similar behaviours, in terms of anodic and cathodic regions, during corrosion testing (Figure 6-26(b-e)). The polished Mg surface showed an anodic dissolution of 0.12 ± 0.01 mm/year and a corrosion potential E_{corr} of -1756 mV. For the case of the LSM modified surfaces, two samples can be arranged with similar E_{corr} as follows: L6-1500 (-1573 mV) and L4-375 (-1570 mV). Yet the same samples had an increase in corrosion current density, returning highest and lowest i_{corr} values of 0.037 and 0.0019 mA/cm^2, respectively.

Figure 6-27 presents corrosion rate data for the as-prepared and LSM processed Mg surfaces as a function of scan speed for various laser powers. Overall, samples modified under scan-speed conditions of 4500 mm/minute (spot size 2 mm) and 5400 mm/minute (spot size of 3 mm), corresponding to the most uniform processing conditions, showed the highest corrosion resistance significantly lower than the as-polished surface. Application of a low laser beam power of 375 W produced a LSM modified surface with a corrosion rate of 0.04 mm/year at 4500 mm/minute, significantly lower than the as-polished surface (0.12 mm/year). Interestingly, increasing the spot size to 3 mm returned a lower corrosion rate of 0.05 mm/year for the higher energy processing conditions associated with 525 W laser power and a scan speed of 5400 mm/minute. The LSM processed surfaces treated with highest input energies corroded faster than the as-polished Mg, with the L6-1500 sample showing the highest corrosion rate of 0.86 mm/year, although it is noted that this corrosion value improved to 0.21 mm/year after polishing the surface to remove Mg oxidation. It is noted that Mg has a linear thermal expansion coefficient of 25.9×10^{-6} mm/mm°C in the temperature range 20-100°C, hence thermal stresses at high power and low scan speed are expected to be higher than at low power and high scan speed, explaining the

tendency for small crack formations on re-casting, following high energy input, which would act to accelerate the corrosion rate of the modified surfaces.
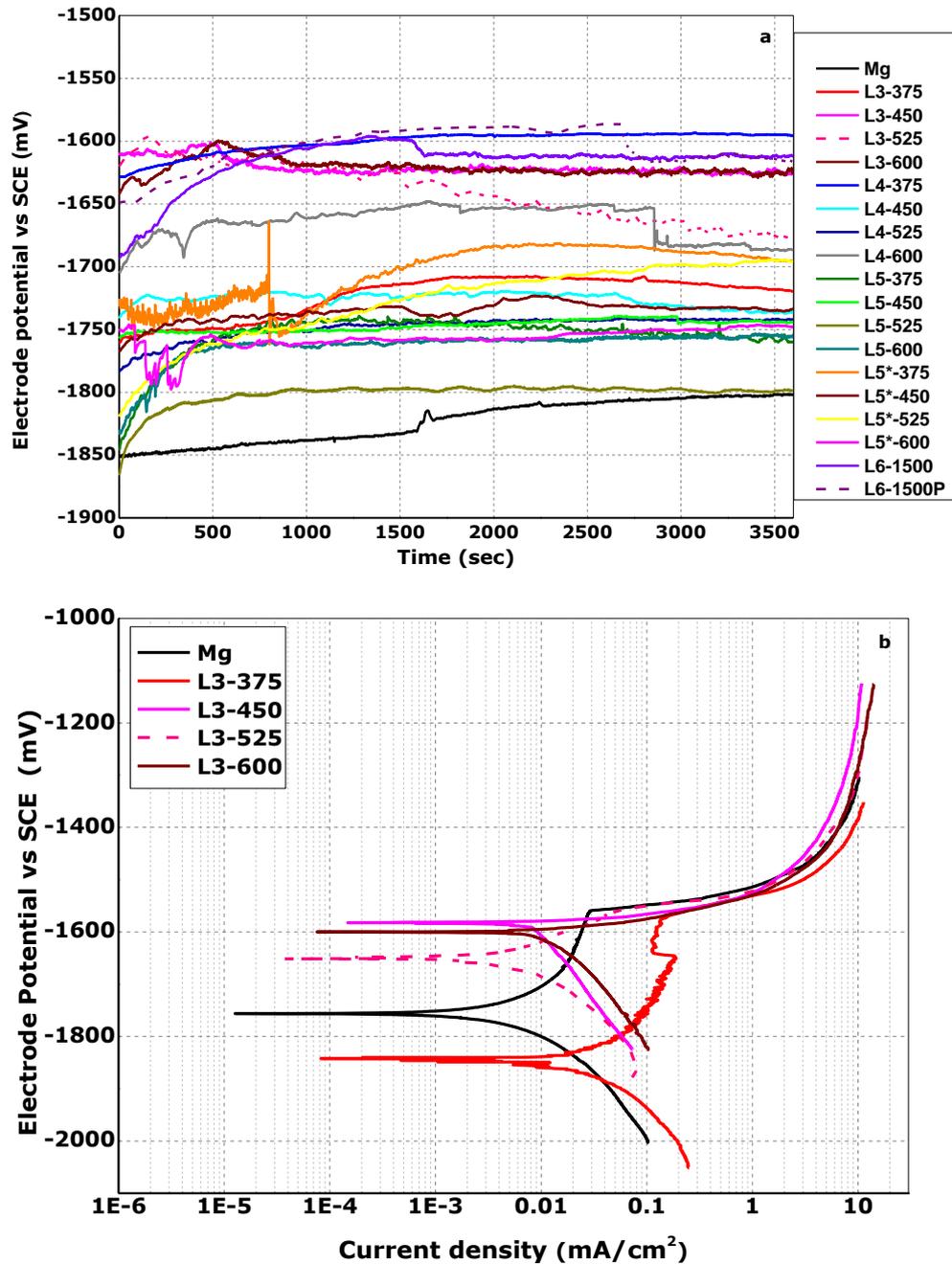
Figure 6-26 (a) OCP and potentiodynamic polarization curves for as-prepared and LSM processed Mg-surfaces for scanning speeds of: (b) 3600 mm/minute, (c) 4500 mm/minute, (d) 5400 mm/minute, and (e) scanning speed of 5400 and 6300 mm/minute (spot size 3 mm).
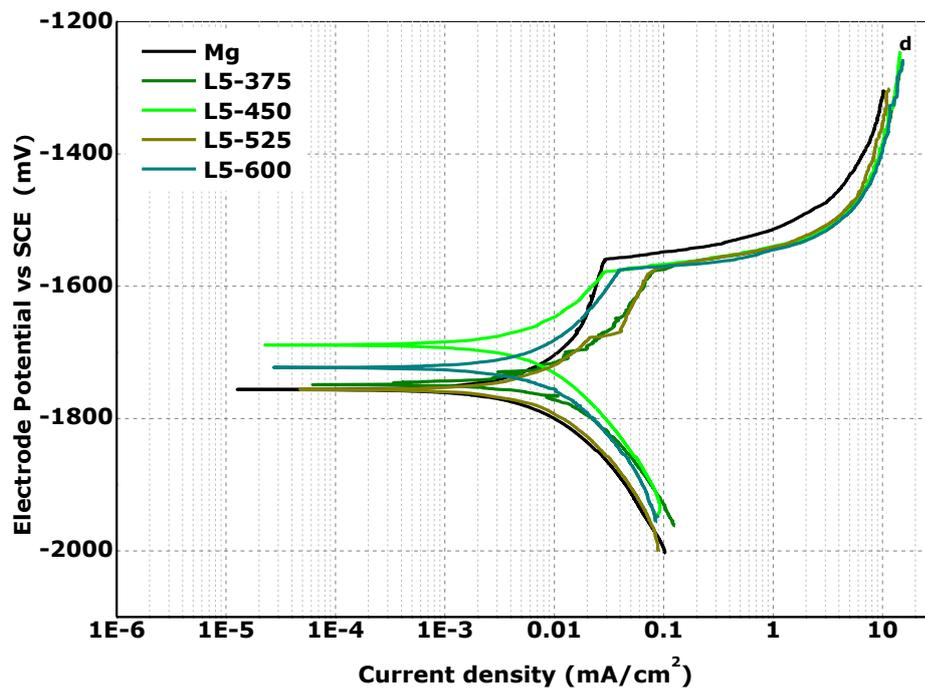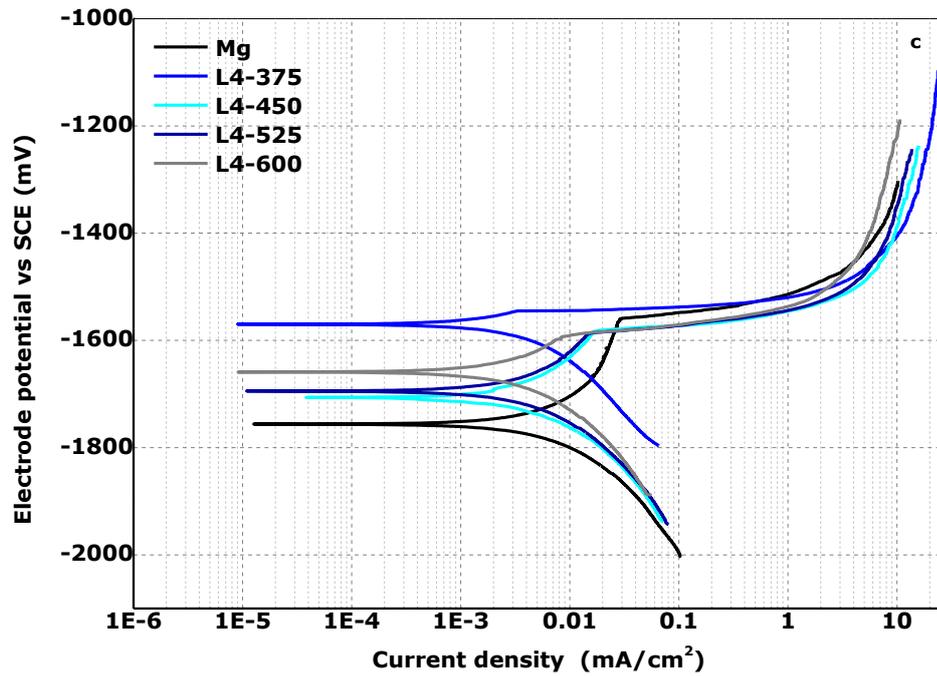
Figure 6-26 continued.., potentiodynamic polarization curves for as-prepared and LSM processed Mg-surfaces for scanning speeds of: (c) 4500 mm/minute, and (d) 5400 mm/minute(spot size 2 mm)
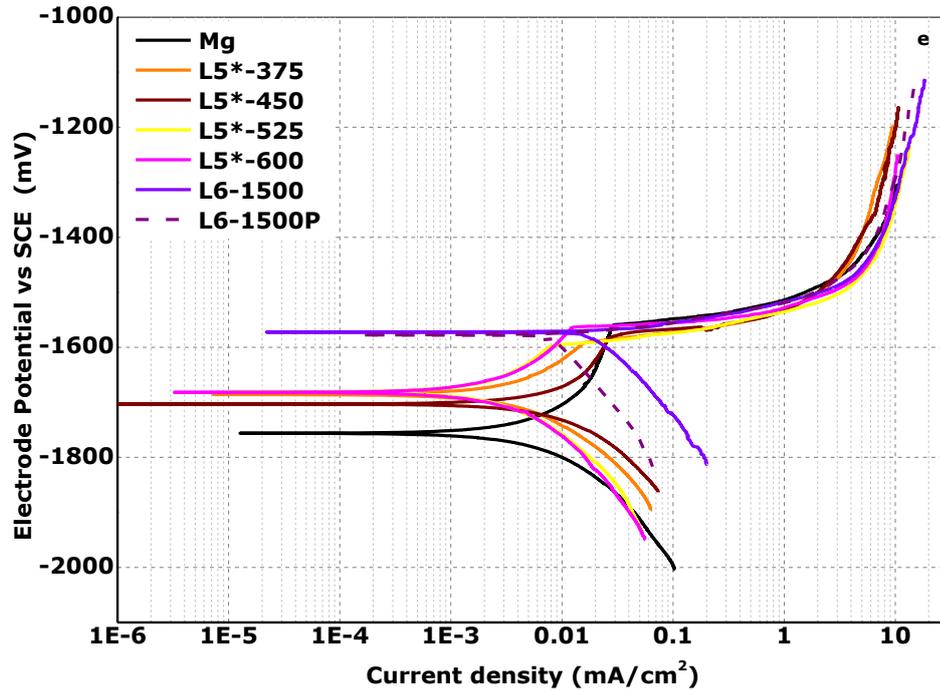
Figure 6-26 continued... potentiodynamic polarization curves for as-prepared and LSM processed Mg-surfaces for scanning speeds of: (e) 5400 and 6300 mm/min (spot size 3 mm).

Table 6-8 Characteristic parameters for as-polished and LSM modified Mg surfaces from their polarization behaviours in PBS at 37°C.

Sample	OCP / mV	E_{corr} / mV	i_{corr} / mA/cm²	E_b / mV	CR / mm/year
Mg	-1801.7	-1756.30	0.0050	-1559.6	0.12 ± 0.01
L3-375	-1718.3	-1842.9	0.0300	-1573.70	0.69 ± 0.08
L3-450	-1623.3	-1581.9	0.0190	-	0.43 ± 0.08
L3-525	-1675.9	-1650.0	0.0052	-1561.40	0.12 ± 0.08
L3-600	-1624.1	-1600.5	0.0250	-	0.45 ± 0.08
L4-375	1594.9	-1569.76	0.0019	-1544.52	0.04 ± 0.02
L4-450	1736.5	-1706.49	0.0034	-1582.60	0.08 ± 0.02
L4-525	1742.2	-1694.31	0.0034	-1588.29	0.08 ± 0.02
L4-600	1686.6	-1659.71	0.0026	-1592.67	0.06 ± 0.02
L5-375	1759.5	-1748.54	0.0080	-1576.95	0.18 ± 0.01
L5-450	1744.4	-1687.68	0.0070	-1577.78	0.15 ± 0.01
L5-525	1798.7	-1754.80	0.0060	-1573.40	0.14 ± 0.01
L5-600	1755.1	-1722.96	0.0060	-1575.96	0.14 ± 0.01
L5*-375	1695.0	-1685.80	0.0030	-1573.70	0.07 ± 0.01
L5*-450	1735.1	-1736.40	0.0052	-1555.80	0.12 ± 0.01
L5*-525	1695.0	-1647.30	0.0020	-1598.30	0.05 ± 0.01
L5*-600	1747.4	-1681.64	0.0025	-1563.32	0.06 ± 0.03
L6-1500	1611.7	-1572.50	0.0375	-	0.86 ± 0.03
L6-1500P	1614.6	-1577.18	0.0090	-	0.21 ± 0.03
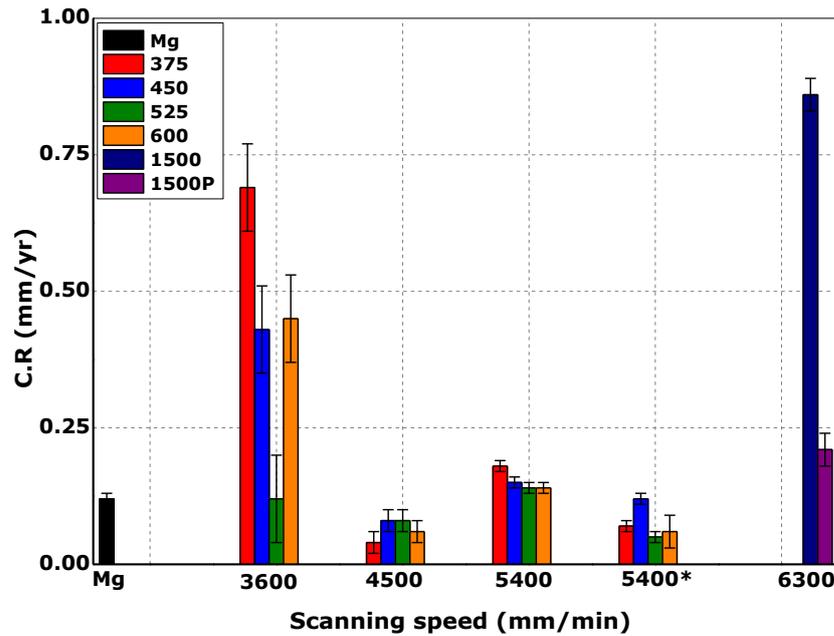
Figure 6-27 Corrosion rate as a function of laser scanning speed, for various laser powers.

6.3.2.2 Immersion testing

Figure 6-28 presents corrosion rate data for the as-polished and LSM processed Mg surfaces, as a function of immersion time. For the as-polished Mg surfaces, the corrosion rate decreased from 6.61±0.1 mm/year to 1.78±0.1 mm/year by the third day and to 1.29±0.1 mm/year by the fifth day, but rose again to 1.71±0.1 mm/year after one week immersed in PBS. The error bar represents a loose indication of the variability of this corrosion rate data was acquired from two of the samples tested, and assumed as a generalised value across this sample set.

After one-day immersion in PBS, the corrosion rates of all the LSM processed samples were approximately equal to or less than that of the as-polished Mg surface, with the exception of samples modified under conditions of high power, 600 W (& scan speed of 5400 mm/minute) and 1500 W (& scan speed of 6300 mm/minute). This indicates that the modest modification of the Mg surface under conditions of low power imparts an ability to initially resist corrosion in PBS. Conversely, the highest laser power of 1500 W produced an

LSM modified surface with a corrosion rate of 14.0±0.7 mm/year (Figure 6-28), significantly higher than that of the as-polished Mg.

When the immersion time increased to 3 - 5 days, the differences between the corrosion rates for LSM treated samples and that of the as-polished Mg reduced. The degradation of LSM processed samples was within the variability of the degradation of the as-polished Mg with some of these samples showing higher corrosion rates, which is consistent with the corrosion having removed the near surface modified layer and reached the bulk underneath.
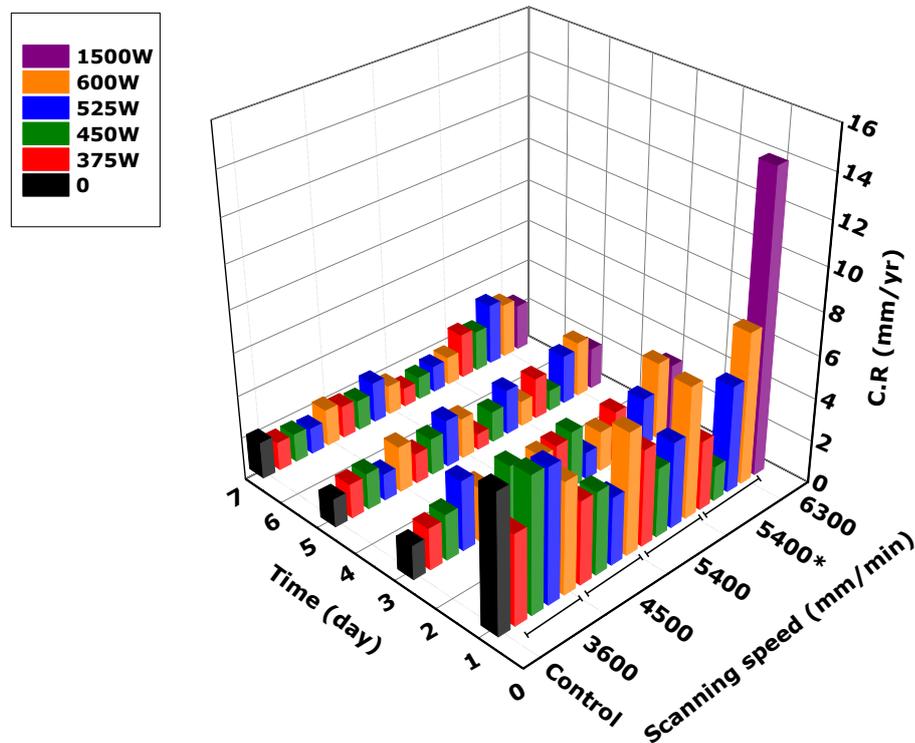
Figure 6-28 Corrosion rate data for Mg and LSM modified Mg surfaces immersed up to 7 days in PBS at 37°C.

The corrosion rate values after 7 days immersion indicated that deep modified material can affect the corrosion behaviour of LSM processed Mg, with most samples returning corrosion rates lower or within the range of the as-polished Mg. The lowest corrosion rate of 0.85±0.14 mm/year was returned for the

lowest laser-beam power of 375 W and highest scan speed of 5400 mm/minute (Figure 6-28). The highest corrosion rate of 2.91±0.3 mm/year corresponded to a surface modified at high energy, under conditions of 525 W power and 5400 mm/minute scan speed (Figure 6-28). Again, indicating that the way that energy is dispersed within a surface is important when tailoring grain structure, to impart improved corrosion resistance into the near surface of Mg.

6.3.2.3 Characterisation of LSM processed Mg surfaces following corrosion

Figure 6-29(a-f) illustrates the surface topographies of the as-prepared and LSM processed Mg surfaces (600 W; 3600 mm/minute) after immersion corrosion testing in PBS at 37°C up to 7 days. In general, after removal of the corrosion products using chromic acid, the as-polished Mg surfaces exhibited a filiform corrosion morphology as well as pitting corrosion, which became severe after seven days (Figure 6-29(a,c,e)). The surface morphologies of the corroded LSM processed Mg surfaces showed that selective dissolution occurred in the overlapping regions between laser tracks, whilst the centres of the tracks were left relatively unaltered or with superficial dissolution – demonstrating that LSM processing had a significant effect on inhibiting the onset of corrosion, on the localised scale. It is particularly notable that corrosion damage was highly localised along the boundaries of the laser tracks after 5 days immersion in PBS (Figure 6-29(b,d), arrowed). The corrosion patterns of LSM processed surfaces, after 7 days immersion, may indicate that corrosion had progressively dissolved the upper modified layer, containing refined grains, and reached the HAZ region where LSM processed material had large enough grains such that corrosion proceeded in a similar

fashion to the bulk, since little difference between the overlapping and laser melted regions was observed (Figure 6-29(f)).
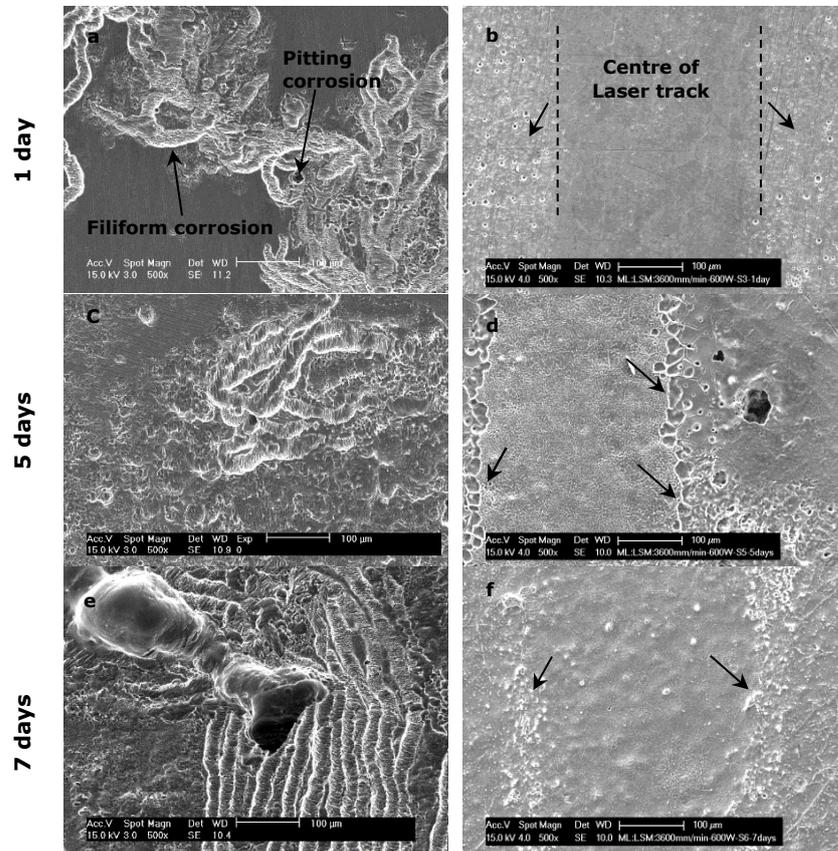
Figure 6-29 Corrosion morphologies of: (a,c,e) as-polished; and (b,d,f) LSM processed Mg surfaces, in plan view orientation, after immersion corrosion testing for 1, 5 and 7 days, respectively, in PBS at 37°C.

The long exposure of the LSM processed surfaces to PBS also induced localised corrosion at the boarder of the lacquered region, due to the effects of crevice corrosion, *i.e.* penetration of the PBS electrolyte underneath the lacquer. It is considered that the covered and exposed surfaces had different oxygen levels, leading to an increase in potential difference, in turn allowing harmful Cl⁻ ions to move under the lacquered region. Hence, the corrosion data reported here is likely to be influenced also by corrosion established at the lacquer-Mg interfaces.

Figure 6-30 presents XRD patterns of the Mg substrate and the LSM processed Mg surface after 1 day immersion in PBS at 37°C, showing Mg from the substrate and recast layer, as well as the $Mg(OH)_2$ surface corrosion product. In addition, a series of sharp intense peaks corresponding to phosphate components, tentatively attributed to $Mg_2(PO_4)OH$ and $Na_4Mg(PO_4)_2$, were detected on the LSM processed Mg corroded surfaces.
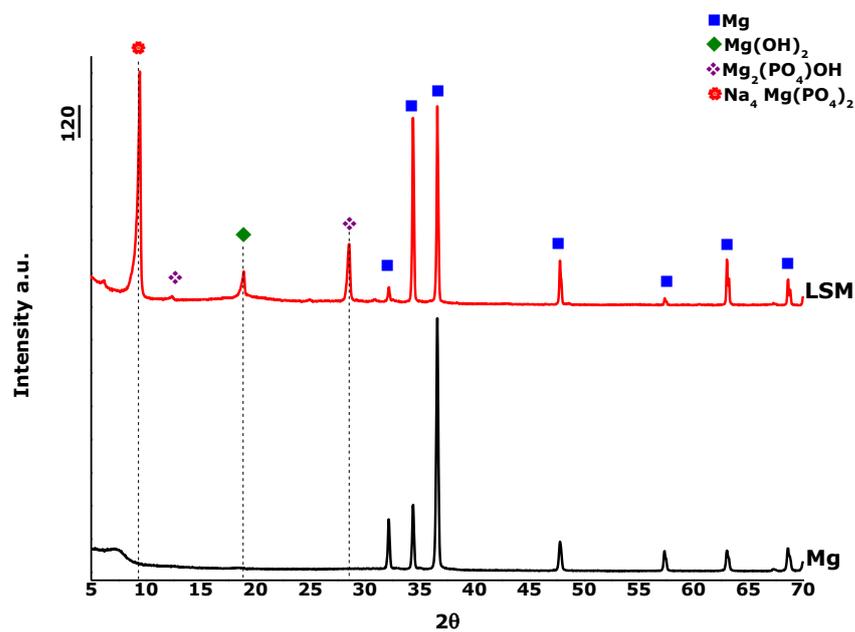
Figure 6-30 XRD patterns of as-polished and LSM processed Mg surfaces after 1 day immersion corrosion testing in PBS at 37°C.

6.3.3 Discussion

As stated in previous chapter, the PVD technique can be used to deposit a protective layer on an Mg surface with view to improving corrosion resistance. However, the quality of this layer is usually not easy to control, including porosity and adhesion to the substrate. LSM has been used to improve the surface properties, by obtaining a processed layer strongly bonded with the Mg matrix [337]. LSM treatments have been successfully used to improve the

corrosion resistance of steel and aluminium alloys [338] [339] [340] [341]. Hence, LSM treatment can also be applied to Mg to achieve better corrosion performance since it does not introduce any difference in composition of the irritated area and substrate underneath [211]. The aim of this work was to study the influence of laser processing parameters on the corrosion behaviour of LSM-Mg. Particularly, the aim was addressed by trying to understand the relation between: i) the LSM parameters of laser power and scanning speed; ii) microstructure; and iii) surface roughness on the corrosion rate, measured by polarization curve and immersion testing.

6.3.3.1 LSM-Mg morphology (microstructural characteristics)

It is well known from normal methods of casting, rapid cooling and solidification that controlling the heat flow process can produce fine and amorphous microstructures, as well as homogenous distribution of elements [214]. During laser processing, the incident laser radiation creates excited electrons which then transfer their energy to phonons. This energy will redistribute through lattice vibrations leading to heat conduction into the substrate, as atoms move from liquid to solid. The advantages of using a defocused laser beam is that it can enhance the diffusion atoms and promote the formation of shallow melting pools that provide more homogenous microstructures and less material ablation.

In this work, the effect of LSM treatment on surface topography was investigated. The proposing action of surface modification under LSM irradiation is shown schematically in Figure 6-31.
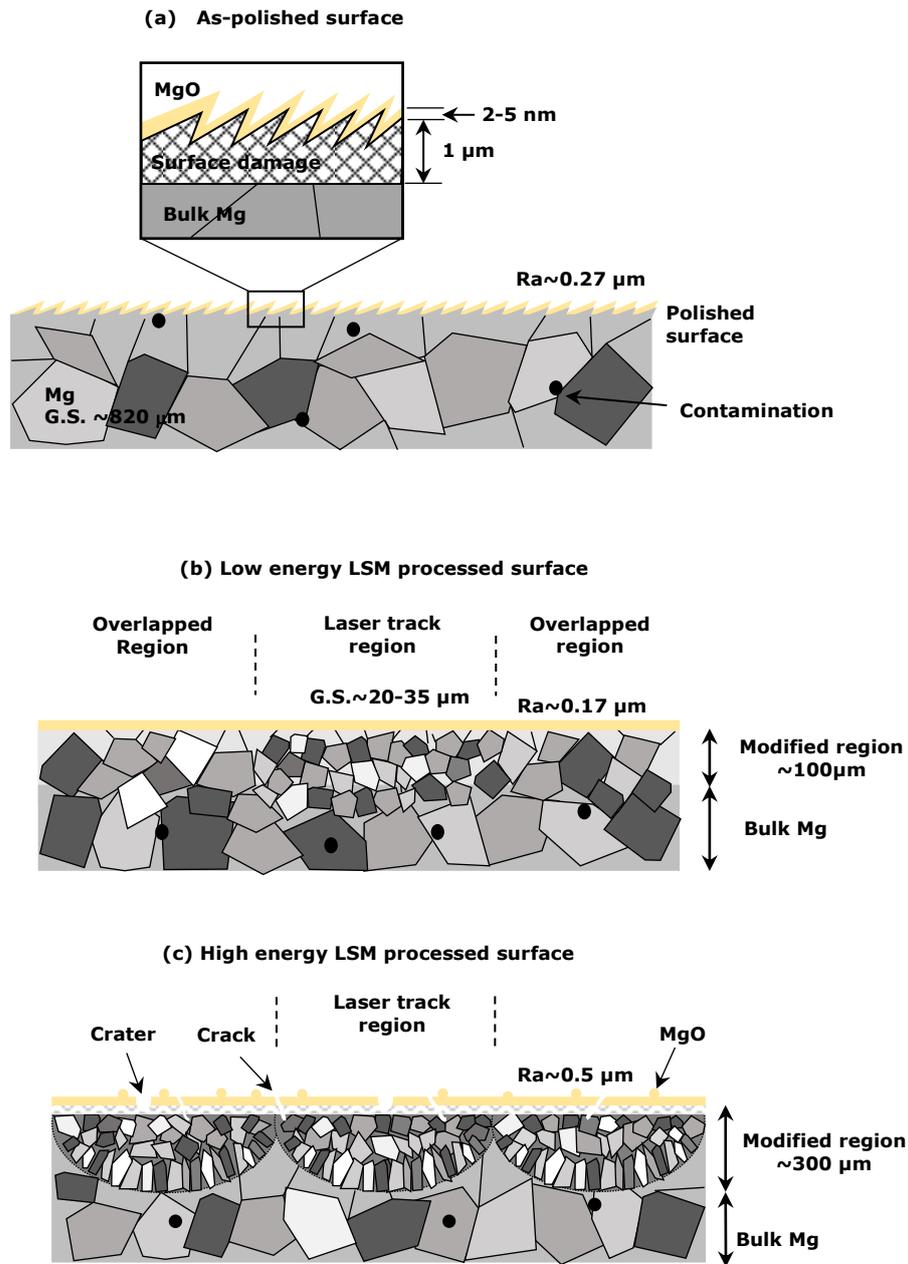
Figure 6-31 Schematic diagrames showing the proposing mechanisms of surface modification under LSM irradiation: (a) as-polished surface; (b) low energy LSM processed surface; and (c) high energy LSM processed surface.

After Mg sectioning and polishing (Figure 6-31(a)), micro-protrusions as deep as 1 μm were present on the surface, along with a spontaneous oxide layer MgO. A rough polished surface (Ra ~ 0.27 μm) was proposed to enhance laser absorptivity instead of mirror-like surface.

Under low energy density of laser irradiation (Figure 6-31(b)), the metal melts rapidly and flows, leading to shallow melting and surface smoothening. The surface roughness can indicate that shallow melting took place on the Mg surface under LSM. In case of low laser power (375-450 W), the input energy was enough to enhance surface planarisation, by melting polishing marks decorating the surface, with surface roughness values reduced to ~ 0.17 μm. Further increase in laser power (600 W) induced more severe deformation of the Mg surface, with obvious attack of grain boundaries (Figure 6-20) leading to increased surface roughness.

Surfaces processed under low energy LSM also showed affects to the surface morphology, with non-uniform deformation resulting from the shape effect of the Gaussian laser beam profile [342]. For example, for a laser beam spot size 2 mm, the FWHM of the laser profile was measured from the profile width of laser track to be ~ 1.0 mm, so the next track should show ~ 50% overlapping. However, the modulation across the areas of interest indicated that some areas received lower energy density (overlapping regions) which decreased in width with increasing laser power, due to a more homogenous distribution of laser power. Further increase in the laser spot size, whilst with keeping the hatch spacing around 50%, further affected the surface morphology, resulting in a more homogenous distribution of the energy density, as no laser tracks were seen on the Mg surfaces (Figure 6-22). Similar observation were reported by Khalfaoui *et al.* [218], noting that the power density within the laser spot is not homogenous, reaching a maximum at the beam centre and decreasing on the periphery.

In addition to surface topography, the microstructure of the Mg-surface was refined by the LSM treatment, with top layer melting and recrystallization leading to small grains distributions, mainly on the laser tracks (Figure 6-31(b)). A comparison between the grain size observed for LSM

processing of the Mg surface (Figure 6-21) and the original surface (average grain size ~ 821 ± 38 μm) showed that the surface had undergone some grain refinement, with the formation of grains of size ~ 12-43 μm (Table 6-7). The results show that for fixed sample traverse speeds, higher laser power increased the level of grain refinement on along the line profile of the laser track (Figure 6-21) with a general trend in increasing grain size (Figure 6-25 and Table 6-7). This is attributed to an increased time in the liquid phase, and as a result of melt homogenisation occurring for the case of the high power laser modified sample [219]. However, it is noted that there was no intermediate zone between the laser melted layer and the Mg matrix, and this may be due to rapid heat exchange during the heating and cooling. Khalfaoui *et al.* [218] argued that the Mg surface absorbs a high quantity of the laser energy in an extremely short time (~ 20×10^9 ns), so that an initial thin layer melts, reaching very high temperatures, whilst the rest of the material is still cold. Hence, the melted zone is subjected to a very high cooling rate, and does not have enough time to form a heat affected zone (HAZ).

In case of high laser energy processed Mg (Figure 6-31(c)), the surface experienced a high energy density, enough to decorate the surface with typical LSM surface morphologies, *i.e.* surface rippling in addition to craters and MgO particles deposited on the surface. This led to an increase the surface roughness as high as Ra ~ 0.51 μm. The topography of these surfaces revealed that the overlapping regions between two neighbouring laser tracks showed planer like surfaces (Figure 6-23 (a,c)) which might be due to insufficient energy distribution on the periphery of Gaussian laser beam distribution [220]. Additionally, during laser irradiation a re-melted process on overlapping regions caused solidified areas that acted as heat sinks for energy, *i.e.* the laser beam can melt more Mg during the first scan, than the following scans.

Evaporation of Mg and the deposition of MgO particles was observed for high energy laser processed surfaces (Figure 6-31(c)). The rapid increase of surface temperature of the irradiated Mg, to a peak temperature of ~ 4000°C, led to excessive surface boiling (the boiling temperature of Mg is 1091°C) and superheating [343]. This superheated surface led to boiling and evaporation of Mg and the formation of both vapour and liquid, in the form of explosive boiling. Guan *et al.* [343] suggested that the threshold value of power density to induce boiling on the Mg surface was in the range of 2.41 × 10^8 - 2.15 × 10^8 W/cm^2. However, these values were cited for Mg surfaces modified by nanosecond pulsed Nd:YAG laser melting, while in the present work, laser melting was performed in continuous wave mode. Hence, it is suggested that a power density of 2.1× 10^4 W/cm^2 is enough to induce boiling of the Mg surface. MgO particles were formed and re-deposited on the Mg surface, due to a reaction of Mg vapour with residual oxygen. Voids were also formed under this high power density, which may be due to the vaporisation of material at high temperature, causing recoil pressure which creates a depression into the liquid and then a hole into the melt pool [344].

The microstructure of Mg modified under high laser energy contains a well-defined melt pool, of depth ~ 300 μm, with varied grain structure (Figure 6-31(c)). Under low power density irradiation, the melting velocity will be low in compression, with the speed of heat conducted to the substrate, so the conduction loss of input energy will be high, leading to a low melting depth [345]. At higher power density, the melting velocity is higher than the rate of heat loss, caused by conduction. Because of the high thermal conductivity, a higher amount of laser energy can be conducted from the Mg surface to the liquid/solid interface and used to melt more material, increasing the melting depth [345].

In the vicinity of the modified layer, columnar microstructures were found on the boundaries of the melt pool (Figure 6-23 (c,d)). The preferred growth direction is usually in the direction of high thermal conductivity [346], and in pure Mg, the preferred growth direction is <0002>. Majumdar *et al.* [211] reported that, after laser surface melting of MEZ-Mg alloy, with a power of 2 kW and a scan speed of 200 mm/min, the microstructure of HAZ consists of fine columnar grains growing epitaxially from the liquid–solid interface. Similar observations were made by Padmavathi *et al.* [213] who found that a very narrow cellular layer formed after laser treatment of surface, due to rapid variation of thermal gradient and solidification rate. The melt depth increases with increasing laser power due to the high energy input, and the depth decreases with increasing the scan speed because of the lessened interaction time between laser and material [223]. Taltavull *et al.* [223] stated that the cooling rate at the end of HAZ is higher than the top, because the Mg matrix acts more efficiently as a heat sink for the melted Mg than the atmosphere above the substrate. Conversely, Guan *et al.* [220] studied the LSM of AZ91 alloy and reported that the cooling rate of solidification increased from the bottom to the top surface of the modified region, in the range 10^4 - 10^6 K/s. Hence, the morphology and texture of Mg will change at different depths for LSM processed areas.

Surfaces modified by high energy also show surface cracks. The presence of cracks may be attributed to the highest power densities and fast scan rates employed at the surface, which induced high input energies combined with rapid cooling rates, causing high thermal stress and hence crack formation in the laser melted regions [219], which has a deleterious effect on the corrosion resistance of LSM modified Mg.

6.3.3.2   Corrosion behaviour of LSM irradiated surfaces.

Microstructural refinement is a factor that can bring some improvement to the corrosion resistance of Mg. An analysis of the set of data from electrochemical measurement and immersion testing indicated that Tafel extrapolation at short immersion times could be used as an indication of the short-term corrosion performance of Mg, when in contact with PBS test solution [347].

LSM treatment improved the passive behaviour of all Mg surfaces which showed a nobler trend of OCP and E_{corr} values up to 207 mV after 1 h, due to a more homogenous passivation layer. Abbas *et al.* [209] also reported that the corrosion potentials of AZ31, AZ61 and WE43 alloys were increased by LSM by up to 50 mV after 24 h. Guan *et al.* [210] noticed that the corrosion potential E_{corr} for LSM treated AZ91D alloy in modified-simulated body fluid (m-SPF) at 37°C was shifted to less negative values (from -1605 to -1412 mV) than that of the as-received alloy (-1725 mV), indicating less susceptibility to corrosion. Nobler corrosion potential was also reported by Khalfaoui *et al.* [218] who noted that E_{corr} of laser-treated ZE41 alloy increased up to 117 mV after 24 h immersion in 0.5 M NaCl.

The nature of the laser process strongly affects the corrosion rate of the modified surface, which is in agreement with Taltavull *et al.* [347]. In general, the corrosion rates of low energy laser processed surfaces were less or within the range of original values (0.12 mm/year). In particular, the surface uniformly modified by a scan speed of 5400 mm/minute and spot size 3 mm had a lower energy density distributed on the Mg surface and showed a significantly lower corrosion rate (Figure 6-27). The corrosion rate significantly increased with increasing laser energy, which may due to the craters and cracks induced in the modified layer, which accounts for the increased tendency of Mg surface towards corrosion initiation. To eliminate the role played by surface defects, the high energy processed surfaces were

grounded and the outer zone of the laser treated surfaces was removed, leaving a smooth surface. Electrochemical measurements indicated a high displacement in the polarisation curve (Figure 6-26(e)) and significant decrease in corrosion rate from 0.86mm/year to 0.21 mm/year (Table 6-8).

Long-term observation of corrosion performance of LSM processed Mg may not significantly improve, under immersion tests, and some treatment parameters such as the high laser power used suggests an increase in the corrosion rate. The proposed corrosion mechanism under immersion testing is schematically illustrated in Figure 6-32(a,b).
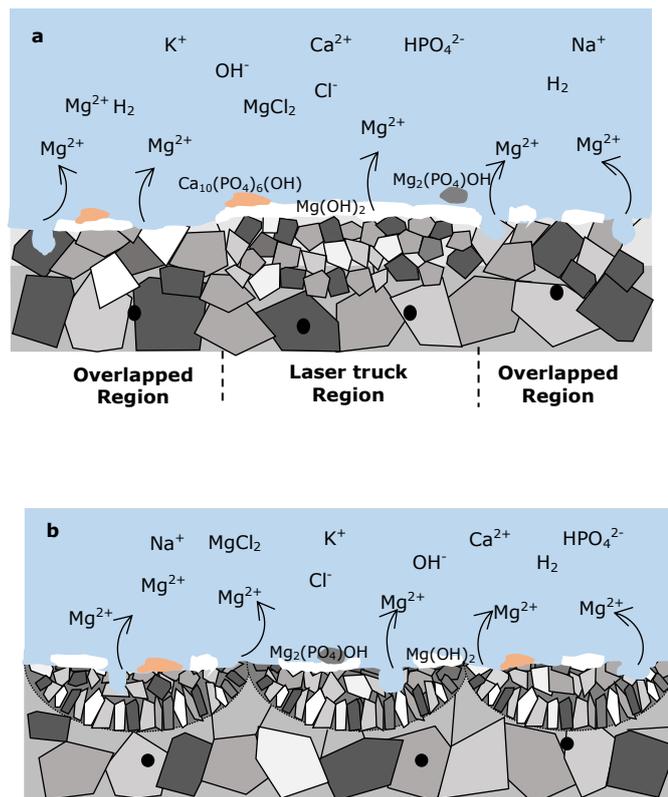
Figure 6-32 Schematic illustration of corrosion mechanism of LSM Mg surface: (a) Low energy LSM processed surface; and (b) high energy LSM processed surface.

As mentioned previously, the passivation layer of Mg consists of a hydroxide film $Mg(OH)_2$ which usually covers the Mg surface, due to the dissolution of Mg (Figure 6-32(a)). Under LSM treatment, the grain refinement will increase the grain boundary area, and hence decrease the anode to cathode area ratio [211] which help to improve the passivation trend for the modified surface (Figure 6-32(a)). However, the presence of chloride ions in the corrosive media can enhance the dissolution of $Mg(OH)_2$ to form soluble $MgCl_2$ at the metal-solution interface. This damage to the protective film results in a fresh Mg surface exposed to the solution, which facilitates new anodic sites for further dissolution. This local attack causes the formation of pits, which rapidly propagate on the surface. From the study of corroded LSM surfaces (Figure 6-29), it is evident that the rate of pit formation, especially on laser track areas with refined grains, was slower than that for the as-prepared Mg surface. Majumdar *et al.* [211] claim that slow pit formation may be due to the slower dissolution of hydroxide film, which is more stable because of the fine grain underneath. It is suggested that the modified layer on the LSM processed surface eliminates filiform corrosion, associated with as-prepared corroded Mg, with just a smaller number of small isolated pits (Figure 6-29(b)), which then grow and inter-connect with each other, leading to more uniform dissolution, as also reported by Majumdar *et al*. [211].

Surfaces processed under high laser energy corroded faster, which may be due to severe deformation, *i.e.* craters, roughness and oxidation (Figure 6-32(b)). Indeed, the increase in surface roughness suggests a higher surface area exposed to the corrosive environment and hence faster dissolution, in addition to difficulty of formation continuous passive layer [336]. Furthermore, the laser melting treatment usually produces tensile stresses in the modified region, due to volume contraction in the melt pool

during rapid solidification and subsequent cooling [214]. Guan *et al.* [210] indicated that with increasing laser power the temperature gradient in the molten layer increases, leading to large thermal tensile stresses and hence cracks and degrade of the corrosion resistance of the modified surface [347].

This trend is compared with that of AZ91D and AM60B alloys, observed by Dubé *et al.* [214], who noted a worsening corrosion resistance with higher incident power densities, under test conditions of 5% NaCl solutions, saturated with $Mg(OH)_2$, conducted for 8 days at 25°C, even though grain refinement had been achieved after laser treatment. Banerjee *et al.* [219] [221] also reported insignificant improvement in the corrosion resistance of ZE41A alloy, melted by a low scan laser rate, while a worsening corrosion rate was recorded for faster scan rate conditions. They attributed this to a similar corrosion mechanism at different interfaces, *i.e.* the corrosion product film/solution interface and the metal/corrosion product film interface.

After a week of immersion, most of the LSM samples showed corrosion rates similar to those of as-prepared surface. This indicates the corrosion rates tended to stabilize under longer immersion times and return to their origin values, due to the underneath grains having larger size, so corrosion processed in a similar trend to bulk Mg.

Even though there was no significant variation in the corrosion rate of LSM modified surface compared to that of as-prepared surface, the aspect of Mg corroded surfaces (Figure 6-29 (b,d)) showed that selective dissolution occurred in overlapping regions, while the centre of laser tracks was left unaltered. It should be noted that refined grains formed on the laser tracks (Figure 6-20 and Figure 6-21), whereas coarser Mg grains formed at overlapping regions. Hence, it is more likely that the overall corrosion resistance of LSM modified surface was affected by this variation in grain size

distribution across the surface, leading to corrosion in similar fashion to large grains [210]. This corrosion pattern is frequently observed after LSM treatment, in which localised corrosion started at overlapping regions between the melt pools [348] [349]. This result is opposite to the observation made by Dubé *et al.* [214] who found that AM60B treated by pulsed Nd:YAG laser suffered severe dissolution within the centre of melt pools, whilst superficial corrosion was reported at the interfaces between the melt pools.

6.3.3.3 Recommendations for process control

Control of the corrosion rate of Mg in human body fluid requires the development of special corrosion properties. Laser surface melting could be a promising way to further explore these possibilities. Even though a wide range of parameters were covered in this study, the results can be indicative of how to establish optimum conditions for superior corrosion resistance.

Over-processing LSM Mg surfaces can lead to Mg evaporation, crater formation, uneven surfaces and cracking. Hence, it is recommended that low laser power should be beneficial, to approach the optimum range to give homogenous and defect free microstructures, which provide for controlled corrosion rates with desired melting depths.

The LSM–Mg processing results indicate that the formation of a homogeneous microstructure comprising both the central region of the laser tracks and the overlapping regions is essential, in order to achieve a higher corrosion resistance surface. Although this work concerned a multi-track study, an initial single track processing would be beneficial, to find out the appropriate hatch spacing, depending on the actual track width.

6.3.4 Summary

The effect of laser surface melting on surface topography and corrosion performance of Mg has been investigated as a function of scanning speed, laser power and spot size. The starting material showed micro-protrusions as deep as 1 µm due to the mechanical polishing process.

Under low energy laser irradiation, Mg surfaces experienced rapid melting, causing surface smoothening. Non-uniform coverage of Mg by laser irradiation due to the Gaussian shape of the laser beam profile resulted in grain refinement centred along the laser beam tracks and coarser grain decorates the overlapping regions. More uniform surface processing was achieved by increasing the laser beam spot size.

Under high energy LSM processing, the Mg surfaces showed a conventional laser melting rippled pattern, craters, cracks and re-deposition of MgO particles, all of which act to increase the surface roughness.

The corrosion performance of laser processed surfaces initially improved, in terms of increase to the onset of corrosion, under potentiondynamic testing, which may be due to the rapid formation of the passivation layer. Low energy LSM uniformly processed surfaces generally showed corrosion rates lower than the as-prepared surface, whereas high energy LSM processed surfaces presented high corrosion rates, due to inclusions such as craters and cracks within the modified layer.

Corrosion performance under immersion testing for different times indicates that the corrosion rate of LSM processed surfaces to be close to the original values, due to non-uniform modification and mixed fine and coarser grains. However, the visual observation of LSM processed Mg surfaces revealed refined grained, laser track regions, able to resist corrosion for longer times

than the coarser grains. This indicates that laser treatment can be a practical

method to improve the surface properties and corrosion resistance of Mg.

CHAPTER 7 General discussion

7.1 Introduction

The thesis has been structured according to the three different strategies used to appraise the corrosion of Mg in physiological media. Firstly, novel Mg-minitubes for stent applications were produced by PVD. The minitubes were subjected to post-deposition annealing processes, in order to achieve refined, equiaxed grains, but was limited due to interface oxidation between the sequentially deposited Mg layers and the stabilisation of elongated grains. Secondly, Al/Al-H and a-Si:H coatings on surfaces of coarse grained, bulk Mg were deposited using PVD, in an Ar/H_2 environment. The Al coatings showed partial conversion into alumina, but were and more prone to dissolution due to coating delamination and cracking, whilst a-Si:H coatings was more promising, providing for improved corrosion resistance of the Mg. Thirdly, the near surface modification techniques of electron beam (EB) or laser surface modification (LSM) were applied to the Mg surface, in order to achieved refined microstructure capable of developing a more continuous passivation layer. This was achieved, but limited for the case of over-processed surfaces.

Although the development of modern manufacturing methods for Mg, to satisfy industry demands, has led to the production of stents with wall thicknesses of ~ 100 μm [121], the grain structure strongly affects the structural and functional properties of a material. In this context, there is need to appraise the effects of grain refinement and surface modification or coating on the corrosion performance of Mg stents.

Hence, the objective of this Chapter is to review the relationship between microstructure, i.e. grain refinement and homogeneity, and corrosion performance for PVD coated and EB or LSM Mg, studied in the present work. The effects of limitations of the techniques used are also considered.

Comparison with literature regarding corrosion performance is briefly mentioned.

7.2 Grain refinement and corrosion kinetics

In this work, it has been shown that surface modification, *e.g.* coating or grain refinement treatments; affect the corrosion behaviour of Mg in the physiological environment. A summary of the effects of different modification processes on corrosion kinetics is illustrated schematically in Figure 7-1.
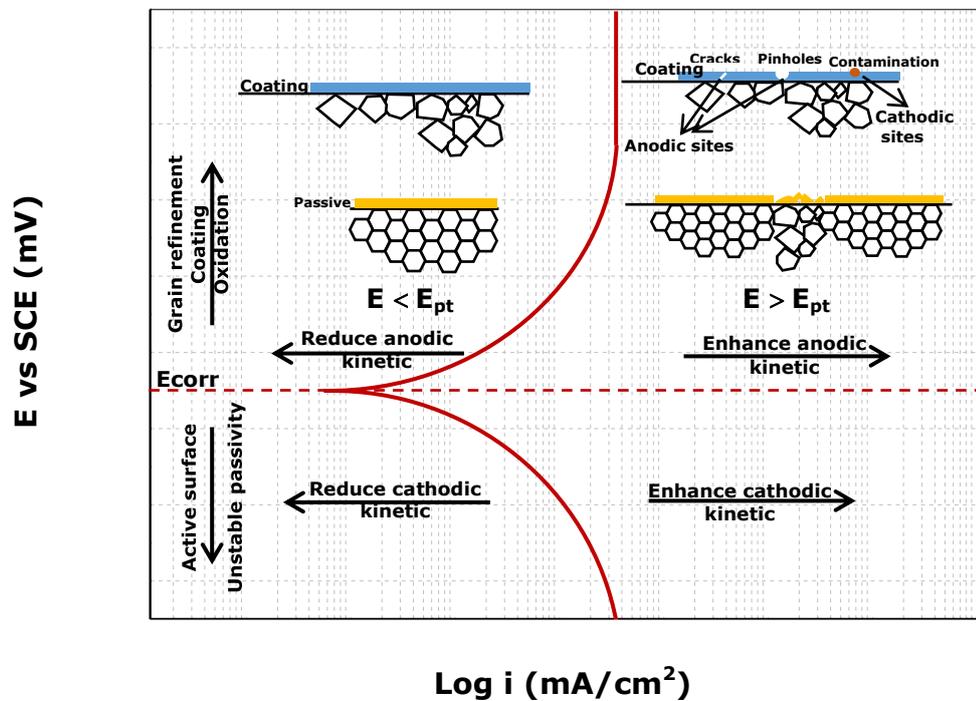
Figure 7-1 Schematic diagram summarising the effects of surface modification processes on the corrosion kinetics of pure Mg

In regard to corrosion potential measured by polarization tests, it is clear that the onset of corrosion was offset by PVD coatings of Al/Al-H and a-Si:H. Coating materials of Al and Si have a standard potential more noble than Mg, so that the overall potential of the coating/Mg system shifts positively when in contact with PBS (Figure 5-9 and Figure 5-20). In the case of Mg stents, the

corrosion potential of annealed Mg-minitubes was higher than that of as-deposited Mg-minitube. This was attributed to the enhanced oxidation of columnar microstructure, allowing more resistance to PBS to penetrate through the grains and hence decrease the surface area exposed to electrolyte. The passivation behaviour, enhanced by grain refinement, could also be promoted for Mg surfaces subjected to EB or LSM. An increase in the corrosion potential E_{corr}, in the early stages of processing (Figure 6-13 and Figure 6-26), was most likely related to activation of the passivation layer of the refined Mg surface. Nevertheless, the more reactive surface which unable to build up a passivation layer, such as in Mg minitube annealed at 550°C (Figure 4-19), exhibited lower corrosion potential E_{corr}. This indicates that the modification of the reactivity between Mg ions and ion species in solution resulted in a change of ion arrangement across the surface/solution interface during the formation of the passivation layer, and hence a change in the corrosion potential of the Mg surface.

Even though E_{corr} provides insight into the build-up of the protective passivation layer, anodic reaction kinetic presented in polarization curves for the different modification process provides more direct insight into the corrosion rate. The results from this study suggest that the corrosion rate can vary for Mg, depending on the characteristics of the grain structure, as influenced by the processing applied.

The quality (homogeneity) of the protective layer / coating can dramatically affect the corrosion performance of the Mg surface. The anodic dissolution and hence the corrosion rates recorded for the applied Al/Al-H coatings on Mg were higher than those for the unprotected surface. This was attributed to the presence of cracks and pinholes (Figure 5-2 and Figure 5-3) which enhanced the formation of galvanic cells between the coating material and the Mg

underneath. However, improvements in corrosion resistance were achieved for the case of a-Si:H coatings, due to the formation of denser, more defect free coatings (Figure 5-15 and Figure 5-22).

Alterations in grain size are related directly to the anodic corrosion kinetic, and can act to lower the overall corrosion rate through the development of a more continuous, uniform and protective oxide/hydroxide layer on the Mg surface during polarization. It can be seen from the polarization curves for the LSM/EB modification process, LSM surfaces significantly reduced anodic kinetics (Figure 6-26). This was also shown in the case of EB modified Mg surfaces where the polarisation curves showed a decrease in anodic kinetics with a shift of the anodic branch to the left (Figure 6-13). However, the evolution of hydrogen, *i.e.* the cathodic reaction, was also increased leading to relatively higher corrosion rate. Ralston *et al.* [115] reported that grain refinement for pure metals can control the anodic reaction rate, but has little effect on the cathodic reaction rate which depends more on electronic conduction than ionic conduction.

However, it can be noted that the effectiveness of near surface modification processes on Mg long-term corrosion performance was limited. This was due to microstructural homogenisation of the modified layer might not be achieved, which leaves the Mg surface with a mixture of anodic and cathodic sites, depending on the size and orientation of the grains. This means the development of corroded areas of coarser grains adjacent to non-corroded regions of fine grains, so galvanic cell activity may cause an acceleration of the overall corrosion rate. This notably was shown for the LSM modified surfaces (Figure 6-29), where the dissolution of Mg occurred preferentially within areas received low input energy, being insufficient to enhance the homogenous re-crystallisation of the surface, compared to the homogenous grains beneath the laser tracks. Similarly, surfaces modified by EB, which

shown a mixed topography of smooth and wavy features (Figure 6-4), resulted from the non-uniform deposition of energy.

It is noted that Mg surfaces with high corrosion rate exhibited more noble E_{corr} values, which might not be expected from a simple consideration of the microstructure-corrosion relationship. When E_{corr} has a value less than the pitting potential E_{pt}, a passivation layer can build up easily, for a longer period, providing for better protection of the Mg surface, and reducing the anodic dissolution of Mg. However, when the potential reaches the pitting potential, the passivation layer breaks down and the dissolution of Mg is enhanced. Song *et al.* [84] stated that a passivation layer covers the sample surface when the applied potential is more negative than the critical potential E_{pt}, which can be ~ 15 mV more negative than the corrosion potential E_{corr}. Above E_{pt} the surface is partially protected by the surface film and its surface coverage declines with a more positive applied potential. Hence, the corrosion resistance of a surface decreases due to a partial protective surface film.

7.3 Technical limitations

It is worth noting that the corrosion rates measured by polarization testing are lower than those measured by immersion testing, which is related to the conditions used for each test. Corrosion rates measured by immersion reflect the dissolution over the period of the test time (1-7 days). However, in electrochemical testing, the measurement is under an applied potential, straight after one-hour immersion in solution. Hence, it is estimated that the corrosion rate after a long period, over one day for instance, becomes more continuous during this time, whereas a lower corrosion rate can be present

during the first hour, as measured by Tafel extrapolation [88]. Accordingly, the short-term corrosion test data differs from the long-term tests. Song and Atrens [350] and Shi *et al.* [88] reported that it is typical to obtain different corrosion rates from Tafel extrapolation and immersion testing for Mg and Mg-alloys, for the following reasons: i) There may be more than one cathodic reaction involved in the cathodic branch of the polarisation curve; ii) The corroded area during solution immersion is different from that proceeding under the polarisation curve; and (iii) The surface could be different and thus the electrochemical reactions are different during immersion testing and measurement of the polarisation curve [88].

Furthermore, due to the limitation of Scherrer's equation to determine the grain size for Mg-minitube, and LSM and EB processed Mg, there was no correlation or a clear dependence trend for corrosion properties and grain size, as measured by these two independent processes. Nevertheless, there was a trend of grain size reduction, for each modification process in isolation.

7.4 Comparison with literature

Comparing the findings of this work with other studies, it is noted that Zhao *et al.* [351] studied the corrosion of pure Mg in 0.1 M NaCl solution, using Tafel extrapolation. The corrosion rates from polarisation data, P_i = 0.21-0.3 mm/year were in agreement, in magnitude, with some of the LSM data presented here. However, their work was performed using NaCl solution, which does not contain Ca and P ions that enhance the formation of HA, as another passive layer. An experiment by El-Taib Heakal *et al.* [352] using PBS, yielded a corrosion rate of 0.88 mm/year for pure Mg, again using Tafel polarization, which was much higher than the values measured in the present work. These high values may be attributed to long periods of

exposure time of Mg in PBS, for 24 h, which allowed the Mg to corrode before proceeding with the polarization measurements. Xue *et al.* [132] reported on the corrosion of pure Mg in PBS for 14 days, and the corrosion rate of 9.04 mm/year measured was much higher than that measured in the present work, and again may be attributed to the longer immersion time. However, their polarization tests showed a degradation rate of 0.09 mm/year which is in good agreement with the results of the present study.

Witte *et al.* [28] reported on the *in vivo* degradation of different Mg-alloys (including AZ31, AZ91, WE43 and LAE442), implanted as 1.5×2.00 mm rods intramedullary into female guinea pigs' femur. They reported the rod area after 6 and 18 weeks' implant duration and found that the corrosion rates slightly increased with time. They also suggested that the participation of calcium phosphate and other corrosion products such as MgO and $Mg(OH)_2$ formed a complex layer on the Mg implants, which acted to slow down the corrosion process, being the same as the corrosion products found in the present study [53]. A similar study by Xu *et al.* [353] reported on the corrosion of MgMnZn Mg-rods implanted into the femora of rats. They indicated that 10–17% of the MgMnZn implant had degraded after 9 weeks, while after 18 weeks' implantation, about 54% of the MgMnZn-alloy had degraded. They analysed the degradation layer and found that it was mainly composed of Mg, Ca, P, O, and C, but the chemical composition was not homogeneous throughout the whole layer. This observation is consistent with the mixed corrosion layer products reported for the Mg surfaces studied here.

In short, the *in vitro* study of the corrosion rate throughout this thesis measured by either polarization or immersion testing and their corresponding corrosion products formed during the Mg dissolution can be considered useable to indicate the degradation behaviour for pure Mg in the physiological environment.

7.5 Summary and recommendations

The main aspects concerning the corrosion performance of pure Mg in PBS solution and their relation to surface coating and grain refinement from surface modification have been addressed. Mg-minitubes produced by PVD and near surface modification by EB and LSM processing showed that the development of fine-grained Mg can affect the electrochemical response of corroded Mg. The corrosion potential shows that the onset of corrosion may moderated by the rapid development of a passivation layer, enhanced by an increase in grain boundary density. The passivation layer can break easily when the corrosion potential reaches the pitting potential, which enhances the dissolution of Mg in PBS.

The high corrosion rate of Al/Al-H coatings was related to the quality of the coatings, *i.e.* being strongly affected by pin-holes and cracks, whereas slow corrosion for annealed Mg minitubes was related to oxidation of Mg columnar grains. The EB and LSM processing can bring improvements to the initial corrosion rate, due to a reduction in anodic reaction, but a non-homogenous distribution of refined Mg grains and surface topography can affect the overall corrosion performance.

The corrosion rate as measured by immersion testing was higher than that determined by potentiodynamic testing, due to the time dependence of dissolution of Mg over the time period of the testing.

In short, the corrosion performance of Mg may be modified by changing the microstructure of the near surface, without changing the Mg composition. This conclusion comes from the electrochemical response of Mg, which can be varied and controlled by microstructural variation. Hence, it is recommended

that the use of microstructural processes to refine pure Mg is beneficial; in order to understand and control factors which can alter relative anodic and cathodic activities in order to further improve corrosion resistance. Furthermore, grain boundaries are areas of high energy which can lead to the formation of galvanic couples between cathodic interior grains and anodic grain boundaries, which act to promote high corrosion rates. However, it can be expected that amorphous or very small grain sized Mg can have low corrosion rates in an alkaline environment by promoting surface passivation, in comparison with coarse polycrystalline Mg grains which show a discontinuous passivation layer. Further protection of a Mg surface may be achieved by the application of a dense, crack-free coating, capable of withstanding aggressive ions in physiological media.

The corrosion rate evaluated by Tafel extrapolation from polarisation curves did not agree with the corrosion rates evaluated from weight loss measurements. Hence, when using Tafel extrapolation to explain electrochemical corrosion of Mg, it is recommended strongly that the research should be complemented by the use of other measurement methods, *e.g.* weight loss, hydrogen evolution, and rate of Mg^{2+} ion dissolution into media.

CHAPTER 8 Conclusions and future work

This Chapter provides the general conclusions drawn, based on this investigation into the use of Mg as a degradable stent. The second section suggests aspects that may need further investigation, extending from this research.

8.1 Conclusions

The degradation mechanisms of pure Mg in the physiological environment have been investigated. An appraisal of Mg surfaces, before and after corrosion processing, using complementary topographical, structural and chemical characterisation techniques, has led to detailed descriptions of the corrosion mechanisms of Mg, following different surface modification techniques.

In Chapter 4, an initial feasibility study of a novel Mg-stent, fabricated by the radio frequency magnetron sputtering PVD technique was presented. The as-deposited Mg minitubes, with a 1.2 mm inner diameter, were formed from the deposition of 10 sequential Mg layers, to give a total wall thickness of 99.6 ± 0.5 μm. The as-deposited minitubes developed a porous columnar structure, with the suggestion of some preferred orientation along the c-axis. The external surface adopted a rough surface, with voids and cracks, while the internal surface exhibited wrinkles and folds, reflecting the templating process. The annealing of Mg-minitubes under ambient gas up to 600°C resulted in microstructural densification and the initiation of some grain refinement, with hardness maximised at 52.0 Hv upon annealing at 500°C. However, full recrystallization at elevated temperature was not achieved,

being attributed to the inhibiting effect of oxidation at the Mg layer interfaces. Further, a less brittle microstructure developed by increasing the annealing temperature. The corrosion performance of the annealed Mg-minitubes generally exhibited nobler potential, compared to the as-deposited minitubes, along with improved onset of corrosion. Further, a reduction in the rate of corrosion became more pronounced with increasing annealing temperature, being attributed to the microstructural enhancement effects of densification and grain refinement, combined with Mg-minitube oxidation. The best corrosion performance of these grain refined Mg minitubes, annealed at 550°C, was close to that of the commercial prototype Mg:Dy alloy stent. Typical corrosion layer reaction products, consists of $Mg(OH)_2$ and (PO_4)-components, developed on the Mg:Dy stent struts and Mg minitube surfaces.

In Chapter 5, the application of the magnetron sputtering PVD technique for the purpose of applying a physical barrier layer, facilitated the development of biocompatible Al- and Si-based coatings on Mg. In case of Al deposited in the presence of Ar or Ar/H_2, the coatings were nanostructured crystalline, with thicknesses depending on the conditions applied. The Al and Al-H coatings followed the Mg surface profile resulting from substrate preparation, with the suggestion that the presence of H_2 acted to restrict the development of Al-Mg alloy and increase the proportion of spontaneous oxide layer formation. Heat treatment in open air at 300°C prompted the partial oxidation and growth of Al_2O_3, whilst growth at an elevated temperature of 450°C was dominated by MgO with strain at the coating/substrate interface leading to coating delamination. As-deposited and heat-treated Al and Al-H coated Mg in PBS showed improved corrosion performance, in the form of resistance to the onset of corrosion, but then more rapid corrosion rates once corrosion became established. The Al/Al-H coated Mg surfaces in PBS formed $Al(OH)_3$ and $Mg(OH)_2$ corrosion products. Pinholes, cracks and particles contamination

within the Al/Al-H coatings provided anodic sites for exposed Mg reaction with PBS and hence acted to decrease the corrosion resistance of the coated surfaces.

In the case of Si-coatings, the as-deposited coating was a dense, crack free amorphous a-Si:H layer of thickness $\sim 1\ \mu m$. FTIR and XPS analyses provided identification of the coating as SiH_2, with some SiO_x due to the presence of residual oxygen in chamber during deposition. The corrosion resistance of *a-Si-H* coated Mg improved notably in contact with PBS, in both potentiodynamic and immersion testing, indicating the ability of the a-Si:H coating to isolate the Mg surface from test solution. The proposed corrosion mechanism involved the formation of silanol Si-OH groups, which promoted the formation of negatively charged $Si\text{-}O^-$, leading to the precipitation of phosphate and carbonate species as additional coating protection.

In Chapter 6, the effect of rapid thermal processing techniques on the corrosion resistance of Mg surfaces was investigated. For Mg modified by LAEB, surfaces treated by low energy EB irradiation experienced slight remelting, no deeper than the depth of the polishing marks, leading to slight improvement in surface roughness, whilst an increase in energy of the EB led to selective ablation, along with delineation of grain boundaries and the formation of shallow pits. In particular, surfaces treated (over-processed) by high energy EB showed the effects of severe ablation, with cracks and wavy features, along with the re-deposition of MgO decorating the periphery. Craters of varied diameter covered the Mg surface, due to localised melting and eruption of the sublayer.

The corrosion performance of EB irradiated surfaces showed improvements to the onset of corrosion, under potentiondynamic testing, due to rapid passivation layer formation. Low energy EB processed surfaces showed corrosion rates slightly lower or within the range of the as-polished surfaces,

with EB surfaces treated by one pulsed at 25 kV showing the best corrosion rate of 0.08 ± 0.01 mm/year. Long corrosion performance under immersion testing in PBS showed improved corrosion resistance during the first day of immersion and then increased to be within the original values of bulk Mg due to dissolution of the modified layer. Over-processed surfaces by high energy EB irradiation showed high corrosion rates, under both potentiodynamic and immersion testing, due to a mixture of topography, craters, cracks and other inclusions within the modified surface, which accounts for the formation of a discontinuous passivation layer.

For Mg surfaces modified by LSM; under low energy LSM processing, shallow melting caused surface smoothening and grain refinement at the centre of the laser track, resulting from the Gaussian profile of the laser beam. An increase in laser spot size provided more uniform surface processing and a disappearance of the laser tracks. Under high energy LSM processing, a conventional laser melting rippled pattern formed, along with craters, cracks and the re-deposition of MgO, causing an increase in surface roughness. The corrosion performance of laser processed surfaces showed improved for the onset of corrosion under potentiondynamic testing. Low energy LSM uniformly processed surfaces generally showed corrosion rates lower than as-prepared surfaces, with the surface processed under 375 W and scanning speed of 4500 mm/minute showing the lowest corrosion rate of 0.04±0.02 mm/year. Conversely, high energy LSM processed surfaces showed high corrosion rates. Corrosion performance under immersion testing showed that LSM processed surfaces had corrosion rates close to the original values, due to the non-uniform modification of mixed refined and coarse grains. In particular, visual observation of the LSM-processed Mg surfaces revealed that refined grains located on the laser tracks were able to resist the dissolution of Mg for a longer time, than the coarser grains located along overlapping regions.

In Chapter 7, the effect of grain refinement processing and coating quality on the corrosion performance of Mg was addressed. Generally, Mg minitubes, Al/Al-H/Si-H coatings and EB/LSM processing all acted to improve the onset of corrosion potential E_{corr} through enhanced passivation behaviour. Grain refinement processing can affect the anodic kinetics by slowing down the anodic reaction and the dissolution of Mg, but had little effect on hydrogen evolution.

8.2 Recommendations for future work

This project covered several different strategies for the modification and surface protection of Mg, but much more work is needed to understanding fully and control the corrosion mechanisms of Mg.

Following the demonstration of the sequential deposition of Mg layers, improvements to the deposition process are required. The use of small Mg targets required the deposition of ~ 10 μm thick Mg per run, but removal of the sample stage from the chamber allowed an oxide layer to build up on the freshly deposited Mg. This deposition strategy leads to weaker structures at the layer interfaces and longer processing times which would not be ideal for industry. The use of larger targets to deposit single layers of the desired thickness would be beneficial.

The Mg-minitubes manufactured during this study were brittle due to their columnar structures, and annealing approaches to improve the mechanical properties of these Mg minitubes were investigated. Even though the post deposition treatment assisted in partial refinement of the structure, an investigation into the effect of deposition parameters, by change the deposition pressure and/or substrate temperature on the Mg microstructure would be beneficial. Alternatively, the use of pre-alloyed targets with suitable

elements to enhance the ductility of Mg could be explored. Further, structures with multi-layer compositional variations, containing degradable or non-degradable elements, could allow for modulated corrosion profiles.

The Mg stents produced by PVD were in the form of minitubes and not in the final shape for a commercial device. PVD techniques can enable the design of more complex, three dimensional patterned devices, when combined with 3D lithography or laser patterning.

This study has shown that the coating of Mg by a suitable barrier layer material is one important step, in order to protect the Mg surface from interaction with electrolyte. Although the focus was on a single layer system, multilayer biocompatible coatings require attention as well. Identifying an optimal coating system for commercial Mg stents or minitubes would be beneficial for extend the device lifetime.

The current study has targeted some first steps, in understanding the response of Mg to near surface modification strategies by rapid thermal processing. Despite the range of the parameters covered for both LSM and EB processing, more test variables can be investigated, especially for low energy density conditions which show promising corrosion resistance behaviour. A combination between the two techniques, *i.e.* LSM and EB could also be addressed to improve the corrosion performance of Mg.

The literature contains many studies on the use of different physiological solutions. In this research, two solutions was targeted, with the conclusion that the concentration of ions at the Mg/PBS interface was affected by the presence of Ca ions, which acted to enhance the performance of the passivation layer. Hence, it would be useful to study the effect of different ions in solution on the corrosion performance of Mg, through detailed investigation using a range of test solutions. In particular, *in vitro* studies

may assist in the characterisation of materials and their comparison in terms of functional properties, in order to progress materials for use *in vivo*.

Finally, this study was concerned with the use of pure Mg and surface processing / grain refinement and coating strategies towards the development of stents. These insights could be translated to the development of new biocompatible Mg-alloys, in order to enhance both processability and corrosion performance.

References

1. Geetha, M., A.K. Singh, R. Asokamani, and A.K. Gogia, *Ti based biomaterials, the ultimate choice for orthopaedic implants - a review.* Progress in Materials Science, 2009. **54**(3).
2. Milinkovic, I., R. Rudolf, K.T. Raic, Z. Aleksic, V. Lazic, A. Todorovic, and D. Stamenkovic, *Aspects of titanium-implant surface modification at the micro and nano levels.* Materiali in Tehnologije, 2012. **46**(3).
3. Ratner, B.D., A.S. Hoffman, F.J. Schoen, and J.E. Lemons, *Biomaterials science - an introduction to materials in medicine (2nd edition).* 2004, Elsevier.
4. Moravej, M. and D. Mantovani, *Biodegradable metals for cardiovascular stent application: Interests and new opportunities.* International Journal of Molecular Sciences, 2011. **12**(7): p. 4250-4270.
5. Brar, H.S., M.O. Platt, M. Sarntinoranont, P.I. Martin, and M.V. Manuel, *Magnesium as a biodegradable and bioabsorbable material for medical implants.* Jom, 2009. **61**(9): p. 31-34.
6. Hanawa, T., *Materials for metallic stents.* Journal of artificial organs, 2009. **12**(2): p. 73-79.
7. Garg, S. and P.W. Serruys, *Coronary stents looking forward.* Journal of the American College of Cardiology, 2010. **56**(10): p. S43-S78.
8. Erne, P., *The road to bioabsorbable stents: Reaching clinical reality?* Cardiovascular and interventional radiology, 2006. **29**(1): p. 11-16.
9. Mani, G., M.D. Feldman, D. Patel, and C.M. Agrawal, *Coronary stents: A materials perspective.* Biomaterials, 2007. **28**(9): p. 1689-1710.
10. Brown, D.A., E.W. Lee, C.T. Loh, and S.T. Kee, *A new wave in treatment of vascular occlusive disease: Biodegradable stents-clinical experience and scientific principles.* Journal of Vascular and Interventional Radiology, 2009. **20**(3): p. 315-324.
11. Witte, F., J. Fischer, J. Nellesen, H.A. Crostack, V. Kaese, A. Pisch, F. Beckmann, and H. Windhagen, *In vitro and in vivo corrosion measurements of magnesium alloys.* Biomaterials, 2006. **27**(7): p. 1013-1018.
12. Witte, F., *The history of biodegradable magnesium implants: A review.* Acta Biomaterialia, 2010. **6**(5): p. 1680-1692.
13. Kirkland, N.T., N. Birbilis, and M.P. Staiger, *Assessing the corrosion of biodegradable magnesium implants: A critical review of current methodologies and their limitations.* Acta Biomaterialia, 2012. **8**(3): p. 925-936.
14. Staiger, M.P., A.M. Pietak, J. Huadmai, and G. Dias, *Magnesium and its alloys as orthopedic biomaterials: A review.* Biomaterials, 2006. **27**(9): p. 1728-34.
15. Geis-Gerstorfer, J., C. Schille, E. Schweizer, F. Rupp, L. Scheideler, H.P. Reichel, N. Hort, A. Nolte, and H.P. Wendel, *Blood triggered corrosion of magnesium alloys.* Materials Science and Engineering B-Advanced Functional Solid-State Materials, 2011. **176**(20): p. 1761-1766.
16. Hermawan, H., *Developments in metallic biodegradable stents.* Acta Biomaterialia, 2009. **6**(5): p. 1693-1697.
17. Waizy, H., A. Weizbauer, M. Maibaum, F. Witte, H. Windhagen, A. Lucas, B. Denkena, A. Meyer-Lindenberg, and F. Thorey, *Biomechanical characterisation of a degradable magnesium-based*

(mgca0.8) screw. Journal of Materials Science-Materials in Medicine, 2012. **23**(3): p. 649-655.

18.   Zainal Abidin, N.I., A.D. Atrens, D. Martin, and A. Atrens, *Corrosion of high purity mg, mg2zn0.2mn, ze41 and az91 in hank's solution at 37°c.* Corrosion Science, 2011. **53**(11): p. 3542-3556.

19.   Chen, Y., Z. Xu, C. Smith, and J. Sankar, *Recent advances on the development of magnesium alloys for biodegradable implants.* Acta Biomaterialia, 2014. **10**(11): p. 4561-4573.

20.   Yang, J., F. Cui, and I.S. Lee, *Surface modifications of magnesium alloys for biomedical applications.* Annals of Biomedical Engineering, 2011. **39**(7): p. 1857-1871.

21.   Hornberger, H., S. Virtanen, and A.R. Boccaccini, *Biomedical coatings on magnesium alloys - a review.* Acta Biomaterialia, 2012. **8**(7): p. 2442-2455.

22.   Witte, F., J. Reifenrath, P.P. Muller, H.A. Crostack, J. Nellesen, F.W. Bach, D. Bormann, and M. Rudert, *Cartilage repair on magnesium scaffolds used as a subchondral bone replacement.* Materialwissenschaft Und Werkstofftechnik, 2006. **37**(6): p. 504-508.

23.   Heublein, B., R. Rohde, V. Kaese, M. Niemeyer, W. Hartung, and A. Haverich, *Biocorrosion of magnesium alloys: A new principle in cardiovascular implant technology?* Heart, 2003. **89**(6): p. 651-656.

24.   Waksman, R., R. Pakala, P.K. Kuchulakanti, R. Baffour, D. Hellinga, R. Seabron, F.O. Tio, E. Wittchow, S. Hartwig, C. Harder, R. Rohde, B. Heublein, A. Andreae, K.H. Waldmann, and A. Haverich, *Safety and efficacy of bioabsorbable magnesium alloy stents in porcine coronary arteries.* Catheterization and Cardiovascular Interventions, 2006. **68**(4): p. 607-617.

25.   Witte, F., N. Hort, C. Vogt, S. Cohen, K.U. Kainer, R. Willumeit, and F. Feyerabend, *Degradable biomaterials based on magnesium corrosion.* Current Opinion in Solid State & Materials Science, 2008. **12**(5-6): p. 63-72.

26.   Fare, S., Q.A. Ge, M. Vedani, G. Vimercati, D. Gastaldi, F. Migliavacca, L. Petrini, and S. Trasatti, *Evaluation of material properties and design requirements for biodegradable magnesium stents.* Materia-Rio De Janeiro, 2010. **15**(2): p. 103-112.

27.   Zeng, R., W. Dietzel, F. Witte, N. Hort, and C. Blawert, *Progress and challenge for magnesium alloys as biomaterials.* Advanced Engineering Materials, 2008. **10**(8): p. B3-B14.

28.   Sun, D.M., Y.M. Zheng, T.Y. Yin, C.J. Tang, Q.S. Yu, and G.X. Wang, *Coronary drug-eluting stents: From design optimization to newer strategies.* Journal of Biomedical Materials Research Part A, 2014. **102**(5): p. 1625-1640.

29.   Ebrahimi, A.P., *Mechanical properties of normal and diseased cerebrovascular system.* Journal of Vascular and Interventional Neurology, 2009. **2**(2): p. 155-162.

30.   Moore, J.J.E. and J.L. Berry, *Fluid and solid mechanical implications of vascular stenting.* Annals of Biomedical Engineering, 2002. **30**(4): p. 498-508.

31.   Sigwart, U., J. Puel, V. Mirkovitch, F. Joffre, and L. Kappenberger, *Intravascular stents to prevent occlusion and restenosis after trans-luminal angioplasty.* New England Journal of Medicine, 1987. **316**(12): p. 701-706.

32.   RelayHealth. *Coronary artery stent*. 2014 [cited 2016 4/11/2016].

33.   Lévesque, J., H. Hermawan, D. Dubé, and D. Mantovani, *Design of a pseudo-physiological test bench specific to the development of biodegradable metallic biomaterials.* Acta Biomaterialia, 2008. **4**(2): p. 284-295.

34.   Schomig, A., A. Kastrati, H. Mudra, R. Blasini, H. Schuhlen, V. Klauss, G. Richardt, and F.J. Neumann, *4-year experience with palmaz-schatz stenting in coronary angioplasty complicated by dissection with threatened or present vessel closure.* Circulation, 1994. **90**(6): p. 2716-2724.

35.   Hoffmann, R., G.S. Mintz, G.R. Dussaillant, J.J. Popma, A.D. Pichard, L.F. Satler, K.M. Kent, J. Griffin, and M.B. Leon, *Patterns and mechanisms of in-stent restenosis - a serial intravascular ultrasound study.* Circulation, 1996. **94**(6): p. 1247-1254.

36.   Boffetta, P., *Carcinogenicity of trace-elements with reference to evaluations made by the international-agency-for-research-on-cancer.* Scandinavian Journal of Work Environment & Health, 1993. **19**: p. 67-70.

37.   Covidien. *Paramount™ mini gps™ balloon-expandable biliary stent system*. 2010 [cited 2016 04/11/2016].

38.   Medical, R. *Self-expanding nitinol stent system*. 2014   [cited 2016 04/11/2016]; www.rontismedical.com].

39.   Grogan, J.A., B.J. O'Brien, S.B. Leen, and P.E. McHugh, *A corrosion model for bioabsorbable metallic stents.* Acta Biomaterialia, 2011. **7**(9): p. 3523-3533.

40.   Stoeckel, D., A. Pelton, and T. Duerig, *Self-expanding nitinol stents: Material and design considerations.* European Radiology, 2004. **14**(2): p. 292-301.

41.   Niinomi, M., *Recent metallic materials for biomedical applications.* Metallurgical and Materials Transactions a-Physical Metallurgy and Materials Science, 2002. **33**(3): p. 477-486.

42.   Gray-Munro, J.E. and M. Strong, *The mechanism of deposition of calcium phosphate coatings from solution onto magnesium alloy az31.* Journal of Biomedical Materials Research Part A, 2009. **90A**(2): p. 339-350.

43.   Wu, G., J.M. Ibrahim, and P.K. Chu, *Surface design of biodegradable magnesium alloys - a review.* Surface and Coatings Technology, 2012.

44.   Johnson, I., K. Akari, and H. Liu, *Nanostructured hydroxyapatite/poly(lactic-co-glycolic acid) composite coating for controlling magnesium degradation in simulated body fluid.* Nanotechnology, 2013. **24**(37).

45.   vanderGiessen, W.J., A.M. Lincoff, R.S. Schwartz, H.M.M. vanBeusekom, P.W. Serruys, D.R. Holmes, S.G. Ellis, and E.J. Topol, *Marked inflammatory sequelae to implantation of biodegradable and nonbiodegradable polymers in porcine coronary arteries.* Circulation, 1996. **94**(7): p. 1690-1697.

46.   Tamai, H., K. Igaki, E. Kyo, K. Kosuga, A. Kawashima, S. Matsui, H. Komori, T. Tsuji, S. Motohara, and H. Uehata, *Initial and 6-month results of biodegradable poly-l-lactic acid coronary stents in humans.* Circulation, 2000. **102**(4): p. 399-404.

47.   Tsuji T , T. H, I. K, Kyo E , K. K, H. T, O. M, N. T, K. H, M. S, and U. H, *Biodegradable polymeric stents.* Current Interventional Cardiology Reports, 2001. **3**(1): p. 10-17.

48.   Serruys, P.W., M.J.B. Kutryk, and A.T.L. Ong, *Drug therapy - coronary-artery stents.* New England Journal of Medicine, 2006. **354**(5): p. 483-495.

49.   Peuster, M., P. Wohlsein, M. Brugmann, M. Ehlerding, K. Seidler, C. Fink, H. Brauer, A. Fischer, and G. Hausdorf, *A novel approach to temporary stenting: Degradable cardiovascular stents produced from corrodible metal - results 6-18 months after implantation into new zealand white rabbits.* Heart, 2001. **86**(5): p. 563-569.

50. Schuessler, A., U. Bayer, G. Siekmeyer, R. Steegmueller, M. Strobel, and A. Schuessler. *Manufacturing of stents: Optimize the stent with new manufacturing technologies*. 2007.

51. Eggebrecht, H., J. Rodermann, P. Hunold, A. Schmermund, D. Bose, M. Haude, and R. Erbel, *Novel magnetic resonance-compatible coronary stent - the absorbable magnesium-alloy stent.* Circulation, 2005. **112**(18): p. E303-E304.

52. Vormann, J., *Magnesium: Nutrition and metabolism.* Molecular Aspects of Medicine, 2003. **24**(1–3): p. 27-37.

53. Witte, F., V. Kaese, H. Haferkamp, E. Switzer, A. Meyer-Lindenberg, C.J. Wirth, and H. Windhagen, *In vivo corrosion of four magnesium alloys and the associated bone response.* Biomaterials, 2005. **26**(17): p. 3557-3563.

54. Xu, L., G. Yu, E. Zhang, F. Pan, and K. Yang, *In vivo corrosion behavior of mg-mn-zn alloy for bone implant application.* J Biomed Mater Res A, 2007. **83**(3): p. 703-11.

55. Xin, Y., T. Hu, and P.K. Chu, *In vitro studies of biomedical magnesium alloys in a simulated physiological environment: A review.* Acta Biomaterialia, 2011. **7**(4): p. 1452-1459.

56. Saris, N.E.L., E. Mervaala, H. Karppanen, J.A. Khawaja, and A. Lewenstam, *Magnesium - an update on physiological, clinical and analytical aspects.* Clinica Chimica Acta, 2000. **294**(1-2): p. 1-26.

57. Nandakumar, K., K.R. Sreekumari, and Y. Kikuchi, *Antibacterial properties of magnesium alloy az31b: In-vitro studies using the biofilm-forming bacterium pseudomonas sp.* Biofouling, 2002. **18**(2): p. 129-135.

58. Heublein, B., R. Rohde, M. Niemeyer, V. Kaese, W. Hartung, and C. Rocken, *Degradation of metallic alloys - a new principle in stent technology?* Journal of the American College of Cardiology, 2000. **35**(2): p. 14A-15A.

59. Di Mario, C., H.U.W. Griffiths, O. Goktekin, N. Peeters, J.A.N. Verbist, M. Bosiers, K. Deloose, B. Heublein, R. Rohde, V. Kasese, C. Ilsley, and R. Erbel, *Drug-eluting bioabsorbable magnesium stent.* Journal of Interventional Cardiology, 2004. **17**(6): p. 391-395.

60. Wang, X.X., S. Cai, G.H. Xu, X.Y. Ye, M.G. Ren, and K. Huang, *Surface characteristics and corrosion resistance of sol-gel derived cao-p2o5-sro-na2o bioglass-ceramic coated mg alloy by different heat-treatment temperatures.* Journal of Sol-Gel Science and Technology, 2013. **67**(3): p. 629-638.

61. O'Brien, B.J., W.M. Carroll, A.J. Conneely, and G.M. O'Connor, *Combined anodizing and picosecond laser treatment to control the corrosion rate of biodegradable magnesium alloy az31.* Proceedings of the Institution of Mechanical Engineers Part L-Journal of Materials-Design and Applications, 2014. **228**(4): p. 278-287.

62. Erbel, R., C. Di Mario, J. Bartunek, J. Bonnier, B. de Bruyne, F.R. Eberli, P. Erne, M. Haude, B. Heublein, M. Horrigan, C. Ilsley, D. Böse, J. Koolen, T.F. Lüscher, N. Weissman, and R. Waksman, *Temporary scaffolding of coronary arteries with bioabsorbable magnesium stents: A prospective, non-randomised multicentre trial.* Lancet, 2007. **369**(9576): p. 1869-1875.

63. Zartner, P., R. Cesnjevar, H. Singer, and M. Weyand, *First successful implantation of a biodegradable metal stent into the left pulmonary artery of a preterm baby.* Catheterization and Cardiovascular Interventions, 2005. **66**(4): p. 590-594.

64. Schranz, D., P. Zartner, I. Michel-Behnke, and H. Akinturk, *Bioabsorbable metal stents for percutaneous treatment of critical*

recoarctation of the aorta in a newborn. Catheterization and Cardiovascular Interventions, 2006. **67**(5): p. 671-673.

65. Zhao, N., N. Watson, Z. Xu, Y. Chen, J. Waterman, J. Sankar, and D. Zhu, *In vitro biocompatibility and endothelialization of novel magnesium-rare earth alloys for improved stent applications.* PLOS ONE, 2014. **9**(6): p. e98674.

66. Mitchell, B.S., *Introduction to materials engineering and science for chemical and materials engineers*. 2004, Hoboken, NJ, USA: John Wiley Press.

67. Wu, M.H., *Fabrication of nitinol materials and components*, in *Shape memory materials and its applications*, Y.Y. Chu and L.C. Zhao, Editors. 2001. p. 285-292.

68. Meyer Kobbe, C. and B. Hinrichs, *The importance of annealing 316 lvm stents.* Medical Device Technology, 2002. **14**(1): p. 20-25.

69. Martinez, A.W. and E.L. Chaikof, *Microfabrication and nanotechnology in stent design.* Wiley Interdisciplinary Reviews-Nanomedicine and Nanobiotechnology, 2011. **3**(3): p. 256-268.

70. Ghali, E., *Corrosion resistance of aluminum and magnesium alloys : Understanding, performance, and testing*. Wiley series in corrosion, ed. W. Revie. 2010, New Jersey: Wiley.

71. Mathaudhu, S.N., *Magnesium technology 2012*. 2012, Hoboken, NJ, USA: Wiley-TMS.

72. Polmear, I.J., *Light alloys: Metallurgy of the light metals*. 1995: Wiley.

73. Roberts, C.S., *Magnesium and its alloys*. 1960: Wiley

74. Emley, E.F., *Principles of magnesium technology*. 1966: Elsevier Science & Technology. 1013.

75. Song, G., *Understanding magnesium corrosion: A framework for improved alloy performance.* Advanced Engineering Materials, 2003. **5**(12): p. 837-858.

76. Ghali, E., *Testing of general and localized corrosion of magnesium alloys: A critical review.* Journal of materials engineering and performance, 2004. **13**(5): p. 517-529.

77. Gray, J.E. and B. Luan, *Protective coatings on magnesium and its alloys — a critical review.* Journal of Alloys and Compounds, 2002. **336**(1–2): p. 88-113.

78. Tanvir, H., *A study of bonding mechanisms and corrosion behaviour of cold sprayed coatings*, in *Material Engineering*. 2011, University of Nottingham Nottingham.

79. Tait, W.S., *An introduction to electrochemical corrosion testing for practicing engineers and scientists*. 1994: PairODocs Publications.

80. Jacobs, J.J., J.L. Gilbert, and R.M. Urban, *Corrosion of metal orthopaedic implants.* Journal of Bone and Joint Surgery-American Volume, 1998. **80A**(2): p. 268-282.

81. Zeng, Z.C., *Review of studies on corrosion of magnesium alloys.* Transactions of Nonferrous Metals Society of China, 2006. **16**.

82. Makar, G.L. and J. Kruger, *Corrosion of magnesium.* International materials reviews, 1993. **38**(3): p. 138-153.

83. Atrens, A., M. Liu, and N.I.Z. Abidin, *Corrosion mechanism applicable to biodegradable magnesium implants.* Materials Science and Engineering B-Advanced Functional Solid-State Materials, 2011. **176**(20): p. 1609-1636.

84. Song, G., A. Atrens, D. Stjohn, J. Nairn, and Y. Li, *The electrochemical corrosion of pure magnesium in 1 n nacl.* Corrosion Science, 1997. **39**(5): p. 855-875.

85. Shi, Z., J.X. Jia, and A. Atrens, *Galvanostatic anodic polarisation curves and galvanic corrosion of high purity mg in 3.5% nacl saturated with mg(oh)2.* Corrosion Science, 2012. **60**(0): p. 296-308.

86. Petty, R.L., A.W. Davidson, and J. Kleinberg, *The anodic oxidation of magnesium metal - evidence for the existence of unipositive magnesium.* Journal of the American Chemical Society, 1954. **76**(2): p. 363-366.

87. Song, G., A. Atrens, D.S. John, X. Wu, and J. Nairn, *The anodic dissolution of magnesium in chloride and sulphate solutions.* Corrosion Science, 1997. **39**(10–11): p. 1981-2004.

88. Shi, Z., M. Liu, and A. Atrens, *Measurement of the corrosion rate of magnesium alloys using tafel extrapolation.* Corrosion Science, 2010. **52**(2): p. 579-588.

89. Williams, G. and H.N. McMurray, *Localized corrosion of magnesium in chloride-containing electrolyte studied by a scanning vibrating electrode technique.* Journal of the Electrochemical Society, 2008. **155**(7): p. C340-C349.

90. Thomaz, T.R., C.R. Weber, T. Pelegrini, L.F.P. Dick, and G. Knornschild, *The negative difference effect of magnesium and of the az91 alloy in chloride and stannate-containing solutions.* Corrosion Science, 2010. **52**(7): p. 2235-2243.

91. Bender, S., J. Goellner, A. Heyn, and S. Schmigalla, *A new theory for the negative difference effect in magnesium corrosion.* Materials and Corrosion-Werkstoffe Und Korrosion, 2012. **63**(8): p. 707-712.

92. McCafferty, E., *Introduction to corrosion science*. 2nd ed. 2010, New York: Springer International Publishing.

93. Nordlien, J.H., S. Ono, N. Masuko, and K. Nisancioglu, *A tem investigation of naturally formed oxide films on pure magnesium.* Corrosion Science, 1997. **39**(8): p. 1397-1414.

94. Liu, M., S. Zanna, H. Ardelean, I. Frateur, P. Schmutz, G. Song, A. Atrens, and P. Marcus, *A first quantitative xps study of the surface films formed, by exposure to water, on mg and on the mg-al intermetallics: Al 3mg 2 and mg 17al 12.* Corrosion Science, 2009. **51**(5): p. 1115-1127.

95. Schmutz, P., V. Guillaumin, R.S. Lillard, J.A. Lillard, and G.S. Frankel, *Influence of dichromate ions on corrosion processes on pure magnesium.* Journal of the Electrochemical Society, 2003. **150**(4): p. B99-B110.

96. Santamaria, M., F. Di Quarto, S. Zanna, and P. Marcus, *Initial surface film on magnesium metal: A characterization by x-ray photoelectron spectroscopy (xps) and photocurrent spectroscopy (pcs).* Electrochimica Acta, 2007. **53**(3): p. 1314-1324.

97. Brady, M.P., G. Rother, L.M. Anovitz, K.C. Littrell, K.A. Unocic, H.H. Elsentriecy, G.L. Song, J.K. Thomson, N.C. Gallego, and B. Davis, *Film breakdown and nano-porous mg(oh)(2) formation from corrosion of magnesium alloys in salt solutions.* Journal of the Electrochemical Society, 2015. **162**(4): p. C140-C149.

98. Brun, C.H., J. Pagetti, and J. Talbot, *Study of corrosion of magnesium in aqueous 3 wt percent sodium-chloride solution at room-temperature.* Memoires Scientifiques De La Revue De Metallurgie, 1976. **73**(10): p. 659-668.

99. Poinern, G.E.J., S. Brundavanam, and D. Fawcett, *Biomedical magnesium alloys: A review of material properties, surface modifications and potential as a biodegradable orthopaedic implant.* American Journal of Biomedical Engineering, 2012 **2**(6): p. 218-240.

100. Ghali, E., W. Dietzel, and K.U. Kainer, *General and localized corrosion of magnesium alloys: A critical review.* Journal of Materials Engineering and Performance, 2013. **22**(10): p. 2875-2891.

101. ASTM, A.S.f.T.a.M., *Standard guide for laboratory immersion corrosion testing of metals astmg31-12a*. 2012, ASTM International: PA,USA.

102. Shi, Z.M. and A. Atrens, *An innovative specimen configuration for the study of mg corrosion.* Corrosion Science, 2011. **53**(1): p. 226-246.

103. Xin, Y., C. Liu, X. Zhang, G. Tang, X. Tian, and P.K. Chu, *Corrosion behavior of biomedical az91 magnesium alloy in simulated body fluids.* Journal of Materials Research, 2007. **22**(7): p. 2004-2011.

104. Zhao, M.-C., M. Liu, G.-L. Song, and A. Atrens, *Influence of ph and chloride ion concentration on the corrosion of mg alloy ze41.* Corrosion Science, 2008. **50**(11): p. 3168-3178.

105. Song, G. and S. Song, *A possible biodegradable magnesium implant material.* Advanced Engineering Materials, 2007. **9**(4): p. 298-302.

106. Ng, W.F., K.Y. Chiu, and F.T. Cheng, *Effect of ph on the in vitro corrosion rate of magnesium degradable implant material.* Materials Science & Engineering C-Materials for Biological Applications, 2010. **30**(6): p. 898-903.

107. ASTM, A.S.f.T.a.M., *Standard practice for calculation of corrosion rates and related information from electrochemical measurements*. 2015, ASTM International.

108. Chen, Y., S.X. Zhang, J.A. Li, Y. Song, C.L. Zhao, and X.N. Zhang, *Dynamic degradation behavior of mgzn alloy in circulating m-sbf.* Materials Letters, 2010. **64**(18): p. 1996-1999.

109. Li, Y., C. Wen, D. Mushahary, R. Sravanthi, N. Harishankar, G. Pande, and P. Hodgson, *Mg–zr–sr alloys as biodegradable implant materials.* Acta Biomaterialia, 2012. **8**(8): p. 3177-3188.

110. Zhang, L.N., Z.T. Hou, X. Ye, Z.B. Xu, X.L. Bai, and P. Shang, *The effect of selected alloying element additions on properties of mg-based alloy as bioimplants: A literature review.* Frontiers of Materials Science, 2013. **7**(3): p. 227-236.

111. Hall, E.O., *The deformation and ageing of mild steel .3. Discussion of results.* Proceedings of the Physical Society of London Section B, 1951. **64**(381): p. 747-753.

112. Gusieva, K., C.H.J. Davies, J.R. Scully, and N. Birbilis, *Corrosion of magnesium alloys: The role of alloying.* International Materials Reviews, 2015. **60**(3): p. 169-194.

113. Liu, X.M., F.P. Yuan, and Y.G. Wei, *Grain size effect on the hardness of nanocrystal measured by the nanosize indenter.* Applied Surface Science, 2013. **279**: p. 159-166.

114. Birbilis, N., K.D. Ralston, S. Virtanen, H.L. Fraser, and C.H.J. Davies, *Grain character influences on corrosion of ecaped pure magnesium.* Corrosion Engineering Science and Technology, 2010. **45**(3): p. 224-230.

115. Ralston, K.D., N. Birbilis, and C.H.J. Davies, *Revealing the relationship between grain size and corrosion rate of metals.* Scripta Materialia, 2010. **63**(12): p. 1201-1204.

116. Argade, G.R., S.K. Panigrahi, and R.S. Mishra, *Effects of grain size on the corrosion resistance of wrought magnesium alloys containing neodymium.* Corrosion Science, 2012. **58**: p. 145-151.

117. Kim, H.S., G.H. Kim, H. Kim, and W.J. Kim, *Enhanced corrosion resistance of high strength mg-3al-1zn alloy sheets with ultrafine grains in a phosphate-buffered saline solution.* Corrosion Science, 2013. **74**: p. 139-148.

118. Kim, H.S. and W.J. Kim, *Enhanced corrosion resistance of ultrafine-grained az61 alloy containing very fine particles of mg17al12 phase.* Corrosion Science, 2013. **75**: p. 228-238.

119. Ben Hamu, G., D. Eliezer, and L. Wagner, *The relation between severe plastic deformation microstructure and corrosion behavior of az31 magnesium alloy.* Journal of Alloys and Compounds, 2009. **468**(1-2): p. 222-229.

120. Hoog, C.O., N. Birbilis, and Y. Estrin, *Corrosion of pure mg as a function of grain size and processing route.* Advanced Engineering Materials, 2008. **10**(6): p. 579-582.

121. Hoog, C.O., N. Birbilis, M.X. Zhang, and Y. Estrin, *Surface grain size effects on the corrosion of magnesium*, in *Progress in surface treatment*, N.E. Mahallawy and M. Zhang, Editors. 2008. p. 229-240.

122. Ambat, R., N.N. Aung, and W. Zhou, *Evaluation of microstructural effects on corrosion behaviour of az91d magnesium alloy.* Corrosion Science, 2000. **42**(8): p. 1433-1455.

123. Jang, Y.H., S.S. Kim, C.D. Yim, C.G. Lee, and S.J. Kim, *Corrosion behaviour of friction stir welded az31b mg in 3.5%nacl solution.* Corrosion Engineering Science and Technology, 2007. **42**(2): p. 119-122.

124. Gollapudi, S., *Grain size distribution effects on the corrosion behaviour of materials.* Corrosion Science, 2012. **62**: p. 90-94.

125. Hofstetter, J., E. Martinelli, A.M. Weinberg, M. Becker, B. Mingler, P.J. Uggowitzer, and J.F. Loffler, *Assessing the degradation performance of ultrahigh-purity magnesium in vitro and in vivo.* Corrosion Science, 2015. **91**: p. 29-36.

126. Liu, M., P.J. Uggowitzer, A.V. Nagasekhar, P. Schmutz, M. Easton, G.L. Song, and A. Atrens, *Calculated phase diagrams and the corrosion of die-cast mg-al alloys.* Corrosion Science, 2009. **51**(3): p. 602-619.

127. Hanawalt, J.D., C.E. Nelson, and J.A. Peloubet, *Corrosion studies of magnesium and its alloys.* Transactions of the American Institute of Mining and Metallurgical Engineers, 1942. **147**: p. 273-298.

128. Eliezer, D., E. Aghion, and F.H. Froes, *Magnesium science, technology and applications.* Advanced Performance Materials, 1998. **5**(3): p. 201-212.

129. Stjohn, D.H., M.A. Easton, M. Qian, and J.A. Taylor, *Grain refinement of magnesium alloys: A review of recent research, theoretical developments, and their application.* Metallurgical and Materials Transactions a-Physical Metallurgy and Materials Science, 2013. **44A**(7): p. 2935-2949.

130. Ralston, K.D. and N. Birbilis, *Effect of grain size on corrosion: A review.* Corrosion, 2010. **66**(7).

131. Pourbaix, M., *Atlas of electrochemical equilibria in aqueous solutions*. 1974: National Association of Corrosion Engineers.

132. Xue, D., Y. Yun, Z. Tan, Z. Dong, and M.J. Schulz, *In vivo and in vitro degradation behavior of magnesium alloys as biomaterials.* Journal of Materials Science & Technology, 2012. **28**(3): p. 261-267.

133. Gu, X.-N. and Y.-F. Zheng, *A review on magnesium alloys as biodegradable materials.* Frontiers of Materials Science in China, 2010. **4**(2): p. 111-115.

134. Song, G.L., *Control of biodegradation of biocompatable magnesium alloys.* Corrosion Science, 2007. **49**(4): p. 1696-1701.

135. Takenaka, T., Y. Narazaki, N. Uesaka, and M. Kawakami, *Improvement of corrosion resistance of magnesium alloys by surface film with rare earth element.* Materials Transactions, 2008. **49**(5): p. 1071-1076.

136. Anicai, L., R. Masi, M. Santamaria, and F. Di Quarto, *A photoelectrochemical investigation of conversion coatings on mg substrates.* Corrosion Science, 2005. **47**(12): p. 2883-2900.

137. Xu, L., *Phosphating treatment and corrosion properties of mg-mn-zn alloy for biomedical application.* Journal of materials science. Materials in medicine, 2009. **20**(4): p. 859-867.

138. Drynda, A., *Development and biocompatibility of a novel corrodible fluoride-coated magnesium-calcium alloy with improved degradation kinetics and adequate mechanical properties for cardiovascular*

applications. Journal of biomedical materials research. Part A, 2010. **93**(2): p. 763-775.

139. Song, Y.W., D.Y. Shan, and E.H. Han, *A novel biodegradable nicotinic acid/calcium phosphate composite coating on mg-3zn alloy.* Materials Science & Engineering C-Materials for Biological Applications, 2013. **33**(1): p. 78-84.

140. Wang, H.X., S.K. Guan, X. Wang, C.X. Ren, and L.G. Wang, *In vitro degradation and mechanical integrity of mg-zn-ca alloy coated with ca-deficient hydroxyapatite by the pulse electrodeposition process.* Acta Biomaterialia, 2010. **6**(5): p. 1743-1748.

141. Ma, W.H., Y.J. Liu, W. Wang, and Y.Z. Zhang, *Improved biological performance of magnesium by micro-arc oxidation.* Brazilian Journal of Medical and Biological Research, 2015. **48**(3): p. 214-225.

142. Wang, C.J., B.L. Jiang, M. Liu, and Y.F. Ge, *Corrosion characterization of micro-arc oxidization composite electrophoretic coating on az31b magnesium alloy.* Journal of Alloys and Compounds, 2015. **621**: p. 53-61.

143. Hiromoto, S. and A. Yamamoto, *Control of degradation rate of bioabsorbable magnesium by anodization and steam treatment.* Materials Science & Engineering C-Materials for Biological Applications, 2010. **30**(8): p. 1085-1093.

144. Rie, K.T. and J. Wohle, *Plasma-cvd of ticn and zrcn films on light metals.* Surface & Coatings Technology, 1999. **112**(1-3): p. 226-229.

145. Sella, C., J. Lecoeur, Y. Sampeur, and P. Catania, *Corrosion-resistance of amorphous hydrogenated sic and diamond-like coatings deposited by rf-plasma-enhanced chemical-vapor-deposition.* Surface & Coatings Technology, 1993. **60**(1-3): p. 577-583.

146. Xin, Y.C., C.L. Liu, K.F. Huo, G.Y. Tang, X.B. Tian, and P.K. Chu, *Corrosion behavior of zrn/zr coated biomedical az91 magnesium alloy.* Surface & Coatings Technology, 2009. **203**(17-18): p. 2554-2557.

147. Yang, J.X., Y.P. Jiao, F.Z. Cui, I.S. Lee, Q.S. Yin, and Y. Zhang, *Modification of degradation behavior of magnesium alloy by ibad coating of calcium phosphate.* Surface & Coatings Technology, 2008. **202**(22-23): p. 5733-5736.

148. Tsubakino, H., A. Watanabe, A. Yamamoto, and S. Fukumoto, *Formation of magnesium films on magnesium alloys by vapor deposition technique*, in *Magnesium alloys 2000*, Y. Kojima, T. Aizawa, and S. Kamado, Editors. 2000. p. 235-240.

149. Yamamoto, A., A. Watanabe, H. Tsubakino, and S. Fukumoto, *Afm observations of microstructures of deposited magnesium on magnesium alloys*, in *Magnesium alloys 2000*, Y. Kojima, T. Aizawa, and S. Kamado, Editors. 2000. p. 241-246.

150. Wan, Y.Z., G.Y. Xiong, H.L. Luo, F. He, Y. Huang, and Y.L. Wang, *Influence of zinc ion implantation on surface nanomechanical performance and corrosion resistance of biomedical magnesium-calcium alloys.* Applied Surface Science, 2008. **254**(17): p. 5514-5516.

151. Jamesh, M.I., G. Wu, Y. Zhao, D.R. McKenzie, M.M.M. Bilek, and P.K. Chu, *Effects of zirconium and oxygen plasma ion implantation on the corrosion behavior of zk60 mg alloy in simulated body fluids.* Corrosion Science, 2014. **82**(0): p. 7-26.

152. Xu, R.Z., X.B. Yang, K.W. Suen, G.S. Wu, P.H. Li, and P.K. Chu, *Improved corrosion resistance on biodegradable magnesium by zinc and aluminum ion implantation.* Applied Surface Science, 2012. **263**: p. 608-612.

153. Nakatsugawa, I., R. Martin, and E.J. Knystautas, *Improving corrosion resistance of az91d magnesium alloy by nitrogen ion implantation.* Corrosion, 1996. **52**(12): p. 921-926.

154. Pardo, A., M.C. Merino, M. Mohedano, P. Casajus, A.E. Coy, and R. Arrabal, *Corrosion behaviour of mg/al alloys with composite coatings.* Surface & Coatings Technology, 2009. **203**(9): p. 1252-1263.

155. Pardo, A., M.C. Merino, P. Casajus, M. Mohedano, R. Arrabal, and E. Matykina, *Corrosion behaviour of mg-al alloys with al-11si thermal spray coatings.* Materials and Corrosion-Werkstoffe Und Korrosion, 2009. **60**(12): p. 939-948.

156. Pardo, A., P. Casajus, M. Mohedano, A.E. Coy, F. Viejo, B. Torres, and E. Matykina, *Corrosion protection of mg/al alloys by thermal sprayed aluminium coatings.* Applied Surface Science, 2009. **255**(15): p. 6968-6977.

157. Arrabal, R., A. Pardo, M.C. Merino, S. Merino, P. Casajus, M. Mohedano, and P. Rodrigo, *Corrosion behavior of mg-al alloys with aluminum thermal spray coatings in humid and saline environments.* Corrosion, 2009. **65**(12): p. 817-830.

158. Majumdar, B., R. Galun, B.L. Mordike, Lia, and Lia, *Excimer laser treatment of magnesium alloy surface.* Icaleo(r) 2000: Proceedings of the laser materials processing conference, vol 89. Vol. 89. 2000. D151-D160.

159. Hiraga, H., T. Inoue, Y. Kojima, S. Kamado, and S. Watanabe, *Surface modification by dispersion of hard particles on magnesium alloy with laser*, in *Magnesium alloys 2000*, Y. Kojima, T. Aizawa, and S. Kamado, Editors. 2000. p. 253-258.

160. Montemor, M.F., *Functional and smart coatings for corrosion protection: A review of recent advances.* Surface & Coatings Technology, 2014. **258**: p. 17-37.

161. Xu, X.H., J. Cheng, C.H. Zhang, X.L. Yan, T.B. Zhu, K.D. Yao, L. Cao, and Y. Liu, *Bio-corrosion and polymer coating modification of magnesium alloys for medicine.* Rare Metal Materials and Engineering, 2008. **37**(7): p. 1225-1228.

162. Wang, H., Y. Estrin, and Z. Zuberova, *Bio-corrosion of a magnesium alloy with different processing histories.* Materials Letters, 2008. **62**(15): p. 2476-2479.

163. Liu, C.L., Y.C. Xin, G.Y. Tang, and P.K. Chu, *Influence of heat treatment on degradation behavior of bio-degradable die-cast az63 magnesium alloy in simulated body fluid.* Materials Science and Engineering a-Structural Materials Properties Microstructure and Processing, 2007. **456**(1-2): p. 350-357.

164. Rudd, A.L., C.B. Breslin, and F. Mansfeld, *The corrosion protection afforded by rare earth conversion coatings applied to magnesium.* Corrosion Science, 2000. **42**(2): p. 275-288.

165. Shigematsu, I., M. Nakamura, N. Saitou, and K. Shimojima, *Surface treatment of az91d magnesium alloy by aluminum diffusion coating.* Journal of Materials Science Letters, 2000. **19**(6): p. 473-475.

166. Kelly, P.J. and R.D. Arnell, *Magnetron sputtering: A review of recent developments and applications.* Vacuum, 2000. **56**(3): p. 159-172.

167. Wu, S.K., S.C. Yen, and T.S. Chou, *A study of r.F.-sputtered al and ni thin films on az91d magnesium alloy.* Surface and Coatings Technology, 2006. **200**(8): p. 2769-2774.

168. Reiners, G. and M. Griepentrog, *Hard coatings on magnesium alloys by sputter deposition using a pulsed dc bias voltage.* Surface & Coatings Technology, 1995. **76-77**(1-3): p. 809-814.

169. Zhang, J., D.H. Yang, and X.B. Ou, *Microstructures and properties of aluminum film and its effect on corrosion resistance of az31b*

substrate. Transactions of Nonferrous Metals Society of China, 2008. **18**: p. S312-S317.

170. Zhang, J., J. Zhang, and D. Yang, *Effect of aluminum coating by magnetron sputtering on corrosion resistance of az31b alloy.* 2011.

171. Taha, M.A., N.A. El-Mahallawy, R.M. Hammouda, and S.I. Nassef, *Pvd coating of mg-az31 by thin layer of al and al-si.* Journal of Coatings Technology and Research, 2010. **7**(6): p. 793-800.

172. Diplas, S., P. Tsakiropoulos, and R.M.D. Brydson, *Development of physical vapour deposited mg-zr alloys - part 1 - characterisation of as deposited alloys.* Materials Science and Technology, 1999. **15**(12): p. 1349-1357.

173. Diplas, S., P. Tsakiropoulos, R.M.D. Brydson, and J.F. Watts, *Development of physical vapour deposited mg-zr alloys - part 2 - characterisation of corrosion products.* Materials Science and Technology, 1999. **15**(12): p. 1359-1372.

174. Diplas, S., P. Tsakiropoulos, and R.M.D. Brydson, *Development of physical vapour deposited mg-zr alloys - part 3 - comparison of alloying and corrosion behaviour in mg-v and mg-zr physical vapour deposited alloys.* Materials Science and Technology, 1999. **15**(12): p. 1373-1378.

175. Diplas, S., P. Tsakiropoulos, and R.M.D. Brydson, *Development of mg-v alloys by physical vapour deposition part 1 - bulk and surface characterisation.* Materials Science and Technology, 1998. **14**(7): p. 689-698.

176. Diplas, S., P. Tsakiropoulos, R.M.D. Brydson, S. Dodd, and R.W. Gardiner, *Characterisation of physical vapour deposited mg-v alloys.* Proceedings of the third international magnesium conference, ed. G.W. Lorimer. 1997. 285-298.

177. Diplas, S., P. Tsakiropoulos, R.M.D. Brydson, and J.F. Watts, *A study of charge transfer in vapour deposited mg-v crystalline alloys via changes in auger parameters.* Philosophical Magazine a-Physics of Condensed Matter Structure Defects and Mechanical Properties, 1998. **77**(4): p. 1067-1079.

178. Mitchell, T., S. Diplas, and P. Tsakiropoulos, *Characterization of in situ mechanically worked pvd mg-ti alloys.* Philosophical Magazine, 2005. **85**(24): p. 2733-2756.

179. Hollstein, F., R. Wiedemann, and J. Scholz, *Characteristics of pvd-coatings on az31hp magnesium alloys.* Surface & Coatings Technology, 2003. **162**(2-3): p. 261-268.

180. Hoche, H., S. Groß, T. Troßmann, J. Schmidt, and M. Oechsner, *Pvd coating and substrate pretreatment concepts for magnesium alloys by multinary coatings based on ti(x)n.* Surface and Coatings Technology, 2013. **228, Supplement 1**(0): p. S336-S341.

181. Senf, J. and E. Broszeit, *Wear and corrosion protection of aluminum and magnesium alloys using chromium and chromium nitride pvd coatings.* Advanced Engineering Materials, 1999. **1**(2): p. 133-137.

182. Senf, J. and E. Broszeit, *Wear and corrosion protection using cr and crn (pvd coating on al and mg).* Materialwissenschaft Und Werkstofftechnik, 1999. **30**(5): p. 262-268.

183. Hoche, H., D. Allebrandt, H. Scheerer, E. Broszeit, and C. Berger, *Design of wear and corrosion resistant pvd-coatings for magnesium alloys.* Materialwissenschaft Und Werkstofftechnik, 2007. **38**(5): p. 365-371.

184. Fukumoto, S., K. Sugahara, A. Yamamoto, and H. Tsubakino, *Improvement of corrosion resistance and adhesion of coating layer for magnesium alloy coated with high purity magnesium.* Materials Transactions, 2003. **44**(4): p. 518-523.

185. Wu, G.S., X.Q. Zeng, W.B. Ding, X.W. Guo, and S.S. Yao, *Characterization of ceramic pvd thin films on az31 magnesium alloys.* Applied Surface Science, 2006. **252**(20): p. 7422-7429.

186. Wu, G.S., X.M. Wang, K.J. Ding, Y.Y. Zhou, and X.Q. Zeng, *Corrosion behavior of ti-al-n/ti-al duplex coating on az31 magnesium alloy in nacl aqueous solution.* Materials Characterization, 2009. **60**(8): p. 803-807.

187. Wu, G.S., K.J. Ding, X.Q. Zeng, X.M. Wang, and S.S. Yao, *Improving corrosion resistance of titanium-coated magnesium alloy by modifying surface characteristics of magnesium alloy prior to titanium coating deposition.* Scripta Materialia, 2009. **61**(3): p. 269-272.

188. Wu, G.S., W. Dai, H. Zheng, and A.Y. Wang, *Improving wear resistance and corrosion resistance of az31 magnesium alloy by dlc/aln/al coating.* Surface & Coatings Technology, 2010. **205**(7): p. 2067-2073.

189. Zhang, K.M. and J.X. Zou, *Formation of surface nano- and textured austenite induced by pulsed electron beam irradiation under melting mode.* Journal of Nanomaterials, 2013.

190. Surla, V. and D. Ruzic, *High-energy density beams and plasmas for micro- and nano-texturing of surfaces by rapid melting and solidification.* Journal of Physics D-Applied Physics, 2011. **44**(17).

191. Dong, C., A. Wu, S. Hao, J. Zou, Z. Liu, P. Zhong, A. Zhang, T. Xu, J. Chen, J. Xu, Q. Liu, and Z. Zhou, *Surface treatment by high current pulsed electron beam.* Surface & Coatings Technology, 2003. **163**: p. 620-624.

192. Hao, S.Z., Y. Qin, X.X. Mei, B. Gao, J.X. Zuo, Q.F. Guan, C. Dong, and Q.Y. Zhang, *Fundamentals and applications of material modification by intense pulsed beams.* Surface and Coatings Technology, 2007. **201**(19–20): p. 8588-8595.

193. Uno, Y., A. Okada, K. Uemura, P. Raharjo, S. Sano, Z. Yu, and S. Mishima, *A new polishing method of metal mold with large-area electron beam irradiation.* Journal of Materials Processing Technology, 2007. **187**: p. 77-80.

194. Okada, A., Y. Uno, N. Yabushita, K. Uemura, and P. Raharjo, *High efficient surface finishing of bio-titanium alloy by large-area electron beam irradiation.* Journal of Materials Processing Technology, 2004. **149**(1-3): p. 506-511.

195. Gao, Y.K., *Surface modification of ta2 pure titanium by low energy high current pulsed electron beam treatments.* Applied Surface Science, 2011. **257**(17): p. 7455-7460.

196. Gao, Y.K., *Surface modification of tc4 titanium alloy by high current pulsed electron beam (hcpeb) with different pulsed energy densities.* Journal of Alloys and Compounds, 2013. **572**: p. 180-185.

197. Gao, B., S. Hao, J. Zou, W. Wu, G. Tu, and C. Dong, *Effect of high current pulsed electron beam treatment on surface microstructure and wear and corrosion resistance of an az91hp magnesium alloy.* Surface and Coatings Technology, 2007. **201**(14): p. 6297-6303.

198. Proskurovsky, D.I., V.P. Rotshtein, G.E. Ozur, A.B. Markov, D.S. Nazarov, V.A. Shulov, Y.F. Ivanov, and R.G. Buchheit, *Pulsed electron-beam technology for surface modification of metallic materials.* Journal of Vacuum Science & Technology A, 1998. **16**(4): p. 2480-2488.

199. Proskurovsky, D.I., V.P. Rotshtein, G.E. Ozur, Y.F. Ivanov, and A.B. Markov, *Physical foundations for surface treatment of materials with low energy, high current electron beams.* Surface and Coatings Technology, 2000. **125**(1–3): p. 49-56.

200. Zhang, X.D., J.X. Zou, S. Weber, S.Z. Hao, C. Dong, and T. Grosdidier, *Microstructure and property modifications in a near alpha ti alloy*

induced by pulsed electron beam surface treatment. Surface & Coatings Technology, 2011. **206**(2-3): p. 295-304.

201. Hao, S., B. Gao, A. Wu, J. Zou, Y. Qin, C. Dong, J. An, and Q. Guan, *Surface modification of steels and magnesium alloy by high current pulsed electron beam.* Nuclear Instruments and Methods in Physics Research Section B: Beam Interactions with Materials and Atoms, 2005. **240**(3): p. 646-652.

202. Gao, B., Y. Hao, G.F. Tu, W.X. Shi, F.X. Yu, and S.W. Li, *Compounded surface modification of zk60 mg alloy by high current pulsed electron beam plus micro-plasma oxidation.* Plasma Science & Technology, 2010. **12**(1): p. 67-70.

203. Gao, B., Y. Hao, G.F. Tu, S.W. Li, S.Z. Hao, and C. Dong, *Enhanced wear resistance of al-15si and zk60-1y mg alloys induced by high current pulsed electron beam treatment*, in *Manufacturing process technology, pts 1-5*, Z.Y. Jiang, et al., Editors. 2011. p. 1204-1207.

204. Gao, B., S.Z. Hao, J.X. Zou, T. Grosdidier, L.M. Jiang, J.Y. Zhou, and C. Dong, *High current pulsed electron beam treatment of az31 mg alloy.* Journal of Vacuum Science & Technology A, 2005. **23**(6): p. 1548-1553.

205. Ye, H., R. Chen, and Z.L. Yan, *Study on surface modification of pure magnesium and magnesium alloy with high current pulsed electron beam*, in *Materials processing technology, pts 1-3*, X.H. Liu, Z. Jiang, and J.T. Han, Editors. 2012. p. 950-953.

206. Bo, G., H. Yi, T. Ganfeng, and Z. Wenfeng, *Surface modification of mg alloys az31 and zk60-1y by high current pulsed electron beam*. 2011: INTECH Open Access Publisher.

207. Gao, B., Y. Hao, G.F. Tu, S.W. Li, F.X. Yu, L. Zuo, and L. Hu, *Surface modification of mg-67-zn-30-y-3 quasicrystal alloy by high current pulsed electron beam.* Surface & Coatings Technology, 2013. **229**: p. 42-45.

208. Zhang, X.D., S.Z. Hao, T. Grosdidier, J.X. Zou, B. Gao, B. Bolle, N. Allain-Bonasso, Y. Qin, X.N. Li, and C. Dong, *Surface modification of light alloys by low-energy high-current pulsed electron beam.* Journal of Metallurgy, 2012. **2012**.

209. Abbas, G., Z. Liu, and P. Skeldon, *Corrosion behaviour of laser-melted magnesium alloys.* Applied Surface Science, 2005. **247**(1-4): p. 347-353.

210. Guan, Y.C., W. Zhou, and H.Y. Zheng, *Effect of laser surface melting on corrosion behaviour of az91d mg alloy in simulated-modified body fluid.* Journal of Applied Electrochemistry, 2009. **39**(9): p. 1457-1464.

211. Majumdar, J.D., R. Galun, B.L. Mordike, and I. Manna, *Effect of laser surface melting on corrosion and wear resistance of a commercial magnesium alloy.* Materials Science and Engineering a-Structural Materials Properties Microstructure and Processing, 2003. **361**(1-2): p. 119-129.

212. Mondal, A.K., S. Kumar, C. Blawert, and N.B. Dahotre, *Effect of laser surface treatment on corrosion and wear resistance of acm720 mg alloy.* Surface and Coatings Technology, 2008. **202**(14): p. 3187-3198.

213. Padmavathi, C., J.K.S. Sundar, S.V. Joshi, and K.P. Rao, *Effect of pulsed nd : Yag laser melting treatment on microstructural and corrosion behaviour of az91c mg alloy.* Materials Science and Technology, 2006. **22**(5): p. 583-589.

214. Dube, D., M. Fiset, A. Couture, and I. Nakatsugawa, *Characterization and performance of laser melted az91d and am60b.* Materials Science and Engineering a-Structural Materials Properties Microstructure and Processing, 2001. **299**(1-2): p. 38-45.

215. Guan, Y.C., W. Zhou, Z.L. Li, and H.Y. Zheng, *Influence of overlapping tracks on microstructure evolution and corrosion behavior in laser-melt magnesium alloy.* Materials & Design, 2013. **52**: p. 452-458.

216. Gao, Y., C. Wang, M. Yao, and H. Liu, *Corrosion behavior of laser melted az91hp magnesium alloy.* Materials and Corrosion-Werkstoffe Und Korrosion, 2007. **58**(6): p. 463-466.

217. Guo, L.F., T.M. Yue, and H.C. Man, *Excimer laser surface treatment of magnesium alloy we43 for corrosion resistance improvement.* Journal of Materials Science, 2005. **40**(13): p. 3531-3533.

218. Khalfaoui, W., E. Valerio, J.E. Masse, and M. Autric, *Excimer laser treatment of ze41 magnesium alloy for corrosion resistance and microhardness improvement.* Optics and Lasers in Engineering, 2010. **48**(9): p. 926-931.

219. Banerjee, P.C., R.K.S. Raman, Y. Durandet, and G. McAdam, *Influence of laser processing parameters on microstructure and corrosion kinetics of laser-treated ze41 magnesium alloy.* Metallurgical and Materials Transactions a-Physical Metallurgy and Materials Science, 2013. **44A**(5): p. 2346-2357.

220. Guan, Y.C., W. Zhou, Z.L. Li, and H.Y. Zheng, *Study on the solidification microstructure in az91d mg alloy after laser surface melting.* Applied Surface Science, 2009. **255**(19): p. 8235-8238.

221. Banerjee, P.C., R.K.S. Raman, Y. Durandet, and G. McAdam, *Electrochemical investigation of the influence of laser surface melting on the microstructure and corrosion behaviour of ze41 magnesium alloy - an eis based study.* Corrosion Science, 2011. **53**(4): p. 1505-1514.

222. Liu, S.Y., J.D. Hu, Y. Yang, Z.X. Guo, and H.Y. Wang, *Microstructure analysis of magnesium alloy melted by laser irradiation.* Applied Surface Science, 2005. **252**(5): p. 1723-1731.

223. Taltavull, C., B. Torres, A.J. Lopez, P. Rodrigo, and J. Rams, *Novel laser surface treatments on az91 magnesium alloy.* Surface & Coatings Technology, 2013. **222**: p. 118-127.

224. Coy, A.E., F. Viejo, F.J. Garcia-Garcia, Z. Liu, P. Skeldon, and G.E. Thompson, *Effect of excimer laser surface melting on the microstructure and corrosion performance of the die cast az91d magnesium alloy.* Corrosion Science, 2010. **52**(2): p. 387-397.

225. Guo, K.W., *A review of magnesium_magnesium alloys corrosion and its protection.* Recent Patents on Corrosion Science, 2010. **2**: p. 13-21.

226. Witte, F., *Biodegradable synthetic implant materials. Clinical applications and immunological aspects.* Der Orthopäde, 2008. **37**(2): p. 125-130.

227. Kirkland, N.T., J. Lespagnol, N. Birbilis, and M.P. Staiger, *A survey of bio-corrosion rates of magnesium alloys.* Corrosion Science, 2010. **52**(2): p. 287-291.

228. Fry, C., *Development of magnesium-based multilayer pvd coatings for hydrogen storage applications*, in *Mechanical, Materials and Manufacturing Engineering*. 2013, University of Nottingham.

229. Hu, J.J., G.B. Zhang, H.B. Xu, and T.C. Xu, *Study progress of material surface modification with large scale pulse electron beam*, in *Materials and computational mechanics, pts 1-3*, H.X. Zhang, et al., Editors. 2012. p. 1147-1151.

230. Misumi, S., A. Okada, Y. Okamoto, and M. Inoue, *Fundamental study on sputter deposition of ceramic film by large-area electron beam irradiation*, in *Proceedings of the seventeenth cirp conference on electro physical and chemical machining*, B. Lauwers and J.P. Kruth, Editors. 2013. p. 486-491.

231. Murray, J.W.H., *Damage, contamination and surface treatment of electrical discharge machined materials*, in *Material Engineering* 2014, University of Nottingham: Nottingham , UK.

232. Li, C., *Al-co-ce glass forming alloys and their corrosion behaviour*, in *Material Engineering* 2014, University of Nottingham: Nottingham, UK.

233. Watt, I.M., *The principles and practice of electron microscopy*. 1997: Cambridge University Press.

234. Goldstein, J., D.E. Newbury, P. Echlin, D.C. Joy, A.D. Romig Jr, C.E. Lyman, C. Fiori, and E. Lifshin, *Scanning electron microscopy and x-ray microanalysis: A text for biologists, materials scientists, and geologists*. 2012: Springer Science & Business Media.

235. Stokes, D., *Rms - royal microscopical society : Principles and practice of variable pressure : Environmental scanning electron microscopy (vp-esem) (1)*. 2008, Chichester, GB: Wiley.

236. Krumeich, F. *Bragg's law of diffraction*. [cited 2015; http://www.microscopy.ethz.ch/bragg.htm].

237. Wagner, J.M., *X-ray photoelectron spectroscopy*. 2011: Nova Science Publishers.

238. Rees, O.J., *Chemical engineering methods and technology : Fourier transform infrared spectroscopy: Developments, techniques and applications*. 2010, New York, US: Nova.

239. Almeida, T., *Hydrothermal synthesis and characterisation of α-fe2o3 nanorods*, in *Mechanical, Materials and Manufacturing Engineering*. 2010, University of Nottingham.

240. ASTM, A.S.f.T.a.M., *Standard test method for conducting cyclic potentiodynamic polarization measurements to determine the corrosion susceptibility of small implant devices*. 2015, ASTM International: PA, USA.

241. Werkhoven, R.J., W.H. Sillekens, and J.B.J.M. van Lieshout, *Processing aspects of magnesium alloy stent tube*, in *Magnesium technology 2011*. 2011, John Wiley & Sons, Inc. p. 419-424.

242. Gupta, V., A.D. Johnson, V. Martynov, and L. Menchaca, *Nitinol thin-film three-dimensional devices: Fabrication and applications*. Smst-2003: Proceedings of the international conference on shape memory and superelastic technologies, ed. A.R. Pelton and T. Duerig. 2004. 639-650.

243. Blawert, C., D. Manova, M. Stormer, J.W. Gerlach, W. Dietzel, and S. Mandl, *Correlation between texture and corrosion properties of magnesium coatings produced by pvd.* Surface & Coatings Technology, 2008. **202**(11): p. 2236-2240.

244. Garces, G., M.C. Cristina, M. Torralba, and P. Adeva, *Texture of magnesium alloy films growth by physical vapour deposition (pvd).* Journal of Alloys and Compounds, 2000. **309**(1-2): p. 229-238.

245. Stormer, M., C. Blawert, H. Hagen, V. Heitmann, and W. Dietzel, *Structure and corrosion of magnetron sputtered pure mg films on silicon substrates.* Plasma Processes and Polymers, 2007. **4**: p. S557-S561.

246. Grant, D.M., *Selective laser sintering of magnesium*. 2016, University of Nottingham: Nottingham.

247. Movchan, B.A. and Demchish.Av, *Study of structure and properties of thick vacuum condensates of nickel, titanium, tungsten, aluminium oxide and zirconium dioxide.* Physics of Metals and Metallography-Ussr, 1969. **28**(4): p. 83-&.

248. Thornton, J.A., *High-rate thick-film growth.* Annual Review of Materials Science, 1977. **7**: p. 239-260.

249. Thornton, J.A., *Influence of substrate temperature and deposition rate on structure of thick sputtered cu coatings.* Journal of Vacuum Science & Technology, 1975. **12**(4): p. 830-835.

250. Petrov, I., *Microstructural evolution during film growth.* Journal of vacuum science & technology. A, An international journal devoted to vacuum, surfaces, and films, 2003. **21**(5): p. 117.

251. Gautam, Y.K., A.K. Chawla, V. Chawla, R.D. Agrawal, and R. Chandra, *Influence of sputtering gas on morphological and optical properties of magnesium films.* Journal of Materials Science & Technology, 2011. **27**(1): p. 51-58.

252. Kogut, I. and M. Record, *Growth of magnesium suicide thin films on si(100), si(111) and soi substrates during rapid thermal processing.* Intermetallics, 2013. **32**: p. 184-193.

253. Tong, W., J. Chen, X. Li, J. Feng, Y. Cao, Z. Yang, and X. Zhang, *Preferred orientation of plasma sprayed hydroxyapatite coatings* Journal of Materials Science, 1995. **31**(14).

254. Bohne, Y., D. Manova, C. Blawert, M. Stormer, W. Dietzel, and S. Mandl, *Influence of ion energy on morphology and corrosion properties of mg alloys formed by energetic pvd processes.* Nuclear Instruments & Methods in Physics Research Section B-Beam Interactions with Materials and Atoms, 2007. **257**: p. 392-396.

255. Garcés, G. and P. Adeva, *Development and evolution of texture in mg–zr alloy deposited by physical vapor deposition.* Journal of Materials Research, 2011. **17**(3): p. 614-619.

256. Okui, N., *Relationship between crystallization temperature and melting temperature in crystalline materials.* Journal of Materials Science, 1990. **25**(3): p. 1623-1631.

257. Sahoo, S.K., R.K. Sabat, S. Panda, S.C. Mishra, and S. Suwas, *Mechanical property of pure magnesium: From orientation perspective pertaining to deviation from basal orientation.* Journal of Materials Engineering and Performance, 2015. **24**(6): p. 2346-2353.

258. Malheiros, L.R.C., R.B. Figueiredo, and T.G. Langdon, *Grain size and microhardness evolution during annealing of a magnesium alloy processed by high-pressure torsion.* Journal of Materials Research and Technology, 2015. **4**(1): p. 14-17.

259. Ichikawa, R., *Recrystallization temperature of high purity magnesium (part 4).* Journal of Japan Institute of Light Metals, 1956. **1956**(20): p. 93-98.

260. Thompson, C.V., *Structure evolution during processing of polycrystalline films.* Annual Review of Materials Science, 2000. **30**: p. 159-190.

261. Roy, R.K., *Recrystallization behavior of commercial purity aluminium alloys.* 2014.

262. Jr, S.F., J.C. Galván, A. Pardo, M.C. Merino, and R. Arrabal, *Native air-formed oxide film and its effect on magnesium alloys corrosion* The Open Corrosion Journal, 2010. **3**: p. 80-91.

263. Huang, R. and A.H. Kitai, *Temperature-dependence of the growth orientation of atomic layer growth mgo.* Applied physics letters, 1992. **61**(12): p. 1450-1452.

264. Vočadlo, L., A. Wall, S. Parker, and G.D. Price, *Absolute ionic diffusion in mgo—computer calculations via lattice dynamics.* Physics of the Earth and Planetary Interiors, 1995. **88**(3): p. 193-210.

265. *Material science and engineering hand book* Second ed, ed. J. Shackelford, W. Alexander, and J. Park. 1994, United State: CRC.

266. Khalajabadi, S.Z., M.R.A. Kadir, S. Izman, and R. Ebrahimi-Kahrizsangi, *Fabrication, bio-corrosion behavior and mechanical*

properties of a mg/ha/mgo nanocomposite for biomedical applications. Materials & Design, 2015. **88**: p. 1223-1233.

267. Yang, L., F. Feyerabend, K.U. Kainer, R. Willumeit, and N. Hort, *Corrosion behavior of as-cast binary mg-dy alloys*, in *Light metals technology v*, H. Dieringa, N. Hort, and K.U. Kainer, Editors. 2011. p. 417-421.

268. Yang, L., Y.D. Huang, Q.M. Peng, F. Feyerabend, K.U. Kainer, R. Willumeit, and N. Hort, *Mechanical and corrosion properties of binary mg-dy alloys for medical applications.* Materials Science and Engineering B-Advanced Functional Solid-State Materials, 2011. **176**(20): p. 1827-1834.

269. Oyane, A., H.M. Kim, T. Furuya, T. Kokubo, T. Miyazaki, and T. Nakamura, *Preparation and assessment of revised simulated body fluids.* Journal of Biomedical Materials Research Part A, 2003. **65**(2): p. 188-195.

270. Chen, X.B., N. Birbilis, and T.B. Abbott, *Effect of ca2+ and po43- levels on the formation of calcium phosphate conversion coatings on die-cast magnesium alloy az91d.* Corrosion Science, 2012. **55**: p. 226-232.

271. Song, Y., D. Shan, R. Chen, F. Zhang, and E.H. Han, *Biodegradable behaviors of az31 magnesium alloy in simulated body fluid.* Materials Science and Engineering C, 2009. **29**(3): p. 1039-1045.

272. Combes, C., B. Miao, R. Bareille, and C. Rey, *Preparation, physical-chemical characterisation and cytocompatibility of calcium carbonate cements.* Biomaterials, 2006. **27**(9): p. 1945-1954.

273. Creus, J., C. Berziou, S. Cohendoz, A. Perez, C. Rébéré, M. Reffass, S. Touzain, C. Allely, Y. Gachon, C. Héau, F. Sanchette, and A. Billard, *Reactivity classification in saline solution of magnetron sputtered or ebpvd pure metallic, nitride and al-based alloy coatings.* Corrosion Science, 2012. **57**: p. 162-173.

274. Cremer, R., K. Reichert, D. Neuschutz, G. Erkens, and I. Leyendecker, *Sputter deposition of crystalline alumina coatings.* Surface & Coatings Technology, 2003. **163**: p. 157-163.

275. Koski, K., J. Holsa, and P. Juliet, *Properties of aluminium oxide thin films deposited by reactive magnetron sputtering.* Thin Solid Films, 1999. **339**(1-2): p. 240-248.

276. Shih, T.-S. and Z.-B. Liu, *Thermally-formed oxide on aluminum and magnesium.* Materials Transactions, 2006. **47**(5): p. 1347-1353.

277. Zuzjakova, S., P. Zeman, and S. Kos, *Non-isothermal kinetics of phase transformations in magnetron sputtered alumina films with metastable structure.* Thermochimica Acta, 2013. **572**: p. 85-93.

278. Engelhart, W., W. Dreher, O. Eibl, and V. Schier, *Deposition of alumina thin film by dual magnetron sputtering: Is it gamma-al2o3?* Acta Materialia, 2011. **59**(20): p. 7757-7767.

279. Jeurgens, L.P.H., Z.M. Wang, and E.J. Mittemeijer, *Thermodynamics of reactions and phase transformations at interfaces and surfaces.* International Journal of Materials Research, 2009. **100**(10): p. 1281-1307.

280. Olsson, M.K., K. Macak, and W. Graf, *Reactive d.C. Magnetron sputter deposited al2o3 films: Large-area coatings for industrial applications.* Surface & Coatings Technology, 1999. **122**(2-3): p. 202-207.

281. Xin, Y., J. Jiang, K. Huo, G. Tang, X. Tian, and P.K. Chu, *Corrosion resistance and cytocompatibility of biodegradable surgical magnesium alloy coated with hydrogenated amorphous silicon.* Journal of Biomedical Materials Research Part A, 2009. **89A**(3): p. 717-726.

282. Dahmen, C., A. Janotta, D. Dimova-Malinovska, S. Marx, B. Jeschke, B. Nies, H. Kessler, and M. Stutzmann, *Surface functionalization of*

amorphous silicon and silicon suboxides for biological applications. Thin Solid Films, 2003. **427**(1-2): p. 201-207.

283. Liu, X.Y., P.K. Chu, and C.X. Ding, *Formation of apatite on hydrogenated amorphous silicon (a-si : H) film deposited by plasma-enhanced chemical vapor deposition.* Materials Chemistry and Physics, 2007. **101**(1): p. 124-128.

284. Wang, J., Y.-H. Yu, S.C. Lee, and Y.-W. Chung, *Tribological and optical properties of crystalline and amorphous alumina thin films grown by low-temperature reactive magnetron sputter-deposition.* Surface and Coatings Technology, 2001. **146–147**: p. 189-194.

285. Lin, S.-S., *Effect of fibered morphology on the properties of al2o3 nanoceramic films.* Ceramics International, 2013. **39**(3): p. 3157-3163.

286. Pranevicius, L., D. Milcius, L.L. Pranevicius, and G. Thomas, *Plasma hydrogenation of al, mg and mgal films under high-flux ion irradiation at elevated temperature.* Journal of Alloys and Compounds, 2004. **373**(1–2): p. 9-15.

287. Sun, G.J. and S.S. Kim, *Microstructure evolution of sputter-deposited al0.75mg0.25 alloy films.* Metals and Materials International, 2013. **19**(2): p. 211-215.

288. Shedden, B.A., M. Samandi, and B. Window, *Stoichiometry of unbalanced magnetron sputtered al-mg alloy coatings.* Surface & Coatings Technology, 1997. **97**(1-3): p. 557-563.

289. Zhang, J., D.-h. Yang, and X.-b. Ou, *Microstructures and properties of aluminum film and its effect on corrosion resistance of az31b substrate.* Transactions of Nonferrous Metals Society of China, 2008. **18, Supplement 1**(0): p. s312-s317.

290. ASM, I., *Asm handbook / prepared under the direction of the asm international alloy phase diagram and handbook committees.* Vol. 3. 1992: American Society for Metals International

291. Ambat, R. and E. Dwarakadasa, *Effect of hydrogen in aluminium and aluminium alloys: A review.* Bulletin of Materials Science, 1996. **19**(1): p. 103-114.

292. Grubac, Z., I.S. Roncevic, M. Metikos-Hukovic, R. Babic, M. Petravic, and R. Peter, *Surface modification of biodegradable magnesium alloys.* Journal of the Electrochemical Society, 2012. **159**(6): p. C253-C258.

293. Reichel, F., L.P.H. Jeurgens, G. Richter, and J. Mittemeijer, *Amorphous versus crystalline state for ultrathin al(2)o3 overgrowths on al substrates.* Journal of Applied Physics, 2008. **103**(9).

294. Borisova, N.V., E.P. Surovoy, and I.V. Titov, *Thermal transformations of aluminium-aluminium oxide systems in nanosize layers.* Bulletin of the Томск Polytechnic University, 2007. **310**(1): p. 102-106.

295. Nie, H.Q., M. Schoenitz, and E.L. Dreizin, *Oxidation of magnesium: Implication for aging and ignition.* Journal of Physical Chemistry C, 2016. **120**(2): p. 974-983.

296. Sleppy, W.C., *Oxidation of molten high-purity aluminum in dry oxygen.* Journal of the Electrochemical Society, 1962. **109**(8): p. C213-C213.

297. Xiong, D.P., X.G. Tang, W.R. Zhao, Q.X. Liu, Y.H. Wang, and S.L. Zhou, *Deposition of zno and mgzno films by magnetron sputtering.* Vacuum, 2013. **89**(0): p. 254-256.

298. Khana I A, R.A., Fatimaa A, Shahida M A K , Bokharib T H, Ahmadc R, *Cost effective deposition of aluminum oxide layers.* Journal of Basic & Applied Sciences, 2013. **9**: p. 252-258.

299. Zeng, R.C., Z.D. Lan, L.H. Kong, Y.D. Huang, and H.Z. Cui, *Characterization of calcium-modified zinc phosphate conversion*

coatings and their influences on corrosion resistance of az31 alloy. Surface & Coatings Technology, 2011. **205**(11): p. 3347-3355.

300. Ghali, E., *Corrosion resistance of aluminum and magnesium alloys : = understanding, performance, and testing / edward ghali*. Wiley series in corrosion. 2010: Wiley.

301. Carlisle, E.M., *Silicon as an essential trace-element in animal nutrition.* Ciba Foundation Symposia, 1986. **121**: p. 123-139.

302. Deal, B.E. and A. Grove, *General relationship for the thermal oxidation of silicon.* Journal of Applied Physics, 1965. **36**(12): p. 3770-3778.

303. Roushdey, S., *Defect related luminescence in silicon dioxide network: A review*, in *Crystalline silicon - properties and uses*, S. Basu, Editor. 2011, INTECH EUROPE: CROATIA. p. 1-344.

304. Falk, M., *Frequencies of h-o-h, h-o-d and d-o-d bending fundamentals in liquid water.* Journal of Raman Spectroscopy, 1990. **21**(9): p. 563-567.

305. Young, T.F., C.P. Chen, J.F. Liou, Y.L. Yang, and T.C. Chang, *Study on the si-si vibrational states of the near surface region of porous silicon.* Journal of Porous Materials, 2000. **7**(1-3): p. 339-343.

306. Gupta, P., V.L. Colvin, and S.M. George, *Hydrogen desorption-kinetics from monohydride and dihydride species on silicon surfaces.* Physical Review B, 1988. **37**(14): p. 8234-8243.

307. Fukaya, K., A. Tabata, and T. Mizutani, *Dependence on gas pressure of mu c-si : H prepared by rf magnetron sputtering.* Vacuum, 2004. **74**(3-4): p. 561-565.

308. Wang, W., J. Huang, X. Zhang, Y. Yang, W. Song, and F. Huang, *Crystallization of as-deposited amorphous silicon films on glass prepared by magnetron sputtering with different substrate biases and temperatures.* Journal of Crystal Growth, 2011. **321**(1): p. 50-54.

309. Savvides, N., *Deposition parameters and film properties of hydrogenated amorphous silicon prepared by high rate dc planar magnetron reactive sputtering.* Journal of Applied Physics, 1984. **55**(12): p. 4232-4238.

310. Lucovsky, G., J. Yang, S.S. Chao, J.E. Tyler, and W. Czubatyj, *Oxygen-bonding environments in glow-discharge deposited amorphous silicon-hydrogen alloy-films.* Physical Review B, 1983. **28**(6): p. 3225-3233.

311. Gunde, M.K., *Vibrational modes in amorphous silicon dioxide.* Physica B: Condensed Matter, 2000. **292**(3–4): p. 286-295.

312. Landreau, X., B. Lanfant, T. Merle, C. Dublanche-Tixier, and P. Tristant, *A thorough ft-ir spectroscopy study on micrometric silicon oxide films deposited by atmospheric pressure microwave plasma torch.* European Physical Journal D, 2012. **66**(6).

313. Pai, P.G., S.S. Chao, Y. Takagi, and G. Lucovsky, *Infrared spectroscopic study of siox films produced by plasma enhanced chemical vapor-deposition.* Journal of Vacuum Science & Technology a-Vacuum Surfaces and Films, 1986. **4**(3): p. 689-694.

314. Ono, H., T. Ikarashi, K. Ando, and T. Kitano, *Infrared studies of transition layers at sio2/si interface.* Journal of Applied Physics, 1998. **84**(11): p. 6064-6069.

315. Dove, P.M., N. Han, A.F. Wallace, and J.J. De Yoreo, *Kinetics of amorphous silica dissolution and the paradox of the silica polymorphs.* Proceedings of the National Academy of Sciences, 2008. **105**(29): p. 9903-9908.

316. Cerofolini, G.F., A. Giussani, F.C. Fabiani, A. Modelli, D. Mascolo, D. Ruggiero, D. Narducci, and E. Romano, *Combined ir and xps analysis of the native (100) surface of single-crystalline silicon after hfaq etching.* Surface and Interface Analysis, 2007. **39**(10): p. 836-844.

317. Weldon, M.K., K.T. Queeney, A.B. Gurevich, B.B. Stefanov, Y.J. Chabal, and K. Raghavachari, *Si-h bending modes as a probe of local chemical structure: Thermal and chemical routes to decomposition of h2o on si(100)-(2x1).* Journal of Chemical Physics, 2000. **113**(6): p. 2440-2446.

318. Brangule, A., K.A. Gross, and Iop, *Importance of ftir spectra deconvolution for the analysis of amorphous calcium phosphates*, in *12th russia/cis/baltic/japan symposium on ferroelectricity and 9th international conference on functional materials and nanotechnologies*. 2015.

319. Lee, J.H. and H.B. Lee, *A wettability gradient as a tool to study protein adsorption and cell-adhesion on polymer surfaces.* Journal of Biomaterials Science-Polymer Edition, 1993. **4**(5): p. 467-481.

320. Uno, Y., A. Okada, K. Uemura, P. Raharjo, T. Furukawa, and K. Karato, *High-efficiency finishing process for metal mold by large-area electron beam irradiation.* Precision Engineering-Journal of the International Societies for Precision Engineering and Nanotechnology, 2005. **29**(4): p. 449-455.

321. Zou, J., K. Zhang, T. Grosdidier, and C. Dong, *Analysis of the evaporation and re-condensation processes induced by pulsed beam treatments.* International Journal of Heat and Mass Transfer, 2013. **64**(0): p. 1172-1182.

322. Li, L., X. Xiang, Y. Lei, W. Liao, X.D. Yuan, S.B. He, X.D. Jiang, W.G. Zheng, and X.T. Zu, *A new method to investigate the intense pulsed ion beam ablation of silica.* Nuclear Instruments & Methods in Physics Research Section B-Beam Interactions with Materials and Atoms, 2013. **312**: p. 131-136.

323. Markov, A.B. and V.P. Rotshtein, *Calculation and experimental determination of dimensions of hardening and tempering zones in quenched u7a steel irradiated with a pulsed electron beam.* Nuclear Instruments & Methods in Physics Research Section B-Beam Interactions with Materials and Atoms, 1997. **132**(1): p. 79-86.

324. Zou, J.X., Y. Qin, C. Dong, X.G. Wang, A.M. Wu, and S.Z. Hao, *Numerical simulation of the thermal-mechanical process of high current pulsed electron beam treatment.* Journal of Vacuum Science & Technology A, 2004. **22**(3): p. 545-552.

325. Zhu, X.P., M.K. Lei, Z.H. Dong, S.M. Miao, and T.C. Ma, *Ablation of irradiated metals by high-intensity pulsed ion beam.* Journal of the Korean Physical Society, 2003. **42**: p. S787-S790.

326. Dong, Z.H., Z. Zhang, C. Liu, X.P. Zhu, and M.K. Lei, *Droplets from the metal surfaces irradiated by a high-intensity pulsed ion beam.* Applied Surface Science, 2006. **253**(5): p. 2557-2564.

327. Ptitsin, V.E., *On the theory of the electron beam ablation phenomenon*, in *Physica status solidi c: Current topics in solid state physics, vol 9, no 1*, W. Lei and Z. Zhao, Editors. 2012.

328. Li, P. and T.X. Peng, *Surface morphology of magnesium alloy irradiated by high-intensity pulsed ion beam.* Applied Surface Science, 2012. **258**(24): p. 9961-9968.

329. Jian-xin, Z., Q. Ying, G. Bo, Z. Ke-min, H. Sheng-zhi, W. Xiao-gang, and D. Chuang, *Surface melting and evaporation of pure mg bombarded by high current pulsed electron beam.* Transactions of Materials and Heat Treatment, 2005. **5**(1009-6264).

330. Qin, Y., C. Dong, X.G. Wang, S.Z. Hao, A.M. Wu, J.X. Zou, and Y. Liu, *Temperature profile and crater formation induced in high-current pulsed electron beam processing.* Journal of Vacuum Science & Technology A, 2003. **21**(6): p. 1934-1938.

331. Qin, Y., J.X. Zou, C. Dong, X.G. Wang, A.M. Wu, Y. Liu, S.Z. Hao, and Q.F. Guan, *Temperature-stress fields and related phenomena induced by a high current pulsed electron beam.* Nuclear Instruments & Methods in Physics Research Section B-Beam Interactions with Materials and Atoms, 2004. **225**(4): p. 544-554.

332. Qin, Y., C. Dong, Z. Song, S. Hao, X. Me, J. Li, X. Wang, J. Zou, and T. Grosdidier, *Deep modification of materials by thermal stress wave generated by irradiation of high-current pulsed electron beams.* Journal of Vacuum Science & Technology A, 2009. **27**(3): p. 430-435.

333. Zhang, K.M., J.X. Zou, T. Grosdidier, N. Gey, D.Z. Yang, S.Z. Hao, and C. Dong, *Surface modification of ni (50.6 at.%) ti by high current pulsed electron beam treatment.* Journal of Alloys and Compounds, 2007. **434**: p. 682-685.

334. Li, P., M.K. Lei, and X.P. Zhu, *Surface composition, microstructure and corrosion resistance of az31 magnesium alloy irradiated by high-intensity pulsed ion beam.* Materials Characterization, 2011. **62**(6): p. 599-605.

335. Zhang, K.M., D.Z. Yang, J.X. Zou, T. Grosdidier, and C. Dong, *Improved in vitro corrosion resistance of a niti alloy by high current pulsed electron beam treatment.* Surface & Coatings Technology, 2006. **201**(6): p. 3096-3102.

336. Walter, R. and M.B. Kannan, *Influence of surface roughness on the corrosion behaviour of magnesium alloy.* Materials & Design, 2011. **32**(4): p. 2350-2354.

337. Zhang, K., J. Zou, J. Li, and Z. Yu, *Ebsd characterization of the laser remelted surface layers in a commercially pure mg.* Journal of Materials Science & Technology, 2014. **30**(3): p. 263-267.

338. Kwok, C.T., K.H. Lo, W.K. Chan, F.T. Cheng, and H.C. Man, *Effect of laser surface melting on intergranular corrosion behaviour of aged austenitic and duplex stainless steels.* Corrosion Science, 2011. **53**(4): p. 1581-1591.

339. Kwok, C.T., F.T. Cheng, and H.C. Man, *Microstructure and corrosion behavior of laser surface-melted high-speed steels.* Surface and Coatings Technology, 2007. **202**(2): p. 336-348.

340. Chong, P.H., Z. Liu, P. Skeldon, and G.E. Thompson, *Large area laser surface treatment of aluminium alloys for pitting corrosion protection.* Applied Surface Science, 2003. **208–209**: p. 399-404.

341. Osório, W.R., N. Cheung, J.E. Spinelli, K.S. Cruz, and A. Garcia, *Microstructural modification by laser surface remelting and its effect on the corrosion resistance of an al–9 wt%si casting alloy.* Applied Surface Science, 2008. **254**(9): p. 2763-2770.

342. Laazizi, A., B. Courant, F. Jacquemin, and H. Andrzejewski, *Applied multi-pulsed laser in surface treatment and numerical-experimental analysis.* Optics and Laser Technology, 2011. **43**(7): p. 1257-1263.

343. Guan, Y., W. Zhou, Z. Li, and H. Zheng, *Boiling effect in crater development on magnesium surface induced by laser melting.* Surface & Coatings Technology, 2014. **252**: p. 168-172.

344. Pierron, N., P. Sallamand, and S. Mattei, *Study of magnesium and aluminum alloys absorption coefficient during nd : Yag laser interaction.* Applied Surface Science, 2007. **253**(6): p. 3208-3214.

345. Xie, J. and A. Kar, *Mathematical modeling of melting during laser materials processing.* Journal of Applied Physics, 1997. **81**(7): p. 3015-3022.

346. Zhang, K.M., J.X. Zou, J. Li, and Z.S. Yu, *Ebsd characterization of the laser remelted surface layers in a commercially pure mg.* Journal of Materials Science & Technology, 2014. **30**(3): p. 263-267.

347. Taltavull, C., B. Torres, A.J. Lopez, P. Rodrigo, E. Otero, A. Atrens, and J. Rams, *Corrosion behaviour of laser surface melted magnesium alloy az91d.* Materials & Design, 2014. **57**: p. 40-50.

348. Virtanen, S., H. Bohni, R. Busin, T. Marchione, M. Pierantoni, and E. Blank, *The effect of laser-surface modification on the corrosion behavior of fe and al base alloys.* Corrosion Science, 1994. **36**(9): p. 1623-&.

349. Watkins, K.G., Z. Liu, M. McMahon, R. Vilar, and M.G.S. Ferreira, *Influence of the overlapped area on the corrosion behaviour of laser treated aluminium alloys.* Materials Science and Engineering: A, 1998. **252**(2): p. 292-300.

350. Song, G. and A. Atrens, *Understanding magnesium corrosion. A framework for improved alloy performance.* Advanced Engineering Materials, 2003. **5**(12): p. 837-858.

351. Zhao, X., L.-l. Shi, and J. Xu, *A comparison of corrosion behavior in saline environment: Rare earth metals (y, nd, gd, dy) for alloying of biodegradable magnesium alloys.* Journal of Materials Science & Technology, 2013. **29**(9): p. 781-787.

352. Heakal, F.E.-T., O.S. Shehata, and N.S. Tantawy, *Degradation behaviour of az80e magnesium alloy exposed to phosphate buffer saline medium.* Corrosion Science, 2014. **86**: p. 285-294.

353. Xu, L.P., G.N. Yu, E. Zhang, F. Pan, and K. Yang, *In vivo corrosion behavior of mg-mn-zn alloy for bone implant application.* Journal of Biomedical Materials Research Part A, 2007. **83A**(3): p. 703-711.